



Multifunctional Magnetically loaded Polyorganosiloxane Nanocomposites for Biomedical Applications

Dissertation

zur Erlangung des Grades
„Doktor der Naturwissenschaften“
im Promotionsfach Chemie

am Fachbereich Chemie, Pharmazie und Geowissenschaften
der Johannes Gutenberg-Universität Mainz.

Stefanie Utech

Geboren in Neustadt/Wstr.

Mainz 2011

Die vorliegende Arbeit wurde im Zeitraum von Dezember 2007 bis Februar 2011 am Institut für Physikalische Chemie der Johannes Gutenberg-Universität Mainz angefertigt.

Dekan:

1. Berichterstatter:

2. Berichterstatter:

Tag der mündlichen Prüfung:

Curiosity is the essence of the scientific mind.

Bill Watterson, Calvin and Hobbes

Abstracts

Multifunktionelle magnetisch beladene Polyorganosiloxan Nanopartikel für biomedizinische Anwendungen

Während der letzten Jahrzehnte haben funktionelle Nanopartikel zunehmend wissenschaftliches Interesse geweckt. Besonders in biomedizinischen Anwendungen finden multifunktionelle polymere Materialien vielseitige Einsatzmöglichkeiten beispielsweise als farbstofffunktionalisierte Marker oder wirkstoffbeladene Transportsysteme. Der Einbau magnetischer Nanopartikel ermöglicht zusätzlich eine magnetische Detektion und Manipulation. Ein vielversprechendes System auf dem Weg zu multifunktionellen Nanopartikeln stellen Polyorganosiloxan Partikel dar. Durch Polykondensation von Silanmonomeren in wässriger Dispersion können Polyorganosiloxan Nanopartikel im Größenbereich von 10 bis 150 nm im Durchmesser hergestellt werden. Die vielseitige Silanchemie ermöglicht den Aufbau multifunktionaler Netzwerksysteme. In der vorliegenden Arbeit, konnten hydrophile Eisenoxidnanopartikel effizient und unter Erhalt ihrer superparamagnetischen Eigenschaften in die Polymerpartikel eingebaut werden. Der Einfluss verschiedener Partikelgrößen sowie verschiedener Eisenoxidgehalte wurde untersucht. Durch den Aufbau einer Kern-Schale-Architektur konnte eine gezielte Modifizierung des Partikelinneren und der Partikeloberfläche erreicht werden. Durch den Einbau fluoreszenzmodifizierter Monomere konnte eine Farbstoffmarkierung des Partikelkerns erzielt werden. Zusätzlich wurde eine hydrophile Oberflächenmodifizierung mittels Polyethlenoxid durchgeführt. Die Funktionalisierungen wurden unabhängig voneinander sowie in Kombination durchgeführt und der Einfluss der Funktionalisierung auf die Effizienz der magnetischen Beladung untersucht. Die Anwendbarkeit der synthetisierten Partikel in biomedizinischen Anwendungen wurde mit Hilfe von Zellaufnahme und Toxizitätstests nachgewiesen. Des Weiteren wurden biofunktionalisierte Partikel mittels EDC-Kopplung mit Biotin und Insulin hergestellt.

Multifunctional Magnetically Loaded Polyorganosiloxane Nanoparticles for Biomedical Applications

For the last few decades, the interest in functional nanomaterials is steadily increasing. Especially, in biomedicine the range of possible applications of multifunctional nanoparticles including dye-labeled markers and drug loaded carrier systems is extraordinary large. The incorporation of magnetic nanoparticles allows for an additional magnetic detection and manipulation. One promising system on the way to multifunctional nanomaterials is the polyorganosiloxane system. Via polycondensation of silan monomers in aqueous dispersion polyorganosiloxane nanoparticles with particle diameter between 10 and 150 nm can be synthesized. The versatile silane chemistry allows for the design of multifunctional network structures. In this work, hydrophilic iron oxide nanoparticles could be encapsulated into the polymeric particles in a highly efficient process whereat the superparamagnetic nature of the inorganic particles was restrained. The influence of different sized particles as well as the amount of the incorporated material was investigated. Using a core-shell architecture, controlled core and surface modifications could be achieved. An effective fluorescent labeling was performed via incorporation of dye-labeled monomers. Additionally, a hydrophilic surface modification was carried out via a grafting onto process of poly(ethylene glycol). Individual core and surface functionalization was achieved and the influence of the modification on the efficiency of the magnetic loading was tested. The applicability of the multifunctional particles in biological systems was proved via cellular uptake and toxicity testings. Furthermore, biofunctionalized particles were synthesized by EDC coupling using biotin and insulin.

Contents

1 Introduction	13
1.1 Introduction.....	13
1.2 Motivation.....	16
2 Theoretical Background	17
2.1 Magnetic Nanoparticles	17
2.1.1 Magnetism.....	17
2.1.2 Magnetic fields are described by the magnetic induction B and the magnetic field strength H . In vacuum the following equation results:	17
2.1.2.1 Superparamagnetism	19
2.1.2.1.1 Blocking Temperature.....	20
2.1.2.1.2 Size-Dependence of the Magnetization.....	20
2.1.3 Magnetic Iron Oxide Nanoparticles	21
2.1.4 Synthesis	22
2.1.4.1 Coprecipitation Process.....	22
2.1.4.2 Thermal Decomposition.....	24
2.1.4.3 Sol-Gel Process	25
2.1.5 Magnetic Nanoparticles for Biomedical Applications	25
2.1.5.1 Functionalization of Magnetic Particles for Biomedical Applications	27
2.1.5.2 Biomedical Applications	27
2.1.5.2.1 Magnetic Resonance Imaging (MRI).....	28
2.1.5.2.2 Magnetic Separation.....	29
2.1.5.2.3 Drug Delivery.....	29
2.1.5.2.4 Hyperthermia.....	30
2.2 Polyorganosiloxane Nanoparticles.....	32
2.2.1 Hydrolysis of Alkoxysilanes	32
2.2.2 Condensation of Alkoxysilanes.....	33
2.2.3 Polycondensation of Alkoxysilanes in Aqueous Dispersions	35
2.2.4 Redispersable Polyorganosiloxane Networks	36
2.2.5 Functional Polyorganosiloxane Networks	37
2.2.5.1 Dye-labeled Monomers	38
2.2.5.2 Heterofunctional Poly(ethylene glycol)	40
2.2.5.3 Biofunctionalization.....	41

3 Characterization Methods.....	43
3.1 Transmission Electron Microscopy.....	43
3.1.1 Transmission Electron Microscopy (TEM).....	43
3.1.2 Cryogenic Electron Microscopy (cryo-TEM).....	44
3.1.3 Energy Dispersive X-ray Spectroscopy (EDX).....	44
3.2 Asymmetrical Flow Field-Flow Fractionation (AF-FFF).....	44
3.3 Light Scattering,.....	45
3.3.1 Static Light Scattering (SLS).....	46
3.3.2 Dynamic Light Scattering (DLS).....	48
3.3.3 The ρ -ratio.....	50
3.4 Super Conducting Quantum Interference Device (SQUID).....	51
3.5 Mössbauer Spectroscopy.....	52
3.6 X-ray Powder Diffraction (XRD).....	54
3.7 Matrix Assisted LASER Desorption/Ionisation-Time of Flight Mass Spectrometry (MALDI-TOF).....	54
3.8 Gel Permeation Chromatography (GPC).....	55
3.9 Fluorescence Measurements.....	56
3.9.1 Fluorescence Spectroscopy.....	56
3.9.2 Fluorescence Microscopy.....	57
3.10 ζ -Potential.....	58
3.11 Ultraviolet/Visible Light Spectroscopy (UV/VIS spectroscopy).....	61
4 Results and Discussion.....	63
4.1 Magnetic Iron Oxide Nanoparticles.....	63
4.1.1 Introduction.....	63
4.1.2 Magnetic Iron Oxide Nanoparticles.....	64
4.1.3 Summary.....	71
4.2 Magnetically loaded Polyorganosiloxane Nanospheres.....	72
4.2.1 Introduction.....	72
4.2.2 Magnetically loaded Polyorganosiloxane Nanoparticles.....	74
4.2.2.1 Incorporation of Particles with $R_h = 3.2$ nm (Fe_xO_y -I).....	74
4.2.2.2 Magnetic Separation.....	82
4.2.2.3 Incorporation of larger Iron Oxide Nanoparticles.....	88
4.2.2.3.1 Incorporation of Particles with $R_h = 5.6$ nm (Fe_xO_y -II).....	89
4.2.2.3.2 Incorporation of Particles with $R_h = 9.2$ nm (Fe_xO_y -IV).....	90
4.2.2.3.3 Comparison of the Encapsulation Efficiency of different sized Particles.....	91
4.2.2.4 Summary.....	93

4.2.3 Functionalizations	95
4.2.3.1 Introduction.....	95
4.2.3.2 Core Modification: Fluorescent Labeling	95
4.2.3.3 Surface Modification: Biocompatibility through Grafting onto of PEG.....	104
4.2.3.3.1 Heterofunctional Poly(ethylene glycol)	105
4.2.3.3.2 Hydrosilation Reaction.....	106
4.2.3.4 Combination of Core and Surface Modification: Water-soluble Magnetofluorescent Polyorganosiloxane Nanoparticles.....	112
4.2.3.4.1 Fluorescence Measurements	117
4.2.3.4.2 Particle Behavior in Solution: Fluorescence Microscopy Analysis	119
4.2.3.4.3 Interactions with Biological Systems: Cell Testings.....	125
4.2.3.5 Biofunctionalization.....	130
4.2.3.5.1 Introduction	130
4.2.3.5.2 Biotinylation of Flu-Fe _x O _y -I _{2.3%} @POS-PEG-II.....	131
4.2.3.5.3 Insulin-Functionalization of Flu-Fe _x O _y -I _{2.3%} @POS-PEG-II	135
4.2.3.6 Summary	136
5 Conclusions and Outlook.....	139
5.1 Conclusion	139
5.2 Outlook.....	141
6 Materials and Methods.....	143
6.1 Materials.....	143
6.1.1 Synthesis of Magnetic Iron Oxide Nanoparticles.....	143
6.1.2 Encapsulation of Magnetic Nanoparticles into Polyorganosiloxane System	143
6.1.2.1 End Capping Process.....	144
6.1.2.2 Magnetic Separation.....	144
6.1.3 Magnetofluorescent Polyorganosiloxane Nanoparticles	144
6.1.3.1 Fluorescent labeling of ClBz-T (DyeBz-T)	144
6.1.3.2 Magnetofluorescent Polyorganosiloxane Nanoparticles (Dye-Fe _x O _y -I@POS)	145
6.1.4 Surface Functionalization of Magnetofluorescent Polyorganosiloxane Nanoparticles	145
6.1.4.1 Hydrid-functionalized Polyorganosiloxane Nanoparticles	145
6.1.4.2 Synthesis of Heterofunctional Poly(ethylene glycol) (PEG)	146
6.1.4.3 Hydrosilation Reaction.....	146
6.1.5 Biomodification.....	147
6.2 Methods.....	147
6.2.1 Electron Microscopy	147

6.2.1.1 Transmission Electron Microscopy (TEM).....	147
6.2.1.2 Cryogene Electron Microscopy (cryo-TEM)	147
6.2.2 Asymmetrical flow field-flow fractionation (AF-FFF)	147
6.2.3 Light Scattering	147
6.2.4 Super Conducting Quantum Interference Device (SQUID).....	148
6.2.5 Mössbauer Spectroscopy	148
6.2.6 MALDI-TOF	148
6.2.7 Size Exclusion Chromatography (SEC)	148
6.2.8 Fluorescence Measurements.....	148
6.2.8.1 Fluorescence Spectroscopy	148
6.2.8.2 Fluorescence Microcopy	148
6.2.9 ζ -potential.....	148
6.2.10 Cell Testings.....	149
7 Appendix	151
8 Abbreviations.....	167
9 Acknowledgement	171
10 Curriculum vitae	173

1 Introduction

1.1 Introduction

“There’s Plenty of Room at the Bottom”, stated Richard Feynmans in 1959 in this famous talk at the Annual Meeting of the American Physical Society.¹ He proposed the scaling down to nano level. The foundation for nanotechnology was laid. The word “nano” derives from the ancient Greek word *nanos* (“dwarf”) and describes the part of a billion (10^{-9}). Nanotechnology deals with materials with sizes between 1 and 100 nm. In this dimension, surface properties become significantly important due to the large surface to volume ratio of small particles. Additionally, unique size-dependent properties of materials emerge. Beside the extraordinary high reactivity of nano-sized materials, fascinating and so-far unknown optical and magnetical properties were discovered. For example, gold and CdSe nanoparticles (so-called quantum dots) show size-dependent optical properties due to the existence of discrete energetic states. Another specific property of nanomaterials concerning magnetism was found, since sufficiently small magnetic nanoparticles behave like individual magnets. The atomic moments maintain their ordered state relative to each other while the resulting magnetic moment of the particle is free to rotate above a characteristic temperature.² In presence of an external magnetic field, the particles show extraordinary strong magnetic properties.

This so-called superparamagnetic behavior was a stunning new discovery, even though magnetism has been known for millennia. Reports on magnetic materials and their specific properties can be found already 800 BC. According to the “Naturalis Historia” which was published 50 BC, the word “magnet” can be traced back to the shepherd Magnes.³ The legend tells that the nails of his shoes adhered to the ground while he was herding his sheep. The phenomenon magnetism has been studied intensively, starting from early investigations and interpretations in the 13th century where Petrus Pergrinus published the “Epistola de Magnete”. This study on free pivoting compass needles was the first detailed investigation on the properties of magnetic materials. In 1600, the English physicist William Gilbert systematically studied the properties of magnetic ores in his book “De magnete magneticisque corporibus et de magno magnete Tellure physiologia nova” (On the Magnet and Magnetic Bodies, and on the Great Magnet the Earth). He could prove that the earth itself behaves as a

¹ Feynman; R. P. *There is plenty of room at the bottom*. Presented at the „Annual Meeting of the American Physical Society“ Pasadena, **1959**

² Pankhurst, Q. A.; Connelly, J.; Jones, S. K.; Dobson, J. *J. Phys. D: Appl. Phys.* **2003**, *36*, R167

³ Gaius Plinius Secundus *Historia Naturalis*

giant magnet and that this is the reason for compass needles pointing to the north.⁴ The first quantitative measurement of magnetic properties and magnetic fields were possible in 1760 when John Michell invented a balance which allowed for the measurement of magnetic forces.⁵ In the late 1860th James Clerk Maxwell defined the famous Maxwell Equations. These four equations describe the relations between electric and magnetic fields as well as the important statement that magnetic monopoles do not exist meaning that the basic entity for magnetism is the inseparable magnetic dipole. Today, the area of applications covers daily life, science and technology and is steadily increasing. The discovery of superparamagnetic materials dramatically amplified the area of application. In the 1950s, the “National Aeronautics and Space Administration” (NASA) was searching for a way to controll liquids in space. To solve this problem, S. Pappell developed a liquid that could be controlled by magnetic fields.⁶ This development was an important step towards modern magnetic materials. These so-called ferrofluids are stable dispersions of superparamagnetic iron oxide nanoparticles. In presence of a magnetic field, the viscosity of the dispersion changes due to the magnetic interactions between the superparamagnetic particles. The applications of ferrofluids cover almost all fields of today’s technology, including industrial use as sealing and damping materials as well as medical examinations where superparamagnetic nanoparticles are used as contrast agents in magnetic resonance imaging. Superparamagnetism is preferred for biomedical applications because an easy distribution and transport of the particles in the biological system is guaranteed since the particles show no specific interaction with each other during the absence of the magnetic field.^{7,8}

Nanoparticles are generally of high interest for biomedical applications. Their small size which is in the comparable to those of viruses (20-450 nm), proteins (5-50 nm) or genes (2 nm wide and 10-100 nm long) allows them to penetrate biological barriers and get close to the entity of interest.² Cellular uptake of nanoparticles occurs via different pathways depending on the particle size (phagocytosis in case of particle sizes above approximately 0.5 μm and pinocytosis for smaller particles). Additionally, adequate surface properties are necessary to provide cellular uptake; not only regarding receptor mediated endocytosis. The surface properties are in general one of the most important factors for the applicability of nanoparticles in biomedical applications. Typically, the stability of colloidal particles is extremely sensitive to environmental conditions. Physiological salt concentrations and pH-ranges are challenging conditions for the stability of nanoparticles.⁹ Additionally, undesired interactions either between the particles themselves or between the particles and the biological environment can occur. In order to prevent aggregation or sedimentation of the particles and biodegradation, an

⁴ Langdon-Brown, W. *Nature* **1944**, 154, 136

⁵ Cavendish, H. *Philos. Trans. R. Soc. Lond.* **1798**, 88, 469

⁶ Berger, P.; Adelman, N. B.; Beckman, K. J.; Campbell, D. J.; Ellis, A. B.; Lisensky, G. C. *J. Chem. Ed.* **1999**, 79, 943

⁷ a) Bangs, L. B. *Pure Appl. Chem.* **1996**, 68, 1873; b) Joubert, J. C. *Anales de Quimica Int. Ed.* **1997**, 93, 70

⁸ Rye, P. D. *Bio/Technology* **1996**, 14, 155

⁹ Tartaj, P.; del Puerto Morales, M.; Veintemillas-Verdaguer, S.; González-Carreño, T.; Serna, C. J. *J. Phys. D: Appl. Phys.* **2003**, 36, R182

adequate stabilization of the particles becomes mandatory. In case of inorganic nanoparticles, ensuring water-solubility and biocompatibility is an additional afford. An outranging number of biocompatible nanomaterials is reported in literature.^{2,10} Different stabilization materials are mentioned including inorganic materials like TiO₂ or SiO₂, synthetic polymers, polystyrene, poly(ethylene glycol), e.g., and biomolecules (for example dextrane, liposides). One of the most promising coating materials are synthetic polymers. The availability of versatile polymeric materials in combination with the possibility of subsequent modification and functionalization makes them excellent candidates for this task. The interest in multifunctional nanomaterials is steadily increasing.¹¹ During the last few decades, biomedical research started to focus on new therapeutic and analytic methods in particular cancer treatments. The trend is leading to quick, easy, versatile and well-tolerated methods. The investigation of multifunctional nanoparticles plays an important role in this development. The combination of different functionalizations within one particle allows simultaneous analysis and therapy. For example, the use of drug loaded nanocontainers functionalized with biomolecules like antigens or antibodies, can drastically reduce the dose of the applied drug. These so-called drug delivery systems allow for a controlled transport of the drug to the affected region in the body. Hence, a distribution of the drug in the whole body is avoided and the dose of the drug can be reduced as well as undesired influences on healthy cells and tissue. The specific interaction or recognition between the particles and target molecules can be used for controlled distribution of the particles and therefore, delivery of the drug e.g. to the malignant cell. By preparation of drug-loaded, dye labeled particles, simultaneous imaging and therapy becomes possible.

One promising system on the way to multifunctional coating materials are polyorganosiloxane nanoparticles.¹² The polycondensation of alkoxy silanes in aqueous dispersion leads to the formation of polyorganosiloxane nanoparticles. By using di- and trifunctional monomers, network structures are created. The particles are very flexible with respect to particle size, architecture, composition and network density. The versatility of silane chemistry offers the possibility of many different functionalizations.^{13, 14, 15} In combination with a core-shell architecture multifunctional, multicompartiment nanoparticles can be obtained.

¹⁰ Berry, C. C.; Curtis, A. S. G. *J. Phys. D* **2003**, *36*, R198

¹¹ Gao, J.; Gu, H.; Xu, B. *Acc. Chem. Res.* **2009**, *42*, 1097

¹² Jungmann, N.; Schmidt, M.; Maskos, M.; Weis, J.; Ebenhoch, J. *Macromolecules* **2002**, *35*, 6851

¹³ Diehl, C.; Fluegel, S.; Fischer, K., Maskos, M. *Prog. Colloid Polym. Sci.* **2008**, *134*, 128

¹⁴ Jungmann, N.; Schmidt, M.; Ebenhoch, J.; Weis, J.; Maskos M. *Angew. Chem. Int. Ed.* **2003**, *42*, 1713

¹⁵ Jungmann, N.; Schmidt, M.; Maskos, M. *Macromolecules* **2003**, *36*, 3974

1.2 Motivation

In previous work, the polyorganosiloxane system was intensively studied regarding particle size and particle size distribution.^{16, 17} In recent investigations, the potential use of nanoparticles as nanocontainers and nanoreactors was tested, along with biomedical applicability.¹³

The aim of this work was the development of a multifunctional magnetically loaded polyorganosiloxane system. The magnetic functionalization of polymeric nanoparticles is of high interest for biomedical applications since a magnetic manipulation of the particles becomes possible. In combination with a multicompartment architecture, an extraordinary large field of imaginable applications arises. For example, magnetically accessible nanocontainers can be synthesized which are promising material for drug delivery approaches since the distribution of the particles can be controlled using external magnetic fields. Due to the flexibility of the polyorganosiloxane system and the versatile silane chemistry, various applications like imaging, drug delivery, hyperthermia, e.g., can be imagined.

This study included the synthesis and characterization of magnetic nanoparticles as well as the encapsulation of these particles into the polyorganosiloxane network. Different magnetic nanoparticles were synthesized and incorporated into the polymeric system to probe the efficiency of the encapsulation process and to provide a highly efficient magnetic loading. For versatility, a core-shell architecture was chosen. Controlled functionalization or modification of the different compartments inside the polymeric system was investigated. This included fluorescent core and hydrophilic surface modifications as well as the coupling of biomolecules to the particle surface. Besides the synthesis and characterization, the interaction between the particles and the biological environment with respect to cytotoxicity and cellular uptake was tested.

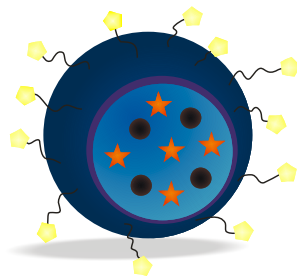


Figure 1.1 Schematic illustration of multifunctional magnetically loaded polyorganosiloxane nanoparticles (● polyorganosiloxane core; ● polyorganosiloxane shell; ● magnetic particle; ★ fluorescent dye; ~ hydrophilic polymer; ◆ biomolecules)

¹⁶ a) Jungmann, N.; Schmidt, M.; Maskos, M. *Macromolecules* **2001**, *34*, 8347; b) Scherer, C.; Noskov, N.; Utech, S.; Bantz, C.; Mueller, W.; Krohne, K.; Maskos, M. *J. Nanosci. Nanotechnol.* **2010**, *10*, 6834

¹⁷ Scherer, C.; Utech, S.; Scholz, S.; Noskov, S.; Kindervater, P.; Graf, R.; Thünemann, A. F.; Maskos, M. *Polymer* **2010**, *51*, 5432

2 Theoretical Background

2.1 Magnetic Nanoparticles

The interest in magnetic nanoparticles has been increasing over the last few decades in nearly all areas of materials science and engineering research. Possible applications cover range from magnetic sensor technology, catalyses, data-storage, to biotechnology and biomedical applications.¹⁸ Numerous publications can be found in the literature investigating synthesis and properties of nanoparticles of different materials, sizes and shapes. The most crucial factors to be considered for a given application are particle size, magnetic properties and stability of the particles e.g. agglomeration under the conditions required by the respective application.

2.1.1 Magnetism

2.1.2 Magnetic fields are described by the magnetic induction B and the magnetic field strength H . In vacuum the following equation results¹⁹:

$$B = \mu_0 H, \quad 2.1$$

with the magnetic field strength of the external field H and the permeability in vacuum μ_0 . When a body is placed in a homogenous magnetic field, an inner magnetic induction results. This internal induction depends on the relative magnetic permeability μ_r of the material:

$$B_{\text{internal}} = \mu_r B_{\text{external}}, \quad 2.2$$

with $\mu_r = \mu/\mu_0$ or the magnetic polarization J

$$B_{\text{internal}} = B_{\text{external}} + J. \quad 2.3$$

The magnetic polarization is defined as

$$J = \chi_V B_{\text{external}}, \quad 2.4$$

with the magnetic susceptibility χ_V which depends on the atomic structure, the temperature and the external magnetic field being applied. The susceptibility χ_V and the magnetic permeability μ_r are related via the

¹⁸ Lu, A-H; Salabas, E. L.; Schüth, F. *Angew. Chem.* **2007**, *119*, 1242

¹⁹ Riedel, E. *Anorganische Chemie*, 5th edition, Walter de Gruyter, **2002**

following equation:

$$\chi_v = \mu_r - 1 \quad 2.5$$

Commonly, the magnetization M is used to describe the behaviour of magnetic materials:

$$J = \mu_0 M \quad 2.6$$

and

$$M = \chi_v H_{external} \quad 2.7$$

The magnetization M of the magnetic material is defined as the magnetic moment μ_{mag} per volume V .

$$M = \frac{\mu_{mag}}{V} \quad 2.8$$

For the study of magnetic properties, magnetization curves are investigated by plotting M versus H (Figure 2.1).

The atomic moments of diamagnetic and paramagnetic materials are randomly distributed in absence of an external magnetic field; the resulting magnetization is zero. In the case of ferro-, ferri- or antiferromagnets, ordered states are observed in absence as well as in presence of an external field when $T < T_C$. This magnetization is caused by the interaction between spins of paramagnetic components in the material. Below the characteristic temperature T_C , termed Curie temperature, an alignment of the spins results from the interaction between neighboured spins. This coupling is limited to small areas, the so-called Weiss areas. A spontaneous magnetization occurs. Ferromagnetic materials are characterized by a parallel alignment, antiferromagnetic materials by an antiparallel orientation of the spins. In case of ferrimagnetic materials, an antiparallel orientation of different sized spins is observed.¹⁹ Above the Curie temperature, the spin order in the Weiss domains is lost and the material shows paramagnetic properties. The typical hysteresis loop found for ferro- and ferrimagnetic materials is the result of the irreversible magnetization induced by the collective ordering of the atomic spins: In order to remove the magnetization, a certain field has to be applied.

In case of colloidal magnetic matter, the width of the hysteresis loop depends on the size of the particles. In large particles (micrometer range) multi-domain states are dominant. The domain walls are easily moved and therefore, thin hysteresis loops are obtained. Such materials are called soft magnetic materials. Smaller, nano-sized particles are typically single-domain materials. The domain walls are fixed. To alter the magnetization, the magnetic moments need to be shifted. Thus, high coercivity and remanence result causing a broadening of the hysteresis loop which is characteristic for magnetically hard materials. A further decrease in particle size leads to the so-called

superparamagnetism.

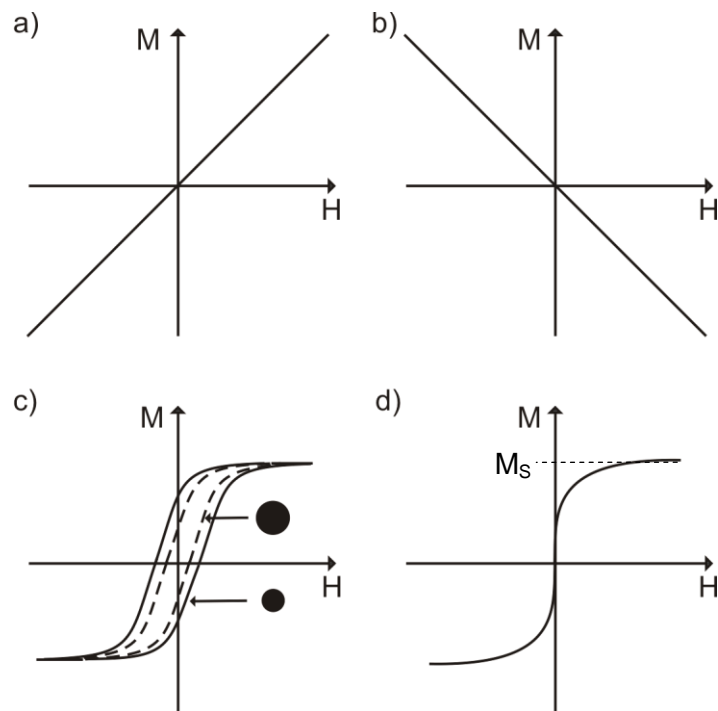


Figure 2.1 Magnetization curves of different classes of magnetic materials: a) paramagnetic, b) diamagnetic, c) ferromagnetic, d) superparamagnetic (M = magnetization, H = external magnetic field strength, M_S = saturation magnetization)²

2.1.2.1 Superparamagnetism

In nanoparticles with sizes in the order of tens of nanometers or below, an individual magnetic moment per particle is found. The particle moment is free to fluctuate while the atomic moments of the particle maintain in their order relative to each other. In absence of a magnetic field, the thermal energy kT (with Boltzmann constant k and temperature T) is strong enough to cause this fluctuation to result in an unordered state of the magnetic moments. Hence, no magnetization occurs. If a magnetic field is applied, the magnetic moments of the particles are aligned and magnetization takes place. Since this phenomenon resembles the behavior of paramagnetic systems, with the difference that much stronger magnetizations are monitored, the expression “superparamagnetism” is used. In Figure 2.1d the typical magnetization curve of superparamagnetic systems is illustrated. Typically for this behavior, neither coercivity nor remanence is observed.² The crucial point for the appearance of superparamagnetism is the size of the particles. Typically, superparamagnetism is found for particle sizes below 20 nm. The critical size for the superparamagnetic behavior can be calculated using the following equation:

$$r = \sqrt[3]{\frac{6kT}{K_u}}, \quad 2.9$$

with Boltzmann constant k , temperature T and crystalline magnetic anisotropy K_u . The magnetic anisotropy describes the direction dependence of the magnetic properties of the material. In magnetically isotropic materials, the magnetic moment has no preferential orientation. In contrast, magnetically anisotropic materials show an alignment of the magnetic moment in the energetically favoured direction.

2.1.2.1.1 Blocking Temperature

The magnetization of a material does not only depend on the external magnetic field but also on the temperature. In case of superparamagnetic systems, the blocking-temperature T_B is the crucial factor, governing the response to a magnetic field. Above the blocking temperature the thermal energy is high enough to overcome the magnetic interaction between the particles. The magnetic moments are able to fluctuate and the magnetization is lost even in presence of a magnetic field. Below T_B the thermal energy is too low to induce a fluctuation of the magnetic moments and magnetic alignment will take place if an external magnetic field is applied (Figure 2.2).

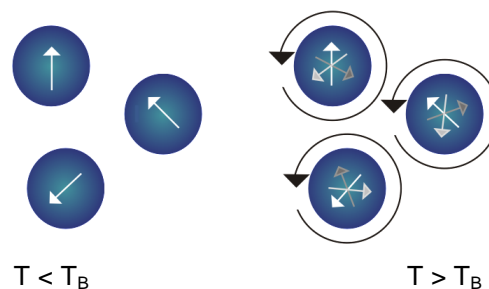


Figure 2.2 Schematic illustration of the blocking temperature²

To determine the blocking temperature of a sample, temperature dependent magnetization measurements under the application of low magnetic fields are used.

2.1.2.1.2 Size-Dependence of the Magnetization

In 1968, Berkowitz et al. discovered a size-dependence of the magnetization.²⁰ They found a direct relation between the magnetization and the size of the magnetic particles. To determine the theoretical saturation magnetization M_s , they developed the core-shell model.

²⁰ Berkowitz, A. E.; Schuele, W. J.; Flanders, P. J. *J. Appl. Phys.* **1968**, 39, 1261

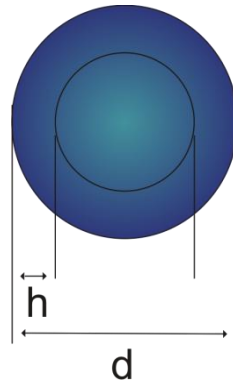


Figure 2.3 Core-shell model of Berkowitz (h = size of diamagnetic shell, d = particle diameter)

Considering that a magnetic particle with the particle diameter d is covered by a non-magnetic oxide layer of a certain thickness h , the saturation magnetization of the particle with size d ($M_s(d, T)$) can be determined relatively to the bulk material ($M_s(\infty, T)$):

$$\frac{M_s(d, T)}{M_s(\infty, T)} = \frac{V_{core}}{V_{particle}} = 1 - 6 \frac{h}{d} \quad 2.10$$

2.1.3 Magnetic Iron Oxide Nanoparticles

Magnetic iron oxide nanoparticles are widely investigated due to a number of desirable properties: First, the synthesis is relatively cheap, fast and easy. The particles (single domains of about 5-20 nm in diameter) show a superparamagnetic behavior with high saturation magnetizations, rendering them ideal candidates for stimuli response applications like delivery or hyperthermia approaches. Additionally, they are excellent candidates for biomedical applications since their biocompatibility has been proven.^{21, 22}

Mostly, maghemite ($\gamma\text{-Fe}_2\text{O}_3$) or magnetite (Fe_3O_4) particles are reported in literature. Magnetite crystallizes in an inverse spinel structure with a face-centred cubic unit cell. 32 O^{2-} ions are forming a regular cubic close packing. Both divalent (Fe^{II}) and trivalent (Fe^{III}) iron species are present in the crystal. Tetrahedral sites are occupied by Fe^{III} , octahedral sites are distributed between Fe^{II} and Fe^{III} . This distribution results in the written formula $\text{Fe}^{\text{III}}[\text{Fe}^{\text{II}}\text{Fe}^{\text{III}}]\text{O}_4$ with the brackets denoting the octahedral sites. Therefore, eight formula units form one unit cell.

The crystal structure of maghemite is a defect structure of magnetite which is formed via oxidation. The oxidation of ferrous ions is correlated with the migration of cations through the lattice framework which causes the generation of vacancies to maintain the charge balance.²³ Hence, in maghemite, only trivalent iron is present. The resulting formula is $0.75\text{Fe}^{\text{III}}[\text{Fe}^{\text{III}}_{5/3}\square_{1/3}]\text{O}_4$ (\square : vacant site).²¹ The iron

²¹ Gupta, A. K.; Gupta, M. *Biomaterials* **2005**, *26*, 3995

²² Cornell, R. M.; Schwertmann, U. *The Iron Oxides*, Wiley-VCH, **1996**

²³ Laurent, S.; Forge, D.; Port, M.; Roch, A.; Robic, C.; Elst, L.V.; Muller, R. N. *Chem. Rev.* **2008**, *108*, 2064

oxides are typical representatives of ferrimagnetic materials. The existence of different oxidative species inside the spinel structures causes an imbalance between the spin orientations. Hence, ferrimagnetism results. Due to this structural similarity magnetite becomes easily oxidized to maghemite. However, many synthetic methods are leading to mix-structures of both oxides.

Concerning magnetism, magnetite shows a higher saturation magnetization than maghemite. Nevertheless, the unstable oxidation state of magnetite precludes it from many applications.

Table 2.1 Magnetic properties of iron oxides in the bulk state ²⁴

iron oxide	$M_S(T = 5 \text{ K}) / \text{emu/g}$	$M_S(T = 300 \text{ K}) / \text{emu/g}$
Fe_3O_4	98.0	92.0
$\gamma\text{-Fe}_2\text{O}_3$	84.0	78.0

2.1.4 Synthesis

The synthesis of magnetic nanoparticles is an extensively investigated research area. The main challenge in magnetic nanoparticle synthesis is the formation of colloidal stable, uniform and monodispers particles with high saturation magnetizations. Several approaches have been reported in the literature. The most important procedures are coprecipitation, high temperature decomposition of organic precursors and sol-gel processes.^{18,23} In the following Chapter, the applications of these methods for the synthesis of magnetic iron oxide nanoparticles are discussed.

2.1.4.1 Coprecipitation Process

The simplest and most effective method for the preparation of iron oxide nanoparticles is the coprecipitation of iron salts in basic solution. The first controlled synthesis of superparamagnetic iron oxide nanoparticles via coprecipitation of FeCl_2 and FeCl_3 was reported by Massart in 1981.²⁵ The obtained particles showed an average size in the range of 8 nm in diameter with a broad size-distribution and a roughly spherical shape. In contrast to other synthetic methods, no capping-agent is necessary. The particles are stabilized via electrostatic interaction as illustrated in Figure 2.4 and are dispersible in aqueous solutions.

²⁴ Odenbach, S. in *Handbook of Magnetic Materials*, volume 16, Elsevier, Amsterdam, 2006

²⁵ Massart, R. *IEEE Trans. Magn.* **1981**, 17, 1247

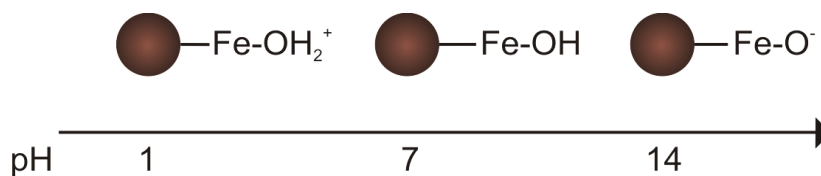


Figure 2.4 Electrostatic stabilization of magnetic iron oxide nanoparticles synthesized via coprecipitation in basic solution

After the first report, the synthetic parameters have systematically been studied. It was found that the properties of the resulting nanoparticles (size, shape, composition and magnetic properties) depend on the iron salts (chlorides, nitrates, sulphates, e.g.), the ration between Fe(II) to Fe(III), the pH-value, the reaction temperature and the ionic strength.^{26,27,28} Generally, particle sizes are found to decrease with increasing pH, ionic strength and temperature.^{23,26} The composition of the particles is strongly influenced by the Fe(II):Fe(III) ratio: Small values lead to goethite (α -FeO(OH)) formation while larger ratios result in maghemite and magnetite formation. From thermodynamic calculations, a Fe(II):Fe(III) ratio of 0.5 should lead to pure magnetite particles.²³ However, typically a mixture of magnetite and maghemite is obtained due to the magnetites sensitivity to oxidation. Several other parameters like the concentration of iron salts, the rate of mixing and the nature of the alkaline medium are known to influence the particle size and composition.^{23,28,29} The saturation magnetization of the material varies between 30 and 80 emu/g; a value which is relatively low compared to bulk material. The accessible size regime is in the range of 2-20 nm. Generally, broad size distributions are obtained.

The polydispersity of the particles can be decreased using organic additives acting as chelating (for example citrate or oleic acid) or surface complexing (dextran, poly(vinyl alcohol), poly(ethylene glycol), e.g.) agents.³⁰ Bee et al. revealed a decrease of the particle size in presence of high citrate concentrations. Organic ions are known to affect the formation of metal oxide particles via two different processes: 1. Chelation of the metal ions hinders nucleation and hence, causes the formation of larger particles due to the decreased number of nuclei formed. 2. Adsorption of ions on the nuclei inhibits the growth of the particles which results in the formation of smaller particles.^{30d} Both effects are reported in literature: Ishikawa et al. revealed an increase in the particle size in presence of EDTA

²⁶ Babes, L.; Denizot, B.; Tanguy, G.; Le Jeune, J. J.; Jallet, P. *J. Colloid Interface Sci.* **1999**, *212*, 474

²⁷ a) Tominaga, M.; Matsumoto, M.; Soejima, K.; Taniguchi, I. *J. Colloid Interface Sci.* **2006**, *299*, 761; b) Weissleder, R. *U.S. Patent* 5,492,814, **1996**; *Chem. Abstr.* **1997**, *124*, 283285; c) Sjorgren, C. E.; Briley-Saebo, K.; Hanson, M.; Johansson, C. *Magn. Reson. Med.* **1994**, *31*, 268; d) Itoh, H.; Sugimoto, T. *J. Colloid Interface Sci.* **2003**, *265*, 283; e) Pardoe, H.; Chua-anusorn, W.; St. Pierre, T. G.; Dobson, J. *J. Magn. Mater.* **2001**, *225*, 41; f) Khalafalla, S. E.; Reimers, G. W. *IEEE Trans. Magn.* **1980**, *16*, 178

²⁸ Thapa, D.; Palkar, V. R.; Kurup, M. B.; Malik, S. K. *Mater. Lett.* **2004**, *58*, 2692

²⁹ Massart, R.; Roger, J.; Cabuil, V. *Braz. J. Phys.* **1995**, *25*, 135

³⁰ a) Lee, J.; Isobe, T.; Senna, M. *Colloids Surf. A* **1996**, *109*, 121; b) Bee, A.; Massart, R.; Neveu, S. *J. Magn. Mater.* **1995**, *149*, 6; c) Willis, A. L.; Turro, N. J.; O'Brien, S. *Chem. Mater.* **2005**, *17*, 5970; d) Cushing, B. L.; Kolesnichenko, V. L.; O'Connor, C. J. *Chem. Rev.* **2004**, *104*, 3893

which can be attributed to the first process described above.³¹ The contrary phenomenon was found in case of citrate ions which are supposed to adsorb on the nuclei and thus, cause the formation of smaller particles.^{30b} The addition of polymers to the precipitation media generally induces a decrease in the particle size and particle size distribution due to adsorption on the nuclei and surface of the growing particles.^{27f}

2.1.4.2 Thermal Decomposition

Uniformly monodisperse particles with a controlled particle size and shape can be synthesized via thermal decomposition of an organic precursor in a high boiling solvent. Typically, the use of surfactant is necessary to prevent aggregation and sedimentation of the particles. Various precursor materials have been reported, e.g. $\text{Fe}(\text{Cup})_3$, $\text{Fe}(\text{CO})_5$, or $\text{Fe}(\text{acac})_3$. Classical surfactants are fatty acids, oleic acid or hexadecyl amine. The decomposition temperature varies from approximately 100 to 300°C. The most common method for the preparation of iron oxide nanoparticles is the decomposition of iron pentacarbonyl in octyl ether in presence of oleic acid. First, pure iron nanoparticles are formed which are unstable under environmental condition and can easily be transferred into maghemite by addition of a mild oxidant (trimethylamine oxide ($(\text{CH}_3)_3\text{NO}$), e.g.). The resulting particles are remarkable uniform and monodisperse (Figure 2.5). The oleic acid coating leads to hydrophobic particles that can be dispersed in organic solvents like toluene.

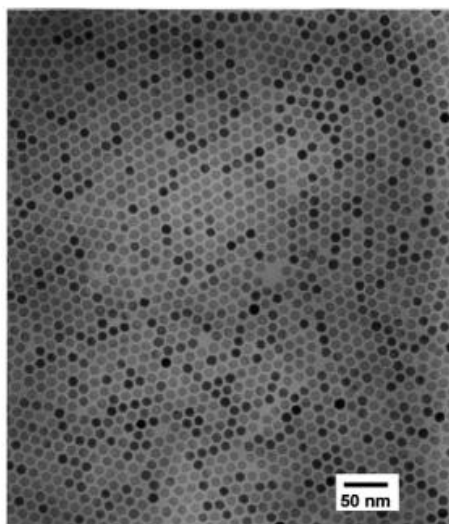


Figure 2.5 Magnetic $\gamma\text{-Fe}_2\text{O}_3$ nanoparticles synthesized by Hyeon³²

The particle size strongly depends on the nucleation process and the surface energy of the particles. Short nucleation times which may be achieved by rapidly injection of the precursor are well known to support the formation of monodispers particles. Additionally, the growth should be clearly separated from the nucleation period and Ostwald ripening should be hindered to prevent the broad size

³¹ Ishikawa, T.; Kataoka, S.; Kandori, K. *J. Mater. Sci.* **1993**, *28*, 2693

³² Hyeon, T.; Lee, S. S.; Park, J.; Chung, Y.; Na, H. B. *J. Am. Chem. Soc.* **2001**, *123*, 12798

distributions.³³ Controlled heating rates and high temperature annealing generally support the uniformity of the particles.²³ The choice of surfactant and the ratio of precursor and surfactant show distinct influence the size of the structures. According to general considerations regarding colloidal stability, the particle size increases with decreasing surfactant concentration.³² Additionally, it was found that the size of Fe₃O₄ particles increases with prolonged reaction time.³⁴

The preparation of different morphologies is also possible via thermal decomposition. Since the formation of metastable, high-energy forms is difficult under thermodynamic control, high growth rates, in the kinetically controlled growth regime, are commonly used for the formation of highly anisotropic shapes.³³ Peng et al. described the synthesis of cubic and point-shaped nanocrystals while Cheon et al. reported the preparation of diamond and triangle shaped structures.³⁵ The main drawback of the thermal decomposition is the requirement of expensive and toxic chemicals as well as the high sensitivity of the particle formation towards heating rate and annealing time.

2.1.4.3 Sol-Gel Process

The synthesis of nanoparticles in constrained environments, like emulsions or micelles, offers the possibility to control size and shape very precisely. Another benefit of the nanoparticle synthesis in nanodroplets is the broad size regime. Normally, aqueous metal salt solutions are encapsulated inside a nano- or micron-sized droplet by organic surfactants like oleic acid, DBS, SDS or long-chain polymers.³⁶ In 1982, Inouye et al. reported the first synthesis of magnetic nanoparticles in micelles by oxidation of Fe²⁺ to γ -Fe₂O₃ and Fe₃O₄.³⁷ Using reverse micelles, Lee et al. enhanced this method to produce uniform and highly crystalline particles in an inexpensive large-scale synthesis.³⁸ Most important factors for the process control are the proportions of iron salt, surfactant and solvent as well as the temperature. However, the restricted practicability and the relative low yields compared to the coprecipitation or thermal decomposition process is a significant drawback for emulsion based processes.

2.1.5 Magnetic Nanoparticles for Biomedical Applications

For biomedical applications, various magnetic systems are reported in the literature. The sort of material used depends on the desired application. Considering the magnetic material, iron oxides nanoparticles are preferred for use in biomedical applications due to their low cytotoxicity.^{7,9}

As the particles have to be reasonably small, e.g. to be able to enter cells, a sufficiently high magnetization is a crucial parameter in the choice of material considered. Magnetic iron oxide

³³ Yin, Y.; Alivisatos, P. *Nature* **2005**, *437*, 664

³⁴ Chen, D.; Xu, R. *Mater. Res. Bull.* **1998**, *33*, 1015

³⁵ a) Jana, N. R.; Chen, Y.; Peng, X. *Chem. Mater.* **2004**, *16*, 3931; b) Cheon, J.; Kang, N.-J.; Lee, S.-M.; Lee, J.-H.; Yoon, J.-H.; Oh, S. J. *J. Am. Chem. Soc.* **2004**, *126*, 1950

³⁶ a) Liu, C.; Zou, B.; Rondinone, A. J.; Zhang, Z. *J. Phys. Chem. B* **2000**, *104*, 1141; b) Woo, K.; Lee, H. J.; Ahn, J.-P.; Park, Y. S. *Adv. Mater.* **2003**, *15*, 1761

³⁷ Inouye, K.; Endo, R.; Otsuka, Y.; Miyashiro, K.; Kaneko, K.; Ishikawa, T. *J. Phys. Chem.* **1982**, *86*, 1465

³⁸ Lee, Y.; Lee, J.; Bae, C. J.; Park, J. G.; Noh, H. J.; Park, J. H.; Hyeon, J. H. *Adv. Funct. Mater.* **2005**, *3*, 503

nanoparticles show superparamagnetic behavior, which means that the particles show high saturation magnetizations (M_s) in the presence of a magnetic field that disappears as soon as the magnetic field is switched off (see Chapter 2.1.2.1). This phenomenon is highly desirable for biomedical applications because an easy distribution and transport of the particles in the biological system is warranted since the particles show no magnetic interaction to each other during the absence of the magnetic field.⁸ For *in vivo* applications like drug delivery for example, cellular uptake has to be guaranteed. While small molecules and ions are incorporated into cells via diffusion based membrane transports and active transports via transporter proteins and ion pumps, the cellular uptake of nanoparticles is performed via endocytosis (Figure 2.6).³⁹

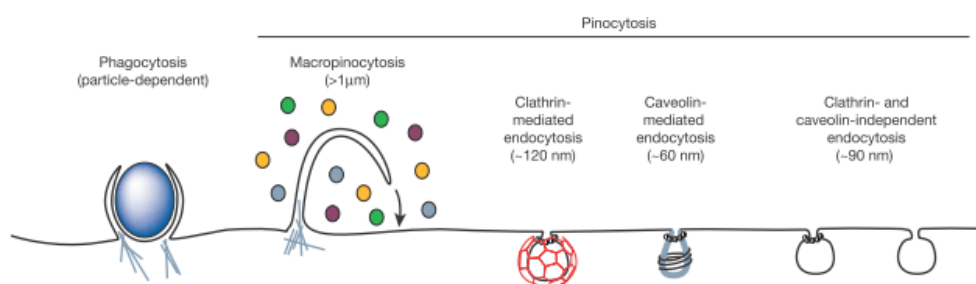


Figure 2.6 Portals of entry into mammalian cells via endocytosis³⁹

In analogy to proteins and bacteria, e.g., nanoparticles are transported into the cell via invagination of the cell membrane (endocytosis). The resulting vesicle, the so-called endosome, transports the incorporated material to the lysosomes inside the cell where enzymatic conversion occurs. Generally, two different categories are described: Phagocytosis defines the incorporation of solid materials like bacteria or smaller cells with sizes above approximately $0.5 \mu\text{m}$. This process is characteristic for special cell types including phagocytes and is among others an important mechanism of immune defense. Phagocytosis can be supported by the adsorption of proteins onto the nanoparticle surface. This so-called opsonins act as binding enhancers between the particles and phagocytic cells which enhances phagocytosis. Typically, phagocytosis is heavily undesired in nanoparticle applications since it leads to the elimination of the particles via the reticuloendothelial system (RES) which is part of the immune system. Pinocytosis describes the uptake of liquids including dissolved macromolecules and proteins with comparably small sizes (below $0.5 \mu\text{m}$). Pinocytosis is carried out by almost all sorts of cells and can be further categorized in receptor-mediated and non-receptor-mediated processes. In case of receptor-mediated endocytosis, the specific interaction between molecules or particles and membrane receptors causes the invagination of the material. In receptor-independent endocytosis, a non-specific uptake of extracellular liquids occurs. Besides this size-determining parameter a compromise between the required strength of the magnetic properties and the interaction with the

³⁹ Conner, S. D.; Schmid, S. L. *Nature* **2003**, *422*, 37

targeted biological system has to be found.⁴⁰ By this means, micron-sized particles can be used for magnetic separation whereas imaging applications typically require materials below 100 nm. For many biomedical applications, the magnetic nanoparticles need to be covered by a protective coating to protect them from environmental influences and increase the stealthiness.

2.1.5.1 Functionalization of Magnetic Particles for Biomedical Applications

In the last few decades, the encapsulation of magnetic nanoparticles into a polymeric shell gained a lot of attention.⁴¹ The main benefit is the combination of the properties of both materials. The polymer shell can be used for functionalization of the particles, for example to adapt them to their surroundings. The encapsulated inorganic particles allow for benefit from the material specific effects such as magnetism, luminescence/fluorescence or contrast enhancement. Especially in biomedical applications, the bare magnetic nanoparticles are often not suitable. In the simplest case, the polymeric material acts as some kind of protective coating mainly to increase the colloidal stability and biocompatibility and to avoid undesired biodegradation. Of course, the coating material can also be used to create multifunctional systems. Such systems are of great scientific interest due to the broad range of possible applications. Multiple approaches can be found in literature using several coating materials e.g. inorganic oxides like TiO₂ or SiO₂ as well as organic polymers like polystyrene, polyethylene glycol or dextran.¹⁰ Independent from the used materials, considerable care has to be taken concerning the following points: I) the particles have to be stable in solution in order to prevent aggregation, II) the encapsulation must be complete and permanent so that the magnetic particles are protected against environmental influences that could cause oxidation or degradation, III) the magnetic content must be high enough for a magnetic response at room temperature, IV) in case of biomedical applications biocompatibility has to be ensured.⁴²

2.1.5.2 Biomedical Applications

In biomedicine, various applications for magnetic nanoparticles and magnetically functionalized polymeric systems can be imagined. Analytic approaches, like magnetic resonance imaging (MRI) or sensing methods are using magnetic particles to image certain parts of the body. The application of magnetic particles provides a drastic increase in contrast of the monitored biological system. In magnetic cell sorting or magnetic cell separation, the specific interaction between magnetic beads and target molecules is used to isolate or concentrate cells or biomolecules of interest which are further analysed. This isolation allows to reduce the sample volume and increases the statistics of following analysis. Specific interactions between polymeric systems and target molecules are also used in drug delivery applications. Thus, a controlled distribution of drugs which are encapsulated inside or

⁴⁰ Berkowitz, A. E.; Schuele, W. J. *J. Appl. Phys.* **1968**, *39*, 1207

⁴¹ Roca, A. G.; Costo, R.; Rebolledo, A. F.; Veintemillas-Verdaguer, S.; Tartaj, P.; González-Carreño, T.; Morales, M. P.; Serna, C. J. *J. Phys. D: Appl. Phys.* **2009**, *42*, 224002

⁴² Ramirez, L. P.; Landfester, K. *Macromol. Chem. Phys.* **2003**, *204*, 22

attached to the polymeric system can be realized. Hence, a reduction of the applied dose as well as undesired side effects on healthy tissues can be achieved. For accumulation and trapping of drug loaded particles, magnetic materials can also be utilized. Another application for magnetic particles is the hyperthermia treatment. This therapeutic approach uses an induced heating to destroy pathological cells. In the following section, the described methods are highlighted.

2.1.5.2.1 Magnetic Resonance Imaging (MRI)

The magnetic resonance imaging (MRI) or magnetic resonance tomography (MRT) is a well-established and routinely used technique in diagnostic medicine. MRI is an imaging method which is used visualizes detailed internal structures in the body and to differentiate between healthy and pathological tissues. The MRI technique uses the interactions between magnetic moments of protons, present in tissues, and an external magnetic field. The magnetic nanoparticles act as contrast agents, helping to increase the resolution by altering the behavior of protons in their vicinity. The principle system of the MRI is based on the nuclear magnetic resonance (NMR) spectroscopy. Under normal circumstances, the magnetic moments are randomly distributed. In presence of an external magnetic field, the magnetic moments of the cores are aligned and a measureable magnetization is generated. Applying a second, time-varying magnetic field perpendicular to the static field results in a tilting of the magnetization. Due to relaxation effects, the overall-magnetization starts to precess around the static field. This rotation can be detected via induced currents in pick-up coils in the scanner.

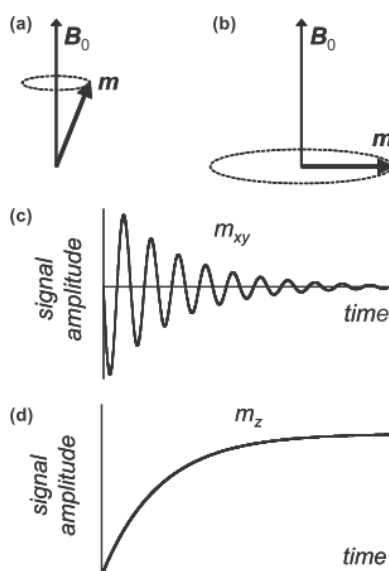


Figure 2.7 Net magnetization a) in a static magnetic field and b) after application of magnetic pulse perpendicular to the static field; relaxation of signal amplitude in c) in plane and d) longitudinal to initial orientation of the magnetization²

Iron oxide nanoparticles are most commonly used in MRI. Typically, a dextran coating is applied to prevent particles from biodegradation and to increase biocompatibility. These particles show a selectively uptake into reticuloendothelial cells and are excreted via the liver after the treatment.²¹

2.1.5.2.2 Magnetic Separation

The analysis and diagnosis of biological samples is often a challenging task due to the low sample concentrations. Hence, the isolation and concentration of biological samples is crucial for biomedical applications. The magnetic separation or magnetic sorting uses specific interactions between target molecules and magnetic beads in combination with a fluid-based magnetic separation device. Typically, micron- or sub-micron-sized magnetic iron oxide particles coated with biocompatible molecules (dextran, poly(vinyl alcohol) or poly(ethylene glycol), e.g.) are used. Specific binding sites on the particle surface like hormones, charged molecules, antibodies etc. target the corresponding molecules on the cell surfaces or biomolecules. In the simplest case the magnetic separation is carried out by the application of an external magnetic field to the wall of a test tube and removal of the supernatant. Higher efficiency can be achieved using a magnetic field gradient inside a magnetic column. In the last decades, the interest in so-called micro-TAS (“micro-total analysis systems”) and lab-on-a-chip systems is steadily increasing. In this technique, the particles are separated and directly analysed on a small chip-like device. This approach overcomes the disadvantages of other systems like time-resuming procedures or the requirement of a laboratory for the analysis of the sample.⁴³

2.1.5.2.3 Drug Delivery

The main drawback of medicamentous therapies is the lack of specificity, which causes the need of high drug doses and leads to undesired side-effects. Smart drug delivery systems aim to overcome these problems using recognition systems for a specific targeting of morbid cells or tissues. The most important goal is to reduce dose and undesired distribution of the drug in healthy tissue.² The targeting can be achieved by three basic mechanisms: I) “physical” targeting based on pH-value or temperature, II) magnetic targeting using external magnetic fields and III) chemical targeting, benefiting from the specific affinities or interactions of certain molecules.⁴⁴ “Physical” drug targeting is based on the different properties of pathological tissues compared to normal cells. It is known that cancer cells usually show acidosis or hyperthermia. Thus, stimuli-responsive drug carriers can be used to deliver and release the drug in the area of interest. Therefore, even undirected distribution becomes irrelevant since the drug is only released in the malignant tissue.

The most obvious and natural way of targeted drug delivery is the use of molecular recognition mechanisms between two moieties, for example antibodies or their fragments, lectins, proteins, hormones, charged molecules and low molecular weight ligands.⁴⁴

⁴³ a) Blankenstein, G.; Larsen, U. D. *Biosensors & Bioelectronics* **1998**, *13*, 427; b) Miltenyi, S., Mueller, W., Weichel, W.; Radbruch, D. *Cytometry* **1990**, *11*, 231

⁴⁴ Torchilin, V. *European Journal of Pharmaceutical Sciences* **2000**, *11*, 81

The clinical studies using magnetic drug targeting were published by Lübbe et al.⁴⁵ The 100 nm particles of a ferrofluid were coated with a starch polymer which is able to electrostatically interact with the drug epirubicin. By applying an external magnetic field in a distance less than 0.5 cm to the tumor, it could be shown that the particles were successfully targeted to the malignant tissue. Orekhova et al. reported to use magnetically loaded red blood cells for the delivery of aspirin in animal experiments.⁴⁶ Of course, the ability of a magnetic targeting depends on the magnetic field and therefore on the construction of strong magnets. Another important factor are blood flow rates. The efficiency of delivery is higher in smaller blood vessels where lower blood flow rates are found.⁴⁷

The use of multifunctional carriers like micro- and nanocapsules, nanoparticles, liposomes, micelles and cell ghosts, suggested by H. Ringsdorf in the 1970th, is a useful combination of the drug delivery approaches discussed above.^{44,48} Using loaded, reservoir-like systems, the amount of drug per carrier can be increased while the required number of targeting moieties per drug molecule can be decreased. Additionally, the size of the drug delivery system can easily be adjusted.

2.1.5.2.4 Hyperthermia

Hyperthermia is an extensively studied technique for cancer treatment. The basis for hyperthermia is the observation that several types of cancer cells are more sensitive to temperatures above 41 °C compared to normal cells.⁴⁹ Hence, the heating of morbid cells or tissues to temperatures between 41 and 46 °C can be used for preferential killing of cancer cells.⁵⁰ The heating can be induced by different external fields like microwaves or ultrasonication which were used in the past. Nowadays, research focuses on the application of magnetic treatments. Therefore, magnetic nanoparticles, preferably superparamagnetic fluids, are injected into the region of interest. When the particles are exposed to an external, time-varying magnetic field, the magnetic moments are aligned towards the applied magnetic field. Due to relaxation effects, the magnetic moments precess around their former orientation until they return to their equilibrium condition. This process leads to the exposure of heat which immediately conducts into the surrounding tissue (Néel relaxation). Another possible process is the physical rotation of the whole particle (Brownian rotation). In this case, the heating is induced by friction caused by the particles motion. The attractiveness of this therapy is the specific treatment which will only affect the infected cells. Surrounding healthy tissue is not affected.

Magnetic iron oxide nanoparticles (γ -Fe₂O₃) was first used by Gilchrist et al. in 1957.⁵¹ 20-100 nm size

⁴⁵ Lübbe, A. S.; Alexiou, C.; Bergemann, C. *J. Surg. Res.* **2001**, *95*, 200

⁴⁶ Orekhova, N. M.; Akchurin, R. S.; Belyaev, A. A.; Smirnov, M. D.; Ragimov, S.E.; Orekhov, A. N. *Thromb. Res.* **1990**, *57*, 611

⁴⁷ Widder, K.J., Marino, P.A., Morris, R.M., Senyei, A.E., In: Goldberg, E. (Ed.) *Targeted Drugs*, John Wiley and Sons, **1983**

⁴⁸ Ringsdorf, H. *J. Polym. Sci.* **1975**, *51*, 135

⁴⁹ a) Jordan, A.; Wust, P.; Scholz, R.; Tesche, B.; Fahling, H.; Mitrovics, T.; Vogl, T.; Cervos-Navarro, J.; Felix, R. *Int. J. Hyperthermia* **1996**, *12*, 705; b) Neilsen, O. S.; Horsman, M.; Overgaard, J. E. *J. Cancer* **2001**, *37*, 1587

⁵⁰ Jordan, J. *J. Magn. Magn. Mater* **1999**, *201*, 413

⁵¹ Gilchrist, R. K.; Medal, R.; Shorey, W. D.; Hanselman, R. C.; Parrott, J. C.; Taylor, C. B. *Ann. Surg.* **1957**, *146*, 596

particles were injected to various tissues and exposed to a 1.2 MHz magnetic field. Since then, a large number of studies have been published using different types of magnetic materials, field strength, frequencies as well as targeting and delivering methods.² However, hyperthermia has not become a standard method in cancer therapy. Technical details like the focussation of the external magnetic field or the measurement of the temperature inside the tissue are still restraining the clinical use of hyperthermia.

2.2 Polyorganosiloxane Nanoparticles

In 1949, the first study on defined network structures was published by Baker.⁵² He synthesized network-structured particles with diameters below 1 μm via emulsion polymerization. These so-called microgels differed from the known networks, since no infinite branching occurs, additionally, the microgels can be dissolved in different solvents. It must be noted that macroscopic networks show a swelling behavior instead of solubility.

The polyorganosiloxane networks, first been reported by F. Baumann, M. Schmidt and C. Roos, were steadily gaining interest due to their convenient handling and low toxicity.⁵³ Another important feature of the polyorganosiloxane system is the high flexibility regarding particle size, composition, network density and architecture as well as the possibility of various functionalizations which will further be discussed in Chapter 2.2.5.

The starting materials for the polyorganosiloxane synthesis, the alkoxy silanes, offer a large range of possible variations due to their enormous versatility. The four different kinds of monomers (mono-, di-, tri- and tetra-functional) are illustrated in Figure 2.8.

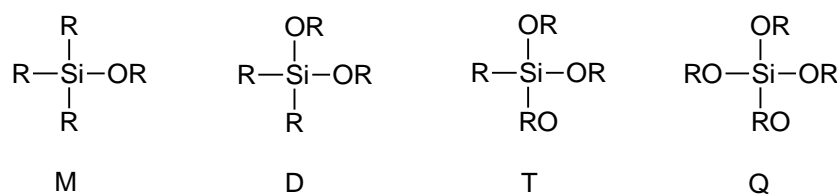


Figure 2.8 Mono-, di-, tri- and tetrafunctional silane monomers

The variation of the organic rest R does not only permit the specific introduction of functional groups, it also influences the reaction process. The reaction rate strongly depends on the character of the organic group. The monomers shown in Figure 2.8 react in a classic polycondensation reaction that can be catalyzed using acidic as well as basic catalysts. Nevertheless, the choice of the reaction conditions has consequences on the products. The reaction process can be classified in two steps, hydrolyses and condensation.

2.2.1 Hydrolysis of Alkoxy silanes

The hydrolysis of alkoxy silanes can be described using the following reaction scheme.



$$n = 0, 1, 2, 3$$

$$\text{R} = \text{methyl, ethyl, propyl, } \dots$$

$$\text{R}' = \text{alkyl, aryl, vinyl}$$

⁵² Baker, W. O. *Industrial and Engineering Chemistry* **1949**, *41*, 511

⁵³ Baumann, F.; Schmidt, M. *Advanced Materials* **1997**, *9*, 955

The reaction can be catalyzed under acidic as well as basic conditions, which was shown in 1980 by Pratt et al.⁵⁴ The pH-dependent reaction rate k_h shows a V-shaped progression with a minimum at 6-7 (Figure 2.9).

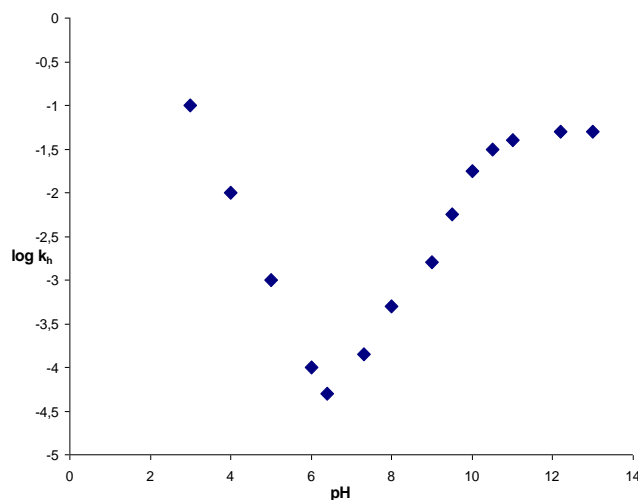


Figure 2.9 pH-dependence of the reaction rate k_h for the hydrolysis of alkoxy silanes

As mentioned before, the pH value does not only influence the reaction rate but also the mechanism. In case of an acidic catalyzed reaction, an electrophilic attack of a proton takes place at the oxygen atom of the Si-O-bond. Afterwards, a corresponding alcohol is separated under addition of a water molecule. Thereby, the silanol is formed. By contrast, the basic catalyzed reaction directly leads to the formation of the silanol via a nucleophilic attack of a hydroxyl-group on the silicium atom.

The reaction rate of the acidic and basic catalysed hydrolysis of alkoxy silanes also shows some deviations. The alkoxy group has a much stronger $-I$ -effect compared to the hydroxyl group. Hence, the electrophilic character of the silicon atoms increases with progressing hydrolysis. This results in an increasing reaction rate in case of basic catalysis.

$$k_{h1} < k_{h2} < k_{h3} < k_{h4}, \quad 2.12$$

whereas the acidic catalysis results in a decreasing reaction rate:

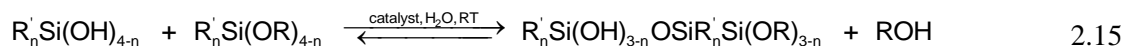
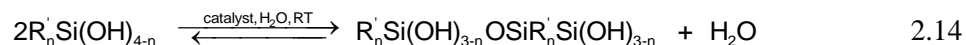
$$k_{h1} > k_{h2} > k_{h3} > k_{h4} \quad 2.13$$

2.2.2 Condensation of Alkoxy silanes

The reaction equation for the condensation reaction of alkoxy silanes can be described in a chemical equilibrium (Figure 2.10). It resembles the hydrolysis with respect to the pH-dependence as shown in

⁵⁴ McNeil, K. J.; Walsh, D. A.; Pratt, R. F. *J. Am. Chem. Soc.* **1980**, *102*, 1859

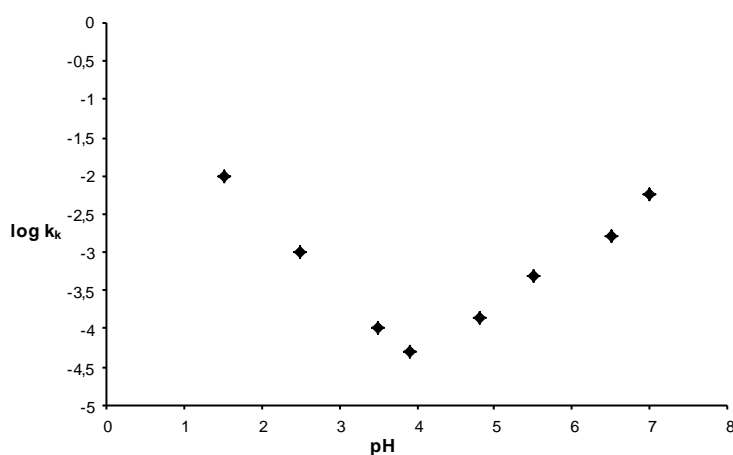
Figure 2.10. The minimum is slightly shifted to a more acidic value of 4.



$n = 0, 1, 2, 3$

$R = \text{methyl, ethyl, propyl, ...}$

$R' = \text{alkyl, aryl, vinyl}$

Figure 2.10 pH-dependence of the reaction rate k_c for the condensation reaction of alkoxy silanes

In contrast to the hydrolysis, the reaction mechanism shows no pH-dependence. In all cases, a nucleophilic substitution reaction with a S_N2 mechanism takes place on the silicon atom. Another difference between the hydrolysis and condensation is the pH-dependent reaction rate. Generally, the reaction rate decreases with increasing number of organic groups. This can be explained by the +I-effect of the alkyl groups that increases the negative character of the silicon atom and therefore hinders the nucleophilic attack resulting in the following order of reactivity:



Comparing the reaction rate of the hydrolysis and condensation reaction, the hydrolysis turns out to be the rate-determining step in case of a basic catalysis.



Hence, hexaalkoxy siloxanes $(\text{RO})_3\text{Si-O-Si}(\text{OR})_3$ are the dominate species in the early state of the condensation. In an acidic catalysed reaction, the condensation is the rate-determining step leading to hexahydro siloxanes $(\text{HO})_3\text{Si-O-Si}(\text{OH})_3$ as condensation products.

$$k_h > k_k \quad 2.19$$

This behavior also influences the final products. In basic media, the highly branched alkoxyfunctionalized polymers, which are formed during hydrolysis, hinder condensation reaction. The resulting gels consist of heterogeneously cross-linked systems. In contrast, the hexahydrosiloxanes, formed in the case of an acidic catalyzed reaction, can easily be hydrolyzed to form optically transparent, homogeneous systems.

2.2.3 Polycondensation of Alkoxysilanes in Aqueous Dispersions

The polycondensation in aqueous dispersion is a popular method for the synthesis of monodisperse, spherical micro-networks and particles.⁵⁵ The resulting structures are in the size range of 15 -200 nm in radius. Theoretically, the particle size is strongly correlated to the so-called fleet ratio S , which is defined as the ratio between the mass of surfactant and the mass of the monomer:

$$S = \frac{m_s}{m_m} \quad 2.20$$

In 1995, the first quantitative investigations on the polycondensation of alkoxysilanes in aqueous dispersion was published by Baumann et al.⁵⁶ They synthesized spherical polyorganosiloxane networks using diethoxydimethylsilane (D) as chain-forming agent in combination with the cross-linking agent trimethoxymethylsilane (T).

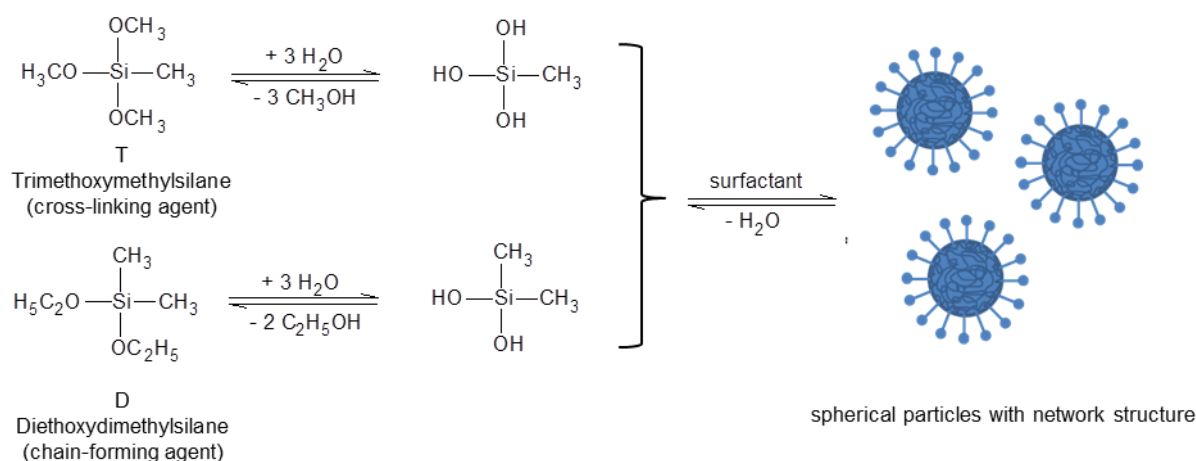


Figure 2.11 Schematic scheme of the polycondensation of alkoxysilanes in aqueous dispersion

They proved that the particle stabilization is achieved by a combination of two effects: The hydrophilic hydroxyl, alkoxy and silicate groups at the surface are self-stabilizing, while the surfactant

⁵⁵ Arshady, R. *Colloid. Polym. Sci.* **1992**, 270, 717

⁵⁶ Baumann, F. *Dissertation*, Bayreuth, **1995**

acts as a stabilization agent for the hydrophobic surface areas build by methyl and ethyl groups. In basic media, the reaction is catalyzed with sodium hydroxide while benzethonium chloride is used as surfactant. In case of the reaction in acidic medium, dodecylbenzenesulfonic acid (DBS) acts as catalyst as well as surfactant (Figure 2.12).

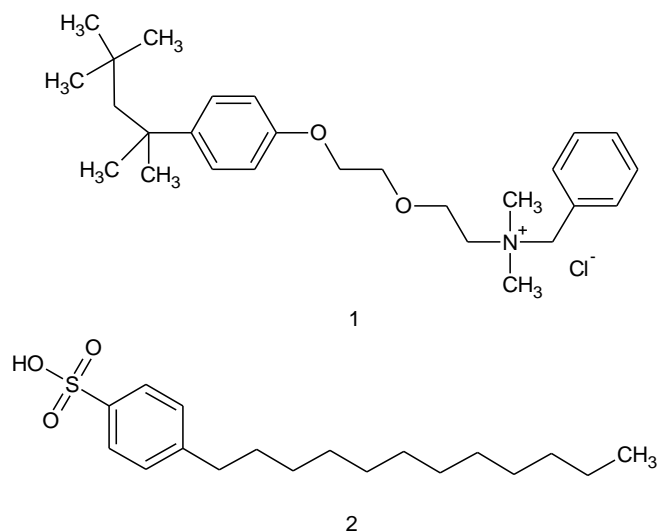


Figure 2.12 Surfactants used for the polycondensation of alkoxy silanes: benzethonium chloride (1); dodecylbenzenesulfonic acid (DBS) (2)

By altering and subsequent addition of the monomer mixtures, polyorganosiloxane nanoparticles with various architectures can be formed. The synthesis of solid and hollow spheres as well as core-shell systems have been reported.¹²

2.2.4 Redispersible Polyorganosiloxane Networks

The polyorganosiloxane nanoparticles synthesized via polycondensation in dispersion carry active surface groups like hydroxy, alkoxy and silicate groups which can lead to undesired aggregation as soon as the stabilizing surfactant is removed. The resulting macroscopically linked system is not redispersible. To avoid this effect, Baumann developed the so-called end-capping or end-stopping process.⁵⁶ With this method the functional surface groups are saturated using a monofunctional silane monomer (e.g. trimethylmethoxysilane (M)), also called end-capping agent (Figure 2.13).

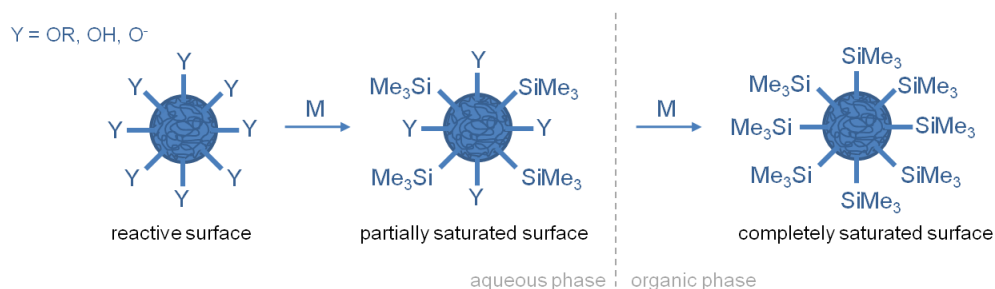


Figure 2.13 End-capping process

In the first step, the surface is partially saturated by addition of the end-capping agent to the aqueous dispersion. To obtain a fully inactive surface, the particles are transferred into an organic solution and additional end-capping agent is added. The obtained particles do not show any aggregation due to further condensation and can easily be redispersed in organic solvents.

Alternatively, the end-capping process can also be used to exchange the surface groups to other functionalities which can later be used for further modifications. This aspect will be discussed in the subsequent section.

2.2.5 Functional Polyorganosiloxane Networks

The polyorganosiloxane system described in this work is formed as a core-shell structure. This architecture offers the possibility of both, core and surface functionalization. The two types of modifications can be carried out independently from each other, thus, offering a broad range of orthogonal functionalizations. Thereby, a highly flexible system is obtained.

Various different types of surface modifications can be considered. The functional groups on the particle surface can be varied with ease during the end-capping process simply by altering the end-capping agent. Figure 2.14 illustrates a few examples of commercially available end-capping agents and the resulting surface functionalities. As described before, the end-capping agent M is used to produce a totally saturated and therefore unreactive surface. The monomers M-H and M-Ac carry supplementary functional groups, which can be used for further surface modifications like the hydrosilation reaction or click-chemistry. Using one of these mechanisms almost every desired polymer can be grafted onto the surface.

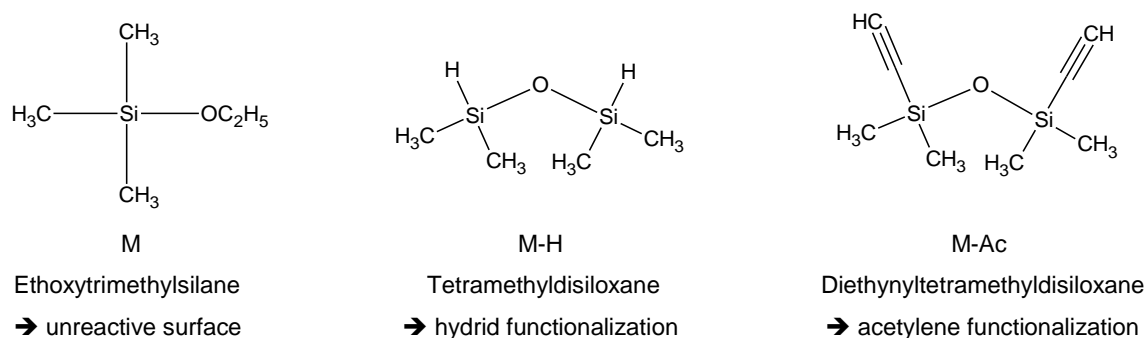


Figure 2.14 Commercially available end-capping agents

For the hydrophilic surface modification presented in this work, tetramethyldisiloxane (M-H) was used as end-capping agent. Poly(ethylene glycol) (PEG) was grafted onto the particles surface in a hydrosilation reaction as described in Chapter 2.2.5.2.

Additionally, functional monomers can be integrated into the network structure during polymerization. Hence, the core of the system can be functionalized as well. Figure 2.15 shows examples of monomers which have already been used for the core modification.

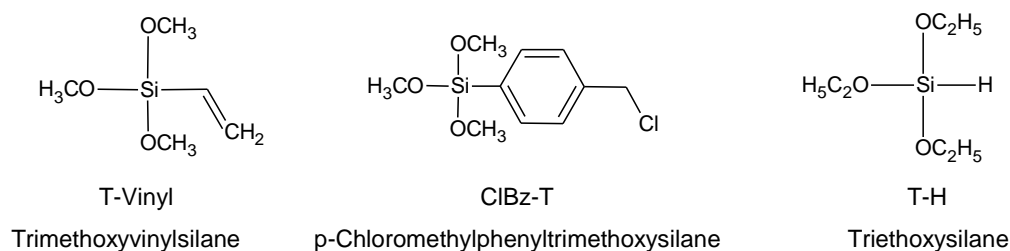


Figure 2.15 Functional cross-linking monomers

The T-Vinyl monomer was incorporated by N. Jungmann into the polyorganosiloxane system to provide a π -bonding that can be used for the fixation of metal ions inside the network.⁵⁷ The ClBz-T monomer possesses various useful properties. Its characteristic UV-absorption band in the range of 250-290 nm provides the opportunity of an easy analysis and detection. Furthermore, the chlorine atom can react in a quaternization or substitution reaction and amphiphilic nanocontainers or for example dye modified nanoparticles can be obtained. In the first case, electrostatic interactions are utilized while in the second case a covalent attachment is generated.

In this work, the ClBz-T monomer was labeled with fluorescent dyes to obtain a dye modified monomer Dye-Bz-T which was then polymerized into the core of the polyorganosiloxane system (see Chapter 2.2.5.1).

The T-H monomer can be used in addition to the M-H end-capping agent. Thus, the availability of hydride groups for the hydrosilation reaction is increased, leading to higher yields.

2.2.5.1 Dye-labeled Monomers

For biomedical applications, the possibility of imaging and detection of nanoparticles is an important issue. Generally, labeling can be achieved with different approaches like the incorporation of gold nanoparticles, quantum dots or fluorescent dye molecules. The polyorganosiloxane structures can easily be labeled using fluorescent dyes. The p-chloromethylphenyltrimethoxysilane monomer (ClBz-T) provides the opportunity of a substitution reaction of the chlorine atom in a S_N2-reaction mechanism using caesium salts of dye molecules. Caesium iodide can be added to the reaction solution to increase the reactivity of the benzyl groups. In a Finkelstein reaction the chlorine atom of the ClBz-T monomer is exchanged against an iodide atom providing a better leaving group for the following substitution reaction. To increase the solubility of the dye 18-crown-6 ether is added. The reaction scheme is shown in Figure 2.16. It is also possible to perform the substitution reaction after the polymerization inside the polyorganosiloxane network. Small molecules can penetrate the network and covalently bind to the chloromethylphenyl groups inside the network.⁵⁸ Nevertheless, performing the substitution reaction using the monomer pointed out to be more convenient, especially if an

⁵⁷ Jungmann, N. *Dissertation*, Johannes Gutenberg-Universität Mainz, 2000

⁵⁸ Graf, C. *Dissertation*, Johannes Gutenberg-Universität Mainz, 1999

additional surface modification was performed besides the incorporation of dye labels.

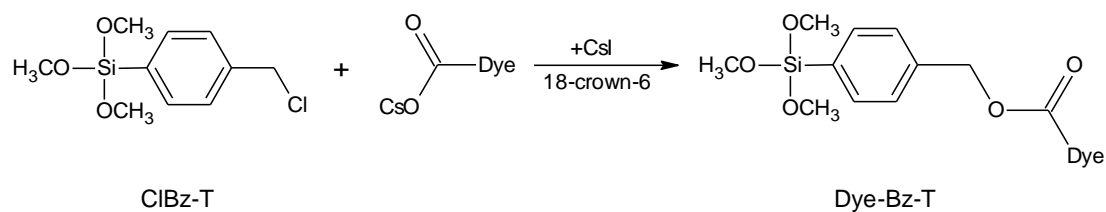


Figure 2.16 Reaction scheme of the fluorescent labeling of ClBz-T via a substitution reaction

In this work, three different fluorescent dyes were covalently bound to the ClBz-T monomer. The molecular structures of the investigated dye-functionalized monomers Dye-Bz-T are presented in Figure 2.17.

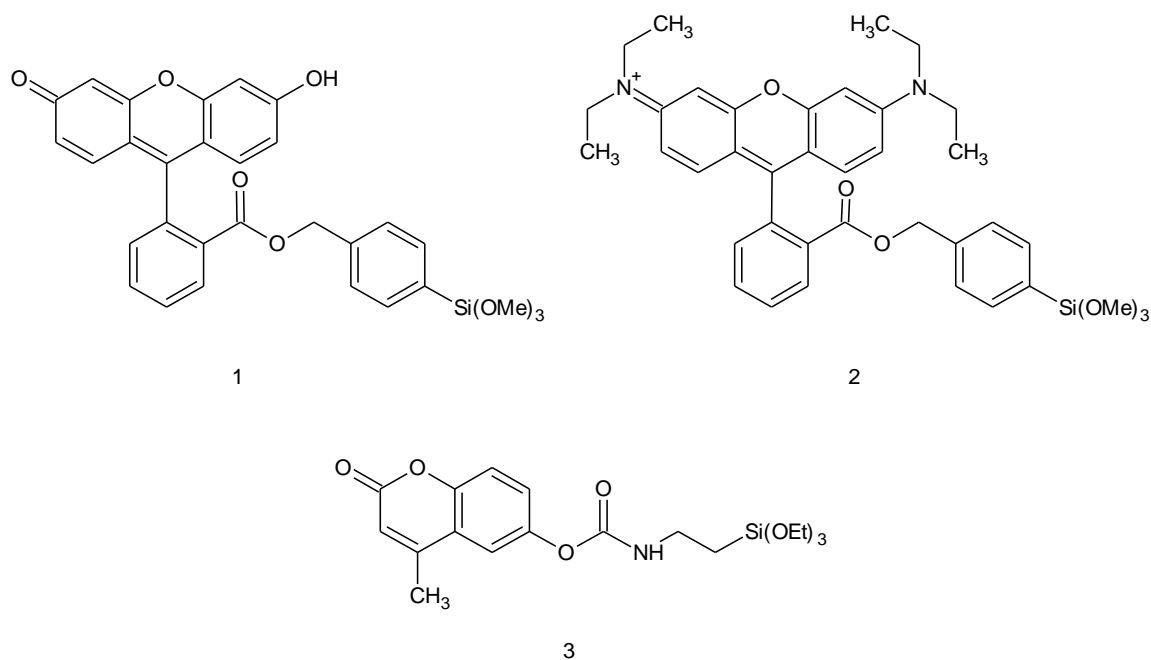


Figure 2.17 Molecular structure of dye-functionalized monomers: Flu-Bz-T (1); Rho-Bz-T (2); Coum-T (3)

The monomers Flu-Bz-T and Rho-Bz-T were synthesized using the procedure described above (Flu-Bz-T: *p*-fluoreceinylmethylphenyltrimethoxysilane, Rho-Bz-T: *p*-rhodaminylmethylphenyltrimethoxysilane, Coum-T: *O*-4-methylcoumarinyl-*N*-[3-(triethoxysilyl)-propyl]-carbamate). The Coum-T monomer is commercially available and was purchased from ABCR.

2.2.5.2 Heterofunctional Poly(ethylene glycol)

S. Scholz, C. Diehl and S. Flügel proved that the hydrosilation reaction is a useful tool to obtain water-soluble polyorganosiloxane nanoparticles that are biocompatible as well.^{13,59,60} A heterofunctional poly(ethylene glycol), synthesized via anionic polymerization, is covalently bound to the surface. The PEG carries an allyl as well as a carboxyl end-group. Therefore, a free binding site is available after the grafting process, offering the opportunity of further modification, thus, providing a highly flexible system with respect to the surface functionality.

The reaction scheme for the synthesis of allyl-PEG-carboxyl polymer is shown in Figure 2.18.⁶¹ The terminal allyl group is introduced by using allyl alcohol as an initiator which is deprotonated by potassium naphthalid. Heterofunctionality is obtained by a termination with succinic acid anhydride producing the carboxyl functionalized chain end.

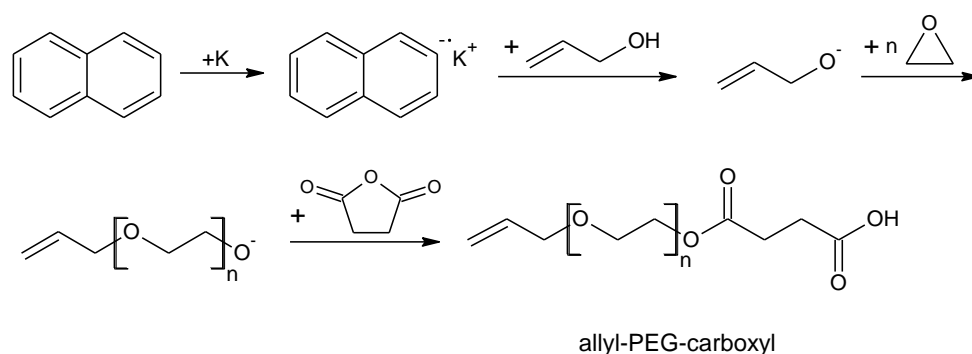


Figure 2.18 Anionic polymerization of ethylene oxide

To graft the poly(ethylene glycol) to the polyorganosiloxane surface a hydrosilation reaction is performed (Figure 2.19). The reaction is catalysed by the so-called Karstedts catalyst (platinum-divinyltetramethylsiloxane) containing 2.0-2.5 % of platinum. Due to the sensibility to oxidation the reaction is carried out in argon atmosphere.

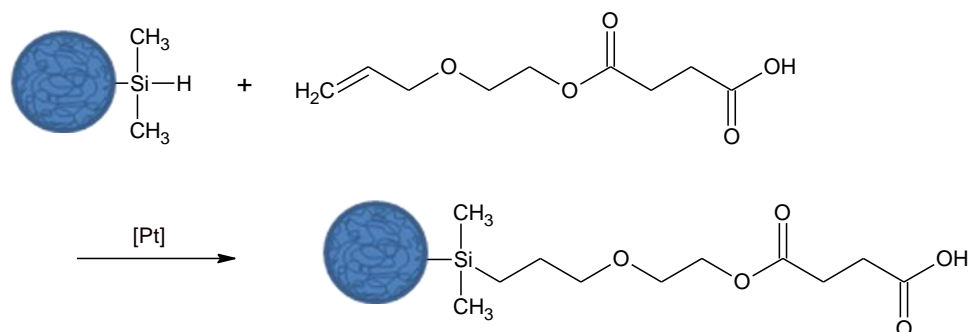


Figure 2.19 Hydrosilation reaction of polyorganosiloxane nanoparticles with PEG

⁵⁹ Scholz, S. *Dissertation*, Johannes Gutenberg-Universität Mainz, **2005**

⁶⁰ Lindenblatt, G. *Dissertation*, Johannes Gutenberg-Universität Mainz, **2000**

⁶¹ Rheingans, O. *Dissertation*, Johannes Gutenberg-Universität Mainz, **2000**

The synthesized particles still carry an active chain end. The carboxyl groups are suitable for further modifications with amine functionalized biomolecules.

2.2.5.3 Biofunctionalization

The combination of nanotechnology and molecular biology impressively broadened the applicability of nanomaterials in *in vivo* and *in vitro* applications.¹¹ The attachment of biomolecules to the surface of nanoparticles provides increased biocompatibility and hinders the recognition by the mononuclear phagocyte system (MPS).⁶² Additionally, specific interactions between particles and target molecules which can be achieved for example between surface attached antibodies and antigens. Specific interactions are of high interest for drug delivery, cell sorting and marking applications. As described before, cell sorting techniques use the interactions between functionalized beads and target molecules for isolation and concentration of cells or DNA segments. Targeted distribution of drug delivery systems is an effective method to reduce the dose of the drug and decrease undesired side effects. Another interesting research area is the determination of nanoparticle uptake mechanisms into various cell types. Various uptake mechanism like diffusion, receptor-mediated endocytosis or non-specific cellular uptake are known. The cellular uptake depends on several effects. One important quality is the surface chemistry of the material. Hence, an adequate surface modification allows for a controlled cellular uptake. Receptor-mediated endocytosis can be induced via surface attached monoclonal antibodies while a non-specific cellular uptake has been reported in case of PEG coated nanomaterials, e.g.. For the attachment of biomolecules to the surface, different techniques are reported in literature, for example physical adsorption, electrostatic binding, specific interactions and covalent binding.^{63, 64} By covalent binding of biomolecules, undesired desorption of surface attached biomolecules can be excluded. One prominent procedure is N-ethyl-N'-dimethylaminopropylcarbodiimid (EDC) coupling between carboxyl and amine functionalized materials which leads to the covalent binding via the formation of amide bonds between the particles and the biomolecule.⁶⁴

⁶² Zhang, Y.; Kohler, N.; Zhang, M. *Biomaterials* **2002**, *23*, 1553

⁶³ Christopoulos, T. K.; Diamandis, E. P. *Clin. Chem.* **1991**, *37/5*, 625

⁶⁴ Hermanson, G. *Bioconjugate Techniques*, Elsevier, **2008**

3 Characterization Methods

3.1 Transmission Electron Microscopy⁶⁵

The electron microscopy is an important imaging method used for micron-sized as well as nano-sized objects. The shorter wavelength of the applied electrons permits a drastic increase in resolution compared to conventional light microscopy. A 200 times better resolution can be obtained. Therefore it is possible to image objects in the sub angstrom range.

3.1.1 Transmission Electron Microscopy (TEM)

The schematic assembly of an electron microscope is shown in Figure 3.1.

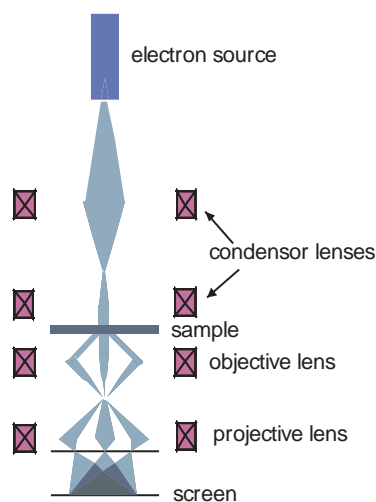


Figure 3.1 Schematic assembly of the light pass in an electron microscope

An assembly of various magnetic lenses are used to focus the electron beam produced by a thermoionic electron source. The generated image is projected onto a light screen or directly to the detector plate of a digital camera. For sample preparation, liquid samples are disposed on a carbon coated copper grid, solid samples have to be cut into ultrathin slices. When the electron beam is passing through the sample, scattering occurs in dependence on the electron density of the material. An electron density distribution is generated which mirrors the electronic structure of the sample. In conventional electron microscopy only dry samples can be investigated. To image dissolved or dispersed structures the cryogenic transmission electron microscope (cryo-TEM) must be used.

⁶⁵ Knoll, M.; Ruska, E. Z. *Physik* **1932**, 78, 31

3.1.2 Cryogenic Electron Microscopy (cryo-TEM)

For cryo-TEM measurements an aqueous sample is deposited on the carbon coated copper grid is flash frozen in liquid ethane or propane. Thereby the crystallization of water can be avoided and glass-like ice is formed. Compared to the grids that are used in conventional TEM measurements, the carbon film of the cryo-TEM grids is interspersed with holes in a defined μm -range in which a water film of approximately 100 nm thickness is formed within the holes during the blotting process.

3.1.3 Energy Dispersive X-ray Spectroscopy (EDX)

The energy dispersive X-ray spectroscopy is used to determine the elemental composition of a sample. The atoms of the material are excited by the electron beam which causes an element specific X-ray emission. By combining an EDX-detector with a scanning electron microscope (SEM-EDX) or a transmission electron microscope (TEM-EDX), a space-resolved element distribution can be obtained. The main advantage of EDX in comparison to other X-ray spectroscopic methods is the possibility of a simultaneous analysis of a variety of elements. However, the detection limit is relatively low especially regarding elements with low atomic numbers.

3.2 Asymmetrical Flow Field-Flow Fractionation (AF-FFF)⁶⁶

The asymmetrical flow field-flow fractionation (AF-FFF) is an efficient method for the determination of particle sizes and particle size distributions as well as for separation and fractionation of samples containing colloidal particles. In comparison to light scattering measurements, one main advantage of the FFF family is the possibility to evaluate bimodalities of samples even if the sizes of the fractions are relatively similar. In dynamic light scattering measurements this information is often lost due to the overestimation of larger particles as well as the averaging.

The basic principles of the AF-FFF are similar to chromatographic methods. A characterization and fractionation of particles according to their size is achieved. However, in AF-FFF measurements no stationary phase is present. The fractionation is induced by an external field applied perpendicular to the flow of the solvent in a channel. Various methods with different external fields are in use, e.g. electrical, magnetical, thermal or flow field-flow fractionation.

In case of a flow field-flow fractionation a second flow of solvent, the so-called cross-flow, is applied. Figure 3.2 shows a schematic setup of an AF-FFF channel. In an AF-FFF experiment three distinct phases take place: 1. Injection, 2. Focusing and Relaxation, 3. Elution. During the focusing process, the particles are accumulated at the lower channel wall (accumulation wall) due to the interaction of the particles with the cross-flow. The accumulation wall consists of a semi-permeable membrane which pore sizes are responsible for the lower rejection limit. The generation of a concentration gradient leads to a directed diffusion of the particles towards the middle of the channel.

⁶⁶ J. C. Giddings: The Field-Flow Fractionation Family: Underlying Principles, in *Field-Flow Fractionation Handbook*, Wiley-Interscience, 2000

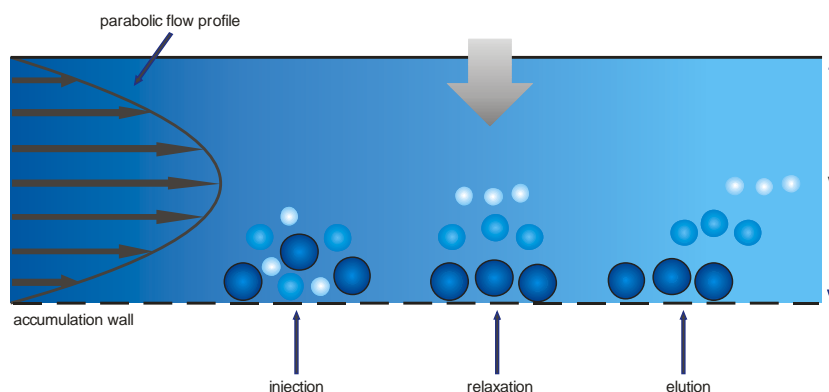


Figure 3.2 Schematic illustration of a cross section of the AF-FFF channel

Since the diffusion coefficient D is proportional to $1/R_h$, smaller particles show a higher diffusion velocity compared to larger particles and will therefore be located in larger distance to the accumulation wall after the relaxation period. By rinsing the channel with the solvent a parabolic flow profile is induced resulting in different flow velocities in different heights of the channel. This leads to a faster elution and consequently a shorter retention time for smaller particles which linger in the middle of the channel and are transported within layers of higher flow rates. This behavior leads to a direct proportionality between hydrodynamic radius R_h and retention time t_R of the particles:

$$t_R \sim R_h \quad 3.1$$

For detection, different detectors like UV-, RI- and light scattering setups are available.

3.3 Light Scattering^{67, 68}

The light scattering analysis is an important tool for the characterization of polymeric samples in solution. During a light scattering experiment a laser beam induces oscillating dipoles in the electron shell of molecules in the sample solution. These induced dipoles are emitting light which is detected and analysed with regard to its intensity, angular- and time-dependence intensity to gain information about static and dynamic properties of the molecules (Figure 3.3).

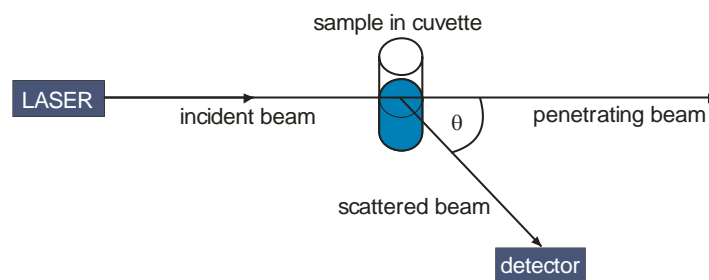


Figure 3.3 Schematic illustration of a light scattering setup (θ = scattering angle)

⁶⁷ Schärftl, W. *Light Scattering from Polymer Solutions*, Springer, Heidelberg, **2007**

⁶⁸ Schmidt, M. *Simultaneous Static and Dynamic Light Scattering in Dynamic Light Scattering*, Brown, W. (editor), Clarendon Press, Oxford, **1993**

In static light scattering, the average intensity of the scattered light is measured over a fixed time interval at various scattering angles θ . This method reveals information about the structure of the studied material such as weight-average molar mass M_w , second virial coefficient A_2 and z-average of the radius of gyration $\langle R_g^2 \rangle_z$.

To obtain information about the dynamic properties of a material, dynamic light scattering is used. By analysis of the time-dependent fluctuations of the scattering intensity, the z-average diffusion coefficient D_z can be determined, that is related to the inverse z-average of the sphere equivalent hydrodynamic radius $\langle 1/R_h \rangle_z^{-1}$ via the Stokes-Einstein as shown below.

3.3.1 Static Light Scattering (SLS)

The theoretical basis for static light scattering (SLS) measurements is the fluctuation theory of Smoluchowski, Einstein and Debye. They showed that the thermal molecular movement is causing variations in density and concentration which will cause fluctuations of the polarizability α . Replacing the fluctuations of the polarizability by fluctuations of the refractive index n_D the following equation results for small molecules (diameter $< \lambda/20$):

$$(I_{solution} - I_{solvent}) \frac{I_{std,abs}}{I_{std}} = b^2 kT \frac{c}{\left(\frac{\partial \pi}{\partial c} \right)_{T,N}}, \quad 3.2$$

with scattering intensity I , Boltzmann constant k , temperature T , concentration c , osmotic pressure π and particle number N . The contrast factor K and the Rayleigh ratio R are defined by the following equations:

$$b^2 = \frac{4\pi^2}{\lambda_0^4 N_L} n_{D,0}^2 \left(\frac{\partial n_D}{\partial c} \right)^2 = K \quad 3.3$$

$$R = (I_{solution} - I_{solvent}) \frac{I_{std,abs}}{I_{std}}, \quad 3.4$$

with the Loschmidts number N_L , the wavelength in vacuum λ_0 and the refractive index of the medium $n_{D,0}$.

Using the van't Hoff law for an ideal solution

$$\frac{\partial \pi}{\partial c} = \frac{kT}{M} \quad 3.5$$

Equation 1.2 can be reduced to the simple form

$$\frac{Kc}{R} = \frac{I}{M}. \quad 3.6$$

Taking into account the particle-solvent interaction that occur in real solutions a supplementary factor containing the 2nd virial coefficient A_2 has to be added in Equation 3.6

$$\frac{Kc}{R} = \frac{I}{M} + 2A_2c + \dots \quad 3.7$$

To describe scattering centres with intraparticle interferences the so-called form factor $P(q)$ is introduced

$$P(q) = 1 - \frac{1}{3} R_g^2 q^2 + \dots, \quad 3.8$$

with the scattering vector q :

$$q = \frac{4\pi n_{D,0}}{\lambda_0} \sin\left(\frac{\theta}{2}\right) \quad 3.9$$

In this case, Equation 3.7 must be transformed into the following expression:

$$\frac{Kc}{R} = \frac{I}{MP(q)} + 2A_2c + \dots \quad 3.10$$

This equation can easily be transformed into the well-known Zimm equation which is the fundamental basis for static light scattering analysis:

$$\frac{Kc}{R} = \frac{I}{M} \left(1 + \frac{1}{3} R_g^2 q^2\right) + 2A_2c + \dots, \quad 3.11$$

with the scattering angle q and the radius of gyration R_g .

In case of polydisperse samples average values of the molecular mass M and the radius of gyration R_g are obtained:

$$M_w = \frac{\sum c_i M_i}{\sum c_i} \quad (\text{weight-average}) \quad 3.12$$

$$\langle R_g^2 \rangle_z = \frac{\sum c_i M_i^2 R_{g,i}^2}{\sum c_i M_i^2} \quad (\text{z-average}), \quad 3.13$$

with the radius of gyration R_g .

Figure 3.4 shows a typical Zimm plot. Kc/R is plotted against $q^2 + kc$ with the scaling constant or

spreading-factor k . Extrapolation of $c \rightarrow 0$ and $q \rightarrow 0$ allows the determination of the weight-average molecular weight M_w , the 2nd virial coefficient A_2 and the z-average radius of gyration $\sqrt{\langle R_g^2 \rangle_z}$.

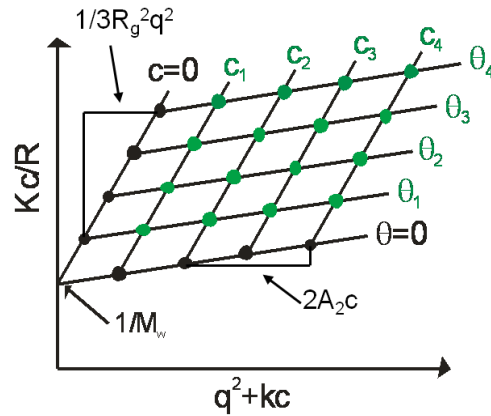


Figure 3.4 Zimm plot with extrapolation of $c \rightarrow 0$ and $q \rightarrow 0$

3.3.2 Dynamic Light Scattering (DLS)

In dynamic light scattering the time-dependent fluctuation of the scattering intensity $I(t)$ is measured. These fluctuations are caused by the diffusion of molecules in the scattering volume. As the diffusion depends on the size of the objects present, an analysis of the time-dependent fluctuation of the scattering intensity provides information about the molecule sizes present in the sample.

An autocorrelation function $g_2(t)$ is applied to correlate the measured fluctuations in time

$$g_2(t) = \langle I(0)I(n\tau) \rangle_{\text{abs}}, \quad 3.14$$

with the scattering interval $n\tau$. Figure 3.5 illustrates the transformation of the scattering signal to $g_2(t)$.

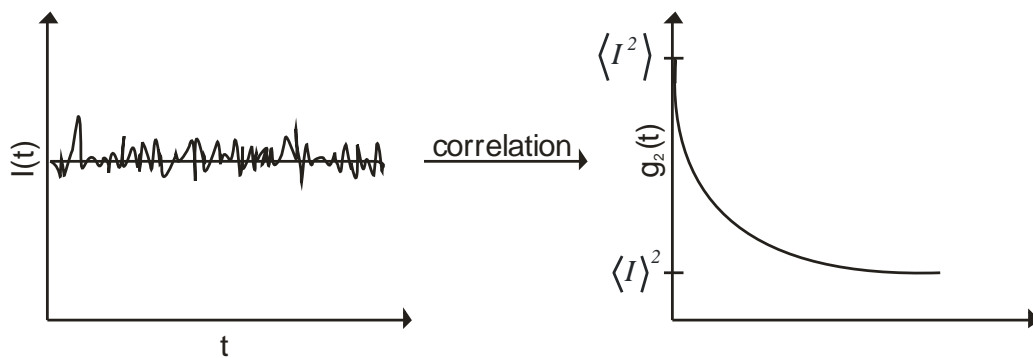


Figure 3.5 Time-dependent fluctuation of scattering intensity and scattering autocorrelation function $g_2(t)$

The intensity $I(0)$ corresponding to $t=0$ is correlated with the scattering intensity $I(n\tau)$ at $t=n\tau$. Thereby, an exponential decreasing autocorrelation function results which decreases from $\langle I \rangle$ to $\langle I \rangle^2$. For small particles a faster decrease of the correlation function results due to their higher diffusion coefficient compared to larger particles.

Using the so-called Siegert relation a correlation function of the scattering amplitude $g_I(t)$ can be calculated:

$$g_I(t) = \sqrt{\frac{g_2(t) - A}{A}}, \quad 3.15$$

with the experimental determined baseline A ($A = \langle I \rangle^2$).

The correlation function $g_I(t)$ shows a monoexponential decay for monodisperse, spherical particles:

$$g_I(t) = B \exp(-q^2 D t). \quad 3.16$$

The constant B represents the signal-to-noise ratio which depends on the experimental setup. The scattering vector q is calculated from the scattering angle θ and the wavelength λ used during the measurement:

$$q = \frac{4\pi}{\lambda} \sin\left(\frac{\theta}{2}\right). \quad 3.17$$

Dealing with small, polydisperse particles the correlation function $g_I(t)$ is given by the sum of the exponential function of the single components i :

$$g_I(t) = B \frac{\sum m_i M_i \exp(-q^2 D_i t)}{\sum m_i M_i}. \quad 3.18$$

An apparent diffusion coefficient D_{app} can be determined from the initial slope in a logarithmical plot:

$$\left[\frac{d(\ln g_I(t))}{dt} \right]_{t \rightarrow 0} = -q^2 \frac{\sum m_i M_i D_i}{\sum m_i M_i} = -q^2 D_{app}. \quad 3.19$$

In case of larger particles where intraparticle interferences occur, the particle form factor has to be taken into account:

$$\left[\frac{d(\ln g_I(t))}{dt} \right]_{t \rightarrow 0} = -q^2 \frac{\sum m_i M_i P_i(q) D_i}{\sum m_i M_i P_i(q)} = -q^2 D_{app}. \quad 3.20$$

Typically, a series expansion, called the cumulant method, is used to determine the diffusion coefficient of polydisperse samples:

$$\ln g_1(t) = -\Gamma t + \frac{\mu_2}{2!} \Gamma^2 t^2 - \frac{\mu_3}{3!} \Gamma^3 t^3 + \dots, \quad 3.21$$

with

$$\Gamma = \overline{D_{app}^2} q^2. \quad 3.22$$

In case of hard spheres the second cumulant μ_2 is a quantity for the polydispersity of the sample:

$$\mu_2 = \frac{\left(\overline{D_z^2} - \overline{D_z}^2 \right)}{\overline{D_z}^2} = \sigma_D^2. \quad 3.23$$

μ_2 values between 0.05 and 0.1 correspond to relatively monodisperse particles while polydisperse samples give rise to μ_2 values larger than 0.1.

Extrapolating the apparent diffusion coefficient D_{app} to $q \rightarrow 0$ and $c \rightarrow 0$ leads to the z-average of the diffusion coefficient D_z :

$$\lim_{q,c \rightarrow 0} (D_{app}(q)) = D_z. \quad 3.24$$

To obtain information about the sizes of the investigated particles the Stokes-Einstein equation

$$R_h = \left\langle \frac{l}{R_h} \right\rangle_z^{-1} = \frac{kT}{6\pi\eta_0 D_z} \quad 3.25$$

is used to calculate the sphere-equivalent hydrodynamic radius R_h (η_0 = viscosity of solvent).

3.3.3 The ρ -ratio

The ρ -ratio is defined as the quotient of the radius of gyration R_g and the sphere-equivalent hydrodynamic radius R_h :

$$\rho = \frac{\sqrt{\left\langle R_g^2 \right\rangle_z}}{\left(\left\langle \frac{l}{R_h} \right\rangle_z \right)^{-1}}. \quad 3.26$$

A comparison between the theoretical and the experimentally determined ρ -ration gives information about the topology of the system as demonstrated in Table 3.1.

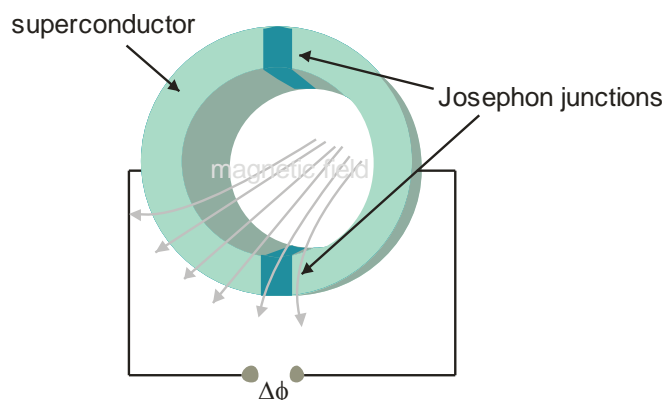
Table 3.1 ρ -ratios of different topologies

Topology	ρ -ratio
homogeneous sphere	0.775
hollow sphere	1
random polymer coil	1.505

3.4 Super Conducting Quantum Interference Device (SQUID)^{69,70}

The super conducting quantum interference device, abbreviated SQUID, is commonly utilized to measure weak magnetic fields.

A SQUID consists of a superconducting loop containing one (DC SQUID) or two (RF SQUID) insulating barriers. Cooper pairs, responsible for conduction of electric current in superconductors, are able to tunnel through these barriers if they are sufficiently thin. This effect was discovered by Brian Josephson in 1962 and is therefore known as Josephson effect.



3.6 Schematic illustration of a RC-SQUID

A second important effect for the functionality of a SQUID magnetometer is the quantization of the magnetic flux in superconductive loops. The magnetic flux is always an integer multiple of the elemental magnetic flux quantum. A change in the external magnetic field is directly inducing a modification of the magnetic flux within the superconductive loop. By applying a direct voltage in case of the DC-SQUID or an alternating voltage in case of the RF-SQUID, which is high enough to allow the tunnelling of a Cooper pair, it is possible to tap a measureable voltage. Changing the external magnetic field leads to compensating current to abide the flux quantization. Thereby voltage fluctuations can be detected.

In a typical SQUID measurement a sample containing gelatine capsule is placed inside the superconducting loop. The interaction between the sample and the external magnetic field causes

⁶⁹ Clarke, J.; Braginski, A. I. *The SQUID Handbook*, Wiley-VCH, 2004

⁷⁰ Josephson, B. D. *Phys. Lett.* **1962**, 1, 251

alterations of the superconducting current in the loop. The resulting voltage can be measured in dependence on the position of the sample. Afterwards, this signal can be converted into the magnetization of the material in dependence on the external magnetic field strength. Thus, the typical magnetization curves are observed. This setup is extremely sensible and can be used to measure magnetic field as low as 5×10^{-18} T.

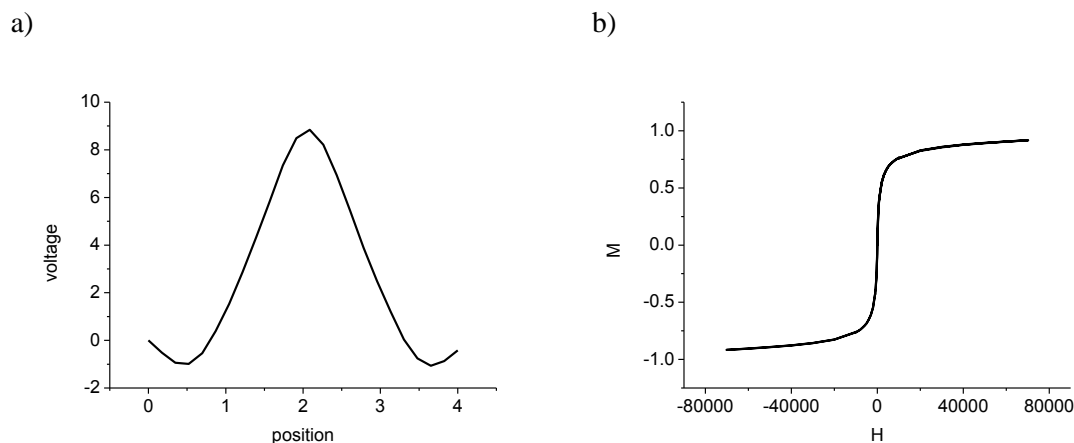


Figure 3.7 a) Position dependent voltage measurement and resulting b) field-dependent magnetization determined via SQUID measurements

3.5 Mössbauer Spectroscopy⁷¹

In 1958 Rudolph Mössbauer discovered a resonance phenomenon which he described as recoil-free γ -emission. In today's research this phenomenon, called the Mössbauer effect, is used to determine bonding properties, molecular symmetries, magnetic properties as well as dynamic processes in solid states.

γ -emission occurs if an atomic core (the so-called source) in a high-energy state transits to a low-energy or ground state. Under certain conditions, the emitted γ -quantum can be absorbed by an identical core, the absorber, resulting in an excitation of the second core. The requirement for this resonance is a total consistence between the energy of the γ -quantum E_0 and the transition energy between the two energy states E_1 and E_2 of the absorber:

$$E_0 = E_1 - E_2 \quad 3.27$$

Due to the conservation of momentum rules the nuclei of a free-moving atom or molecule feels a recoil during γ -quantum emission. This would result in a decrease of the γ -quantums energy meaning that no resonance between two identical cores could follow.

⁷¹ a) Gütlich, P. *Chemie in unserer Zeit* **1970**, 4/5, 133; b) Gütlich, P. *Chemie in unserer Zeit* **1970**, 5/5, 131

If γ -emission of a core occurs in a solid the whole lattice recoils resulting in a negligible recoil energy due to the enormous mass of the solid material. Thus, in crystalline solids a recoil-free γ -emission can be observed.

To induce slight changes in E_0 the Doppler effect is used which is realized via slow movement of source and absorber against each other. Thus, an energetic spectrum is obtained that is used to probe resonance states of the absorber material.

The number and the position of the resonance peaks depends on the electronic and magnetic fields present at the particular nuclei. To describe these properties three parameters are used: isomeric shift δ , quadrupole splitting ΔE_Q and hyperfine splitting H_{hf} .

The isomeric shift δ results from the possibility of an electron to be present in the atom nuclei. This would change the energy of the nucleus ground state and therefore, changing the energy of the emitted or absorbed γ -quantum. As a consequence, the appearance of the resonance peak is shifted relative to the velocities of core and absorber.

The presence of an inhomogeneous electric field at the nucleus results in a quadrupole moment leading to a splitting of the cores energetic levels. The transition between the arising sub-levels generates a splitting of the resonance spectrum.

In case of nuclei with magnetic dipole moments and in presence of an external magnetic field, a second splitting of the levels can be observed, the so-called hyperfine splitting H_{hf} .

The described effects are imaged in Figure 3.8 as well as the resulting Mössbauer spectrum.

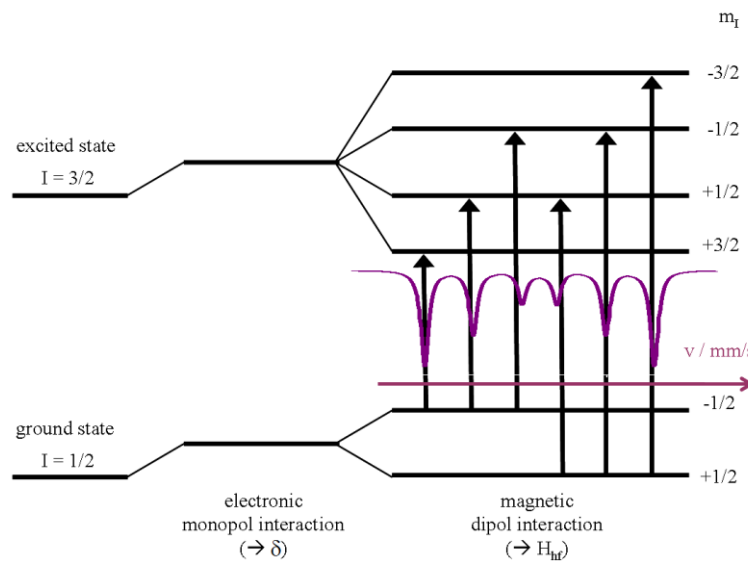


Figure 3.8 Splitting of energy levels and resulting Mössbauer spectrum

3.6 X-ray Powder Diffraction (XRD)⁷²

Powder diffraction is a common technique to analysis crystalline samples regarding their crystal structure and composition. In crystalline powders, every possible crystalline orientation is present. An incident x-ray beam is scattered at the lattice planes of the material as described by the Bragg Equation:

$$n\lambda = 2d \sin\theta, \quad 3.28$$

with $n = 1, 2, 3, \dots$, wavelength λ , spacing between lattice planes d and angle of reflection θ .

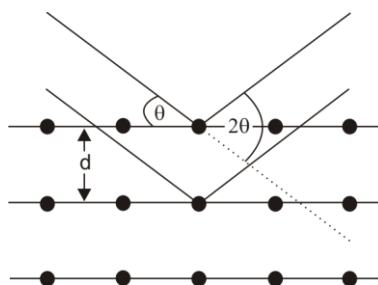


Figure 3.9 Schematic illustration of x-ray diffraction on crystalline materials

By plotting the intensity of the reflected beam against 2θ , a diffraction pattern is obtained. Since every material shows a characteristic diffraction pattern, the composition of the material can be determined by comparing the measured pattern to values reported in literature.

3.7 Matrix Assisted LASER Desorption/Ionisation-Time of Flight Mass Spectrometry (MALDI-TOF)⁷³

For mass analysis of sensitive and unstable molecules like biomolecules or large synthetic polymers the matrix assisted LASER desorption/ionisation time of flight analysis (MALDI-TOF) is used. Therefore, the sample is embedded into a matrix (typically a derivate of benzoic and cinnamon acid). A pulsed laser beam is vaporizing the matrix whereby intact sample molecules are carried into the vapour phase without degradation. Induced ionization and an electric field are used to accelerate the molecules towards a detector. Since the kinetic energy strongly depends on the mass of the analyte, the time of detection or time of flight *tof* is proportional to mass m and charge number z :

$$tof \sim \sqrt{\frac{m}{z}} \quad 3.29$$

⁷² Otto, M. *Analytische Chemie*, Wiley-VCH, 2006

⁷³ Jagtap, R. N.; Ambre, A. H. *Bulletin of Material Science* 2005, 28, 515

Small, light molecules show shorter flight times and reach the detector earlier than the larger and heavier ones.

The MALDI-TOF analysis is an absolute method, which is one main advantage of this technique compared to chromatographic approaches.

3.8 Gel Permeation Chromatography (GPC)⁷⁴

In polymer chemistry, molecular weights and distributions are often determined via the gel permeation (GPC) or size exclusion chromatography (SEC).

The main component of a GPC setup is a column filled with a porous material, the stationary phase. When the sample, being dissolved in the mobile phase, passes through the column all molecules with sizes below the so-called upper exclusion limit are penetrating into the pores of the solid material. Molecules that are larger than the upper exclusion limit are not able to penetrate into the pores. This fraction is directly eluted with the mobile phase. Due to the arising concentration gradient between stationary and mobile phase, the retained molecules are diffusing out of the pores and are eluted in order of their hydrodynamic volume. Larger particles elute first while smaller particles show longer elution times. Particles that are smaller than a certain size, the lower exclusion limit, are temporary retained in the stationary phase. By this means, no separation can be obtained. The molecular weight M can be generated from the elution volume V_e which is directly related to the hydrodynamic volume of the sample:

$$\log M = a - bV_e, \quad 3.30$$

with the constants a and b . The GPC is not an absolute method; a calibration is necessary. Typically, a polystyrene standard with a narrow particle size distribution is used. Based on the Kuhn-Mark-Houwink equation

$$[\eta] = KM^{a_n}, \quad 3.31$$

it is possible to create an universal calibration which can be used for all types of polymers ($[\eta]$: intrinsic viscosity, K , a_n : polymer specific Kuhn-Mark-Houwink parameter).

The universal calibration and a GPC elugram are illustrated in Figure 3.10. Typically, UV- and RI-detectors are used to monitor the elution processes.

⁷⁴ Tieke, B. *Makromolekulare Chemie*, VCH Wiley, 2005

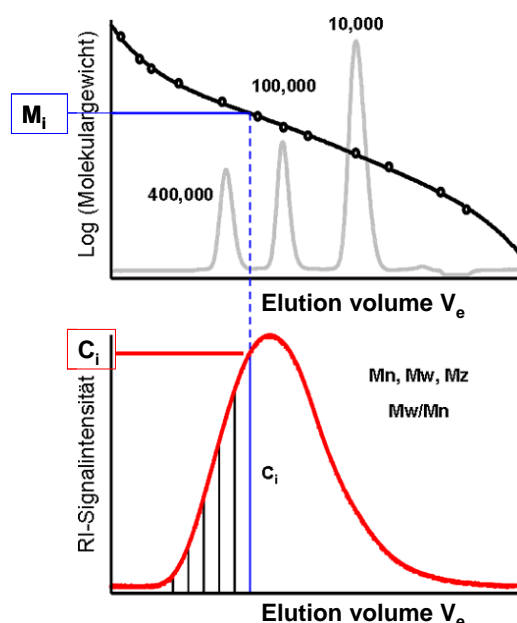


Figure 3.10 Universal calibration and elugram of a GPC measurement

3.9 Fluorescence Measurements⁷⁵

To determine the optical properties of fluorescent dyes or fluorescent labeled molecules various characterization methods are available.

3.9.1 Fluorescence Spectroscopy

In fluorescence spectroscopy an electromagnetic beam in the UV/VIS-range is used to excite the electrons of a fluorescent molecule to one of its higher energetic electronic states. Once an excited level is reached relaxation processes (vibrational relaxations) occur. The electrons are passing various vibrational states of the excited electronic state with or without transmission between different electronic levels (internal conversion) until they are reaching the lowest vibrational state. 10^{-10} to 10^{-7} s after the excitation, a transition to the electronic ground state takes place under the emission of light. The emitted fluorescent radiation can be detected and used to analyse the sample molecules. The transmissions that can be observed during spectroscopic measurements are illustrated in the Jablonski diagram shown in Figure 3.11.

⁷⁵ Lakowicz, J. R. *Principles of Fluorescence Spectroscopy*, Springer, 2006

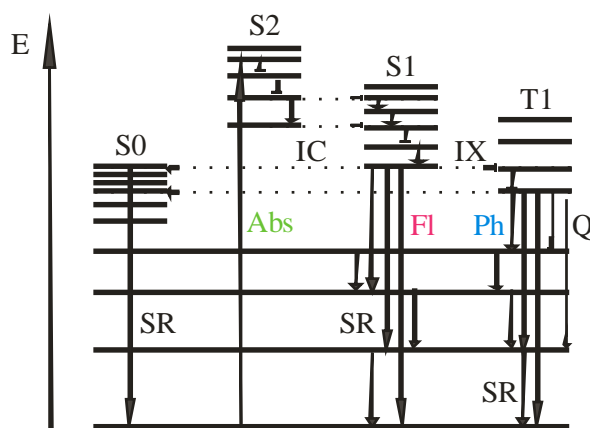


Figure 3.11 Jablonski diagram: S, T: electronic states; SR: irradiationfree relaxation; IC: internal conversion; IX: intersystem crossing; Abs: absorption; FI: fluorescence; Ph: phosphorescence⁷⁶

3.9.2 Fluorescence Microscopy

Fluorescence microscopy is applied to image fluorescent molecules in solid state or in solution. It is extensively used to investigate particle distribution in biological systems (for example in cell testing applications). It is also possible to image particle dynamics and movements in solution or biological systems.

The epifluorescence microscope is a widely used fluorescence microscope. An excitation filter is used to select the wavelength which is suitable to excite the fluorophores present in the sample. The beam is distracted by a dichroitic mirror which is only permeable by the fluorescent light. The emitted fluorescent light is separated from the illumination beam by passing an emission filter before detection. A typical setup of an epifluorescence microscope is illustrated in Figure 3.12.

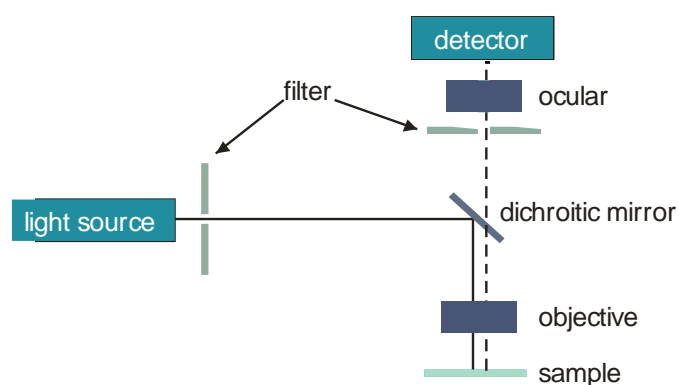


Figure 3.12 Schematic illustration of an epifluorescence microscope

⁷⁶ Petzke, F. *Praktikums-Skript Spektroskopie*, Johannes Gutenberg-Universität Mainz 2003

3.10 ζ -Potential⁷⁷

The electrical potential of a surface is a very important property of colloidal systems as well as other systems with sharply defined interfaces. The electrical surface potential strongly influences the interparticular interactions and therefore, the behavior in dispersions and suspensions.

The surface charge of colloidal particles is compensated by the counter-ions in the solution. In close vicinity to the surface, two different layers are build-up: the Stern layer and the diffuse layer (Figure 3.13).

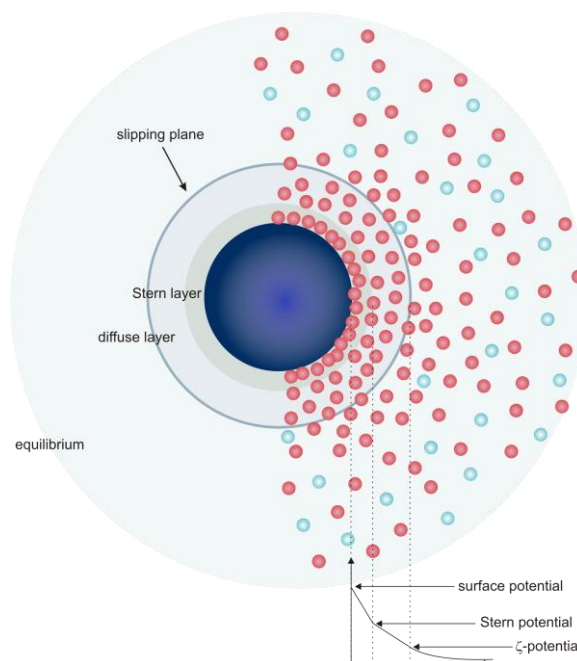


Figure 3.13 Stern and diffuse layer in colloidal solutions (blue: negatively charged, red: positively charged particles/ions)

The Stern layer is formed by ions that are strongly attached to the particle surface. This layer is populated by counter-ions. Next to the Stern layer, in larger distance to the particles surface, the so-called diffuse layer forms. This layer consists of counter-ions as well as a few co-ions, and only lightly interacts with the particle surface. The surface potential shows an exponential decrease within this layer:

$$\Psi = \Psi_0 \exp(-\kappa a), \quad 3.12$$

with the surface potential Ψ , the distance to the surface a and the Debye-Hückel-parameter κ .

⁷⁷ Delgado, A. V.; González-Caballero, F.; Hunter, R. J.; Koopal, L. K.; Lyklema, J. J. *Colloid Interface Sci.* 2007, 309, 194

$$\kappa = \sqrt{\frac{8\pi N_A I}{1000\epsilon kT}}, \quad 3.33$$

with the ionic strength I , Avogadro constant N_A and the dielectric constant ϵ .

The thickness of the diffuse layer is described by κ^{-1} and is typically specified to decrease to $1/e$ at the outer border of the layer ($e =$ elemental charge) which can vary between some tens of nanometers and approximately 100 nm for high and low ionic strength, respectively.

In an external electric field, the colloidal particles are accelerated due to their surface charge which results in a loss of the non-fixed diffuse layer. The particles start to move with a constant speed as soon as the electric or Coulomb force equals the friction ($F_{tr} = 6\pi\eta a v$). The obtained equilibrium is proportional to the charge of the particle and the applied electric field (electrophoretic movement). The detected electric potential is called ζ -potential. Typically, the measured potential is lower than the actual surface potential of the particle due to the screening of the maintaining ions. By this means the resulting ζ -potential corresponds to the potential at the so-called slipping plane (Figure 3.13).

The most commonly applied method for the determination of the electrophoretic mobility μ is the electrophoretic light scattering (ELS). This technique is based on the principles of dynamic light scattering: In dynamic light scattering the mobility of the particles is caused by Brownian motion. In electrophoretic light scattering these fluctuations result from the electrophoretic movement or electrophoretic mobility μ . The electrophoretic mobility μ is linked to the ζ -potential by the Henry formula

$$\mu = \frac{2\epsilon\zeta}{3\eta} f_1(\kappa a), \quad 3.34$$

with the correction factor or Henry function $f_1(\kappa a) = 1 + 1/(2(1 + \delta/\kappa a)^3)$ and $\delta = 2.5/(1 + 2e^{-\kappa a})$.⁷⁸

The Henry function is a monotonically varying function which increases from 1.0 for $\kappa a = 0$ to 1.5 for $\kappa a = \infty$. Hence, at the lower limit (in case of thick double layers, $\kappa a \ll 1$) Equation 3.33 becomes

$$\mu = \frac{2\epsilon\zeta}{3\eta} \quad 3.35$$

which is also known as Hückel equation. For thin double layers ($\kappa a \gg 1$), the Smoluchowski equation results:

⁷⁸ a) Hunter, R. J. *Foundations of Colloid Science*; Oxford University Press: New York, **2001**; b) Ohshima, H. J. *Colloid Interface Sci.* 2001, 239, 587–590

$$\mu = \frac{\varepsilon\zeta}{\eta} \quad 3.36$$

Alternatively the simplified Helmholtz-Smoluchowski approximation can be used for $\kappa a \gg 1$:

$$\zeta = \mu \frac{4\pi\eta}{\varepsilon\varepsilon_0} \quad 3.37$$

The ζ -potential and the surface charge σ are directly related to each other in the Gouy-Chapman formula:

$$\sigma = \varepsilon\zeta \left(1 + \frac{1}{\kappa a} \right) \quad 3.38$$

For ζ -potential measurements, an electric field is applied to the particle dispersion. The surface charge causes the particles to move towards the oppositely charged electrode. This electrophoretic velocity can be measured via the Doppler anemometry. An incident beam is splitted into two beams using a beam splitter. The two beams are distracted to meet within the measuring chamber. Hence, an interference pattern is generated. If the LASER light is scattered by a particle, a frequency shift occurs which is proportional to the velocity of the particle due to the Doppler effect. From this frequency shift the electrophoretic mobility can be calculated and converted into the ζ -potential via the Henry formula.

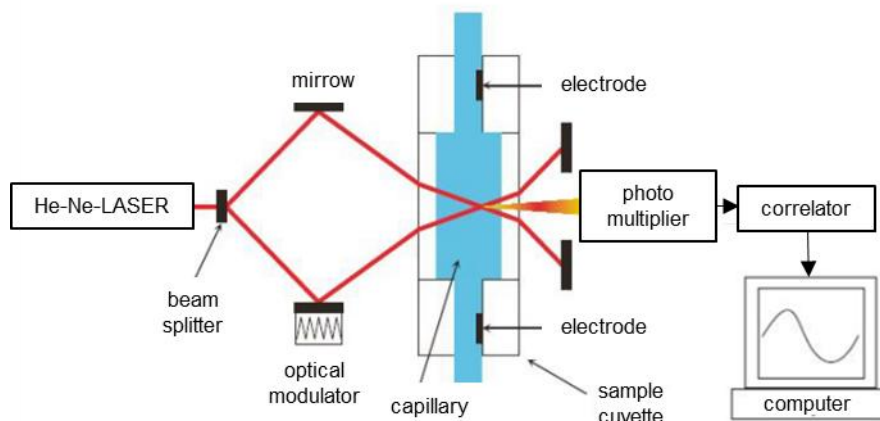


Figure 3.14 Schematic illustration of a Malvern Zetasizer Nano ZS⁷⁹

3.11 Ultraviolet/Visible Light Spectroscopy (UV/VIS spectroscopy)⁸⁰

In UV/VIS spectroscopy the absorption of electromagnetic radiation by matter is probed. A light source emitting light between 200 - 800 nm is used. A sample is placed into the beam and the whole spectrum of available wavelength is scanned to probe absorption phenomena. These occur when the wavelength of the beam is suitable to excite electronic states of the sample molecules. The resulting absorption provides information about the binding properties as well as the presence of certain molecular fragments.

In a conventional UV/VIS spectrometer, a light source emits in the UV/VIS-range to irradiate the sample. A monochromator is used to select the wavelength of interest. Depending on the experimental setup prisms as well as diffraction gratings are applied. A beam splitter divides the emitted light into two beams. A mirror is used to direct the emitted light which is either passing the reference or the sample cuvette. A wavelength-dependent absorption is detected by a photomultiplier.

In addition to information about the molecular structure an estimation of concentration is possible after an adequate calibration has been performed.

⁸⁰ Petzke, F. *Praktikums-Skript Spektroskopie*, Universität Mainz **2003**

4 Results and Discussion

4.1 Magnetic Iron Oxide Nanoparticles

4.1.1 Introduction

Magnetic nanoparticles are of high scientific and technological interest. Especially iron oxide nanoparticles (either magnetite (Fe_3O_4) or maghemite ($\gamma\text{-Fe}_2\text{O}_3$)) gained a lot of attention due to their superparamagnetic properties, their low toxicity and the availability of large scale synthesis. Despite intensive investigations on the nanoparticles fabrication, the synthesis of monodisperse, uniform particles with high saturation magnetizations remains challenging. As demonstrated in Chapter 2.1.4, there are various procedures for the synthesis of magnetic iron oxide nanoparticles. The best results are achieved via high temperature decomposition of organic precursors which leads to the formation of uniform, monodisperse particles with high saturation magnetizations.²³ Nevertheless, the synthetic procedures are relatively complex; the required chemicals are generally expensive and toxic. The coprecipitation process offers the advantage of a rapid, simple, high-yield synthesis using nontoxic chemicals. In this procedure, magnetic nanoparticles are formed via coprecipitation of Fe(II) and Fe(III) salts in basic solution. The particles are stabilized via electrostatic interactions and are stable in aqueous media. The presence of a capping-agent is not necessary. Particle size and composition depend on the Fe(II)/Fe(III)-ratio, the nature of the precipitation medium as well as pH-value, ionic strength and temperature.^{23,29} The particles synthesized via coprecipitation typically consist of both magnetic iron oxides. By adjusting the ratio between iron(II) chloride and iron(III) chloride to 1:2 or 2:3, the magnetite fraction can be increased. However, the high susceptibility of magnetite to oxidation complicates the synthesis of pure magnetite nanoparticles. Various studies showed that the nanoparticle size correlates with the size of the cation of the precipitation base. Vayssières et al. reported smaller particle sizes in case of precipitation in Na-salts compared to NH_4 -salts.⁸¹ Choosing high ionic strength or high pH-values for example by using strong alkalines like KOH also causes the formation of small nanoparticles and narrow size distributions. These parameters influence the chemical composition of the particle surface and consequently the electrostatic surface charge and surface tension causing the formation of smaller particles.⁸¹ Comparatively larger particles are obtained by coprecipitation at high temperatures (300 - 340 K).⁸²

In the following chapter, iron oxide nanoparticles synthesized under different reaction conditions are compared with respect to size, composition, magnetic properties and ζ -potential. All these properties

⁸¹ Vayssières, L.; Chanèac, C.; Tronc, E.; Jolivet, J. P. *J. Coll. Inter. Sci.* **1998**, *205*, 205

⁸² Gribanov, N. M.; Bibik, E. E.; Buzunov, O. V.; Naumov, V. N. *J. Magn. Magn. Mater.* **1990**, *85*, 7

are important factors for the encapsulation of inorganic nanoparticles into polymeric systems. This coating process is necessary to increase the particles stability and protect them from environmental influences. Especially with respect to biomedical applications a protective coating is mandatory to avoid undesired biodegradation. In Chapter 4.2 the stabilization of the particles via encapsulation into a polymeric system will be discussed.

4.1.2 Magnetic Iron Oxide Nanoparticles

In the following section, three samples of magnetic iron oxides are investigated. All samples were synthesized using a coprecipitation process of premixed iron chlorides, $\text{FeCl}_2 \cdot 4\text{H}_2\text{O}$ and $\text{FeCl}_3 \cdot 6\text{H}_2\text{O}$, in basic solution. Thereby, the ratio between the iron species and the coprecipitation media was varied as shown in Table 4.1. After synthesis and isolation of the particles, the pH-value was decreased to 3 via HCl addition to obtain stable aqueous dispersions. As explained before, the particles are stabilized via electrostatic interaction. Under neutral conditions, the particles are non-charged due to the hydroxyl groups present on the particles surface and precipitation occurs. By adjusting the pH-value to an acidic or basic range, the particles can be stabilized in aqueous dispersion (Figure 4.1).

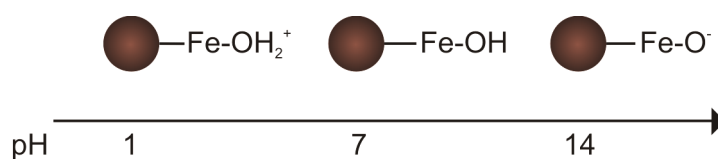


Figure 4.1 Schematic illustration of pH-dependent surface charge of iron oxide nanoparticles

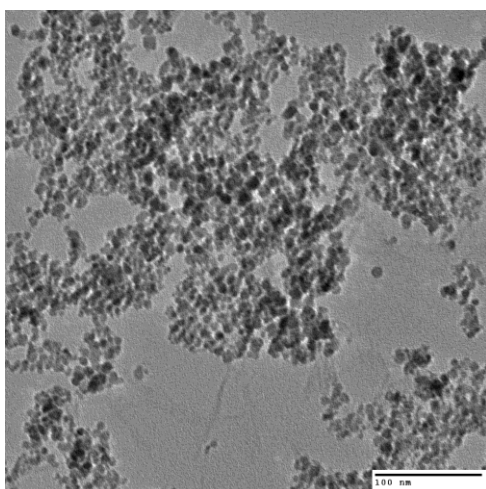
Table 4.1 Synthetic conditions for the synthesis of the iron oxide nanoparticles Fe_xO_y -I to IV

sample	Fe(II) : Fe(III)	coprecipitation medium
Fe_xO_y -I	1 : 1	NaOH
Fe_xO_y -II	1 : 2	NaOH
Fe_xO_y -IV	1 : 2	NH_4OH

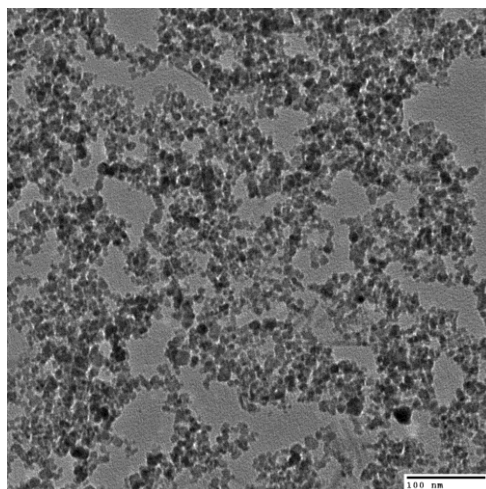
The TEM images of the aqueous particle dispersions in

Figure 4.2 show the presence of nearly spherical particles with a broad size distribution. The appearance of large aggregates results from drying effects caused by the sample preparation. The cryo-TEM image of Fe_xO_y -I in Figure 4.3 clarifies the presence of single particles besides larger aggregates.

a)



b)



c)

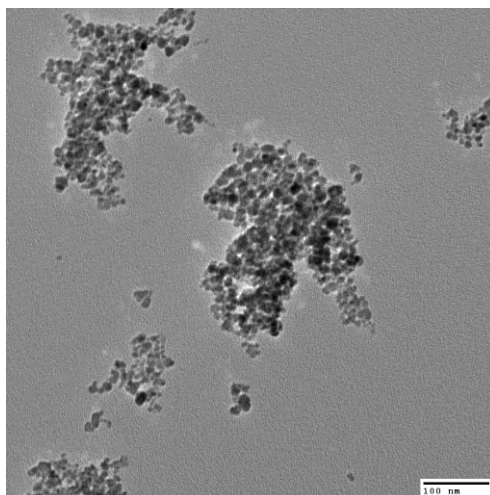


Figure 4.2 TEM images of a) Fe_xO_y -I ($c = 9.0$ g/L), b) Fe_xO_y -II ($c = 12.4$ g/L), c) Fe_xO_y -IV ($c = 14.2$ g/L) after deposition from aqueous dispersion ($\text{pH} = 3$)

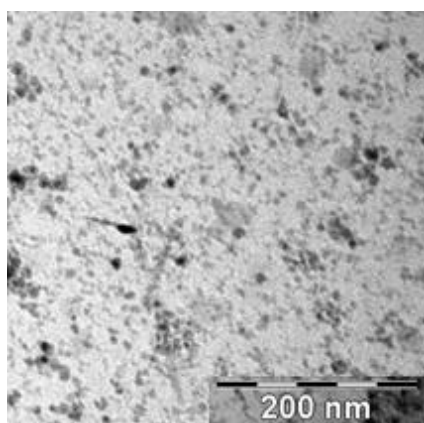
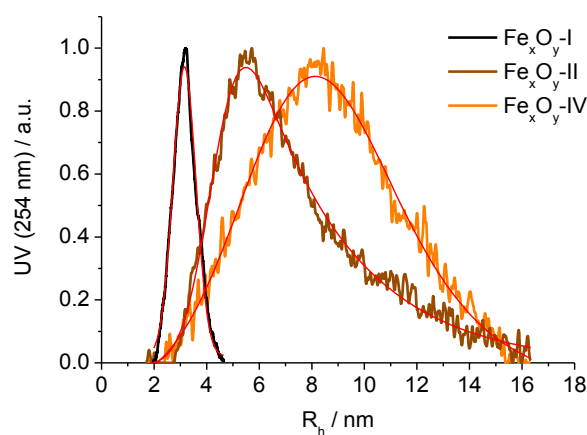


Figure 4.3 Cryo-TEM image of Fe_xO_y -I in aqueous dispersion ($c = 9.0$ g/L, $\text{pH} = 3$)

Due to the high scattering effects of the iron oxide nanoparticles a correct size determination via light scattering experiments was not possible. For this reason, the asymmetrical flow field-flow fractionation was used for particle size and distribution measurements. For all samples particle radii below 10 nm were found. The size-dependent elution profiles show an increase of the particle size with decreasing iron(II) to iron(III) ratio (Figure 4.4). Also, the particles synthesized in NH_4OH solution show higher radii than the samples precipitated into NaOH . The decrease of the particle size in presence of Na^+ ions is in good agreement to results reported by Vayssières et al.⁸¹ Using nitrates as precipitation media, Vayssières found that the efficiency of cations to reduce the particle size increases through the sequence $[\text{N}(\text{CH}_3)_4]^+ < [\text{NH}_4]^+ < \text{Na}^+$.

a)



b)

sample	$\langle R_h \rangle / \text{nm}$
$\text{Fe}_x\text{O}_y\text{-I}$	3.2
$\text{Fe}_x\text{O}_y\text{-II}$	5.6
$\text{Fe}_x\text{O}_y\text{-IV}$	9.2

Figure 4.4 a) Elution profiles of the iron oxide nanoparticles in aqueous dispersion (dilution 1:20)

determined via AF-FFF measurements with Gaussian fit (red line) and b) average particle radii (determined from peak maximum)

It is known that iron oxide nanoparticles synthesized via coprecipitation are typically a mixture of both magnetic iron oxides, maghemite ($\gamma\text{-Fe}_2\text{O}_3$) and magnetite (Fe_3O_4).¹⁸ According to the thermodynamics of the reaction, using a Fe(II)/Fe(III) ratio of 1:2 and pH-values between 8 and 14 in a non-oxidative environment should result in pure magnetite. Although, it is possible to support the formation of magnetite via an adequate adaption of the reaction conditions, maghemite is easily formed via oxidation in air leading to mixtures of both oxides. The formation of pure maghemite particles is more easily achieved via addition of iron(III) nitrate to the synthesized particles.²³ The composition of the three presented species was determined via powder diffraction patterns (Figure 4.5). For all samples, a coexistence of both magnetic iron oxides was revealed. Caused by the synthesis via coprecipitation, an amorphous background is visible. For $\text{Fe}_x\text{O}_y\text{-I}$ (synthesized using Fe(II):Fe(III) = 1 : 1), the ratio between magnetite and maghemite was determined to be 2 : 3 using the

EVA program (Bruker) for phase identification. The iron oxides synthesized using a 1 : 2 ratio show higher magnetite contents which is in good agreement to thermodynamic modelling.⁸³ However, in case of Fe_xO_y -II, an additional nonmagnetic halite phase was identified by comparing the experimental data with values reported in literature (peak positions: $31.8^\circ 2\theta$ and $45.3^\circ 2\theta$).¹⁸ The peaks of the halite phase are indicated by the arrows in Figure 4.5. Halite is a crystalline form of NaCl and seems to form due to the presence of residual Na^+ ions present in the coprecipitation medium.

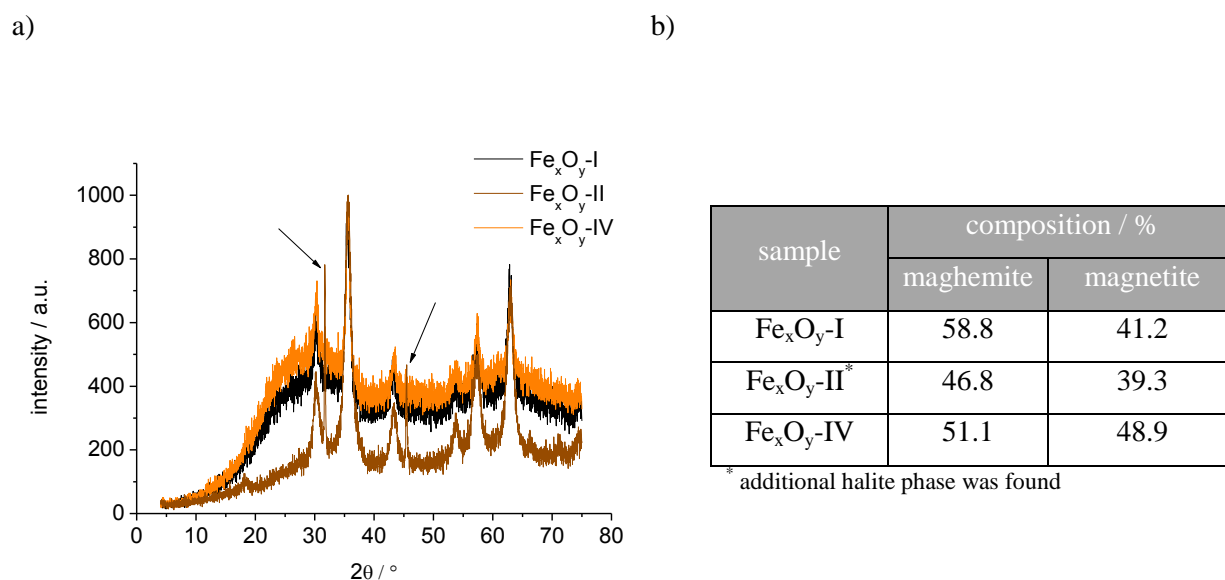


Figure 4.5 a) Powder diffraction patterns (arrows indicate the peak positions of the halite phase⁸⁴) and b) determined compositions of iron oxide nanoparticles

For further investigations on the composition and basic evaluations of the magnetic properties, Mössbauer measurements were performed. An exemplary Mössbauer spectrum of Fe_xO_y -I at 80 and 300 K is shown in Figure 4.6. The isomeric shift was determined to be 0.339 mm/s relative to α -Fe which fits well with the data of maghemite (γ - Fe_2O_3) reported in literature.⁸⁵ The measurements at 80 K showed a central doublet component due to the presence of superparamagnetic iron oxide nanoparticles and several sextets with broad hyperfine field distributions which is characteristic for ferro- and ferromagnetic materials. The appearance of different magnetic behaviors can be attributed to different blocking temperatures T_B . The blocking temperature characterizes the transition between superparamagnetism and ferro-/ferrimagnetic behavior. Above this temperature, the thermal energy is high enough to cause a rotation of the particle magnetic moments. Thus, superparamagnetic behavior results. Below T_B , the magnetic moments are blocked and ferro-/ferrimagnetic properties are found.

⁸³ Kim, D. K.; Zhang, Y.; Voit, W.; Rao, K. V.; Kehr, J.; Bjelk, B.; Muhammed, M. *Scr. Mater.* **2001**, *44*, 1713

⁸⁴ American Mineralogist Crystal Structure Database (<http://ruff.geo.arizona.edu/AMS/amcsd.php>)

⁸⁵ a) Haneda, K.; Morrish, A. H. *Phys. Lett.* **1977**, *64A*, 259; b) Bakker, P. M. A.; de Grave, E.; Vandenberghe, R. E.; Bowen, L. H. *Hyperfine Interact.* **1990**, *54*, 493

The doublet structure indicates that particle species with blocking temperatures below 80 K are present. These particles show superparamagnetic behavior at low temperatures. All components which contribute to the sextet structures have blocking temperatures above 80 K; meaning that no superparamagnetism is observed for these components. Since the blocking temperature is a size-dependent characteristic, the appearance of different blocking temperatures can be attributed to different particle sizes present in the sample. The deep-temperature Mössbauer spectrum of magnetite particles shows a characteristic asymmetry of the peaks.⁸⁶ The data illustrated in Figure 4.6b are relatively symmetric which indicates that maghemite is the dominant species. Nevertheless, the high polydispersity of the particles does not allow for a determination of the oxidative state for all species present. Hence, the existence of magnetite cannot be excluded.

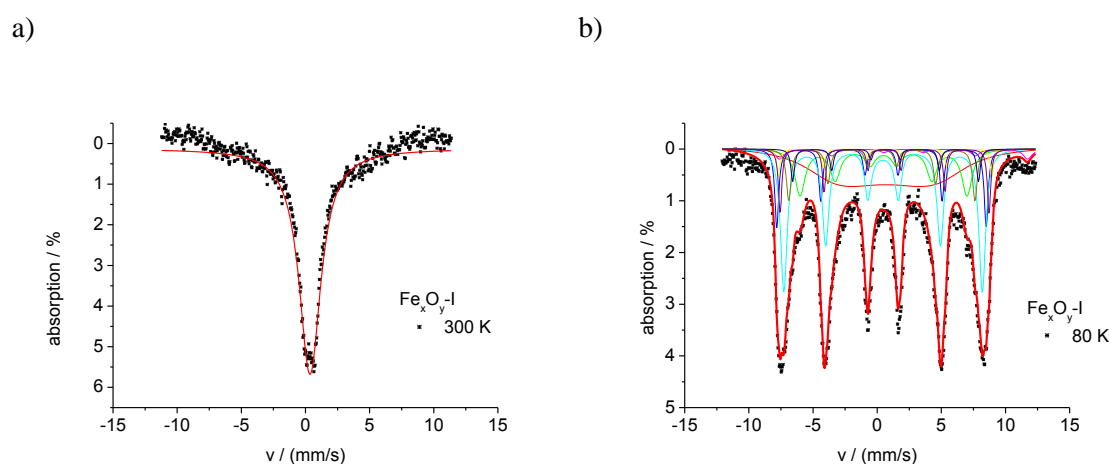


Figure 4.6 Mössbauer spectra of $\text{Fe}_x\text{O}_y\text{-I}$ a) at room temperature (300 K) and b) at 80 K

The magnetic properties of the iron oxide nanoparticles were determined with superconducting quantum interference device (SQUID) measurements of the dried samples. The magnetization curves were obtained by plotting the magnetization M against the magnetic field strength H . The curves show no hysteresis loop meaning that neither remanence nor coercivity was found at room temperature (Figure 4.7). This behavior is characteristic for superparamagnetic materials. At 5 K, the field dependent magnetization curves display a slight hysteresis loop. This result confirms that the iron oxide nanoparticles show a ferrimagnetic behavior at 5 K: The thermal energy is low enough to allow a permanent magnetization of the sample at low temperatures. Hence, the particles are below their blocking temperature. Typically, the blocking temperature of iron oxide nanoparticle in the investigated size range is approximately 80 K.²² Figure 4.7a illustrates the temperature-dependence of the saturation magnetization of $\text{Fe}_x\text{O}_y\text{-I}$. At 5 K, higher saturation magnetizations are revealed due to the hindered thermal movement of the particles. The determination of the saturation magnetization M_s

⁸⁶ Evans, B. J.; Hafner, S. S. *J. Appl. Phys.* **1969**, *40*, 1411

at 300 K revealed an increase from 39.7 to 50.7 emu/g from Fe_xO_y -I to Fe_xO_y -IV. Fe_xO_y -II showed a lowered value of 37.3 emu/g. Comparing the three samples, the lowest saturation magnetization was determined for the sample with the smallest particle size and the highest maghemite content. The sample Fe_xO_y -IV shows high saturation magnetizations corresponding to large particle sizes and a relatively high magnetite content. The saturation magnetization of Fe_xO_y -II is comparable to the values determined for Fe_xO_y -I even though larger particles were found in case of Fe_xO_y -II. However, the additional nonmagnetic halite phase which was revealed by x-ray diffraction causes a decrease in the saturation magnetization.

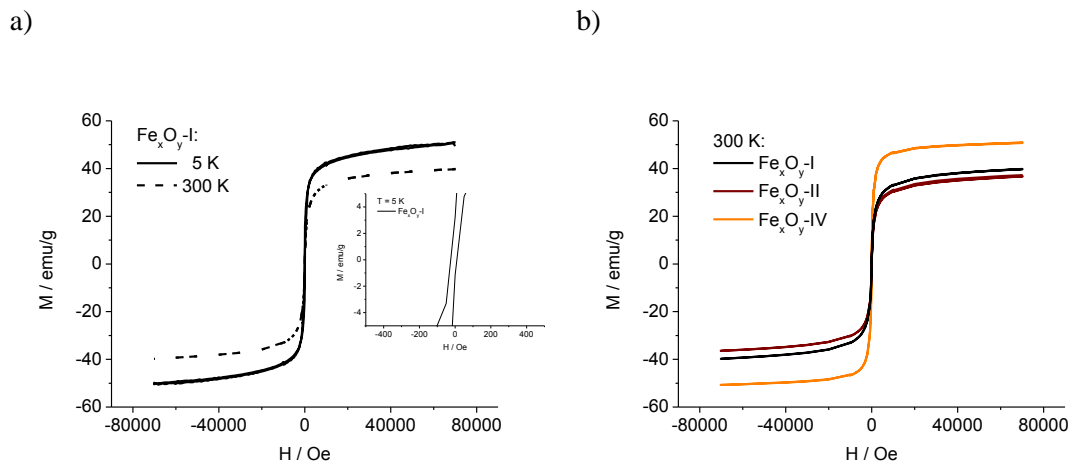


Figure 4.7 Magnetization curves of a) Fe_xO_y -I measured at 5 K and 300 K (inlet: enlargement of hysteresis at 5 K) and b) different sized iron oxide species measured at 300 K using a SQUID magnetometer

Table 4.2 Determined average hydrodynamic radii and magnetic properties of iron oxide nanoparticles

sample	$\langle R_h \rangle^*$ / nm	M_S (300 K) / emu/g
Fe_xO_y -I	3.2	39.7
Fe_xO_y -II	5.6	37.3
Fe_xO_y -IV	9.2	50.7

*determined from peak maximum of AF-FFF measurements

The saturation magnetizations of maghemite reported in literature are 84.0 emu/g at 5 K and 78.0 emu/g at 300 K for the bulk material.²² Magnetite shows even higher saturation magnetizations. The deviation between literature values and the experimentally determined can be explained by the strong size dependence of the saturation magnetization. To calculate the saturation magnetization of magnetic nanoparticles Berkowitz et al. developed the so-called core-shell model.²⁰ They assumed that the magnetic particles are covered with a thin diamagnetic oxide layer. The saturation magnetization of the nanoparticles $M_S(d)$ relative to the bulk material $M_S(\infty)$ can be calculated according to

$$\frac{M_s(d)}{M_s(\infty)} = 1 - 6 \frac{h}{d}, \quad 4.1$$

with total particle diameter d and thickness of diamagnetic shell h . Using Equation 4.1, the theoretic saturation magnetization of maghemite and magnetite particles with a diameter of 6.4 nm was representatively calculated. Based on values reported in literature, a diamagnetic shell thickness of 0.5 nm was considered. A comparison between the calculated and the measured values, revealed good agreement with maghemite which seems to be the predominate species (Table 4.3).

Table 4.3 Saturation magnetization of Fe_xO_y -I, $\gamma\text{-Fe}_2\text{O}_3$ and Fe_3O_4 calculated using Equation 4.1

T / K	M_s / emu/g				
	Fe_xO_y -I	$\gamma\text{-Fe}_2\text{O}_3$		Fe_3O_4	
	d = 6.4 nm	bulk	d = 6.4 nm	bulk	d = 6.4 nm
5	50.5	84.0	45.8	98.0	53.4
300	39.7	78.0	42.5	92.0	50.2

Keeping in mind that magnetic nanoparticles used in biomedical applications need to be covered by a protective coating to hinder undesired interactions between the magnetic particles and the biological surrounding, the surface properties are an important factor for further processing. Especially the incorporation of pre-synthesized nanoparticles into a growing polymeric network, as aspired in this work, strongly depends on the surface properties of the inorganic particles. One important property of the particles surface is the electrostatic surface- or ζ -potential. Figure 4.8 demonstrates that all three iron oxide samples show positive ζ -potentials in aqueous dispersion (pH = 3). This confirms the positive surface charge under acidic conditions (Figure 4.1). The potentials were determined to vary between 41 and 48 mV. The deviation between the determined values lies within the experimental error and can be neglected (Figure 4.8).

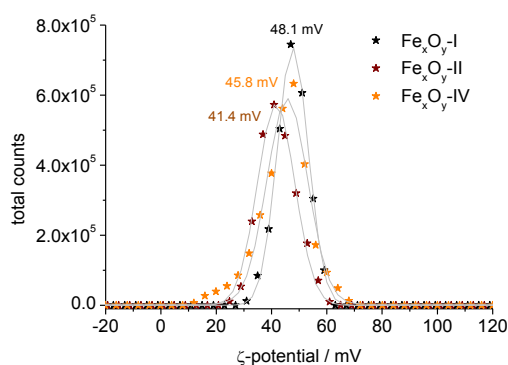


Figure 4.8 ζ -potentials of iron oxides synthesized under various conditions in aqueous dispersions ($c(\text{Fe}_x\text{O}_y\text{-I}) = 9.0$ mg/mL, $c(\text{Fe}_x\text{O}_y\text{-II}) = 12.4$ mg/mL, $c(\text{Fe}_x\text{O}_y\text{-IV}) = 14.2$ mg/mL, pH = 3, $I \approx 1.5 \cdot 10^{-2}$ M)

4.1.3 Summary

Magnetic iron oxide nanoparticles were synthesized via coprecipitation in basic solution. By variation of the Fe(II)/Fe(III) ratio and the coprecipitation media, differently sized nanoparticles were obtained. The ratio between the utilized iron species was varied between 1:1 and 1:2. As precipitation medium NaOH as well as NH₄OH solutions were used. Three different iron oxide species were synthesized and characterized regarding particle size, composition, magnetic and surface properties. An iron salt ratio Fe(II)/Fe(III) of 1:2 as well as the use of NH₄OH solution instead of NaOH as precipitation medium led to an increase in particle size. The radii of the synthesized particles vary from 3.2 to 9.2 nm. The composition of the particles was determined to consist of both magnetic iron oxides (γ -Fe₂O₃ and Fe₃O₄). The sample synthesized using a 1 : 1 ratio between the iron chlorides showed the lowest magnetite content. The highest Fe₃O₄ content was determined for Fe_xO_y-IV which was precipitated in NH₄OH using a 1 : 2 Fe(II):Fe(III) ratio. All synthesized iron oxide nanoparticles show superparamagnetic properties at room temperature. The saturation magnetization increases with increasing particle size and magnetite content. However, lower saturation magnetizations were found for Fe_xO_y-II due to the presence of a nonmagnetic halite phase. Regarding the surface properties no significant deviation between the three systems was revealed. In all cases, positive ζ -potentials were obtained under acidic conditions.

4.2 Magnetically loaded Polyorganosiloxane Nanospheres

4.2.1 Introduction

Polyorganosiloxane nanoparticles are synthesized via condensation of silane monomers in aqueous dispersion. The condensation of di- and trifunctional silane monomers leads to the formation of network structures. By combining different monomers and subsequent addition of monomer mixtures, various architectures like solid spheres, hollow spheres or core-shell structures can be formed. The radii of the resulting nanoparticles can specifically be adjusted between approximately 10 and 70 nm. It has been shown that the core-shell structures are excellent candidates for biomedical applications due to their multicompartment structure which offers a high flexibility with respect to functionalization. The core-shell architecture provides the possibility of independent core and shell/surface modification. Using the monomer p-chloromethylphenyltrimethoxysilane (ClBz-T) different core labelings or functionalizations can be achieved. Amphiphilic nanospheres can be synthesized via a quaternization reaction of chloromethylphenyl groups with dimethylaminoethanol.¹⁵ Thereby, nanocontainers and nanoreactors are obtained which can be loaded with pharmaceuticals for drug delivery approaches or simply with fluorescent dye molecules for marking and imaging applications.¹⁴ Functionalization via covalent binding of fluorescent molecules is also possible. The covalent binding of dye molecules has the advantage of avoiding undesired release of dye molecules during the imaging process as well as interactions between the dye and the environment. Surface functionalization can be used to increase the biocompatibility and provide specific binding sites for biomolecules in drug delivery or cell sorting experiments.^{13,87} The de-coupling of core and surface functionalization offers great opportunities in biomedical applications as independent properties or functionalizations can be selectively attributed to both core and surface. However, in literature the main attention is turned to mere functionalization while the de-coupling is rarely applied in nanoparticles preparation. Hence, the polyorganosiloxane nanospheres are promising systems in the field of functional nanomaterials for biomedical applications.

The incorporation of magnetic nanoparticles into the polyorganosiloxane network further increases the potential biomedical applications. Magnetically controlled targeting and distribution are of great advantage in drug delivery and cell sorting processes. The controlled and accurate distribution of the particles amplifies the efficiency of the methods. The dose of the applied drug can drastically be reduced and influences on healthy tissues can be minimized. Additionally, induced heating treatments like hyperthermia can be combined with the therapeutic applications discussed before. Of course, magnetic detection respectively imaging is another imaginable application for magnetically loaded polyorganosiloxane nanoparticles.

One procedure for the synthesis of magnetically functionalized polyorganosiloxane nanospheres was described before. For the magnetic loading, hydrophilic iron oxide stabilized via oleic acid as

⁸⁷ Koshkina, O. *Diploma thesis*, Johannes Gutenberg-Universität Mainz, 2010

capping-agent was used.⁸⁸ The incorporation of the stabilized magnetic nanoparticles into polyorganosiloxane nanoparticles to obtain magnetically responsive nanocontainers is a major challenge. Typically, the long alkyl chains of the oleic acid will separate from the siloxane network. To make the hydrophobic particles compatible with the siloxanes, the oleic acid coated iron oxide particles were dispersed in octadecyltrimethoxysilane (OD-T). Due to the hydrophobic interactions between the alkyl chains of OD-T and oleic acid, a bilayer is generated. The silane was capable of participation in the reactions of the siloxane network formation enabling the incorporation of the magnetic nanoparticles in the polyorganosiloxane nanospheres. The encapsulation of the particles was generally successful but the resulting magnetic content was very low.

To achieve a more effective magnetic functionalization, hydrophilic iron oxide nanoparticles were used in this work. The magnetic particles form a stable aqueous dispersion and can be incorporated into the polyorganosiloxane system during the condensation reaction of the silane monomers.

In the following sections two basic studies are highlighted:

1. The formation of magnetically loaded polyorganosiloxane nanoparticles via incorporation of different sized iron oxides (Chapter 4.2.2.1 and 4.2.2.3). The different magnetic particles correspond to the iron oxide species presented in Chapter 4.1.2.
2. The synthesis of multifunctional polyorganosiloxane nanoparticles carrying magnetic and fluorescent moieties and/or biocompatible surface layers consisting of poly(ethylene glycol) (Chapter 4.2.3). In Chapter 4.2.3.5, an additional biofunctionalization of the particles is discussed. All investigated systems are schematically illustrated in Figure 4.10.

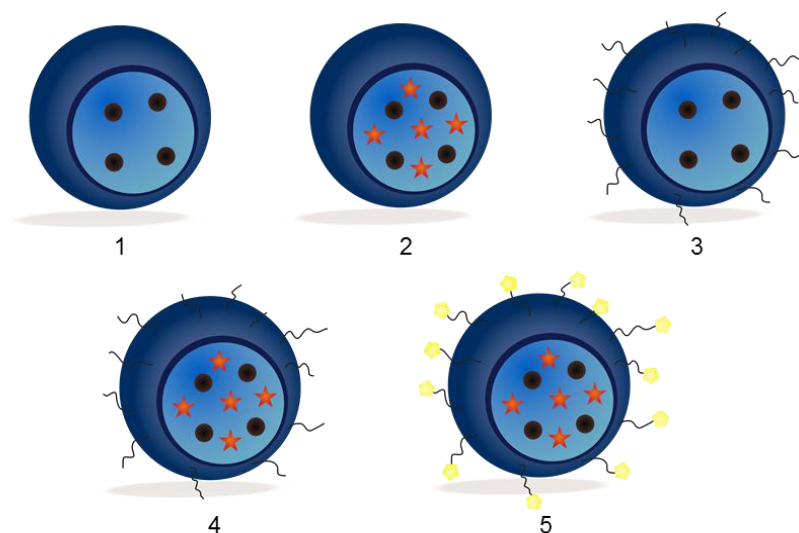


Figure 4.9 Schematic illustration of investigated polyorganosiloxane nanoparticles carrying different functionalizations: magnetic (1), magnetic/fluorescent (2), magnetic/PEG (3), magnetic/fluorescent/PEG (4), magnetic/fluorescent/PEG/biomolecules (5)

⁸⁸ Utech, S.; Scherer, C.; Maskos, M. *J. Magn. Magn. Mater.* **2009**, *321*, 1386

4.2.2 Magnetically loaded Polyorganosiloxane Nanoparticles

Magnetically loaded polyorganosiloxane nanoparticles were synthesized via addition of pre-synthesized iron oxide nanoparticles to a solution containing water and dodecyl benzenesulfonic acid (DBS) which acts as a catalyst and surfactant for the condensation reaction of silane monomers under acidic conditions (Figure 4.10). The DBS concentration was chosen to be 4 g/L with corresponds to a fleet ratio of $S = 0.02$ ($S = \text{mass of surfactant}/\text{mass of monomer}$). This fleet ratio was found to be generally appropriate for the synthesis of polyorganosiloxane nanoparticles and is commonly used. The premixed monomers diethoxydimethylsilane (D), trimethoxydimethylsilane (T) and p-chloromethylphenyltrimethoxysilane (ClBz-T) were added to the reaction solution to form an aqueous dispersion. The core of the siloxane system is formed via polycondensation of the organosilanes. After stirring for one week, a D/T mixture was added to form the shell of the polyorganosiloxane system.

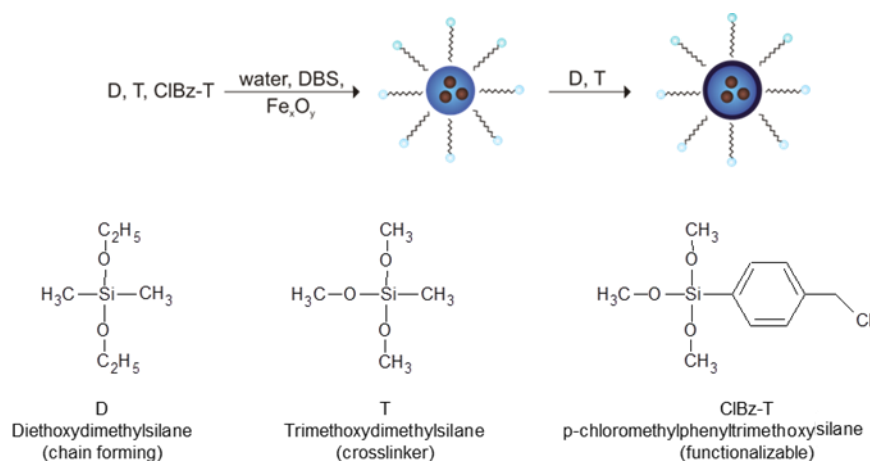


Figure 4.10 Reaction scheme for the preparation of magnetically loaded polyorganosiloxane nanoparticles

4.2.2.1 Incorporation of Particles with $R_n = 3.2$ nm (Fe_xO_y -I)

In this section the encapsulation of the smallest representative of the iron oxide particles (Fe_xO_y -I) presented in Chapter 4.1.2 is discussed. Additionally, the concentration-dependent incorporation of the inorganic particles was probed. Therefore, the amount of the iron oxide Fe_xO_y -I added to the aqueous DBS solution was varied from 1.2 wt-% up to 2.3 wt-% (mass (iron oxide)/mass (polymer + iron oxide)), assuming 100 % monomer conversion and 100 % incorporation of iron oxide) as demonstrated in Table 4.4. A further increase of the iron oxide content led to instable dispersions and was therefore not possible.

Table 4.4 Magnetically loaded polyorganosiloxane nanoparticles prepared with different amounts of $\text{Fe}_x\text{O}_y\text{-I}$

sample	iron oxide content / wt-%
$\text{Fe}_x\text{O}_y\text{-I}_{1.2\%}\text{@POS}$	1.2
$\text{Fe}_x\text{O}_y\text{-I}_{1.5\%}\text{@POS}$	1.5
$\text{Fe}_x\text{O}_y\text{-I}_{2.3\%}\text{@POS}$	2.3

To determine the interactions between the surfactant DBS and the iron oxide nanoparticles, ζ -potentials of the aqueous iron oxide/DBS-mixtures were measured. In all cases, negative ζ -potentials were found. Since the ζ -potentials of pure iron oxide nanoparticles were determined to be positive (see Figure 4.8), an adsorption of DBS on the particles surface seems to take place which fits well to results reported in literature.⁸⁹ The inversion of the surface charge suggests a double layer formation of DBS on the surface of the inorganic material. The slight differences between ζ -potentials of the three solutions can be traced back to screening effects. In low concentrated solutions, the screening of surface charges is negligible compared to higher concentrated solutions. Hence, the effective surface charge is reduced in higher concentrated solutions. Since the ζ -potential is directly correlated to the surface charge, screening effects influence the ζ -potential which causes generally more positive/negative ζ -potentials for diluted solutions.

Table 4.5 ζ -potentials of iron oxide nanoparticles $\text{Fe}_x\text{O}_y\text{-I}$ with and without DBS addition

wt-% iron oxide	ζ -potential	
	without DBS	with DBS
1.2	49.7	-50.0
1.5	43.5	-42.0
2.3	35.4	-34.5

A comparison between cryo-TEM images of pure iron oxide dispersions and iron oxide/DBS mixtures indicates that the adsorption of DBS to the particle surface supports the formation of aggregates (Figure 4.11). This specific aggregation has been reported in literature for similar systems and can be used to synthesize magnetic nanocontainers carrying various inorganic nanoparticles inside one polymeric particle.⁴² The resulting highly magnetically loaded particles are supposed to show a strong magnetic response to external fields. The described aggregates are formed by fast addition of the iron oxide dispersion to the aqueous DBS solution. In the opposite case (addition of DBS to the aqueous iron oxide dispersion) no aggregates are formed. Instead single iron oxide nanoparticles are present in

⁸⁹ Camponeschi, E.; Walker, J.; Garmestani, H.; Tannenbaum, R. in: *Nanoparticles: Synthesis, Stabilization, Passivation, and Functionalization*, ed. Nagarajan, R; Hatton, T. A., American Chemical Society, **2008**

the TEM image of the aqueous Fe_xO_y /DBS mixture (see Appendix). Thus, a high local concentration of iron oxide leads to the formation of aggregates while high local DBS concentrations are sufficient for the stabilization of single particles. This indicates that the stabilization of iron oxide nanoparticles with DBS is a kinetically driven process.

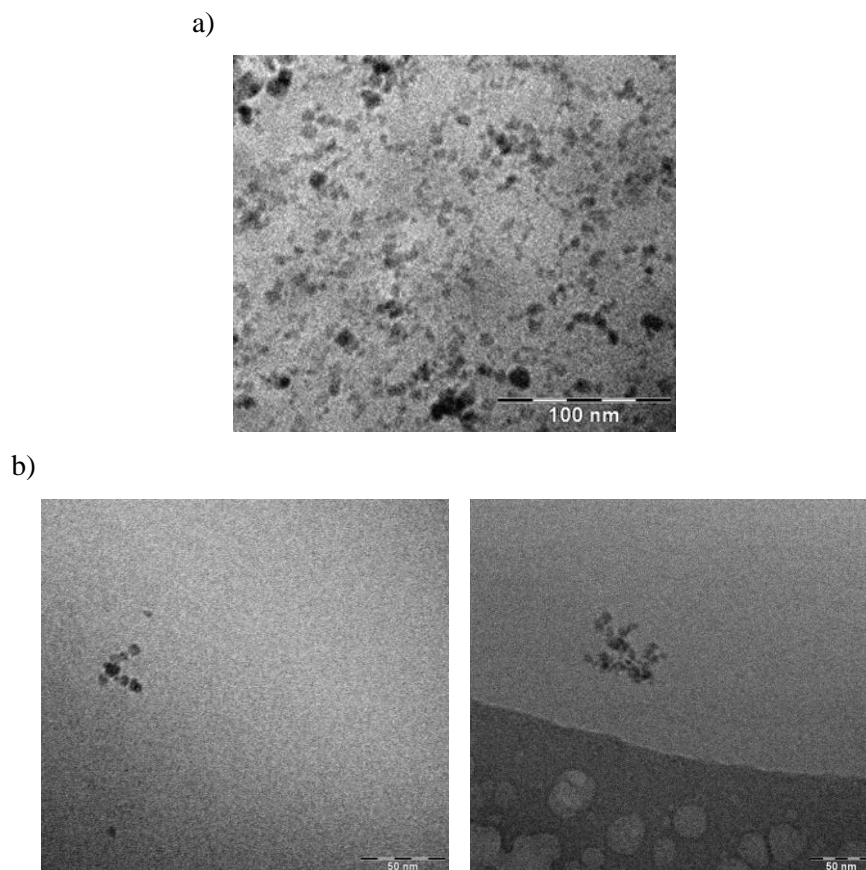


Figure 4.11 Cryo-TEM images of Fe_xO_y -I a) in aqueous solution ($c = 0.02$ g/L corresponding to 2.3 wt-% Fe_xO_y -I, $\text{pH} = 3$) and b) in aqueous DBS solution ($c(\text{Fe}_x\text{O}_y\text{-I}) = 0.02$ g/L, $S = 0.02$, $\text{pH} \approx 3$)

To obtain highly magnetically loaded particles, all samples were prepared by addition of Fe_xO_y to the aqueous DBS solution and subsequent monomer addition. The polyorganosiloxane samples synthesized in presence of the inorganic particles show the typical brownish color of iron oxide containing solutions. To eliminate the influence of free iron oxide nanoparticles which could be present in the aqueous dispersion, an end-capping process was performed. The particle surface was saturated using the monofunctional monomer trimethylmethoxysilane (M). The resulting hydrophobic particles can be dissolved in organic solvents whereas the iron oxide nanoparticles are not stable in organic solutions. As expected, the color changes from light to dark brown with increasing amount of iron oxide present in the sample (Figure 4.12). The characteristic polyorganosiloxane peak at 320 nm is superposed by the iron oxide signal.

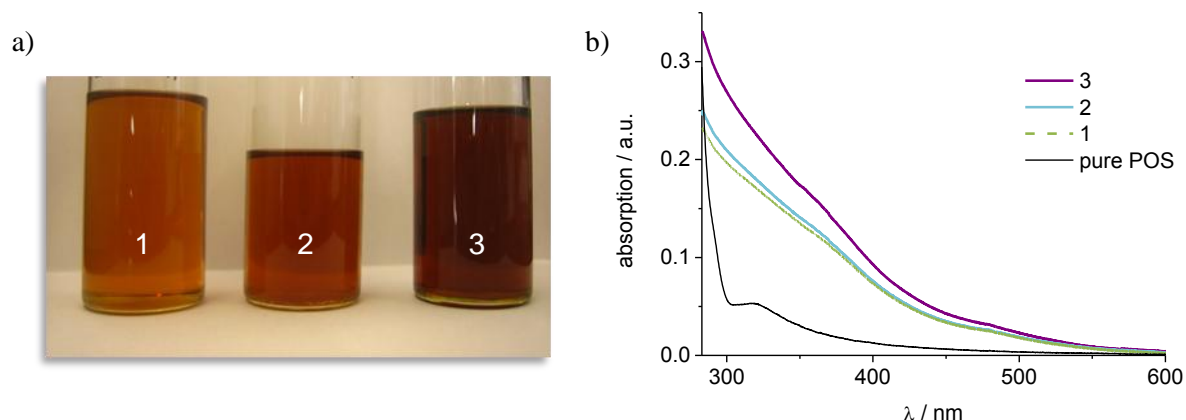


Figure 4.12 a) Photograph and b) absorption spectra of polyorganosiloxane nanoparticle toluene solutions ($c = 20.0 \text{ g/L}$;) synthesized in presence of Fe_xO_y : Fe_xO_y -I content: 1.2 wt-% (1), 1.5 wt-% (2), 2.3 wt-% (3)

Via transmission electron microscopy, the successful encapsulation of the magnetic particles into the polyorganosiloxane system was proven. A representative TEM image of the synthesized nanoparticles is shown in Figure 3.1.

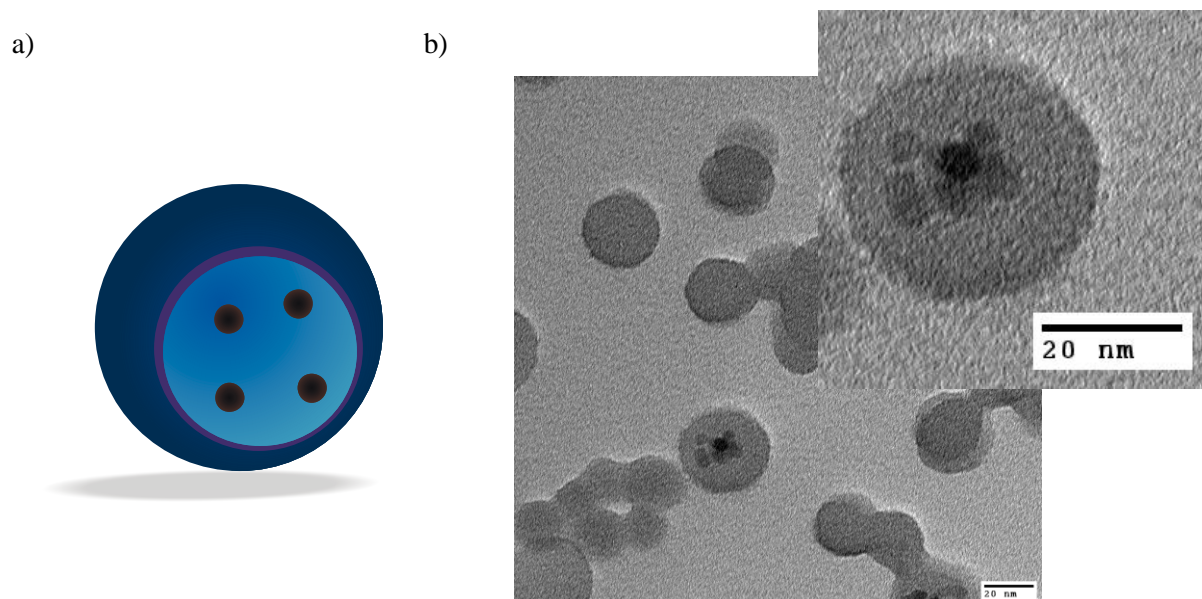


Figure 4.13 a) Schematic illustration and b) TEM image of polyorganosiloxane nanoparticles synthesized in presence of iron oxide nanoparticles after deposition from aqueous dispersion

The iron oxide nanoparticles are clearly visible inside the polyorganosiloxane nanospheres. Due to their high electron density, they show a distinct scattering contrast. Analysing TEM images, the number of particles per capsule was found to vary from 1 to approximately 20 (for TEM images see Appendix). The iron oxide nanoparticles seem to act as nucleation seeds for the growing polyorganosiloxane system leading to a so-called seeded polymerization. The hydrophobic interlayer of the DBS bilayer which is built on the surface of the magnetic nanoparticles can solubilize the monomer which promotes the polymerization close to or at the surface of the nanoparticles (Figure

4.14).⁹⁰ This so-called admicellar polymerization has been explored for the encapsulation of various hydrophobic inorganic materials into polymeric systems.⁹¹ The encapsulation process of the magnetic iron oxide nanoparticles can be imagined to comparable to the mechanism described above.

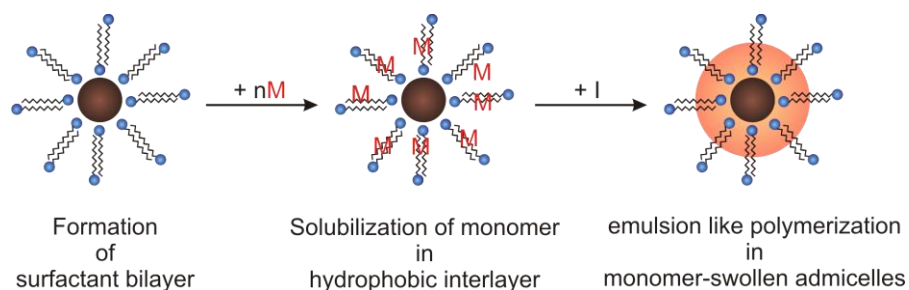


Figure 4.14 Schematic illustration of admicellar polymerization (M = monomer)⁹⁰

Besides the desired magnetically loaded polyorganosiloxane nanoparticles a large number of non-functionalized particles is present in the sample. This could be traced back to the small amount of iron oxide. The admicellar polymerization is known to require an adequate balance between the amount of inorganic material and the amount of monomer. In case of low concentrations of the inorganic compound, a self-nucleation polymerization occurs. This causes the formation of unloaded particles. Nevertheless, the encapsulation of the magnetic nanoparticles was successfully achieved indicating that the presented polymerization occurs in the threshold region between the two nucleation mechanism (Figure 4.15). The precipitation which occurs in case of iron oxide amounts above 2.3 wt-% can probably be attributed to an insufficient surfactant amount.

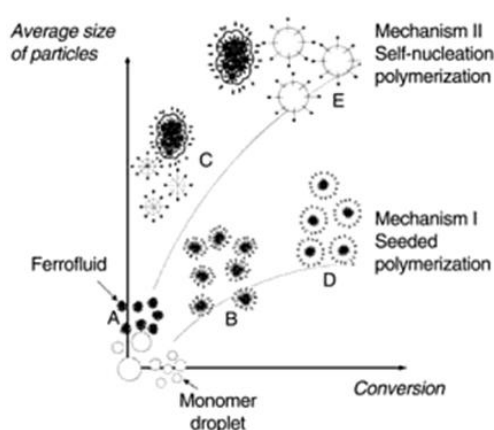


Figure 4.15 Mechanism proposed for the admicellar polymerization⁹⁰

⁹⁰ van Herk, A. M.; Landfester, K. *Hybrid Latex Particles*, Springer, **2010**

⁹¹ a) Meguro, K.; Yabe, T.; Ishioka, S.; Kato, K.; Esumi, K. *Bull. Chem. Soc. Jpn.* **1986**, *59*, 3019; b) Yanase, N.; Noguchi, H.; Asakura, H.; Suzuta, T. *J. Appl. Polym. Sci.* **1993**, *50*, 765

For particle size determinations, AF-FFF as well as light scattering methods were applied. In Figure 4.16, AF-FFF measurements of pure polyorganosiloxane nanoparticles are compared with samples containing different amounts of iron oxide. The data are summarized in Table 4.6.

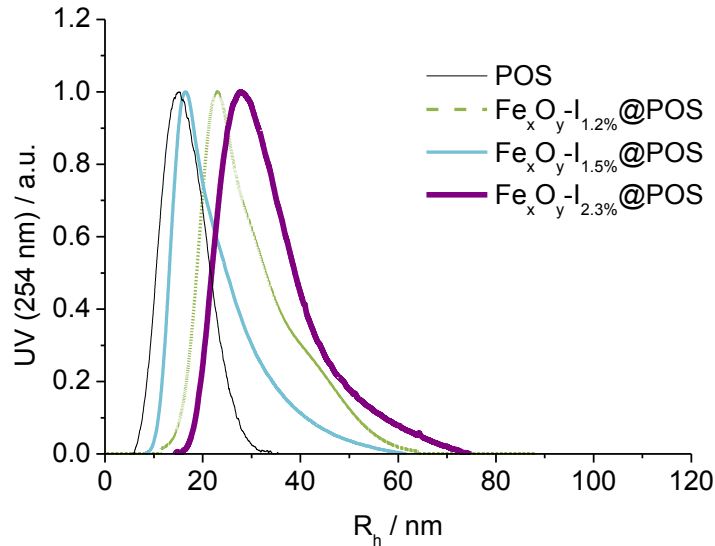


Figure 4.16 AF-FFF measurements of bare and magnetically functionalized polyorganosiloxane nanospheres in aqueous dispersion (dilution 1:20)

Compared to bare polyorganosiloxane nanoparticles, with a peak maximum of approximately 15 nm, the particles synthesized in presence of magnetic material show larger particles sizes with a broader size distribution. The particle sizes of the magnetically loaded samples were determined to be 23.1 nm, 16.4 nm and 27.9 nm in order of increasing iron oxide addition. However, no direct correlation between the particle size and the amount of iron oxide added during synthesis was detected. Instead a statistic distribution of the particle sizes was obtained (Table 4.6). This result could be confirmed via dynamic light scattering (DLS) measurements. The deviations of the values obtained by the two analytical methods are obviously due to the different averaging of the data. However, the results of both methods are in good agreement. The analysed samples contain magnetically and non-magnetically loaded particles as could be seen in the TEM images (Figure 3.1a). Hence, the determined radii correspond to the mixture of those two components. For a further analysis of the magnetically loaded particles a magnetic separation becomes necessary. The characterization of the magnetically loaded fraction as well as the influence of the magnetic particles on the particle size of the resulting particles will be discussed later (Chapter 4.2.2.2).

Table 4.6 Average particle radii of polyorganosiloxane nanoparticles synthesized in presence of various iron oxides amounts determined via DLS and AF-FFF measurements of the aqueous dispersions (dilution: DLS: 1:100, AF-FFF: 1:20)

sample	DLS	AF-FFF
	$\langle R_h \rangle_z / \text{nm}$	$\langle R_h \rangle^* / \text{nm}$
POS	16.6	15.3
$\text{Fe}_x\text{O}_y\text{-I}_{1.2\%}\text{@POS}$	38.1	23.1
$\text{Fe}_x\text{O}_y\text{-I}_{1.5\%}\text{@POS}$	24.6	16.4
$\text{Fe}_x\text{O}_y\text{-I}_{2.3\%}\text{@POS}$	30.7	27.9

* determined from peak maximum

For basic determinations of the magnetic properties, superconducting quantum interference device measurements of the non-fractionated samples were performed. The magnetic measurements shown in Figure 4.17a confirmed the superparamagnetic properties for all three samples. The determination of the saturation magnetizations resulted in 0.44 emu/g of sample for $\text{Fe}_x\text{O}_y\text{-I}_{1.2\%}\text{@POS}$, 0.55 emu/g of sample for $\text{Fe}_x\text{O}_y\text{-I}_{1.5\%}\text{@POS}$ and 0.85 emu/g of sample for $\text{Fe}_x\text{O}_y\text{-I}_{2.3\%}\text{@POS}$. The saturation magnetization is increasing with increasing amount of iron oxide nanoparticles offered during synthesis indicating that a higher initial amount leads to a higher encapsulation of the magnetic particles. A comparison of the relative values for the saturation magnetization and the amount of iron oxide added revealed a good agreement. The ratios between the saturation magnetizations were determined to be $M_S(\text{Fe}_x\text{O}_y\text{-I}_{1.2\%}\text{@POS}):M_S(\text{Fe}_x\text{O}_y\text{-I}_{1.5\%}\text{@POS}) = 0.80$, $M_S(\text{Fe}_x\text{O}_y\text{-I}_{1.5\%}\text{@POS}):M_S(\text{Fe}_x\text{O}_y\text{-I}_{2.3\%}\text{@POS}) = 0.65$. The calculation fits well to the relative amounts of iron oxide added (0.80 and 0.65, respectively). This leads to the conclusion that the yield of magnetically loaded nanoparticles is proportional to the amount of added iron oxide. The low saturation magnetizations compared to pure iron oxide samples can be attributed to the presence of the (surrounding) diamagnetic polyorganosiloxane system. Nevertheless, Figure 4.17b reveals that all samples show the same saturation magnetization of approximately 37 emu/g when the values are normalized to the theoretical amount of iron oxide assuming 100 % conversion. Compared to the pure iron oxide particles with a saturation magnetization of 40 emu/g at room temperature, no noteworthy loss is observed. In analogy to measurements of the bare iron oxide nanoparticles, a slight remanence can be monitored at 5 K. Thus, the iron oxide nanoparticles show no alteration in their magnetic properties. It can be stated that the magnetic particles are incorporated without modification of the existing structures.

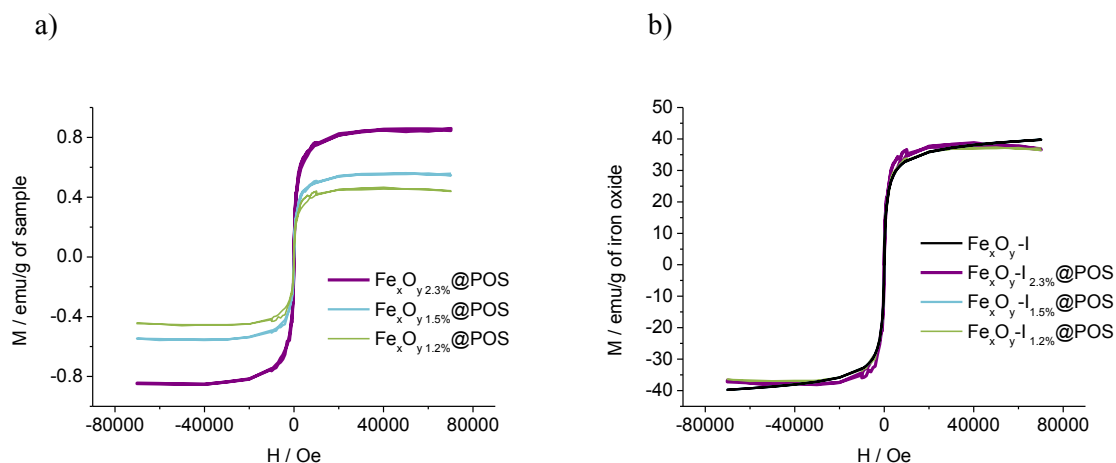


Figure 4.17 Magnetization curves of magnetically loaded polyorganosiloxane particles normalized to a) mass of sample and b) mass of iron oxide at 300 K

Based on the magnetic measurements of pure iron oxide nanoparticles, an evaluation of the encapsulation efficiency can be made. The theoretic saturation magnetizations for samples containing 1.2 to 2.3 wt-% of iron oxide can be calculated from the saturation magnetizations of pure iron oxide nanoparticles. Comparing the resulting values with the measured saturation magnetization, results in an encapsulation efficiency of approximately 92 % for all synthesized particles. This calculation states that the encapsulation of different iron oxide amounts into the polyorganosiloxane system is a highly efficient and well controllable process.

Table 4.7 Saturation magnetizations (at $T = 300$ K) and calculated encapsulation efficiencies of Fe_xO_y - $\text{I}_{1.2\%}$ @POS, Fe_xO_y - $\text{I}_{1.5\%}$ @POS and Fe_xO_y - $\text{I}_{2.3\%}$ @POS

sample	M_S / emu/g sample	M_S / emu/g iron oxide	encapsulation efficiency* / %
Fe_xO_y - $\text{I}_{1.2\%}$ @POS	0.44	37.1	91.7
Fe_xO_y - $\text{I}_{1.5\%}$ @POS	0.55	36.6	91.7
Fe_xO_y - $\text{I}_{2.3\%}$ @POS	0.85	37.8	92.4

* determined from the saturation magnetization of pure Fe_xO_y -I particles $M_S = 39.7$ emu/g (Table 4.2)

The basic characterization highlighted in this section deals with non-fractionated samples. The magnetic content of 2.3 wt-% at most is relatively low compared to magnetically loaded polymeric nanoparticles reported in literature.⁹² Magnetite was reported to be highly efficiently encapsulated in polystyrene with magnetite contents up to 40 wt-% via miniemulsion.⁴² Emulsification/diffusion techniques were successfully explored for the encapsulation of magnetite into poly(lactic-co-glycolic acid) (PLGA) and polycaprotactone (PCL) containing 13.5 wt-% and 25-30 wt-% of magnetic material,

⁹² Landfester, K.; Musyanovych, A.; Mailänder, V. *J. Polym. Sci. Part A* **2010**, *48*, 493

respectively.⁹³ As mentioned before, a large number of non-magnetically loaded particles is still present in the samples prepared in presence of the magnetic iron oxides which gives rise to the low iron oxide content. For further analysis of the magnetically functionalized particles, a magnetic fractionation was carried out to isolate and concentrate the magnetically loaded polyorganosiloxane nanoparticles. Afterwards, the magnetic nanocontainers could easily be analyzed with respect to size, iron oxide nanoparticles content and magnetic properties.

4.2.2.2 Magnetic Separation

For the magnetic separation commercially available magnetic separation columns from Miltenyi Biotec (MACSs separation columns) in combination with NdFeB ring magnets were used. A magnetic separation of the aqueous dispersion was not possible. The presence of functional surface groups (alkoxyl and hydroxyl groups) of the polyorganosiloxane particles causes aggregation of the particles in case of high local particle concentrations as present in the separation columns during the fractionation process. Hence, the particle surface was saturated in the end-capping process before fractionation. A mono-functional silane monomer (ethoxytrimethylsilane (M)) was added to the aqueous dispersion to partially saturate the alkoxyl- and hydroxyl-groups on the particle surface. After the transfer into an organic solvent a complete saturation of the surface was achieved by repeated addition of end-capping agent resulting in hydrophobic polyorganosiloxane nanoparticles. The magnetic separation columns are filled with magnetic iron spheres. Applying a strong magnetic field to the columns induces divergent field strengths. The resulting inhomogenities inside the column allow for a separation of the magnetic material. The samples were filtered through the columns, whereas particles with low or no magnetic content passed through the columns. Highly magnetically loaded particles were restrained. After removal of the magnetic field, the magnetically loaded particles were isolated (Figure 4.18). The TEM image reveals a high efficiency of the magnetic fractionation. Nearly 100 % of the non-magnetic fraction was separated. Additionally, two important points were found: The particles show a high degree of diversity regarding the particle size and the number of encapsulated iron oxide nanoparticles. For further investigations of these phenomena statistical evaluations of the magnetic capsules and DLS measurements were performed.

⁹³ a) Ngaboni Okassa, L.; Marchais, H.; Douziech-Eyrolles, L.; Herve, K.; Cohen-Jonathan, S.; Munnier, E.; Souce, M.; Linassier, C.; Dubois, P.; Chourpa, I. *Eur. J. Pharm. Biopharm.* **2007**, *67*, 31; b) Harmoudeh, M.; Fessi, H. *J. Coll. Interf. Sci.* **2006**, *300*, 584

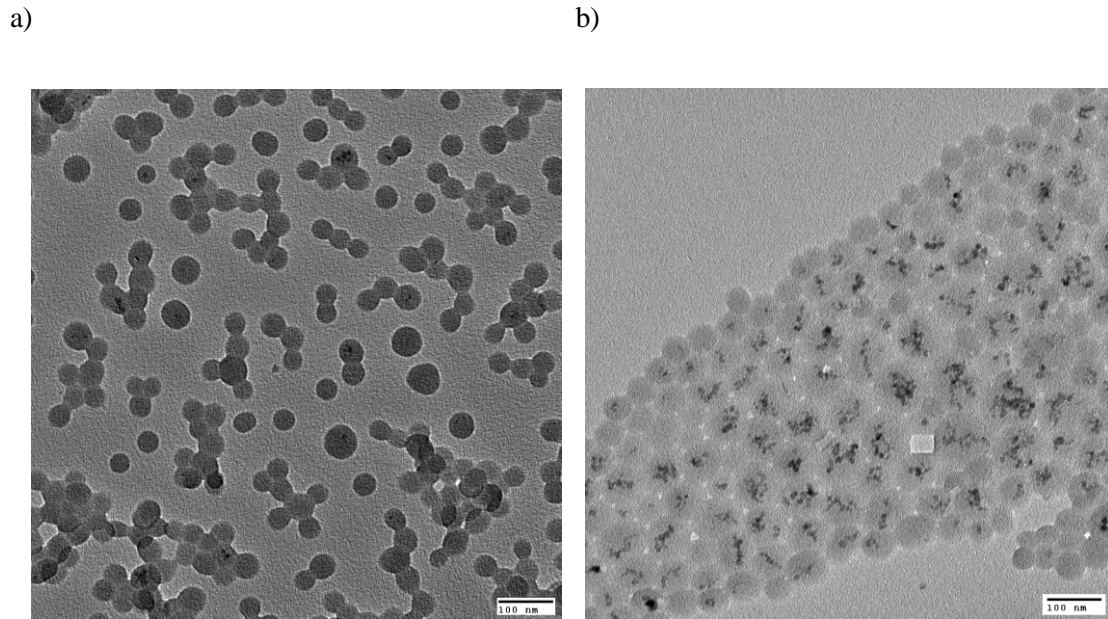
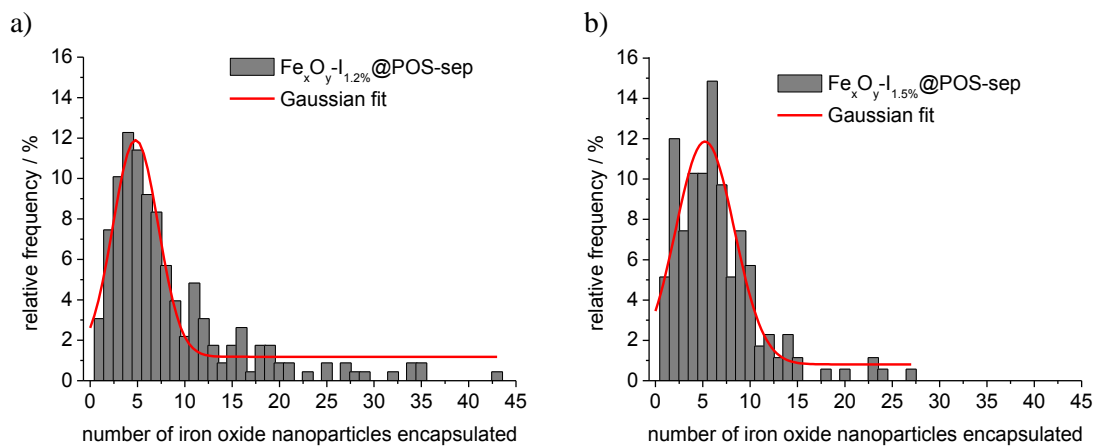


Figure 4.18 TEM image of $\text{Fe}_x\text{O}_y\text{-I}_{2.3\%}\text{@POS}$ a) before and b) after magnetic separation after deposition from toluene solution, scale bar 100 nm

For the statistical evaluations, the TEM images of the three separated samples were enumerated with respect to the number of iron oxide nanoparticles per nanocomposite (for TEM images see Appendix). Fitting the histograms with a Gaussian distribution function an encapsulation of approximately five particles was most frequently found in all three cases. No direct correlation between the amount of iron oxide added and the number of encapsulated particles was found. In Chapter 4.1.2, the ζ -potentials of the iron oxide nanoparticles were discussed. It was found that the potentials decrease with increasing iron oxide content. These deviations do not seem to be relevant for the encapsulation efficiency. This confirms the assumption that the different ζ -potentials can be traced back to concentration-dependent screening effects.



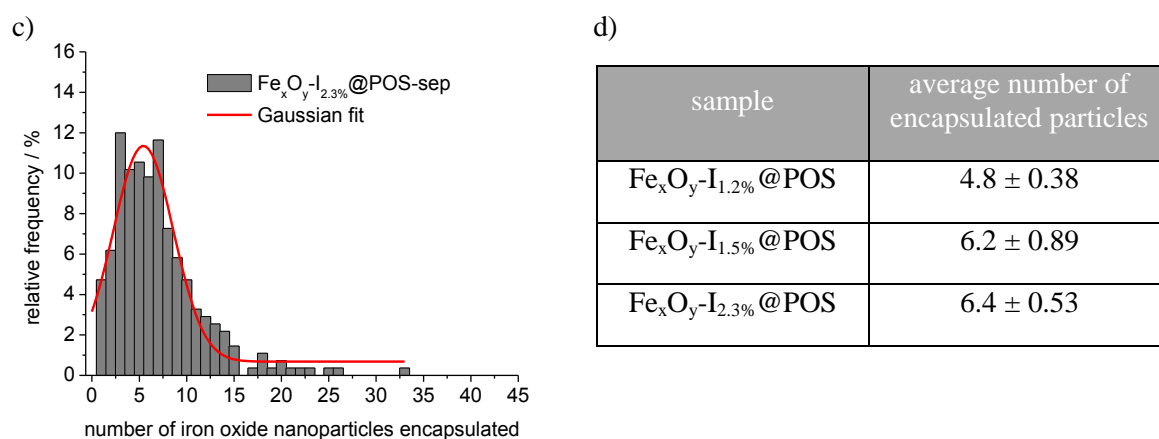


Figure 4.19 a)-c) Histogram of number of iron oxide nanoparticles encapsulated determined from TEM images after deposition from toluene solution with Gaussian fit; d) results of Gaussian fits

For particle size determination both statistic evaluations of the TEM images and DLS measurements were used. The statistic evaluations manifest a proportional relation between the iron oxide content and the average particle size (see Appendix). This result is clarified in the overlay histogram shown in Figure 4.20. The particle size is increasing with increasing amount of iron oxide added during synthesis. By this means, the sample Fe_xO_y-I_{2.3%}POS-sep shows the largest particle radii.

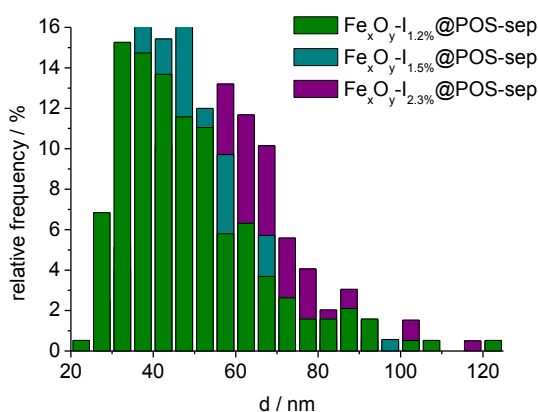


Figure 4.20 Overlay of particle size distributions shown in

This general trend was supported by dynamic light scatterings measurements. However, the TEM and DLS data summarized in Table 4.8 show a distinct deviation between the determined particle radii. The origin of the phenomenon is shrinkage of the polymeric shell in the vacuum of the electron microscope. Additionally, in DLS, the average hydrodynamic radius is dominated by the larger particle fraction due to the higher scattering contrast. (3.3).

Table 4.8 Particle size determinations of magnetic polyorganosiloxane nanocontainers in toluene solution

sample	DLS		TEM
	R_h / nm	μ_2	$\langle R \rangle$ / nm
$\text{Fe}_x\text{O}_y\text{-I}_{1.2\%}\text{@POS-sep}$	59.7	0.12	21.0
$\text{Fe}_x\text{O}_y\text{-I}_{1.5\%}\text{@POS-sep}$	63.4	0.08	23.0
$\text{Fe}_x\text{O}_y\text{-I}_{2.3\%}\text{@POS-sep}$	74.7	0.09	27.6

The reason for the proportionality between particle size and amount of iron oxide present during synthesis can most likely be attributed to the surfactant amount available for the stabilization of the growing siloxane system. As described in Chapter 4.2.2.1, an adsorption of DBS onto the iron oxide surface takes place. The amount of DBS, which is available for the stabilization of the growing siloxane system, is drastically reduced. In previous works, a direct relation between the particle size of acidic catalyzed polyorganosiloxane nanoparticles and the surfactant amount was revealed. C. Scherer could show that the particle size is increasing with decreasing fleet ratio and therefore decreasing surfactant content.⁹⁴ In this case, also a decreased DBS content can be considered presuming that the DBS adsorbs onto the iron oxide surface as indicated by the ζ -potential measurements in Table 4.5. Thereby, the DBS amount which is available during the silane condensation is lowered compared to pure polyorganosiloxane particle synthesis. Thus higher particle radii would result. For the investigated system, this assumption fits well to the trend in particle size determined. The particle size is supposed to grow proportionally to the iron oxide content as shown in Table 4.8.

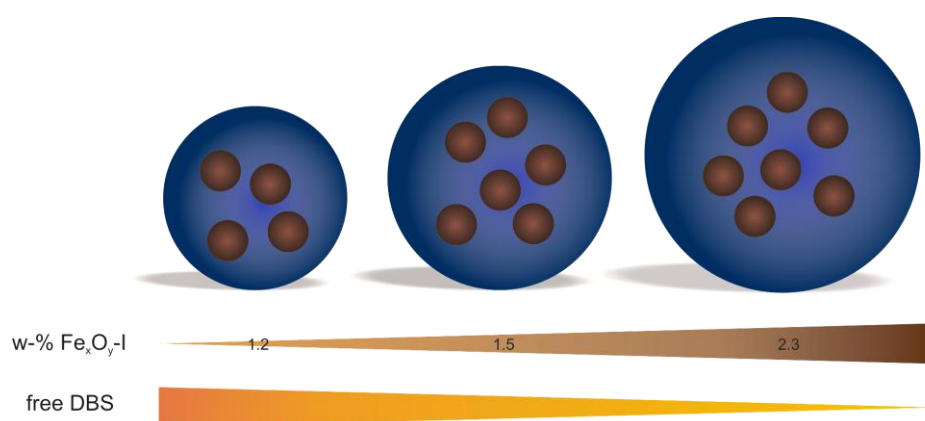


Figure 4.21 Relation between the amount of iron oxide present during synthesis, the DBS content and the size of polyorganosiloxane nanoparticles

⁹⁴ Scherer, C. *Dissertation*, Johannes Gutenberg-Universität Mainz, 2010

The magnetic properties of the separated and the non-separated sample $\text{Fe}_x\text{O}_y\text{-I}_{2.3\%}\text{@POS}$ as determined by SQUID are compared in Figure 4.22. As expected, the separated sample shows a higher saturation magnetization per g of sample (1.7 emu/g of sample) compared to the non-separated material (0.85 emu/g of sample) due to the absence of the bare polyorganosiloxane nanoparticles. Recalculating the magnetic content from the saturation magnetizations of the non-separated sample leads to an approximate value of 4.6 w% iron oxide. The obtained saturation magnetization can easily keep up with results reported in literature for magnetically loaded polymeric systems. Yi et al. reported saturation magnetizations of 3.6 emu/g of sample at 5 K for $\text{SiO}_2/\gamma\text{-Fe}_2\text{O}_3$ nanocomposites with a magnetic content of approximately 10 wt-%.⁹⁵ Liz-Marzán and coworkers reported the synthesis of silica-coated Fe_xO_y particles carrying a magnetic content of approximately 2 wt-%.⁹⁶ The determined saturation magnetizations were in the range of 1.34 emu/g of sample.

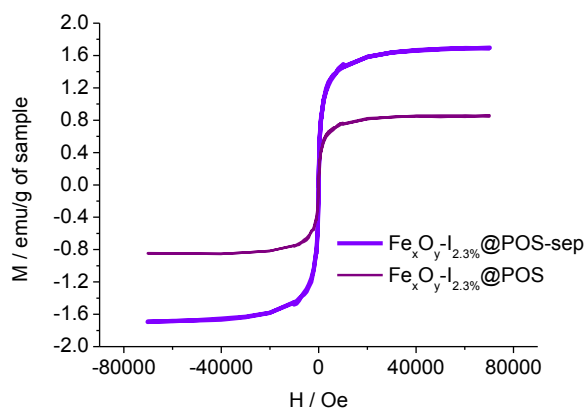


Figure 4.22 Magnetic measurements of the sample $\text{Fe}_x\text{O}_y\text{-I}_{2.3\%}\text{@POS}$ before (dark blue line) and after (blue line) magnetic separation

The results of the SQUID measurements were confirmed using Mössbauer spectroscopy (Figure 4.23). At room temperature, an isomeric shift of 0.29 mm/s was determined for the sample $\text{Fe}_x\text{O}_y\text{-I}_{2.3\%}\text{@POS}$ before and after magnetic separation. The absorption maxima were determined to be 0.45 % for $\text{Fe}_x\text{O}_y\text{-I}_{2.3\%}\text{@POS}$ and 0.86 % for $\text{Fe}_x\text{O}_y\text{-I}_{2.3\%}\text{@POS-sep}$ indicating that the iron oxide content in the separated sample is twice as high compared to the non-separated one. This result coincides well with the values calculated from the saturation magnetizations determined by the SQUID measurements shown in Figure 10.

By measuring Mössbauer spectroscopy of $\text{Fe}_x\text{O}_y\text{-I}_{2.3\%}\text{@POS-sep}$ at 80 K it was possible to resolve the quadrupole splitting from the hyperfine splitting. Hence, a more detailed description of the magnetic properties is possible. The spectrum resembled the one of the pure iron oxide sample, illustrated in

⁹⁵ Yi, D. K.; Lee, S. S.; Papaefthymiou, G. C.; Ying, J. Y. *Chem. Mater.* **2006**, *18*, 614

⁹⁶ Salgueiriño-Maceira, V.; Correa-Duarte, M. A.; Spasova, M.; Liz-Marzán, L. M.; Farle, M. *Adv. Funct. Mater.* **2006**, *16*, 509

Figure 4.6a. It shows a composition of similar sextet components with various hyperfine field distributions representing the polydispersity of the magnetic nanoparticles. Fitting the corresponding data resulted in the typical sextet structure (Figure 4.24).

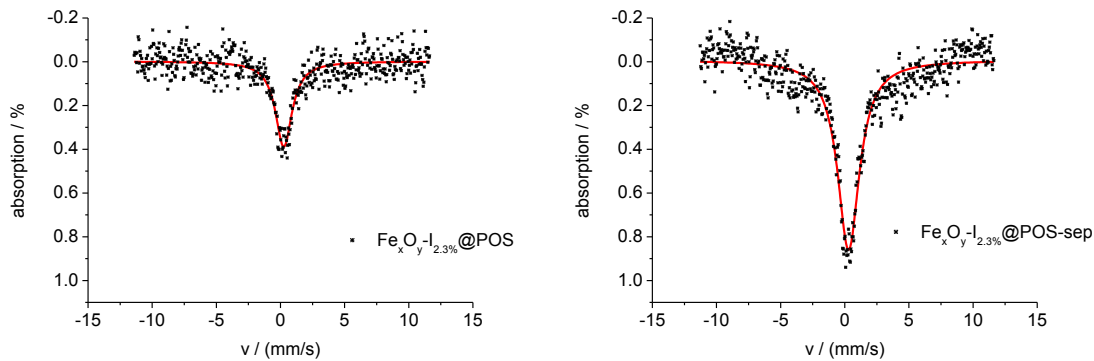


Figure 4.23 Mössbauer measurements of magnetically loaded polyorgansiloxane particles a) before and b) after magnetic separation ($T = 300$ K, absorptions are normalized to g of sample)

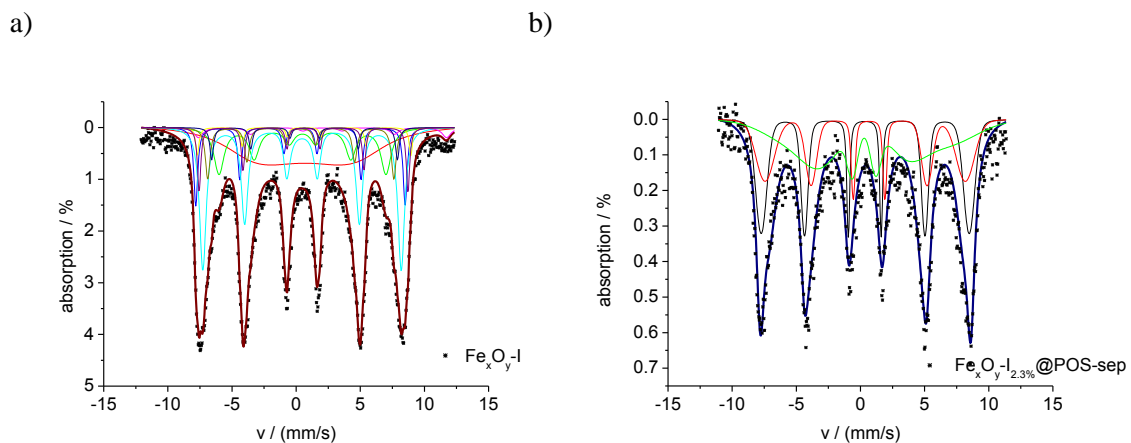


Figure 4.24 Mössbauer spectra of a) pure and b) encapsulated $\text{Fe}_x\text{O}_y\text{-I}$ nanoparticles measured at 80 K

Concluding, the successful encapsulation of magnetic iron oxide nanoparticles into polyorgansiloxane nanospheres was achieved. The magnetically loaded particles show superparamagnetic properties. The saturation magnetization per g of sample and the particle size are strongly influenced by the amount of iron oxide added during synthesis. Saturation magnetizations between 0.44 and 0.85 emu/g of sample were determined. Via magnetic fractionation, magnetically loaded polyorgansiloxane nanoparticles can be separated from non-magnetic material. Thereby, magnetic contents of approximately 5 wt-% and saturation magnetizations of 1.7 emu/g of sample were obtained. The particle radii varied from 60 to 75 nm for the magnetically loaded nanocontainers in dependence on the iron oxide content as determined via DLS measurements. It has to be stated that the particle radii of the non-magnetically functionalized particles which are additionally formed show no correlation to the iron oxide content. The adsorption of DBS onto the iron oxide surface causes a

decrease of the DBS amount which is accessible for the stabilization of the growing polyorganosiloxane particles. This effect should lead to the formation of larger particles. Nevertheless, a decrease in the number of particles formed can also be imaged. Hence, the statistic distribution which was found for the particle sizes of non-magnetically loaded particles can be attributed to a combination of the two discussed effects. Additionally, the acidic catalysed polymerization of silane monomers in aqueous dispersion is known to cause a bimodal size distribution with particle radii that vary within a statistical error.^{17,59,94}

4.2.2.3 Incorporation of larger Iron Oxide Nanoparticles

The previous section discussed the encapsulation of magnetic iron oxide nanoparticles with an average particle radius of 3.2 nm. In the following section, the encapsulation of larger particles is highlighted. The synthesis of the different magnetic particles was presented in Chapter 4.1.2. The surface properties and composition of the particles were found to be comparable in all samples. As shown in Chapter 4.1.2, the pure iron oxide particles carry a positive surface charge under acidic conditions (Figure 4.8). In presence of the surfactant DBS, negative ζ -potentials were determined for all investigated sample. This result indicates that the DBS is adsorbed onto the particle surface leading to partial aggregation of the magnetic nanoparticles. The particle radii and ζ -potentials of the three different iron oxide samples are compared in Table 4.9. For encapsulation, the aqueous inorganic particle dispersions were added to a DBS solution (4 g/L DBS corresponding to $S = 0.02$) which is subsequently used for the polyorganosiloxane synthesis as described before (Chapter 4.2.2.1). The iron oxide amount added to the aqueous solution was 2.3 wt-% (mass (iron oxide)/mass (polymer + iron oxide)), assuming 100 % monomer conversion and 100 % incorporation of iron oxide). This content was found to be the highest amount that could successfully be encapsulated in case of small iron oxide nanoparticles (Fe_xO_y -I) as discussed above.

Table 4.9 Particle sizes and ζ -potentials of iron oxide nanoparticles with and without addition of DBS

sample	R_h^* / nm	ζ -potential with DBS	ζ -potential without DBS
Fe_xO_y -I	3.2	-34.5	48.1
Fe_xO_y -II	5.6	-44.6	41.4
Fe_xO_y -IV	9.2	-46.4	45.8

* determined via AF-FFF measurements

After encapsulation, the resulting magnetically loaded nanocontainers are analysed with respect to the magnetic properties and the encapsulation efficiencies were determined in dependence on the size of the magnetic iron oxides.

4.2.2.3.1 Incorporation of Particles with $R_h = 5.6$ nm ($\text{Fe}_x\text{O}_y\text{-II}$)

A TEM image of polyorganosiloxane particles synthesized in presence of the medium sized iron oxide nanoparticles is shown in Figure 4.27. In analogy to the particles synthesized in presence of iron oxides with particle radii of 3.2 nm, magnetically loaded particles besides non-functionalized nanospheres are visible. The magnetically loaded particles which vary in the number of encapsulated particles are generally larger compared to the unloaded ones. The high fraction of pure siloxane particles probably results from the low content of magnetic material as discussed before for the encapsulation of $\text{Fe}_x\text{O}_y\text{-I}$.

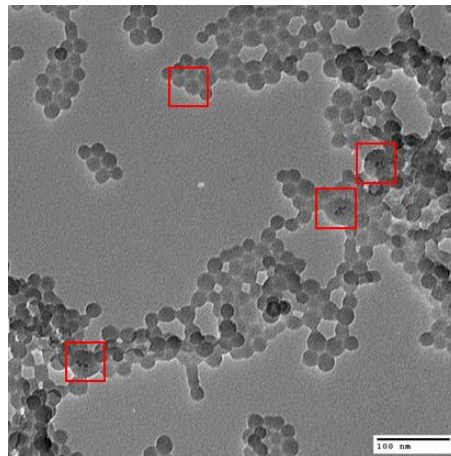


Figure 4.25 TEM images of polyorganosiloxane samples synthesized in presence of iron oxide nanoparticles with an average particle size of 5.6 nm after deposition from aqueous dispersion (magnetically loaded particles are highlighted in the red boxes)

In order to calculate the encapsulation efficiency, magnetization curves were determined via SQUID measurements (Figure 4.26). The saturation magnetizations were determined to be 0.52 emu/g of sample and 22.6 emu/g of iron oxide (Table 4.10).

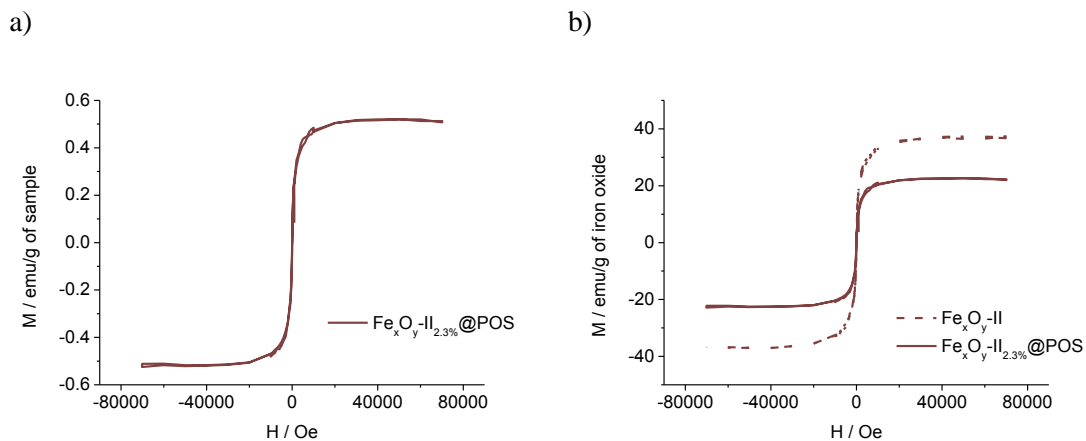


Figure 4.26 Magnetization curves of $\text{Fe}_x\text{O}_y\text{-II}_{2.3\%}\text{@POS}$ a) per g of sample and b) per g of iron oxide in comparison to pure $\text{Fe}_x\text{O}_y\text{-II}$ nanoparticles ($T = 300$ K)

Comparing the magnetization curves of Fe_xO_y -II before and after the encapsulation process reveals a distinct decrease in the saturation magnetization normalized to the mass of iron oxide. Recalculating the encapsulation efficiency results in approximately 61 % which is significantly lower than the value determined for the encapsulation of smaller particles (Fe_xO_y -I, encapsulation efficiency: ≈ 92 %) in Chapter 4.2.2.1.

Table 4.10 Saturation magnetizations and calculated encapsulation efficiency of Fe_xO_y -II_{2.3%}@POS

sample	M_S / emu/g sample	M_S / emu/g iron oxide	encapsulation efficiency* / %
Fe_xO_y -II _{2.3%} @POS	0.52	22.6	60.6

* determined from the saturation magnetization of pure Fe_xO_y -II particles $M_S = 37.3$ emu/g (Table 4.2)

4.2.2.3.2 Incorporation of Particles with $R_h = 9.2$ nm (Fe_xO_y -IV)

The largest representative of the investigated iron oxide nanoparticles (Fe_xO_y -IV) showed an average particle radius of 9.2 nm. The particles could successfully be incorporated into the polyorganosiloxane system as shown in Figure 4.27. The TEM image of the polyorganosiloxane nanoparticles synthesized in presence of Fe_xO_y -IV resembles the previously discussed TEM images using smaller nanoparticles for encapsulation: Magnetically loaded and bare polyorganosiloxane particles are present.

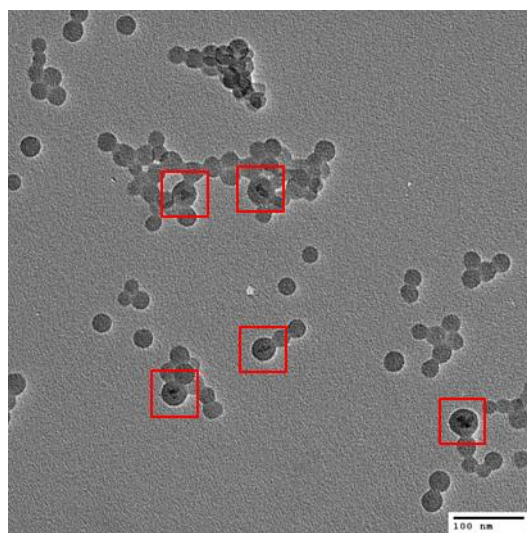


Figure 4.27 TEM images of polyorganosiloxane samples synthesized in presence of iron oxide nanoparticles with an average particle radius of 9.2 nm after deposition from aqueous dispersion (red boxes: magnetically loaded particles)

The analysis of the magnetic properties via SQUID measurements confirms the perpetuation of the superparamagnetic behaviour of the iron oxides (Figure 4.28). The saturation magnetizations were

determined to be 0.65 emu/g and 28.1 emu/g after normalization to sample mass and mass of iron oxide, respectively. These values are surprisingly low compared to the saturation magnetizations of bare Fe_xO_y -IV nanoparticles which showed a saturation magnetization of 50.7 emu/g (see Chapter 4.1.2). Based on the magnetic measurements of the pure Fe_xO_y -IV nanoparticles, the theoretic saturation magnetization for a sample containing 2.3 wt-% of Fe_xO_y -IV was calculated. The resulting value of 1.17 emu/g of sample is almost twice as high as the measured saturation magnetization. This deviation reveals an extraordinary low encapsulation efficiency of approximately 56 % relative to the offered amount of iron oxide (Table 4.11).

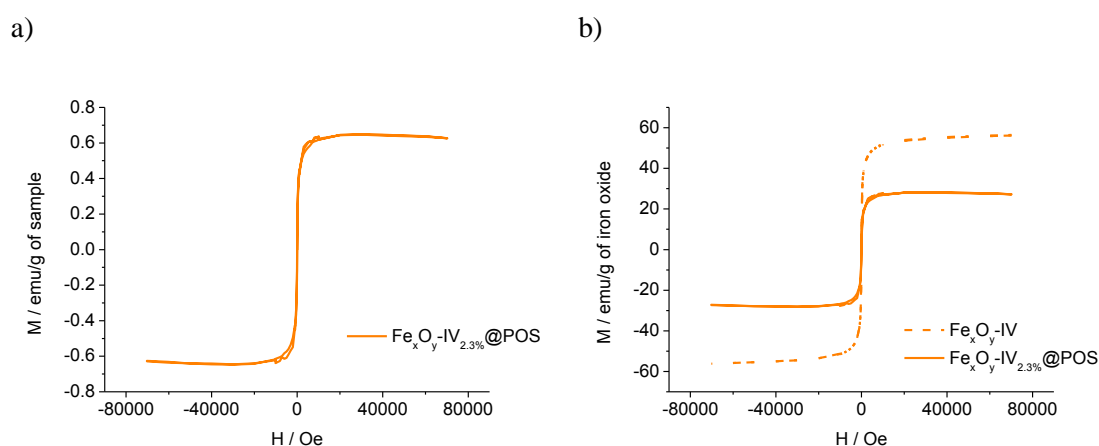


Figure 4.28 Magnetization curves of Fe_xO_y -IV_{2.3%}@POS at 300 K normalized to a) mass of sample and b) mass of iron oxide (dashed line: magnetization curve of pure Fe_xO_y -IV)

Table 4.11 Saturation magnetizations and calculated encapsulation efficiency of Fe_xO_y -IV_{2.3%}@POS

sample	M_S / emu/g iron oxide	M_S / emu/g sample	encapsulation efficiency* / %
Fe_xO_y -IV _{2.3%} @POS	28.1	0.65	55.7

* determined from the saturation magnetization of pure Fe_xO_y -II particles $M_S = 50.7$ emu/g (Table 4.2)

This result implies that the encapsulation of large nanoparticles into the polyorganosiloxane nanoparticles is an unfavorable process. To verify potential parameters that influence the encapsulation process and hence, affect the encapsulation efficiencies, the results obtained for the incorporation of the different sized iron oxide nanoparticles are compared in the following section.

4.2.2.3.3 Comparison of the Encapsulation Efficiency of different sized Particles

In Chapter 4.1.2, the saturation magnetizations of the iron oxide nanoparticles were found to increase in the following order:

$$M_S(\text{Fe}_x\text{O}_y\text{-I}) < M_S(\text{Fe}_x\text{O}_y\text{-II}) < M_S(\text{Fe}_x\text{O}_y\text{-IV})$$

Hence, the sample $\text{Fe}_x\text{O}_y\text{-IV}_{2.3\%}\text{@POS}$ was expected to possess the strongest magnetic properties assuming comparable encapsulation efficiencies for all three iron oxide species. However, low saturation magnetizations were determined for $\text{Fe}_x\text{O}_y\text{-IV}_{2.3\%}\text{@POS}$ (0.65 emu/g of sample and 28.1 emu/g of iron oxide) while $\text{Fe}_x\text{O}_y\text{-I}_{2.3\%}\text{@POS}$ showed the highest saturation magnetizations (0.86 emu/g of sample and 37.2 emu/g of iron oxide) of the three samples which can be attributed to the calculated encapsulation efficiencies as highlighted in Table 4.12.

Table 4.12 Encapsulation efficiencies of magnetically loading using different sized iron oxides

sample	encapsulation efficiency / %
$\text{Fe}_x\text{O}_y\text{-I}_{2.3\%}\text{@POS}$	92.4
$\text{Fe}_x\text{O}_y\text{-II}_{2.3\%}\text{@POS}$	60.6
$\text{Fe}_x\text{O}_y\text{-IV}_{2.3\%}\text{@POS}$	55.7

The following order of the encapsulation efficiency was revealed:

$$\text{Fe}_x\text{O}_y\text{-I} > \text{Fe}_x\text{O}_y\text{-II} > \text{Fe}_x\text{O}_y\text{-IV}$$

This order mirrors the sizes of the iron oxide nanoparticles. Thus, a direct correlation between particle size and encapsulation efficiency seems to be valid. The encapsulation of small inorganic particles ($\text{Fe}_x\text{O}_y\text{-I}$) seems to be the most efficient process. As explained before, the encapsulation of the magnetic iron oxide nanoparticles into the polyorganosiloxane system is based on an admicellar polymerization process (see Chapter 4.2.2.1). This mechanism is known to be extraordinary sensitive to the ratio between the amount of magnetic particles and the amount of initial monomer.⁹⁰ If the monomer amount is too high the bilayer cannot accommodate the offered monomer amount which leads to a destruction of the bilayer. Consequently larger particles are formed via self-nucleation which leads to non-magnetically functionalized particles. Additionally, large aggregates consisting of the magnetic particles are formed which could lead to sedimentation of magnetic material. The described phenomenon could be a potential explanation for the low efficiencies obtained for the encapsulation of larger particles. Even though, the initial mass concentration was equivalent for all investigated iron oxide species, the particle concentration is significantly lower in case of the larger particles (Table 4.13). Hence, the important balance between the amount of iron oxide and the amount of monomer is not given leading to an increased formation and sedimentation of large iron oxide aggregates. Consequently low encapsulation efficiencies result. Additionally, it was found that the number of encapsulated particles per polyorganosiloxane sphere decreases in the same order as the encapsulation efficiencies. To optimize the synthesis of magnetically loaded polyorganosiloxane nanoparticles, higher amounts of $\text{Fe}_x\text{O}_y\text{-IV}$ have to be encapsulated. Since an increase in the iron oxide amount above 2.3 wt-% caused instabilities of the aqueous dispersion and hence, precipitation, an increase of the

DBS amount has to be investigated in addition.

Table 4.13 Determined mass and particle concentrations for the encapsulation of different sized iron oxides

sample	mass concentration / wt-%	particle concentration* / particles/L
Fe _x O _y -I	2.3	37.6·10 ¹⁷
Fe _x O _y -II	2.3	7.0·10 ¹⁷
Fe _x O _y -IV	2.3	1.6·10 ¹⁷

* calculations based on an average particle density of $\rho = 5 \text{ g/cm}^3$

4.2.2.4 Summary

The encapsulation of magnetic iron oxide nanoparticles in polyorganosiloxane nanospheres was investigated. In order to obtain magnetically loaded polyorganosiloxane nanocontainers, superparamagnetic iron oxide nanoparticles were incorporated into the polymeric system during the polymerisation of silane monomers in aqueous dispersion in a “quasi”-admicellar polymerization. The encapsulation process was highly efficient (efficiency of approximately 92 % relative to the offered amount of iron oxide) when small iron oxide particles (Fe_xO_y-I, R_h = 3.2 nm) were used. The particle radii of the magnetically loaded polyorganosiloxane nanospheres varied between 60 nm and 75 nm in dependence on the encapsulated amount of iron oxide. The encapsulated particles showed superparamagnetic properties at room temperature with saturation magnetizations of 0.44 emu/g of sample and 0.85 emu/g of sample for magnetic contents of 1.2 wt-% and 2.3 wt-%. The saturation magnetization per g of iron oxide was determined to be comparable to the values of pure iron oxide nanoparticles. The magnetically loaded polyorganosiloxane nanoparticles could successfully be separated from non-magnetic material using commercially available magnetic separation columns. The magnetic content of the fractionated sample was determined to be 5 wt-%.

Additionally, the encapsulation of larger iron oxide particles (R_h(Fe_xO_y-II) = 5.6 nm, R_h(Fe_xO_y-IV) = 9.2 nm) was carried out successfully. However, the encapsulation efficiency seems to strongly depend on the size of the iron oxide nanoparticles. The encapsulation of 5.6 nm and 9.2 nm sized particles resulted in low saturation magnetizations and encapsulation efficiencies below 65 % relative to the amount of iron oxide offered. By this means, the encapsulation of small nanoparticles is the most effective process for the incorporation of iron oxide nanoparticles into the polyorganosiloxane nanoparticles under the investigated synthetic conditions. This size-dependence can be attributed to the mechanism of the admicellar polymerization which was found to be extremely sensitive to the ratio between the amounts of initial monomer and inorganic material.

In summary, a highly efficient encapsulation process was performed. The resulting nanocontainers carry several magnetic particles and show superparamagnetic behavior at room temperature which makes them excellent candidates for biomedical applications for example as contrast agents in

magnetic resonance imaging. After adequate functionalization, targeting or drug delivery applications can be imagined. The functionalization of the magnetically loaded polyorganosiloxane core-shell system is discussed in the following section.

4.2.3 Functionalizations

4.2.3.1 Introduction

The synthesis of multifunctional nanoparticles is of high interest for biomedical applications. Typically, the particles are labeled using optical markers like fluorescent dyes, quantum dots, gold or silver nanoparticles. Hence, monitoring and imaging of the particles is possible. Depending on the investigated material, a surface coating is mandatory to provide or increase colloidal stability in biological environments and biocompatibility.^{10,21,23} Polymeric stabilizers like poly(ethylene glycol)⁹⁷, poly(vinyl alcohol)⁹⁸ and dextran⁹⁹, inorganic materials, typically silica¹⁰⁰ or gold¹⁰¹, or small molecules, carboxylates or phosphates¹⁰² to name some examples, are commonly used for surface functionalization. In previous works, it was shown that the polyorganosiloxane system offers the opportunity of multicompartment functionalizations.¹² The polyorganosiloxane system can be synthesized in a core-shell structure that provides a multicompartment architecture which offers the possibility of an independent core and surface modification. Dye-molecules can be incorporated into the siloxane core via different synthetic procedures which will be discussed in the following section. This approach minimizes a potential influence of the incorporated dye on the surface properties and interactions between the nanoparticles and biological systems. Surface modifications can be performed via a grafting onto process using poly(ethylene glycol) to provide both, water-solubility and biocompatibility. By using heterofunctional PEG, the free chain-end of the poly(ethylene glycol) can be used for further functionalization. The decoupling of core and surface modification is highly interesting for several applications including biomedical techniques. The core modification like the incorporation of fluorescent dyes, magnetic nanoparticles and drugs, can be performed independently from the surface modification, for examples the attachment of specific binding sites, antibodies or proteins. Hence, the polymeric system can easily be adjusted to the requirements of the aspired applications. The following sections highlight the core and surface modification of magnetically loaded polyorganosiloxane nanoparticles as well as the combination of both functionalizations. Additionally, coupling of biomolecules to the free chain-end of the PEG is demonstrated (Chapter 4.2.3.5).

4.2.3.2 Core Modification: Fluorescent Labeling

In previous works, the fluorescent labeling of the polyorganosiloxane system was performed via various procedures. The generation of charged moieties inside the network, for example via

⁹⁷ Otsuka, H.; Nagasaki, Y.; Kataoka, K. *Adv. Drug Deliv. Rev.* **2003**, *55*, 403

⁹⁸ Pardoe, H.; Chua-anusorn, W.; Pierre, T. G.; Dobson, J. *J. Magn. Magn. Mater.* **2001**, *225*, 41

⁹⁹ Berry, C. C.; Wells, S.; Charles, S.; Curtis, A. S. G. *Biomaterials* **2003**, *36*, 4551

¹⁰⁰ Zhang, C.; Wangler, B.; Morgenstern, B.; Zentgraf, H.; Eisenhut, M.; Unterecken, H.; Kruger, R.; Huss, R.; Seliger, C.; Semmler, W.; Kiessling, F. *Langmuir* **2007**, *23*, 1427

¹⁰¹ Chen, M.; Yamamuro, S.; Farrell, D.; Majetich, S. A. *J. Appl. Phys.* **2003**, *93*, 7551

¹⁰² Sahoo, Y.; Pizem, H.; Fried, T.; Golodnitsky, D.; Burstein, L.; Sukenik, C. N.; Markovich, G. *Langmuir* **2001**, *17*, 7907

quarternization of incorporated p-chloromethylphenyl groups, can be used to electrostatically fix the dyes within the network via phase transfer reactions.¹⁴ Additionally, a covalent binding of carboxylated dyes can be performed via substitution of p-chloromethylphenyl groups in the core of the siloxane system. The resulting nanoparticles show a high fluorescence. However, a complete removal of residual dye molecules is difficult due to the interactions between the dye and the polyorganosiloxane network.^{58,103} Another dye-modification was performed via surface coupling of fluorescent labeled oligonucleotides.¹³ This approach has the disadvantage of potentially undesired interactions between the dye and the environment. Additionally, the fluorescent labeling cannot be performed independently from the surface modification. Thus, the sort of fluorescent dye that can be used for the labeling depends on the availability of dye-functionalized nucleotides.

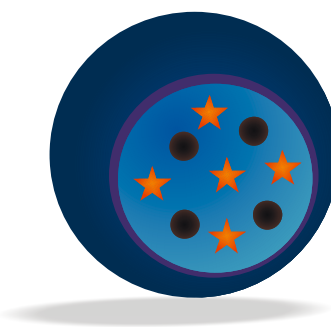


Figure 4.29 Schematic illustration of dye-labeled magnetically loaded polyorganosiloxane nanoparticles

To overcome these problems, the synthesis of the magnetically loaded polyorganosiloxane was slightly modified. The core-monomer ClBz-T was partially replaced by dye-labeled monomers Dye-Bz-T or Dye-T (Dye-Bz-T: fluorescein-(p-trimethoxysilyl)-benzylester (Flu-Bz-T), rhodamine-(p-trimethoxysilyl)-benzylester (Rho-Bz-T); Dye-T: *O*-4-methylcoumarinyl-*N*-[3-(triethoxysilyl)-propyl]-carbamate (Coum-T)).^{87,103} The dye molecules are covalently bonded and therefore trapped inside the core of the polyorganosiloxane particle.

In this work, the dye-labeling is combined with the simultaneous encapsulation of magnetic iron oxide nanoparticles in the polyorganosiloxane network. Both moieties are incorporated during the polycondensation of the silane monomers in aqueous dispersion as illustrated in Figure 4.30. This approach allows for the fast and convenient formation of magnetofluorescent particles in a one-pot synthesis. Particles carrying both, magnetic and fluorescent moieties are of high interest for biomedical applications. These so-called dual markers allow for a fluorescence detection, for example of the particle distribution in biological systems, and additional magnetic detection or contrast enhancement in magnetic resonance imaging.

¹⁰³ Graf, C.; Schärtl, W.; Fischer, K.; Schmidt, M. *Langmuir* **1999**, 15, 6170

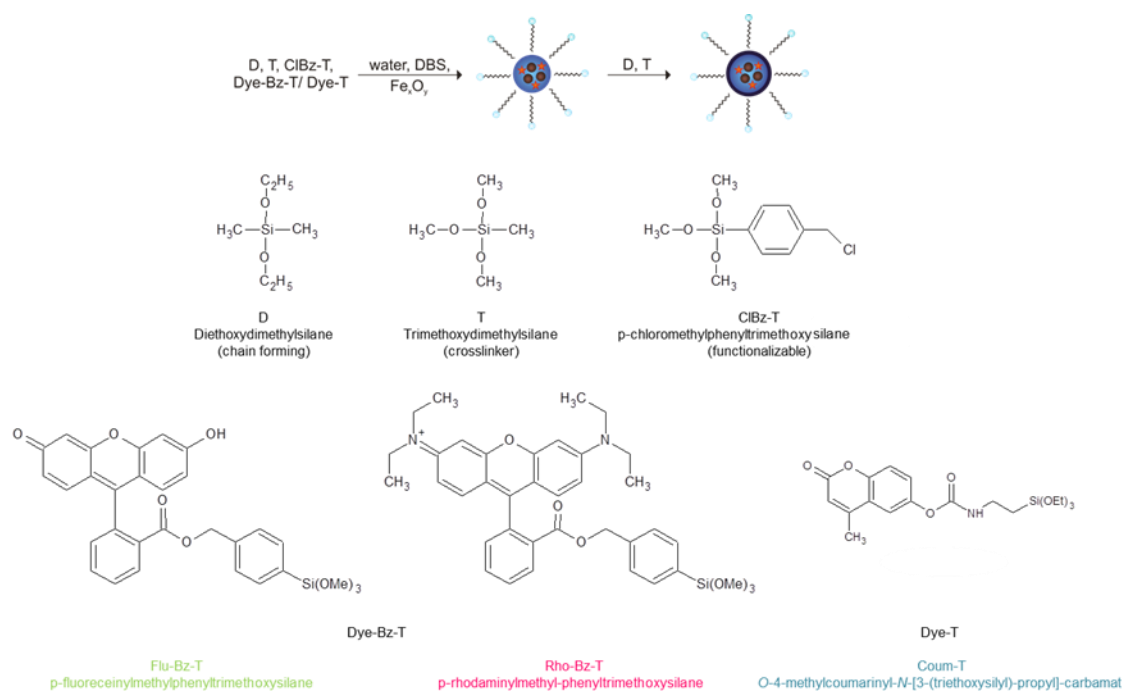


Figure 4.30 Reaction scheme for the preparation of magnetically loaded polyorganosiloxane nanoparticles

Figure 4.31 shows photographs of the aqueous dispersions of polyorganosiloxane nanoparticles synthesized in presence of magnetic nanoparticles and fluorescent monomers. The success of the labeling is directly revealed by the coloration of the aqueous dispersions as well as the fluorescence under UV irradiation. All samples show an intensive fluorescence. The coloration under UV light corresponds to the characteristics of the encapsulated dye: blue for coumarin-, red for rhodamine- and green for fluorescein-labeled systems, respectively.

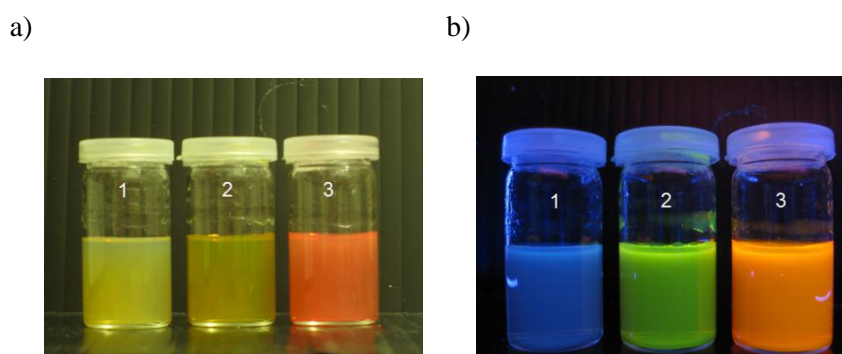


Figure 4.31 Photographs of dye-modified magnetically loaded polyorganosiloxane nanoparticles in aqueous dispersion showing the dye characteristic a) absorption and b) fluorescence: Coum- $\text{Fe}_x\text{O}_y\text{-I}_{2.3\%}\text{@POS}$, $c = 8.4 \text{ g/L}$ (1); Flu- $\text{Fe}_x\text{O}_y\text{-I}_{2.3\%}\text{@POS}$, $c = 9.6 \text{ g/L}$ (2); Rho- $\text{Fe}_x\text{O}_y\text{-I}_{2.3\%}\text{@POS}$, $c = 8.0 \text{ g/L}$ (3)

The different emission wavelength of the three samples can also be observed in the fluorescence emission spectra (Figure 4.32). Compared to the dye-labeled monomers, the emission maxima of the fluorescein-labeled polyorganosiloxane nanoparticles are slightly shifted. Additionally, a second maximum is visible. Similar results were reported by Dr. W. Müller for the hydrophobic loading of

block-co-polymer vesicles (PB₁₃₀-PEO₆₆-COOH) using Nil red that chemical structure is related to fluorescein. The detection of a second maximum can be explained by the change in environmental conditions during the incorporation of the dye into the hydrophobic the poly(butadiene) block.¹⁰⁴ This explanation can be transferred to the incorporation of fluorescein into the hydrophobic environment of the polyorganosiloxane network. The slight blue-shift of the emission maximum of the rhodamine-labeled sample can be explained by dimer formation in high concentrated solutions which has been reported by several groups.¹⁰⁵

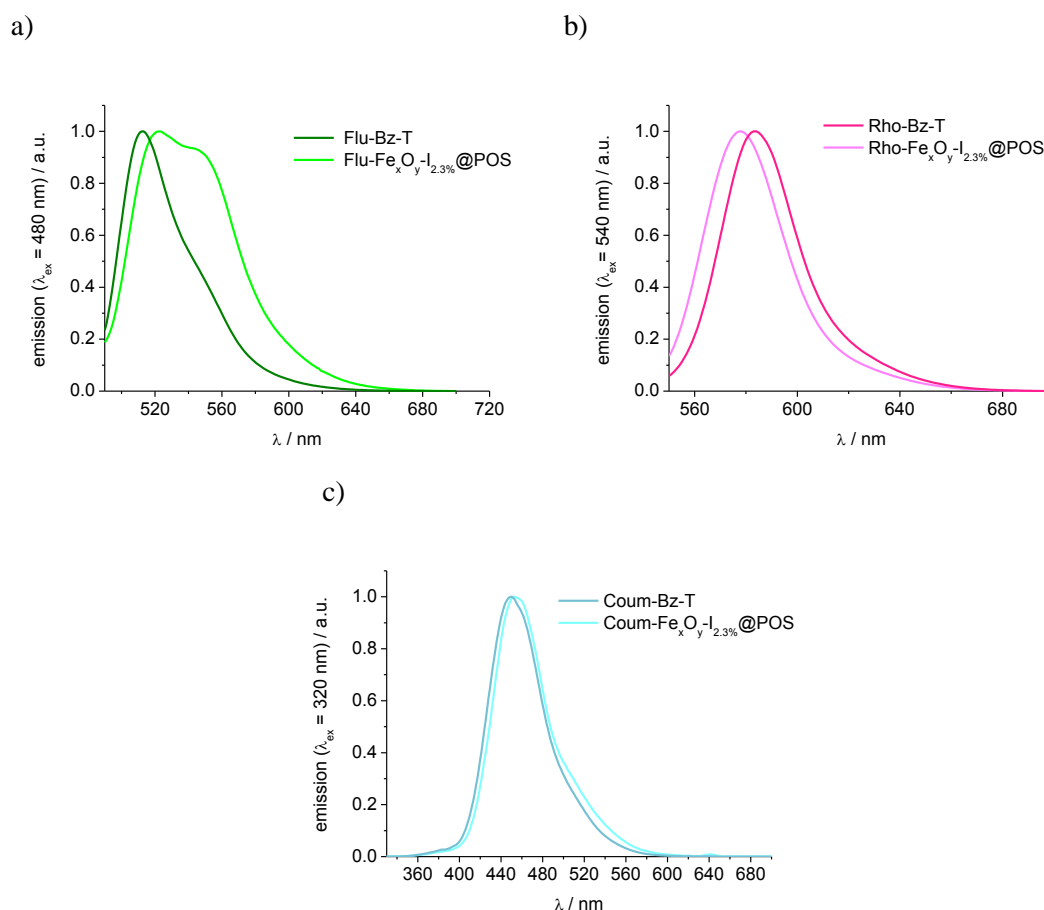


Figure 4.32 Normalized emission spectra of dye modified magnetically loaded polyorganosiloxane nanoparticles (after end-capping process) and monomers in THF: a) fluorescein, b) rhodamine, c) coumarin labeled particles

TEM measurements reveal the successful encapsulation of magnetic nanoparticles in the fluorescent polyorganosiloxane particles (

Figure 4.33). By this means, a simultaneous incorporation of magnetic and fluorescent species was approved. Nevertheless, the use of coumarin-labeled monomers seems to have distinct influence on

¹⁰⁴ Mueller, W.; Koynov, K.; Fischer, K.; Hartmann, S.; Pierrat, S.; Basché, T.; Maskos, M. *Macromolecules* **2009**, *42*, 357

¹⁰⁵ a) Kajiwar, T.; Chambers, R. W.; Kearns, D. R. *Chem. Phys. Lett.* **1973**, *22*, 37; b) Hernando, J.; van der Schaaf, M.; van Dijk, E. M. H. P.; Sauer, M.; García-Parajó, M. F.; van Hulst, N. F. *J. Phys. Chem. A* **2003**, *107*, 43

the particle size and size distribution of the resulting particles. The sample Coum-Fe_xO_y-I_{2.3%}@POS generally consists of larger particles with a high polydispersity.

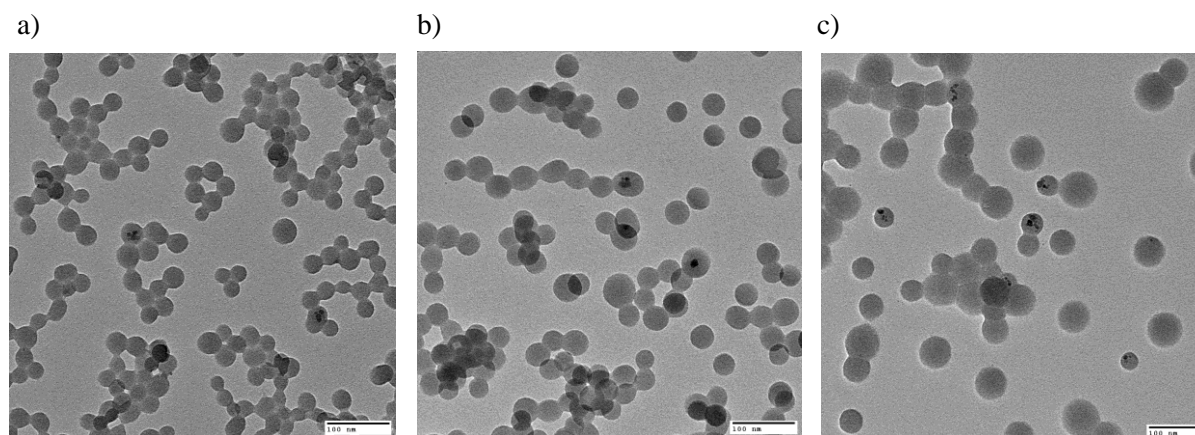


Figure 4.33 TEM images of fluorescent labeled samples: a) Flu-Fe_xO_y-I_{2.3%}@POS; b) Rho-Fe_xO_y-I_{2.3%}@POS; c) Coum-Fe_xO_y-I_{2.3%}@POS after deposition from aqueous dispersion

This impression was confirmed by DLS measurements (Table 4.14). The particle radii of the fluorescein- and rhodamine-modified samples were determined to be in the range of 35 nm which is comparable to the values of the non-labeled particles (Table 4.6). The μ_2 -values, representing the polydispersity of the particles, are in the range of non-labeled particles in both cases. For the coumarin-labeled sample a larger average particle size of 132 nm were found. Compared to the TEM images, the particle sizes of Coum-Fe_xO_y-I_{2.3%}@POS_{aq} measured via DLS are extraordinarily high. This indicates the formation of aggregates in solution. The coumarin-modified particles show significantly higher μ_2 -values. The influence on the particle size distribution most probably results from the solubility of the coumarin-modified monomer: Typically, a mixture of D, T, ClBz-T and Dye-Bz-T monomers was used to synthesize the polyorganosiloxane core. Compared to Flu-Bz-T and Rho-Bz-T, the Coum-T monomer shows a low solubility in the silane monomers D, T and ClBz-T. The presence of insoluble material has strong influences on the concentration of free surfactant. The surfactant adsorbs onto the insoluble material. Hence, the amount of surfactant which is available for the stabilization of the forming polyorganosiloxane nanoparticles is drastically reduced. As mentioned before, it is well known, that a decrease in the DBS content results in the formation of larger polyorganosiloxane particles.¹⁷ The Coum-T monomer does not only differ in the character of the fluorescent dye, the basic structure of the monomer is also different from the Flu- and Rho-Bz-T monomers (Figure 4.30). In case of Flu- and Rho-Bz-T, the dyes are attached to a monomer carrying methylphenyl-groups. The Coum-T monomer, is formed by a silane carrying propylcarbamate-group. The different chemical structures of the monomers could be a reason for the diverse particle sizes and the polydispersity. This effect has also been reported by O. Koshkina for non-magnetic polyorganosiloxane nanoparticles.⁸⁷

Table 4.14 Particle size determination of fluorescent labeled polyorganosiloxane nanoparticles

Sample	λ_{em} / nm	$R_h \text{ (DLS)} / \text{nm}$	μ_2
Flu- $\text{Fe}_x\text{O}_y\text{-I}_{2.3\%}\text{@POS}$	522	36.5	0.15
Rho- $\text{Fe}_x\text{O}_y\text{-I}_{2.3\%}\text{@POS}$	584	33.9	0.16
Coum- $\text{Fe}_x\text{O}_y\text{-I}_{2.3\%}\text{@POS}$	454	132.5	0.22

Concluding, the labeling with fluorescein and rhodamine does not seem to significantly alter the interface properties of the growing siloxane system and therefore the particle size and polydispersity. The incorporation of the coumarin-modified monomer led to larger particle radii, higher polydispersity and the formation of aggregates.

The magnetization curves confirm the persistence of superparamagnetic behavior. Figure 4.34 representatively shows the magnetic measurements for the fluorescein-labeled sample in comparison to a non-fluorescent samples with the same composition. The saturation magnetization of the fluorescein-labeled sample was determined to be 0.59 emu/g of sample (

Table 4.15). This value is 30 % lower than the saturation magnetization of non-fluorescent polyorganosiloxane nanoparticles synthesized under the same conditions. This implies that the fluorescence labeling decreases the encapsulation efficiency of the magnetic loading.

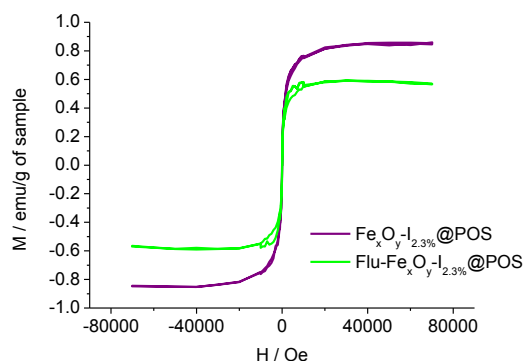


Figure 4.34 Magnetization curves of dye-labeled and non-labeled particles

Table 4.15 Magnetic data for fluorescent-labeled and non-labeled particles

sample	$M_S / \text{emu/g of sample}$	encapsulation efficiency / %
$\text{Fe}_x\text{O}_y\text{-I}_{2.3\%}\text{@POS}$	0.85	92.4
Flu- $\text{Fe}_x\text{O}_y\text{-I}_{2.3\%}\text{@POS}$	0.59	64.1

* determined from magnetic measurements of pure $\text{Fe}_x\text{O}_y\text{-I}$ particles (Figure 4.7)

This loss in magnetization could also be caused by either oxidation of the iron oxide nanoparticles during encapsulation or a decrease of the encapsulation efficiency. An increased oxidation of the particles in presence of the fluorescent monomers seems to be unlikely. The fluorescein-labeling shows no distinct influence on the particle size or particle size distribution of the resulting nanoparticles. Thus, the fluorescein monomer does not seem to have a distinct influence on the reactivity of the silane system or interfacial properties of the growing system. An alteration of the network density, which could cause a loss of magnetic material in case of increased pore size, seems unlikely. Hence, the loss in magnetic properties can probably be attributed to a decreased encapsulation efficiency which could be attributed to the presence of contaminations caused by an insufficient purification of the dye-labeled monomers. The labeling of the monomer CIBz-T was performed in organic solution in presence of 18-crown-6, caesium iodide, the caesium salts of the fluorescent dyes and the CIBz-T monomer. For purification, the organic solvent was evaporated and the monomers were washed three times with water. This step should be adequate to isolate the inorganic salts. However, a removal of the crown ether is not guaranteed. NMR measurements of the purified dye-labeled monomers confirmed this assumption. Impurities which can be attributed to the presence of 18-crown-6 ether are visible in the spectra (for NMR spectra see Appendix). The oxygen atoms of the crown ether are supposed to show a high affinity to the iron oxide surface. The adsorption of 18-crown-6 to the iron oxide nanoparticles could hinder the adsorption of DBS to the iron oxide surface. As described before, the formation of a DBS bilayer is an important factor for the successful encapsulation of the magnetic nanoparticles (see Chapter 4.2.2.1). Therefore, the presence of 18-crown-6 could be a possible reason for the reduced encapsulation efficiency. If the discussed assumptions are true, non-encapsulated iron oxide nanoparticles should be present in the aqueous solution of the dye-labeled samples. Since 18-crown-6 ether is poorly soluble in water, the crown ether coated Fe_xO_y particles are supposed to stick to hydrophobic surfaces, most likely to the surface of the polyorganosiloxane particles. The analysis of TEM images of the fluorescein-labeled sample shows a small number of iron oxide nanoparticles that are attached to the polyorganosiloxane surface (Figure 4.35). This result hints to the mechanism described. For the rhodamine-labeled sample which was also synthesized via the described dye-labeling of the monomer CIBz-T, the same result was found.

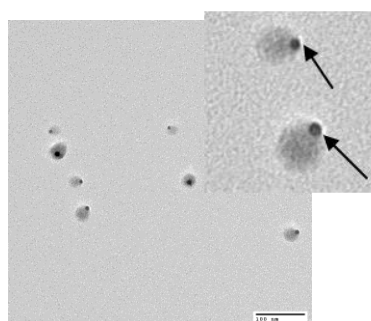


Figure 4.35 TEM image of fluorescein-labeled polyorganosiloxane nanoparticles after deposition from aqueous dispersion

Based on TEM images, a statistic evaluation on the number of encapsulated particles was representatively performed for the fluorescein-labeled particles Flu- $\text{Fe}_x\text{O}_y\text{-I}_{2.3\%}\text{POS-sep}$ (for TEM images see Appendix). Comparing the resulting histogram to the results obtained for a non-fluorescent sample with the same composition ($\text{Fe}_x\text{O}_y\text{-I}_{2.3\%}\text{POS-sep}$) revealed a decrease in the number of encapsulated particles for the dye-labeled sample. The Flu- $\text{Fe}_x\text{O}_y\text{-I}_{2.3\%}\text{POS-sep}$ particles contain 3 nanoparticles most frequently, instead of an average number of 5 nanoparticles as obtained in case of $\text{Fe}_x\text{O}_y\text{-I}_{2.3\%}\text{POS-sep}$. This result fits well to the assumed loss in magnetic material described above.

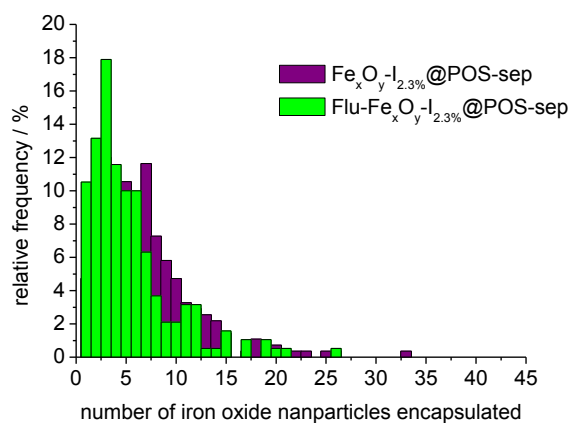


Figure 4.36 Histogram of the number of encapsulated particles derived from statistic evaluations of TEM images for the encapsulation of 2.3 wt-% iron oxide with and without simultaneous fluorescein-labeling

In Figure 4.37 the saturation magnetizations of the three dye-labeled samples are compared. The fluorescein- and rhodamine-labeled particles show comparable magnetic properties which can be explained by the processes described above. The saturation magnetization of Coum- $\text{Fe}_x\text{O}_y\text{-I}_{2.3\%}\text{@POS-H}$ is drastically reduced. As described before, the particle size determinations revealed increased particle sizes for this sample which indicates an effect of the coumarin-monomer on the polymerization process. This influence could alter the network density of the polyorganosiloxane nanoparticles. Thus, an effect on the encapsulation efficiency can be assumed. In case of loose network formation, encapsulated particles would not be captured inside the polymeric system and thus, penetrate through the pores of the network. Hence, the encapsulation efficiency could decrease due to loss of incorporated magnetic particles during synthesis or storage.

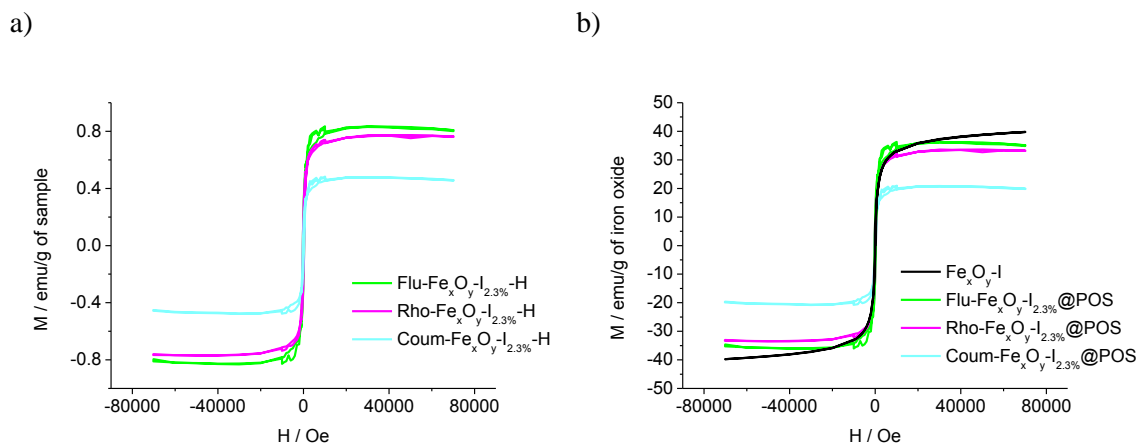


Figure 4.37 Magnetization curves of dye-labeled, magnetic polyorganosiloxane nanoparticles normalized to a) mass of sample and b) mass of iron oxide

In summary, the simultaneous dye-labeling and magnetic loading of polyorganosiloxane nanoparticles was successfully performed. Three different dyes were incorporated into the polymeric system using dye-labeled monomers. The particle sizes of fluorescein- and rhodamine-labeled particles were determined to be in the range of non-fluorescent particles. For coumarin-modified polyorganosiloxane spheres, an increase in particle size and polydispersity as well as partial aggregation was observed. The dye-molecules influence the encapsulation efficiency of the iron oxide nanoparticles. In all three cases, a decrease in the saturation magnetization compared to non-fluorescent magnetically loaded polyorganosiloxane nanoparticles was found. The highest decrease was determined for the coumarin-labeled sample.

The reported fluorescent labeling of the particle core is especially interesting. The use of dye-labeled monomers guarantees that the dye is exclusively located in the particles core. The dye molecules are permanently retained inside the polymeric network system as they are covalently bound which are formed during the condensation reaction. Therefore, the fluorescent molecules should not have appreciable influences on the surface chemistry of the particles and interactions between dyes and environment can be excluded.¹⁰⁶ Of course, this assumes that the dye is exclusively located in the core of the polyorganosiloxane system which could be invalid if delayed condensation of the dye-labeled monomers occurs. In this case, potential influences on the surface properties cannot be excluded.

¹⁰⁶ Utech, S. et al. in preparation

4.2.3.3 Surface Modification: Biocompatibility through Grafting onto of PEG

The *in vivo* application of nanomaterials is often hindered by the rapid recognition of foreign material by the reticuloendothelial system for example by perambulating macrophages. In order to prevent undesired elimination, an adequate surface coating has to be applied.⁹⁷ The polyorganosiloxane system itself is generally not suitable for biomedical applications due to its surface chemistry. Although siloxane or silicon systems are highly biocompatible a further surface modification is necessary to overcome their low water-solubility. In this work, the surface functionalization was performed via a grafting onto process of poly(ethylene glycol). The poly(ethylene glycol) provides water-solubility of the particles and is well known for its high biocompatibility. The PEG coating prevents the nanoparticles from agglomeration and increases their resistance to the adsorption of proteins. Thus, the recognition by macrophage cells can be avoided and the blood circulation time can be increased.^{21,62} Additionally, non-specific cellular uptake due to the high solubility of PEG coated materials in cell membranes has been reported.¹⁰⁷ It has to be stated that the development of anti-PEG antibodies after treatment with PEGylated therapeutics is currently discussed.¹⁰⁸ Additionally, pre-existing immunoglobulins (IgG and IgM) were found to react to intravenously administered PEG.¹⁰⁹ Of course, this would cause a more rapid blood clearance of the PEGylated component and hence, decrease the treatment efficiency. However, a conclusive statement on the crucial factors that cause immune response and hypersensitivity cannot be given at the moment.¹¹⁰ In order to provide the possibility of a further surface modification a heterofunctional PEG polymer was used in this work. In the following sections, the PEG synthesis and the grafting onto process are presented.

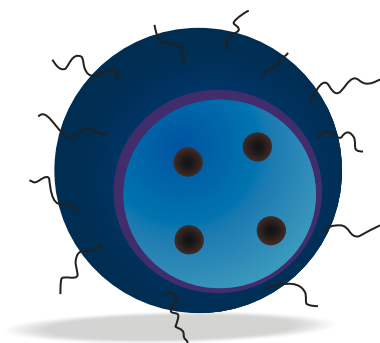


Figure 4.38 Schematic illustration of surface functionalized magnetically loaded polyorganosiloxane nanoparticles

¹⁰⁷ a) Caliceti, P.; Schiavon, O.; Mocali, A.; Veronese, F. M. *Farmaco* **1989**, *44*, 711; b) Yamazaki, M.; Ito, T. *Biochemistry* **1990**, *29*, 1309; c) Boni, L. T.; Hah, J. S.; Hui, S. W.; Mukherjee, R.; Ho, J. T.; Jung, C. Y. *Biochem. Biophys. Acta* **1984**, *775*, 409

¹⁰⁸ Richter, A. W.; Akerblom, E. *Inter. Arch. Allergy Appl. Immunol.* **1983**, *70*, 124

¹⁰⁹ Armstrong, J. K.; Hempel, G.; Koling, S.; Chan, L. S.; Fischer, T.; Meiselman, H. J.; Garratty, G. *Cancer* **2007**, *110*, 103

¹¹⁰ Knop, K.; Hoogenboom, R.; Fischer, D.; Schubert, U. *Angew. Chem. Inter. Ed.* **2010**, *49*, 6288

4.2.3.3.1 Heterofunctional Poly(ethylene glycol)

The heterofunctional poly(ethylene glycol) was synthesized via anionic polymerization. The reaction was initiated by allyl alcohol (Figure 4.39).

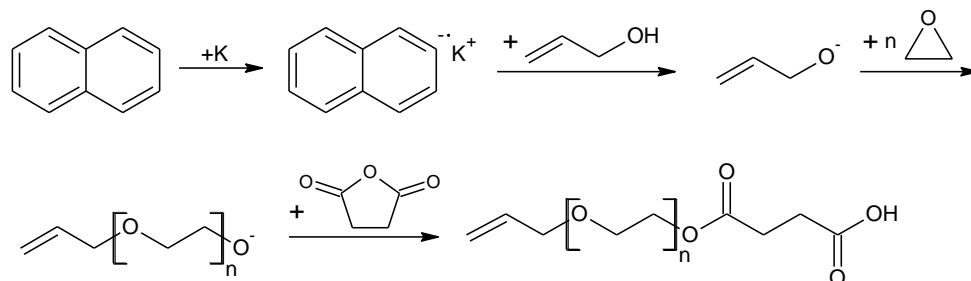


Figure 4.39 Reaction scheme for the anionic polymerization of poly(ethylene glycol)

The resulting α -allyl group can later be used to graft the polymer onto the siloxane surface in a hydrosilylation reaction. By termination with succinic acid anhydride a carboxyl group was introduced at the ω -terminus of the polymer chain. This chain-end is suitable for a further surface modification like the covalent binding of amine functionalized biomolecules via the formation of an amide bond. The PEG polymer was characterized with respect to size and size distribution using MALDI-TOF and GPC measurements.

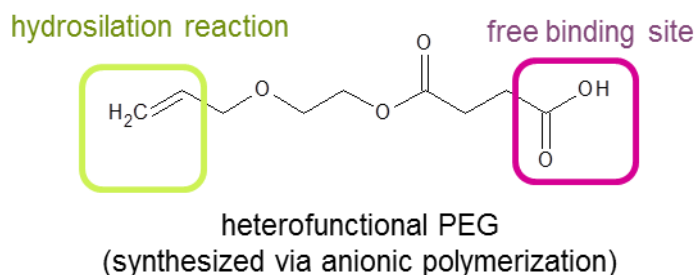


Figure 4.40 Heterofunctional poly(ethylene glycol): allyl-PEG-carboxyl

O. Koshkina could prove that the chain length of the PEG polymer is an important factor for the stabilization of the polyorganosiloxane spheres in aqueous solution.⁸⁷ PEG with a molecular weight of approximately 1000 g/mol is too short to cause a long-term stabilization. The utilization of a long chain polymers ($M = 5000$ g/mol) showed an effective screening of the hydrophobic polyorganosiloxane surface. Though, the chains show a low reactivity in the grafting process and an increased number of aggregates was detected in the resulting particle solution. In this work, poly(ethylene glycol) with a molecular weight of $M_n(\text{PEG-I}) = 2145$ g/mol and $M_n(\text{PEG-II}) = 1671$ g/mol was used (Table 4.16). For GPC and MALDI-TOF measurements see Appendix. It has to be stated that the grafting density achieved via grafting onto techniques is strongly influenced by the

molecular weight of the polymer. As reported in literature, the grafting density decreases with increasing PEG chain length. This phenomenon can be attributed to the excluded volume effect of the surface attached polymer assuming a random coil conformation of the polymeric chains. High molecular weight polymers show a greater excluded volume which hinders tightly packing of the polymers on the surface. Hence, low grafting densities are obtained for high molecular weight polymers.¹¹¹ According to de Gennes, a second regime can be found in case of high grafting densities ($d < R_g$). In this regime, the overlapping regime, the grafted polymer chains are stretched. This stretching depends on the molecular weight of the polymer also showing a decrease with increasing chain length due to the excluded volume effect and gives rise to an alteration of the thickness of the grafted polymeric film.¹¹²

Table 4.16 Molecular weight of allyl-PEG-carboxyl determined via GPC and MALDI-TOF

	PEG-I		PEG-II	
	GPC	MALDI-TOF	GPC	MALDI-TOF
M_n / g/mol	2800	2145	2285	1671
M_w / g/mol	2964	2182	2343	1707
PDI	1.06	1.02	1.03	1.02

4.2.3.3.2 Hydrosilation Reaction

For the stabilization of colloidal particles two different techniques are described: electrostatic and steric stabilization. Electrostatic stabilization is based on Coulomb repulsion between charged particles which results when the diffuse double layers of the particles start to overlap. Additionally, the overlap of the double layers causes an increase in ion concentration which gives rise to a loss in entropy.¹¹³ Steric stabilization is achieved by surface modification using polymeric materials like PEG. Steric stabilization is based on entropic and osmotic effects.¹¹⁴ When two particles approach, the surface attached chains start to entangle which causes a decrease in entropy since the movement of the chains is hindered. Additionally, the high local polymer concentration gives rise to osmotic effects which causes a repulsion of the particles. The steric stabilization is crucially influenced by various parameters like solvent quality (which also gives rise to a temperature-dependence), amount of adsorbed polymer, surface coverage and grafting density, respectively. In good solvents, the polymers expand which causes strong repulsive interactions between the colloidal particles. The collapse of the

¹¹¹ a) Zdyrko, B.; Varshney, S. K.; Luzinov, I. *Langmuir* **2004**, *20*, 6727; b) Ostaci, R.-V.; Damiron, D.; Akhrass, S. A.; Grohens, Y.; Drockenmuller, E. *Polym. Chem.* **2011**, *2*, 348

¹¹² de Gennes, P. G. *Macromolecules* **1980**, *13*, 1069

¹¹³ Holmberg, K.; Jönsson, B.; Kronberg, B.; Lindman, B. *Surfactants and polymers in aqueous solution*, 2nd edition, Wiley, **2003**

¹¹⁴ Hunter, R. J. *Foundations of Colloid Science*, 2nd edition, Oxford, **2001**

polymer chains in poor solvents decreases the repulsive interactions which leads to coagulation of the particles. The surface coverage is a crucial factor in the steric stabilization of colloidal particles. High amounts of adsorbed polymers which are achieved using high molecular weight polymers result in an increase of the hydrodynamic radius which increases the repulsive forces between the particles. In case of grafted polymer chains, the grafting density is of major importance. The repulsive interactions increase with increasing grafting density (or surface coverage) which results in an efficient stabilization of the particles. The grafting density strongly depends on the molecular weight of the grafted polymer chains as discussed above. Of course, additional parameters like chemical structure of the polymer and bridging effects have to be taken into account.

The grafting onto process of poly(ethylene glycol) (PEG-I, $M_n = 2145$ g/mol) was performed via a hydrosilation reaction. To provide the mandatory binding sites, hydride groups were incorporated into the shell of the polyorganosiloxane system. Additionally, a hydride functionalized monomer was used as end-capping agent. PEG-I and polyorganosiloxane particles were dissolved in toluene. The catalyst was added in an argon atmosphere and the reaction solution was stirred for two days at 55 °C. After evaporation of the solvent, a dark grey oil was obtained. After addition of milli-Q-water, sonication and dialysis the solution became clear and yellowish. The progression of the reaction can easily be followed using IR-spectroscopy. The characteristic stretching peak of the Si-H bond at 2125 cm^{-1} clearly disappears after the hydrosilation reaction. This result does not directly prove the success of the coupling reaction since hydrolysis of the Si-H bond would also result in a decrease of this peak. Anyhow, the detection of the Si-C peak at 2350 cm^{-1} after the hydrosilation reaction indicating a successful grafting-onto process of the PEG-I polymer (Figure 4.41). Hydrolysis of the Si-H bond would result in the formation of Si-OH or Si-O-Si bonds with characteristic stretching peaks at 967 cm^{-1} and 1028 cm^{-1} , respectively.¹¹⁵

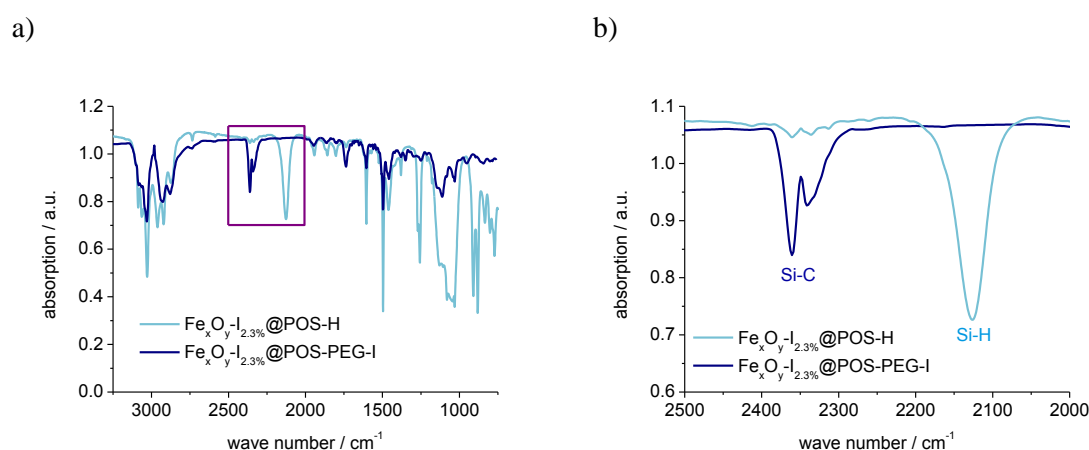


Figure 4.41 IR spectrum of polyorganosiloxane nanoparticles before (light blue) and after (dark blue) hydrosilation reaction: a) complete spectrum, b) enlargement (box in a)

¹¹⁵ McMillan, P. F.; Remmele, R. L. *American Mineralist* **1986**, *71*, 772

Water-soluble magnetically loaded polyorganosiloxane nanoparticles were successfully formed as proven by the TEM images of PEG-coated polyorganosiloxane particles after deposition from aqueous solution and cryo-TEM images (Figure 4.42). Adsorption induced stabilization of the particles can be excluded. Nanoparticles which contained less hydride groups and consequently less binding sites for the hydrosilation reaction could not be transferred into aqueous solution. Thus, the water-solubility can be attributed to covalently bound PEG.

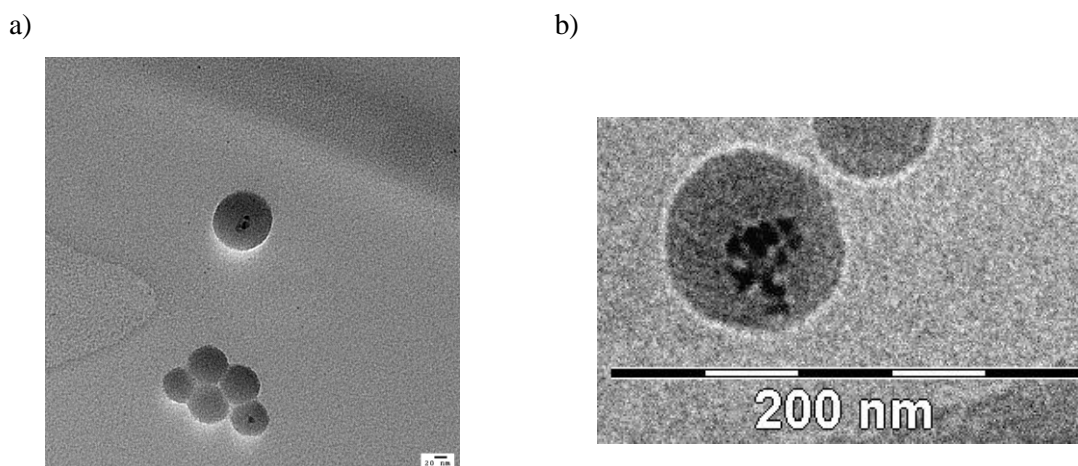


Figure 4.42 a) TEM image after deposition from aqueous solution and b) cryo-TEM image in aqueous solution of surface-modified polyorganosiloxane nanoparticles

Due to the low electron density the poly(ethylene glycol)-coating is invisible in TEM images. Nevertheless, using energy dispersive X-ray spectroscopy (EDX) the polymeric surface coating could be visualized via space-resolved elemental analysis.

Figure 4.43 shows the TEM image including the scanning direction of the beam (indicated by the red line; diameter of beam: approximately 1 nm) and the corresponding EDX spectrum. The onion like architecture of the water-soluble, magnetically loaded particles is clearly visible in Figure 4.43b.

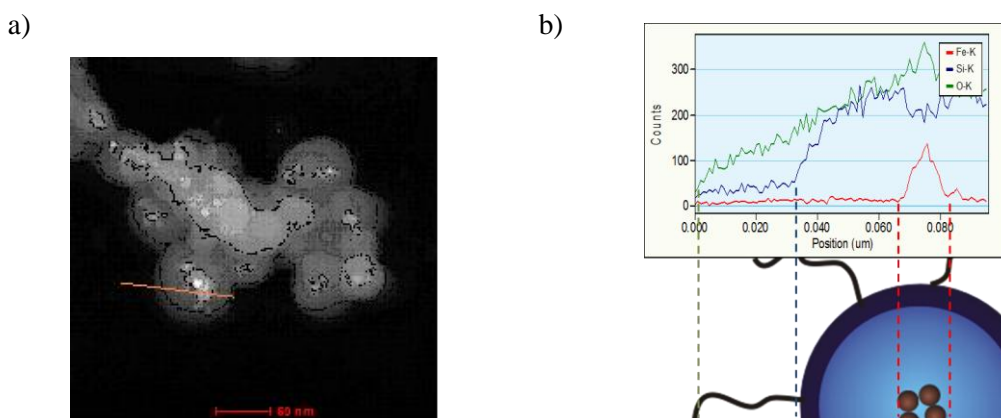


Figure 4.43 EDX measurement of PEG-I grafted polyorganosiloxane particles: a) TEM image, b) EDX spectrum after deposition from aqueous dispersion

The central iron oxide core can easily be detected in both images. The silicon signal decreases relatively sharp at the edge of the polyorganosiloxane particle. At the position of the iron oxide peak, the silicon peak significantly decreases. This result confirms the encapsulation of the inorganic particles. In case of surface-attached particles, no decrease in the silicon signal would be caused. The oxygen peak shows a broad signal over the whole scanning area. Since the oxygen signal decreases to almost zero counts at the end of the scanning line environmental oxygen can be excluded as origin for the signal. Therefore, the signal monitors the oxygen species of both the siloxane system and the PEG-surface coating.

The particle radius before the hydrosilation reaction was determined to be 30.7 nm. After the grafting process, an average hydrodynamic radius of 59.0 nm results from light scattering measurements. The contour length of a PEG-I chain with a molecular weight of 2145 g/mol is below 5 nm. By this means, the measured size seems too large. The PEG coating seems to cause aggregation or interactions between the particles. An interaction between the carboxyl end-groups of the PEG chains could also be imagined. These bridging effects can be eliminated by addition of EDTA which complexes polyvalent ions. This should result in a decrease of the polyorganosiloxane radius if bridging is responsible for the high particle sizes. However, EDTA addition did not cause a distinct decrease in R_h . Thus, the high radii determined via DLS measurements seem to result from particle-particle interactions which could be traced back to van-der-Waals interactions between the PEG chains. Via AF-FFF measurements, a hydrodynamic radius of 28.5 nm was obtained which is more realistic than the values obtained by dynamic light scattering (Table 4.17). By this means, the laminar flow inside the AF-FFF channel seems to be strong enough to hinder the interactions between the PEG chains. Nevertheless, the formation of aggregates caused by an incomplete surface coating cannot be excluded.

Table 4.17 Particle size determinations before and after PEGylation measured in aqueous dispersion

sample	DLS	AF-FFF
	R_h / nm	R_h / nm
$\text{Fe}_x\text{O}_y\text{-I}_{2.3\%}\text{@POS}$	30.7	27.9
$\text{Fe}_x\text{O}_y\text{-I}_{2.3\%}\text{@POS-PEG-I}$	59.0	28.5

The magnetic measurements of the PEGylated particles reveal a decrease in the saturation magnetizations compared to non-PEGylated particles (Figure 4.44). As more non-magnetic material is present in the sample, the saturation magnetization per g of sample has to decrease.

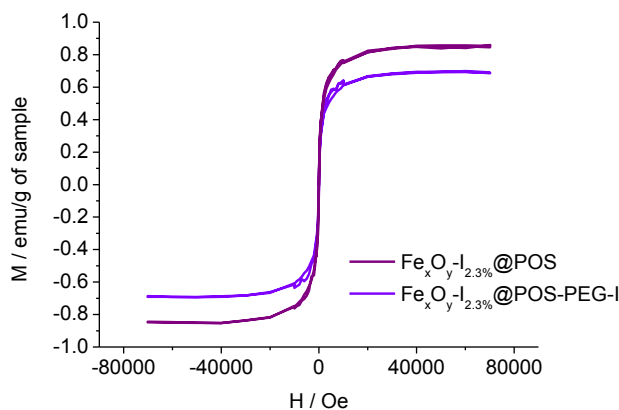


Figure 4.44 Magnetization curves of $\text{Fe}_x\text{O}_y\text{-I}_{2.3\%}\text{@POS}$ before and after surface modification

Assuming that the surface modification did not cause a loss of magnetic material, the PEG content of the sample can be evaluated by comparison with the magnetic measurements of bare iron oxides and non-functionalized particles. From the measurements of bare iron oxide nanoparticles, the iron oxide content of the PEGylated sample was determined to be approximately 1.8 wt-%. Comparing this value to the determined magnetic content before the hydrosilation reaction (approximately 2.0 wt-%, assuming an encapsulation efficiency of 92 % relative to the offered amount of 2.3 wt-% of iron oxide), a PEG content of 24 wt-% can be estimated. An absolute determination of the number of PEG chains per polyorganosiloxane sphere is difficult since the molecular weight of the polyorganosiloxane system could not be measured. The molecular mass of the synthesized particles is too high to allow for osmosis or light scattering based determinations. GPC measurements are also not adequate due to the lack of a suitable standard calibration. Nevertheless, the number of PEG molecules per polyorganosiloxane nanoparticle can roughly be estimated. For the volume of the $\text{O-Si}(\text{CH}_3)_2\text{H}$ -group a value of 0.146 nm^3 is reported in literature. Considering a spherical shape of the hydride group, a spatial expanse of 0.335 nm^2 can be considered. Based on the average hydrodynamic radius determined via DLS the surface coverage is calculated to be approximately 35 000 PEG chains per particle. Since a complete surface coverage is relatively unlikely, the actual number of PEG chain per particle should be lower than the calculated value. The highest grafting densities for the grafting of PEG onto silica surfaces ($M_w(\text{PEG}) = 5000 \text{ g/mol}$) were reported to be 1.5 chains/nm^2 . Compared to this value, the calculated grafting density of 3.0 chains/nm^2 appears too high. Nevertheless, an exact determination of the grafting density requires a molecular weight determination of the polyorganosiloxane nanoparticles which is difficult due to the previously described reasons.

Table 4.18 Saturation magnetization of pure and encapsulated iron oxide nanoparticles before and after PEGylation

sample	M_s / emu/ g of sample	recalculated Fe_xO_y -I content / wt-%
Fe_xO_y -I	49.7	100
Fe_xO_y -I _{2.3%} POS	0.85	2.1
Fe_xO_y -I _{2.3%} POS-PEG-I	0.70	1.8

In summary, a grafting onto process of heterofunctional poly(ethylene glycol) was successfully conducted. The surface modification led to water-soluble polyorganosiloxane nanoparticles. The particle size of the grafted nanospheres was determined to be approximately 30 nm via AF-FFF measurements. Particle size determinations via DLS did result in extraordinary large values which probably result from interactions between the PEG chains attached to the surface. As described before, the use of heterofunctional PEG chains allow for an additional surface modification using biomolecules for example. This issue is discussed below using water-soluble magnetofluorescent particles which are highlighted in the following section.

4.2.3.4 Combination of Core and Surface Modification: Water-soluble Magnetofluorescent Polyorganosiloxane Nanoparticles

Magnetically loaded polyorganosiloxane nanoparticles carrying fluorescent dyes in the siloxane core and poly(ethylene glycol) on the surface were synthesized via sequential functionalization. First, fluorescent labeled magnetic polyorganosiloxane nanospheres were synthesized by adding dye-labeled monomer to the silane monomer mixture in presence of magnetic iron oxide nanoparticles (see Chapter 4.2.3.2). During the shell formation and the following end-capping process, hydride groups were incorporated into the polyorganosiloxane network. Afterwards, poly(ethylene glycol) (PEG-II, $M = 1671$ g/mol) was grafted onto the surface of fluorescent nanospheres via a hydrosilation reaction between the allyl chain-end of the PEG and the hydride surface groups of the polymeric nanoparticles (see Chapter 4.2.3).

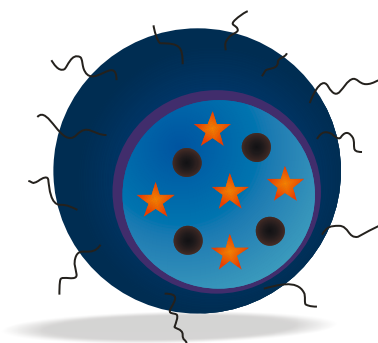


Figure 4.45 Schematic illustration of water-soluble, magnetofluorescent polyorganosiloxane nanoparticles

The resulting water-soluble particles show the typical coloration and fluorescence of the incorporated dyes (Figure 4.46). Compared to the intensities of the non-PEGylated samples in Figure 4.31, the fluorescence intensities after surface modification appear much lower. This issue is further discussed in Chapter 4.2.3.4.1. It has to be stated that the coumarin-labeled particles show a distinct shift in the fluorescence wavelength after surface modification. Before PEGylation, an emission wavelength of 454 nm was found. After the grafting process, the emission wavelength was determined to be 358 nm (Table 4.19). The peak at 358 nm was also detected in repeated fluorescence measurements of the coumarin-labeled monomer after some weeks of storage. This effect indicates a sensitivity of the Coum-T monomer to environmental effects which seem to decrease the long-term stability of the monomer as well as the coumarin-labeled polyorganosiloxane nanoparticles. A partial degradation of the coumarin-dye can be imagined.

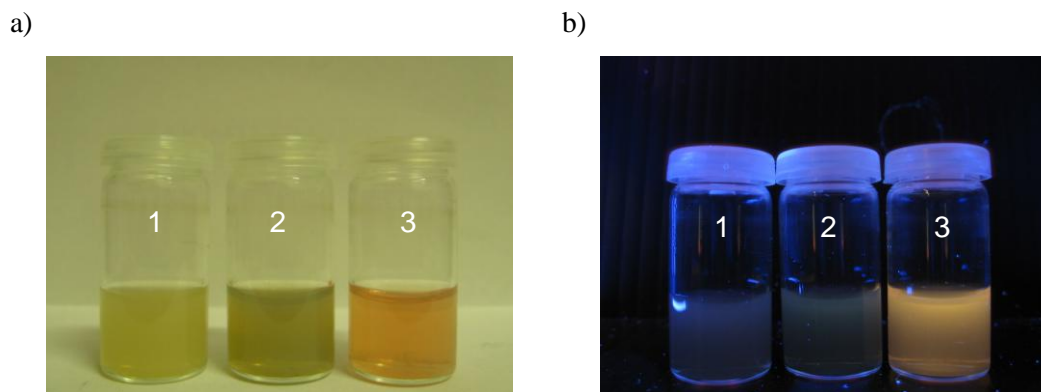


Figure 4.46 a) Absorption and b) fluorescence of magnetofluorescent water-soluble polyorganosiloxane nanoparticles in aqueous solution: Coum- $\text{Fe}_x\text{O}_y\text{-I}_{2.3\%}\text{@POS-PEG-II}$, $c = 9.6 \text{ g/L}$ (1); Flu- $\text{Fe}_x\text{O}_y\text{-I}_{2.3\%}\text{@POS-PEG-II}$, $c = 9.2 \text{ g/L}$ (2); Rho- $\text{Fe}_x\text{O}_y\text{-I}_{2.3\%}\text{@POS-PEG-II}$, $c = 10.8 \text{ g/L}$ (3)

Table 4.19 Emission wavelength of magnetofluorescent, surface grafted polyorganosiloxane nanoparticles in aqueous solution

sample	$\lambda_{\text{em}} / \text{nm}$
Flu- $\text{Fe}_x\text{O}_y\text{-I}_{2.3\%}\text{@POS-PEG-II}$	513
Rho- $\text{Fe}_x\text{O}_y\text{-I}_{2.3\%}\text{@POS-PEG-II}$	570
Coum- $\text{Fe}_x\text{O}_y\text{-I}_{2.3\%}\text{@POS-PEG-II}$	358

The particle sizes were determined via AF-FFF and DLS analysis (Table 4.20). For all samples, the particle sizes were determined before and after a magnetic separation procedure which was used to isolate the magnetically loaded particles from non-magnetic material as described in Chapter 4.2.2.2. In contrast to the procedure described above, the magnetic separation of the PEGylated particles was performed in aqueous dispersion. Due to the hydrophilic surface formation, no aggregation of particles occurred as found for the separation of the aqueous dispersions of unmodified particles which carried unsaturated surface groups. In analogy to the sample $\text{Fe}_x\text{O}_y\text{-I}_{2.3\%}\text{@POS-PEG-I}$, light scattering measurements resulted in extraordinary high hydrodynamic radii. This effect can be traced back to interactions between the surface attached PEG chains or aggregate formation caused by an insufficient surface coating. More reasonable particle sizes were obtained via AF-FFF measurements (for elugrams see Appendix). The particle radii of the separated samples are in the range between 30 nm and 70 nm. For fluorescein-labeled particles, the largest radii were found while coumarin-labeling resulted in much smaller particles. This result is surprising since the hydrodynamic radii determined for the same particles before PEGylation revealed extraordinary large particles in case of coumarin-labeling ($R_h = 123.45 \text{ nm}$), while particle radii of approximately 30 nm were found for fluorescein- and rhodamine-labeled particles before the surface modification (see Table 4.14). The data shown in Table 4.20 indicate that the larger particles which were determined to be present in the coumarin-labeled sample cannot be detected in AF-FFF measurements. The particles seem to be too large to elute within the

detected measurement time. The fluorescein-labeled particles seem to form aggregates which can be detected in both methods (DLS and AF-FFF). Nevertheless, the particle radii determined via AF-FFF measurements are small compared to the described aggregates of the coumarin-labeled sample in Chapter 4.2.3.2 which allows for a detection using AF-FFF measurements. This result indicates that the hydrosilation reaction is hindered in presence of the fluorescein groups that are covalently bound to the polyorganosiloxane core. Hence, incomplete surface coating occurs which causes the formation of aggregates. The influence of the fluorescein molecules on the efficiency of the hydrosilation reaction is further discussed in Chapter 4.2.3.4.1. For the rhodamine-labeled particles reasonable radii were obtained. AF-FFF measurements revealed particle radii that are slightly larger than the values determined for the non-PEGylated sample (Rho-Fe_xO_y-I_{2.3%}@POS = 33.9 nm). The deviation between the radii of Rho-Fe_xO_y-I_{2.3%}@POS-PEG-II obtained by DLS before and after separation could probably result from the larger contribution of large particles to the average hydrodynamic radius since the magnetically loaded particles were found to be generally larger compared to unloaded polyorganosiloxanes. Dynamic light scattering of the separated samples resulted in large radii in all three cases which can also be traced back to PEG induced interparticle interactions and aggregation as described above.

Table 4.20 Light scattering and AF-FFF data of dye-labeled polyorganosiloxane nanoparticles in aqueous dispersion before and after magnetic separation

sample	before separation		after separation		
	R _h / nm	μ ₂	R _h * / nm	R _h / nm	μ ₂
Flu-Fe _x O _y -I _{2.3%} @POS-PEG-II	144.5	0.08	67.8	176.4	0.09
Rho-Fe _x O _y -I _{2.3%} @POS-PEG-II	62.8	0.04	47.8	141.2	0.07
Coum-Fe _x O _y -I _{2.3%} @POS-PEG-II	143.1	0.12	33.0	123.8	0.11

* determined via AF-FFF

In Figure 4.47, the magnetization curves of the sample before and after the grafting process are compared. The saturation magnetization of Flu-Fe_xO_y-I_{2.3%}@POS-PEG was determined to be 0.18 emu/g of sample. In Chapter 4.2.3.2, the theoretic magnetic content of the polyorganosiloxane samples was recalculated from the saturation magnetizations of pure iron oxide nanoparticles. For Flu-Fe_xO_y-I_{2.3%}@POS-H, the magnetic content was determined to be 1.5 wt-% (assuming an encapsulation efficiency of 64.1 % relative to an offered amount of iron oxide of 2.3 wt-%). In case of Flu-Fe_xO_y-I_{2.3%}@POS-PEG-II, the magnetic content is decisively lower and was recalculated to be 0.5 wt-% (Table 4.21).

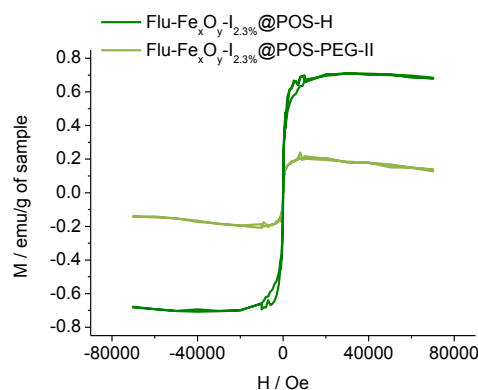


Figure 4.47 Magnetization curves of Flu-Fe_xO_y-I_{2.3%}@POS before (dark green) and after surface modification (light green)

Since a loss of magnetic material during the grafting process can be excluded, the weaker magnetic properties should result from the increased molar mass of the surface coated particles. By this means, an estimation of the PEG content is possible as described before (Chapter 4.2.3.3.2). Based on the saturation magnetizations determined for Flu-Fe_xO_y-I_{2.3%}@POS-H in Chapter 4.2.3.2, a PEG-mass fraction of approximately 66.7 % was calculated. In Chapter 4.2.3.3.2, the surface modification of non-fluorescent polyorganosiloxane nanoparticles was investigated. The PEG content was determined to be 23 wt-%. The deviation between this value and the PEG content determined for the fluorescent-labeled samples can be attributed to the different chain length of the used polymers ($M_n(\text{PEG-I}) = 2145 \text{ g/mol}$, $M_n(\text{PEG-II}) = 1671 \text{ g/mol}$). In Chapter 4.2.3.3.2, the polymer consisted of 50 repeating units (PEG-I). In this Chapter, the degree of polymerization was 38 (PEG-II). Taking the different molecular weights of the polymers into account, a higher grafting density was revealed in case of the short PEG polymer (PEG-II). This result seems to be adequate since the required space is proportional to the chain length. Hence, using short chain polymers, a higher grafting density can be obtained. However, both grafting processes caused sufficient water-solubility.

Table 4.21 Measured saturation magnetizations and recalculated iron oxide contents of non-surface and surface modified particles

sample	M_S / emu/g of sample	recalculated content of Fe _x O _y -I / wt-%
Flu-Fe _x O _y -I _{2.3%} @POS-H	0.59	1.5
Flu-Fe _x O _y -I _{2.3%} @POS-PEG-II	0.18	0.5

The determinations of the saturation magnetizations for the rhodamine- and coumarin-labeled are lower than the values determined for the fluorescein-labeled sample (for magnetization curves see Appendix). The decrease results from the low encapsulation efficiencies for the rhodamine- and coumarin-labeled samples as revealed in Chapter 4.2.3.2. An additional phenomenon is visible in the magnetization curves of the PEGylated, dye-labeled particles. Instead of reaching a saturation

magnetization, the magnetization decreases when high fields are applied. In literature, this effect has been reported for magnetic fluids in magnetic fields. The magnetization was found to decrease with increasing magnetic field intensity and exposure time. According to Pop et al. this phenomenon results from large particle and aggregate sedimentation in the magnetic field.¹¹⁶ The described effect was found to be most pronounced in case of the coumarin-labeled samples which is supposed to consist of the largest particles as discussed above.

Since the dye molecules are covalently bond to the core of the siloxane network, the surface properties of the three dye-labeled samples should show no significant deviations. Nevertheless, ζ -potential measurements revealed slight differences, especially between the fluorescein/rhodamine-labeled and the coumarin-labeled sample (Figure 4.48). This deviation can be traced back to the different particle sizes. Even if the mass concentrations of the measured solutions are comparable, the large dimension of the coumarin-labeled sample causes lower particle concentrations. As discussed before, diluted systems show generally higher ζ -potentials compared to less diluted solutions which fits well to the results obtained for the three dye-labeled samples.

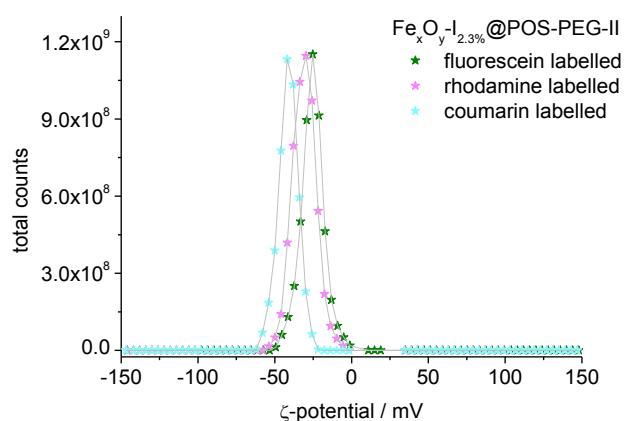


Figure 4.48 ζ -potential measurements of dye-labeled polyorganosiloxane nanoparticles in aqueous dispersion at pH = 7-8 (dilution: 1:10 resulting in mass concentrations of $c(\text{Coum-Fe}_x\text{O}_y\text{-I}_{2.3\%}\text{@POS-PEG-II}) = 0.96 \text{ g/L}$; $c(\text{Flu-Fe}_x\text{O}_y\text{-I}_{2.3\%}\text{@POS-PEG-II}) = 0.92 \text{ g/L}$; $c(\text{Rho-Fe}_x\text{O}_y\text{-I}_{2.3\%}\text{@POS-PEG-II}) = 1.08 \text{ g/L}$)

In this section, the synthesis and characterization of water-soluble, magnetofluorescent particles was presented. The dye-labeling was performed via the incorporation of fluorescent monomers during the condensation of the organosilanes. The resulting polyorganosiloxane nanoparticles were surface modified via a grafting onto process of poly(ethylene glycol). The particles show superparamagnetic behavior, fluorescent properties and a high stability in aqueous solution. For a more detailed analysis of the fluorescent properties of the PEGylated particles, fluorescence spectroscopic measurements were used which is topic of the following section.

¹¹⁶ Pop, L. M.; Buioca, C. D.; Iusan, V.; Zimnicaru, M. *J. Magn. Magn. Mater.* **2002**, *252*, 46

4.2.3.4.1 Fluorescence Measurements

Concentration-dependent measurements of the fluorescence intensity were performed for all three PEGylated samples. The spectra show the typical linear relation for low particle concentrations. For higher concentrations, a decrease in the fluorescence intensity was revealed in case of fluorescein- and rhodamine-labeling. The obtained non-linear relationship has also been found for fluorescein- and rhodamine-labeled proteins and can be attributed to self-quenching.⁷⁵ The dyes display a small Stokes shift (shift between absorption and emission peak). In case of high local dye concentrations and small distances between the fluorophores (within 40 Å), energy can be transferred between different fluorescein groups which causes a decrease in the fluorescence intensity. For the coumarin-labeled sample a linear relation was found (see Appendix). In Figure 4.49, the concentration dependence of the fluorescein-labeled sample before and after surface modification is representatively shown.

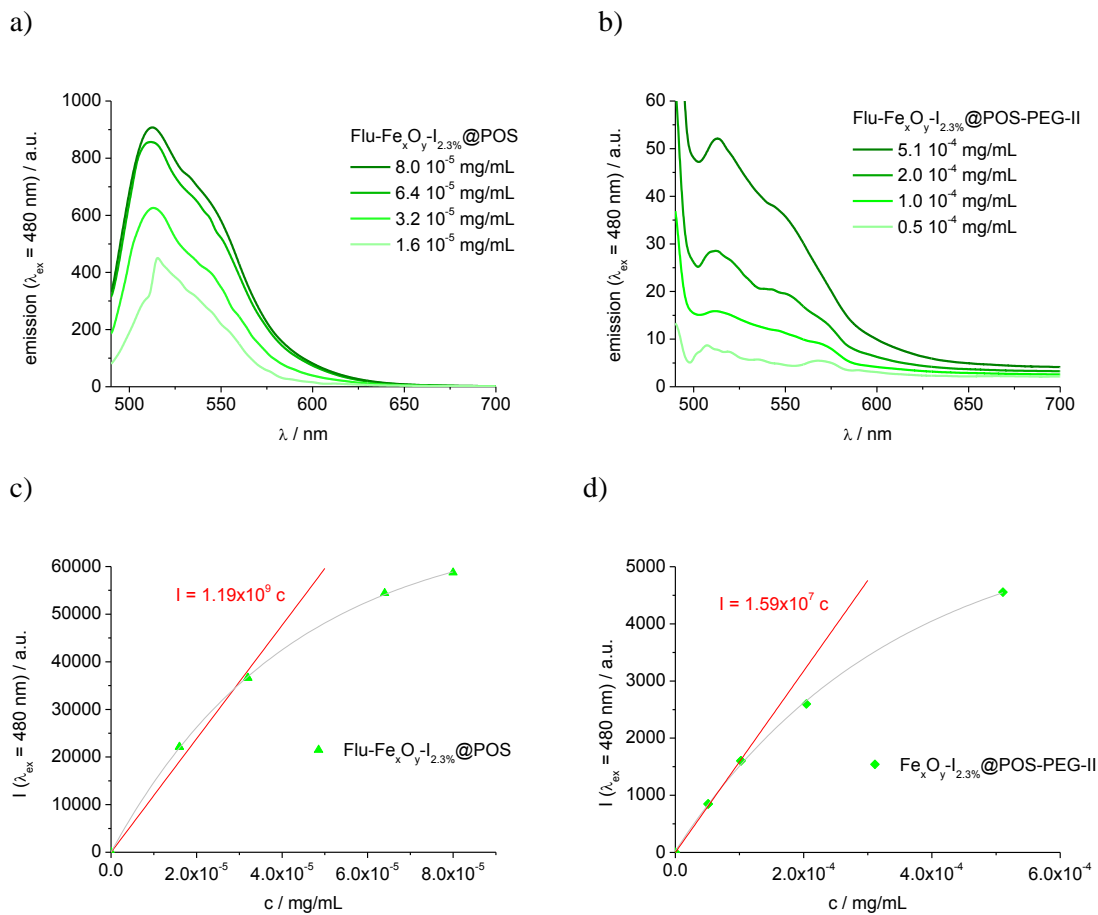


Figure 4.49 Concentration dependent emission spectrum and resulting concentration dependent fluorescence intensity of fluorescein-labeled polyorganosiloxane nanoparticles a)+c) before and b)+d) after surface modification (c = particle mass concentration determined via weighting of dried samples,

$$I = \int_{490\text{nm}}^{700\text{nm}} \text{emission} \, d\lambda$$

As mentioned before, the fluorescence intensities of the surface functionalized particles are much lower compared to non-PEGylated samples. Based on Figure 4.49, the theoretical emission intensity of the PEGylated particles can be calculated for different concentrations. Since the concentration of the encapsulated dyes cannot be accurately determined, the fluorescence intensities are plotted versus the concentration of the polyorganosiloxane nanoparticles. For the surface modified sample, the contribution of the attached PEG chains to the determined mass concentrations of the sample has to be taken into account. Therefore, the measured concentrations were reduced by the PEG content determined in Chapter 4.2.3.4. Using this procedure, the fluorescence intensities of the surface modified sample were calculated to be only 1.4 % compared to the non-PEGylated sample. To determine the reason for this drastic decrease, a toluene solution containing the dye-labeled monomer Flu-Bz-T and the platinum catalyst was heated to 55°C and stirred overnight in an argon atmosphere as performed in the hydrosilation reaction of the dye-labeled polyorganosiloxane nanoparticles. In the absorption spectra of the monomer after catalyst addition no fluorescein absorption peak ($\lambda_{\text{max}} = 480$ nm) could be detected which indicates a destruction of the dye (for spectra see Appendix). Fluorescein is known to undergo a one electron reduction under reductive conditions in aqueous solution.¹¹⁷ This phenomenon could potentially cause the decreased fluorescence intensities due to the reduction itself or following chemical modifications of the fluorescein dye. The described effects can also be imagined to cause the formation of large aggregates as revealed via particle size analysis of the fluorescein-labeled sample after PEGylation (Table 4.20). The platinum induced destruction of the dye competes with the hydrosilation reaction leading to an insufficient surface grafting process and hence, the formation of aggregates.

In case of rhodamine- and coumarin-labeled particles, a residual fluorescence intensity of approximately 30 % and 16 %, respectively was calculated for the surface modified particles relative to the non-PEGylated samples (see Appendix). It has to be stated that the fluorescence intensity of the coumarin-labeled sample after PEGylation was calculated from the emission peak at 358 nm, whereas the determined fluorescence intensity of the non-PEGylated sample was based on the peak at 454 nm. As discussed before, the peak at 358 nm is considered to result from degradation of the coumarin-dye during storage. The potentially formed decomposition product seems less sensitive to the presence of the platinum catalyst compared to the primary coumarin structure. The rhodamine-labeling seems least susceptible to degradation. This result fits well to the particle radii determined for the PEGylated sample (Table 4.20). The comparatively high stability of rhodamine reduces the conversion of platinum in the degradation reaction (compared to the surface grafting of fluorescein-labeled particles). Consequently, the available amount of Karstedt catalyst is sufficient to ensure an adequate surface coating and fewer aggregates are formed resulting in reasonable particle radii of 47.8 nm for Rho-Fe_xO_y-I_{2.3%}@POS-PEG-II.

¹¹⁷ a) Eklund, J. C.; Waller, D. N.; Rebbitt, T. O.; Marken, F.; Compton, R. G. *J. Chem. Soc. Perkin Trans.* **1995**, 2, 1981; b) Aktories, K.; Förstermann, U.; Hofmann, F. B.; Starke, K. *Allgemeine und Spezielle Pharmakologie und Toxicology*, Elsevier, **2009**

Concluding, for fluorescein- and rhodamine-labeled samples a non-linear concentration dependence of the fluorescence intensity was found which can be traced back to self-quenching effects in concentrated solutions. The coumarin-labeled particles show a linear concentration dependence (see Appendix). After surface functionalization with poly(ethylene glycol), a reduced fluorescence intensity was found for all three fluorescent dyes. This decrease can be explained by destruction of the dyes by the platinum catalyst. However, the rhodamine-labeled polyorganosiloxane nanoparticles show comparatively high residual intensities of approximately 30 % relative to the non-PEGylated particles. The rhodamine monomers seems less susceptible to platinum-induced degradation. This results show that the incorporation of dye-labeled monomers in combination with a subsequent surface grafting process via hydrosilation is not optimal for the synthesis of fluorescent, water-soluble particles. As mentioned before, another approach for the synthesis of fluorescent polyorganosiloxane nanoparticles is a subsequent dye-labeling of the PEGylated particles. This procedure eliminates the platinum induced destruction of the dye. Nevertheless, the important drawback of this approach is the presence of residual unbound dye which is difficult to removed. The free dye causes a high fluorescent background which complicates the analysis of the particles as well as the detection of particle distribution in biological environments. Consequently, an alternative labeling procedure has to be developed. For example, the incorporation of fluorescent nanocrystals, quantum dots or radioactive isotopes could be envisioned.^{92,118} Furthermore, the possibility of a platinum-free surface grafting for example via click-chemistry has to be considered.

4.2.3.4.2 Particle Behavior in Solution: Fluorescence Microscopy Analysis

The magnetic properties in solution are of essential interest for *in vivo* and *in vitro* applications. For applications including magnetic manipulation and separation like targeted drug delivery, magnetic separation or hyperthermia, the particles need to be receptive to external magnetic fields in aqueous media.

To investigate the behavior of magnetically loaded polyorganosiloxane nanoparticles, an aqueous dispersion of rhodamine-labeled particles (Rho-Fe_xO_y-I_{2.3%}@POS-PEG-II) was imaged using fluorescence microscopy. The rhodamine-labeled particles can effortlessly be detected due to the bright red fluorescence of the incorporated dye. The particles were put into a glass tube which acts as flow cell (ID: 0.1 mm x 2.0 mm x 100 mm, wall: 0.1 mm¹¹⁹) and their distribution in the fluid volume was monitored in absence and in presence of external field including flow fields and magnetic fields. A schematic illustration of the experimental setup is shown in Figure 4.50.

¹¹⁸ Wu, W.; He, Q.; Jiang, C. *Nanoscale Res. Lett.* **2008**, *3*, 397

¹¹⁹ www.vitrocom.com

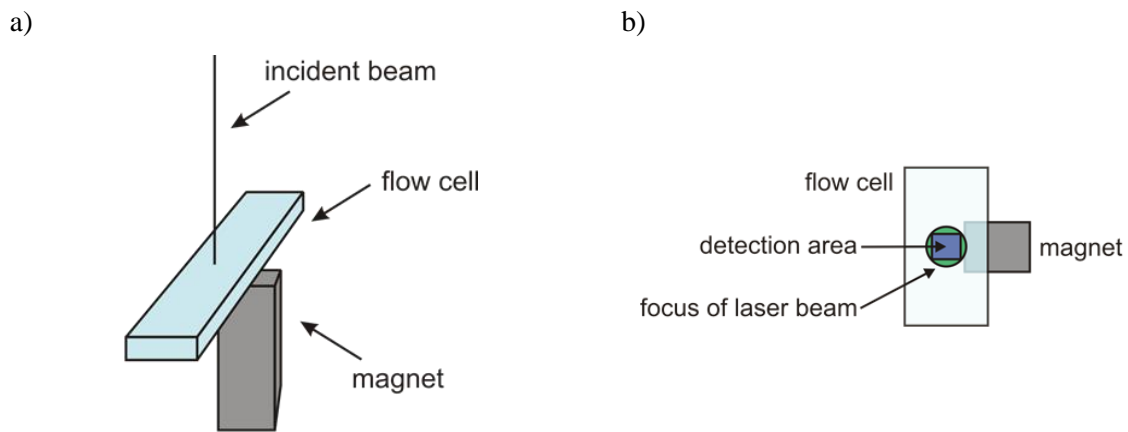
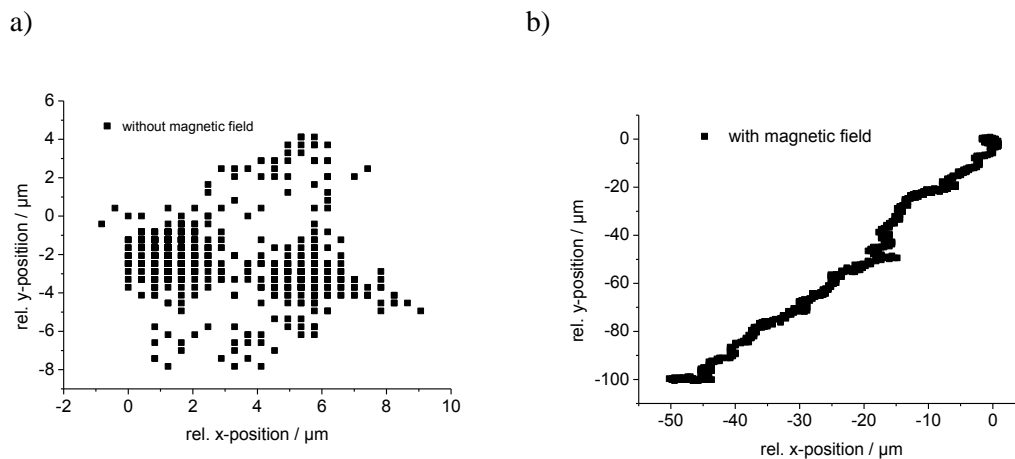


Figure 4.50 Schematic illustration of experimental setup (focus width: 500 μm in diameter, focus depth: 1 μm)

To monitor the particle behaviour in presence of different external fields, various particles were traced using a MATLAB-based computer program. The displacement was measured and converted into a time-dependent position plot (time-trace) of the particle.

In absence of an external field, the particles are randomly distributed in the aqueous medium and the typical Brownian motion can be monitored. The monitored displacement of the particles shows a random distribution (Figure 4.51). By placing a permanent magnet (NdFeB, 10 mm x 5 mm x 30 mm, 350 mT at surface as measured using a Wuntronic teslameter “Koshava 4”) beneath the flow cell (distance between magnet and flow cell approximately 0.4 mm) a magnetic field was applied. A directed movement of the particles was observed as demonstrated in Figure 4.51. Due to the gradient of the magnetic field, the particles start to move towards the highest gradient positions and hence, the center of the magnetic field.



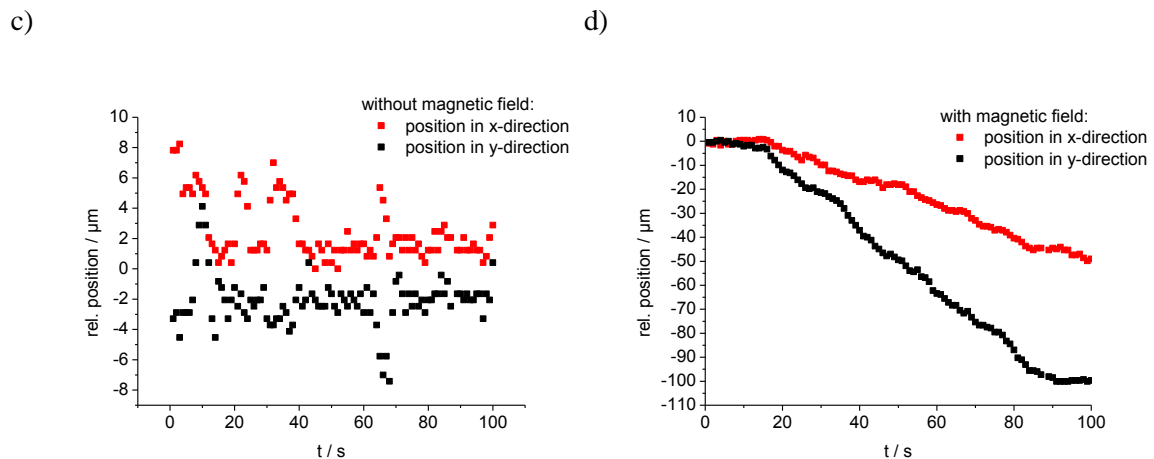


Figure 4.51 Particle position (a) and (c)) and resulting time-trace (b) and d)) of magnetically loaded, rhodamine-labeled particles detected via fluorescence microscopy in a)+c) absence and b)+d) presence of an external magnetic field

The magnetic force on the particles strongly depends on the distance between the particle and the surface of the magnet. The distance-dependent decay is illustrated in Figure 4.52a. However, in the investigated distance (approximately 0.4 mm to outer wall of flow cell) the present magnetic field is still sufficiently strong to be in the saturation range of the magnetically loaded particles (Figure 4.52b). As soon as the magnetic force was removed, the directed movement disappeared and the Brownian motion could be monitored again.

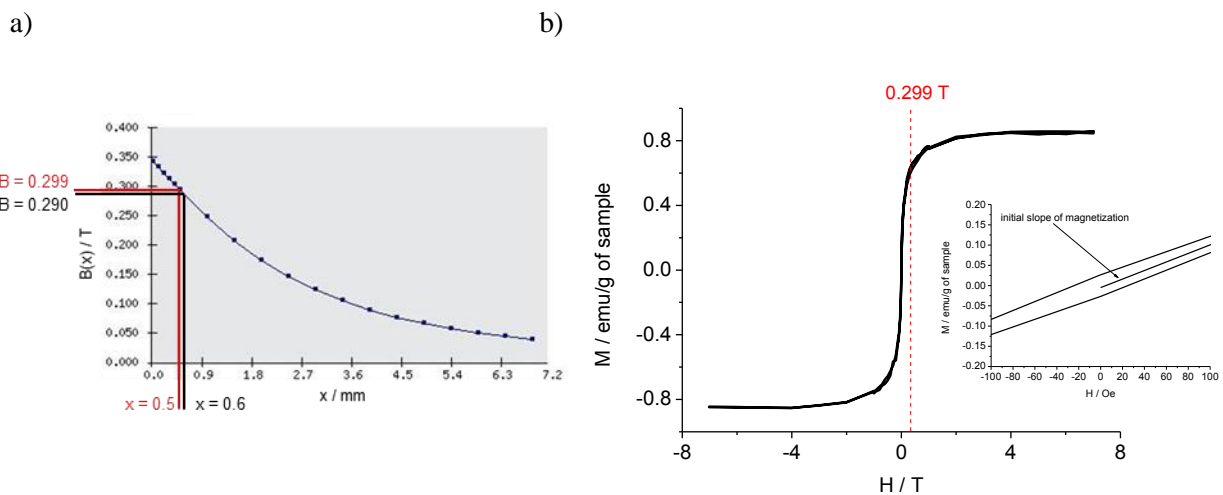


Figure 4.52 a) Distance-dependent magnetic field¹²⁰ and b) magnetization curve of magnetically loaded polyorganosiloxane nanoparticles (inlet: initial slope used for determination of the magnetic susceptibility)

For many *in vivo* applications especially those who involve magnetic delivery, it is important to resist the natural flow rates present in biologic environments. Hence, the magnetic forces must be high enough to exceed the forces exerted on the particles in the blood vessels. To probe the magnetic

¹²⁰ www.ibsmagnet.de

response in presence of additional fields, a flow field was applied. Following the procedure described above, 46 particles were monitored and analysed in presence of a flow field and an external magnetic field. The flow rate was chosen to be 10 $\mu\text{L}/\text{min}$ corresponding to an average velocity of $\langle v \rangle = 0.83$ mm/s inside the channel ($\langle v \rangle = \frac{\dot{V}}{Q}$ with flow rate \dot{V} and channel cross section Q). This value is comparable to velocities in brain capillaries reported in literature.¹²¹ The position plot and the resulting time-trace of one representative particle are illustrated in Figure 4.53. Under application of the flow field, a directed movement in x-direction was observed. After 50 seconds, an external magnetic field is applied which causes a distinct change in movement of the particles. The particles start to move in y-direction and hence, towards the highest field gradient of the magnetic field as described above. This clearly confirms that magnetic response is high enough to resist the solvent flow.

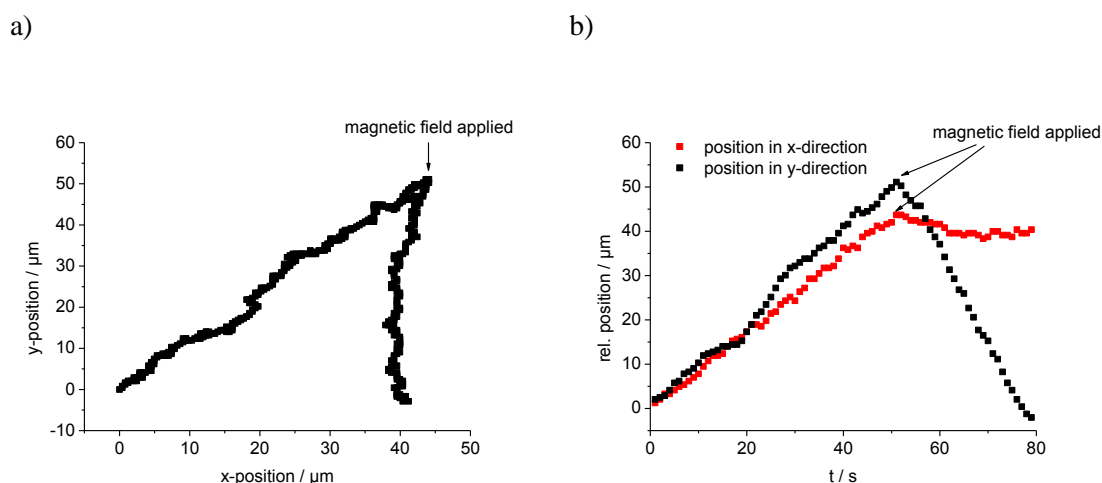


Figure 4.53 a) Position plot and b) time-trace of Rho-Fe_xO_y-I_{2.3%}@POS-PEG-II under application of external magnetic and/or flow fields (position along y-axis (black) and x-axis (red))

Based on the time-traces, a calculation of the forces acting on the magnetically loaded particles can be performed. In fluid media, two forces act on the magnetic nanoparticles: the magnetic force F_m which depends on the gradient of the applied magnetic field B and the Stokes Force or drag force F_S which results from the exerted viscous drag of the surrounding suspension medium on moving particles.¹²²

The magnetic force F_m on a magnetic particle in suspension can be calculated using the following equation:

¹²¹ Ivanov, K. P.; Kalinina, M. K.; Levkovich, Y. I. *Microvasc. Res.* **1981**, 22, 143

¹²² Shevkopyas, S. S.; Sigel, A. C.; Westervelt, R. M.; Prentiss, M. G.; Whitesides, G. M. *Lab Chip* **2007**, 7, 1294

$$F_m = \rho V \nabla (M_0 B) + \frac{V \chi_{particle}}{\mu_0} (B \nabla) B, \quad 4.2$$

with the density ρ and volume V of the particle, the initial magnetization M_0 (magnetization in absence of magnetic fields), the applied magnetic field B and the magnetic susceptibility $\chi_{particle}$. In case of superparamagnetic nanoparticles, an initial magnetization M_0 of zero can be assumed. Hence, Equation 4.2 becomes:

$$F_m = \frac{V \chi_{particle}}{\mu_0} (B \nabla) B \quad 4.3$$

Considering a one-dimensional magnetic field leads to

$$F_m = \frac{V \chi_{particle}}{\mu_0} B \frac{\partial B}{\partial x} \quad 4.4$$

Approximation of $B \frac{\partial B}{\partial x}$ resulted in

$$B \frac{\partial B}{\partial x} = \frac{1}{L} \left(\frac{B_r}{\pi} \right)^2 \quad 4.5$$

with the length of the magnet L and the material-specific remanent flux density B_r ($B_r = 0.7$ T for NeodymAlphaMagnets).¹²⁰ For detailed calculations see Appendix. As reported in literature, the magnetic susceptibility of the particles can be determined from the slope of the initial magnetization curve using the following relationship¹²²

$$\chi_{particle} = \frac{4\pi}{10^3} \rho \frac{\Delta M}{\Delta H}. \quad 4.6$$

Using 1.39 g/cm^3 as density of the magnetically loaded polyorganosiloxane nanoparticles as estimated in Chapter 4.2.2.2., the magnetic susceptibility was calculated to be 0.170 which fits well to results reported in literature for similar systems.¹²²

The drag force F_S is given by the Stokes Equation:

$$F_S = -6\pi\eta R_h v, \quad 4.7$$

with the viscosity of the suspension medium η , the hydrodynamic radius R_h and the velocity v of the particle. Based on the monitored time-traces, the forces acting on the particles were calculated using Equation 4.5 and 4.7. In agreement with procedures reported in literature, the complicated, heterogeneous structure of the magnetically loaded particles was neglected and the particles were treated as ideal magnetic dipoles.¹²² Neglecting the damping effect of the glass wall and considering a wall thickness of 0.1 mm, the magnetic force acting on the particles was determined to decrease from $5.1 \cdot 10^{-12}$ N at the lower wall of the flow cell (distance to magnetic surface: 0.5 mm) to approximately $4.9 \cdot 10^{-12}$ N at the upper wall of the flow cell (distance to magnetic surface: 0.6 mm) (Figure 4.54). Depending on the position of the particles in the flow cell, the particles are transported in different layers of the flow profile of the present laminar flow. Hence, different velocities lead to drag forces between $1.1 \cdot 10^{-15}$ N and $8.4 \cdot 10^{-15}$ N. In terms of energy the relations shown in Table 4.22 result. The calculated values confirm that the forces induced by the solvent flow and the magnetic field are strong enough to overcome the thermal energy kT . Additionally, the determined magnetic force exceeds the present drag force distinctively which explains the behavior of the particles in presence of the applied magnetic fields.

Table 4.22 Calculated energies of kinetic, drag and magnetic force acting on magnetic particles within the flow cell

force	energy / J
kinetic	$5.4 \cdot 10^{-21}$
F_{drag}	$1.1 \cdot 10^{-15} - 8.4 \cdot 10^{-15}$
F_m	$4.9 \cdot 10^{-12} - 5.1 \cdot 10^{-12}$

However, since the natural arterial flow rates are significantly higher (3 mm/s – 500 mm/s) than the fields applied here (approximately $1 \cdot 10^{-6}$ L/min), further experiments are necessary to prove the applicability of the particles in magnetic cell sorting or magnetic manipulation applications.¹²³ For further quantification of the magnetic response, computer simulations for example using the COMSOL Multiphysics model could be imagined. However, the results prove that the magnetic content is sufficient to allow for a magnetic manipulation in aqueous media even if an additional flow field is applied.

¹²³ Schmidt, R. F. *Physiologie des Menschen*, Springer 2007

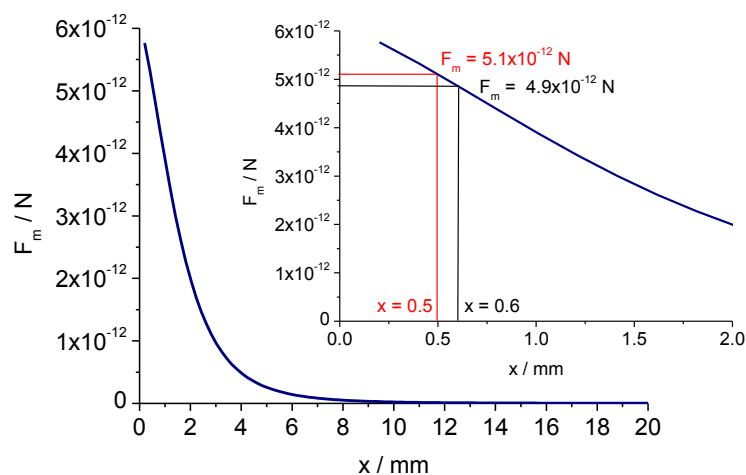


Figure 4.54 Distance-dependence of the magnetic force induced by a NdFeB magnetic (10 mm x 5 mm x 30 mm, 350 mT at surface); inset: enlargement of relevant area

4.2.3.4.3 Interactions with Biological Systems: Cell Testings

Cell testings are the fundamental method to investigate biocompatibility and cellular uptake of nanoparticles and other foreign materials. Various cell types and experimental setups are available to probe the interactions between nanoparticles and the biological system.¹²⁴

To probe the general behavior of the polyorganosiloxane nanoparticles in biological environment, ζ -potential and dynamic light scattering measurements were used. The particle behavior in cell medium is of major importance for the applicability of the particles in biomedical applications. The high salt concentrations in the cell medium can dramatically decrease the colloidal stability of the particles and thus, cause aggregation or sedimentation. The formation of aggregates hinders the cellular uptake of the particles and increases the probability of recognition by the RES which would lead to undesired elimination of the particles. The surface properties of Rho-Fe_xO_y-I_{2.3%}@POS-PEG-II in water and the cell medium RPMI1640 were compared. RPMI1640 is a serum free medium which consists of a buffer system containing amino acids, vitamins, inorganic salts and other components (for detailed information see Appendix). The terminal carboxyl groups of the surface attached PEG causes negative surface charges and therefore, negative ζ -potentials in aqueous solution. In cell medium, less negative ζ -potentials were measured due to screening effects caused by the high salt concentrations of the cell medium. However, due to the pH-value of the cell medium (pH = 7.4), the observation of negative values is reasonable. The particle sizes were determined to be 52.9 nm and 48.1 nm in water (1:10 diluted aqueous dispersion) and cell medium, respectively. The results confirm the colloidal stability of the particles in RPMI1640 medium which is a crucial factor for the applicability of the particles as

¹²⁴ Kroll, A.; Pillukat, M. H.; Hahn, D.; Schnekenburger, J. *Eur. J. Pharm. Biopharm.* **2009**, 72, 370

explained above.

Table 4.23 ζ -potentials of Rho-Fe_xO_y-I_{2.3%}@POS-PEG-II in different aqueous media ($c = 1.08$ g/L, pH(in H₂O) = 7-8), pH(in RPMI1640) = 7.4)

sample	ζ -potential / mV		R_h^* / nm	
	H ₂ O	RPMI1640	H ₂ O	RPMI1640
Rho-Fe _x O _y -I _{2.3%} @POS-PEG-II	-36.1	-16.5	52.9	48.1

*determined via dynamic light scattering

To probe the cellular uptake of the particles, fluorescence microscopy was used. Figure 4.55 shows a fluorescence image of ISO-HAS-1 cells after incubation with rhodamine-labeled particles. In all experiments, 100 μ L of nanoparticles solution ($c \approx 10$ g/L, 10 vol-% aqueous nanoparticles in cell medium) were added to the cell culture medium RPMI1640 containing the corresponding cell type. After 2 h of incubation, 5 μ L of fetal calf serum (FCS, 5 vol-% solution) was added and incubation was continued for 2 h. The nucleus of the cell was labeled with bisBenzimide H 33342 trihydrochloride to show bright blue fluorescence. The red fluorescence of the rhodamine-labeled particles is clearly visible. Even though self-quenching effects and partial degradation of the dye (as described in Chapter 4.2.3.4.1) cause a decrease of the fluorescence intensity of the investigated particles, the fluorescence is still sufficient to provide an efficient analysis in cell culture testings.

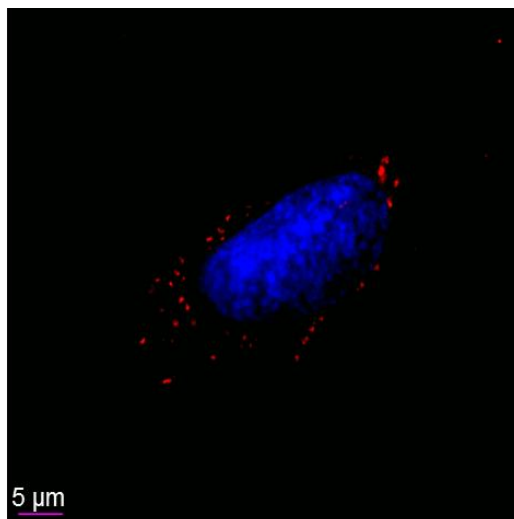


Figure 4.55 Fluorescence microscopic image of rhodamine-labeled particles (Rho-Fe_xO_y-I_{2.3%}@POS-PEG-II) in ISO-HAS-1 cells

The particle appearance close to the nucleus, indicate a successful cellular uptake. In case of non-encapsulated particles which could be located on top of the monitored cell for example, a distribution

covering the whole sample should occur. However, labeling of the cell membrane or the use of endosome markers is a more efficient method to prove cellular uptake. Nevertheless, in combination with toxicity test, a cellular uptake can be assumed since non-incorporated particles should not have significant effects on the viability or membrane integrity of the cells.

For investigations on the behavior of the particles inside the cells membrane integrity (lactate dehydrogenase (LDH) release) and for cytotoxicity viability (MTS) tests were performed. Both methods are sensitive to cytotoxic effects, although different parameters are investigated. The MTS assay is a calorimetric assay used to measure the activity of enzymes. The active compound is a tetrazolium based dye which is reduced to a colored formazan product by reductase enzymes in living cells. The amount of formazan product and hence, the absorbance at 490 nm, is directly proportional to the number of living cells.¹²⁵ LDH is a stable cytosolic enzyme which can be found in the cytoplasm of almost all kind of cells. Destruction of the cell due to damage or disintegration of the cell membrane leads to the release of LDH which is therefore an indication for cytotoxicity. A combination of different toxicity testings is necessary since various effects can cause cytotoxicity of polymeric materials.

Two different cell types were probed: the human lung adenocarcinoma cell line H441 which was purchased from ATCC, ATCC-HTB-174, Promochem, Germany and the human microvascular endothelial cell line, ISO-HAS-1.¹²⁶

Results of LDH release tests are shown in Figure 4.56. For comparison, untreated cells (control) and non-magnetically loaded particles of the same composition (HS114) were tested in addition. After 4 h of incubation, the LDH release is comparable and in the range of the control for both investigated polyorganosiloxane systems. After an incubation time of 4 h, the magnetically functionalized particles show a higher LDH release than the non-magnetically loaded particles. In case of small concentrations, the values are comparable and below the control. In H441 cells, a decreased LDH release after incubation with the magnetically loaded particles compared to non-magnetic particles is observed in case of low concentrations. For the H441 cells, the LDH release of particle concentrations below 150 µg/mL reveals low cytotoxicities. In case of ISO-HAS-1 cells even higher concentrations (300 µg/mL) can be applied without significant influences on the LDH release compared to the natural LDH release (control). Concluding, low cytotoxicities with respect to the membrane integrity were found for the magnetically loaded nanoparticles in the lower range of the investigated concentrations. Nevertheless, the applied concentrations are relatively high compared to studies reported in literature. It is important to keep in mind that the particle sizes and densities of the non-magnetically functionalized particles are smaller than the values determined for the magnetically loaded one. Hence, even if the same concentration is applied, the number of particles differs. However, promising results

¹²⁵ www.promega.com

¹²⁶ a) Masuzawa, M.; Fujimura, T.; Hamada, Y.; Fujita, Y.; Hara, H.; Nishiyama, S.; Katsuoka, K.; Tamauchi, H.; Sakurai, Y. *Int. J. Cancer* **1999**, *81*, 305; b) Unger, R.E.; Krump-Konvalinkova, V.; Peter, K.; Kirkpatrick, C. J. *Microvasc. Res.* **2002**, *64*, 384

are obtained regarding both, magnetically and non-magnetically loaded particles.

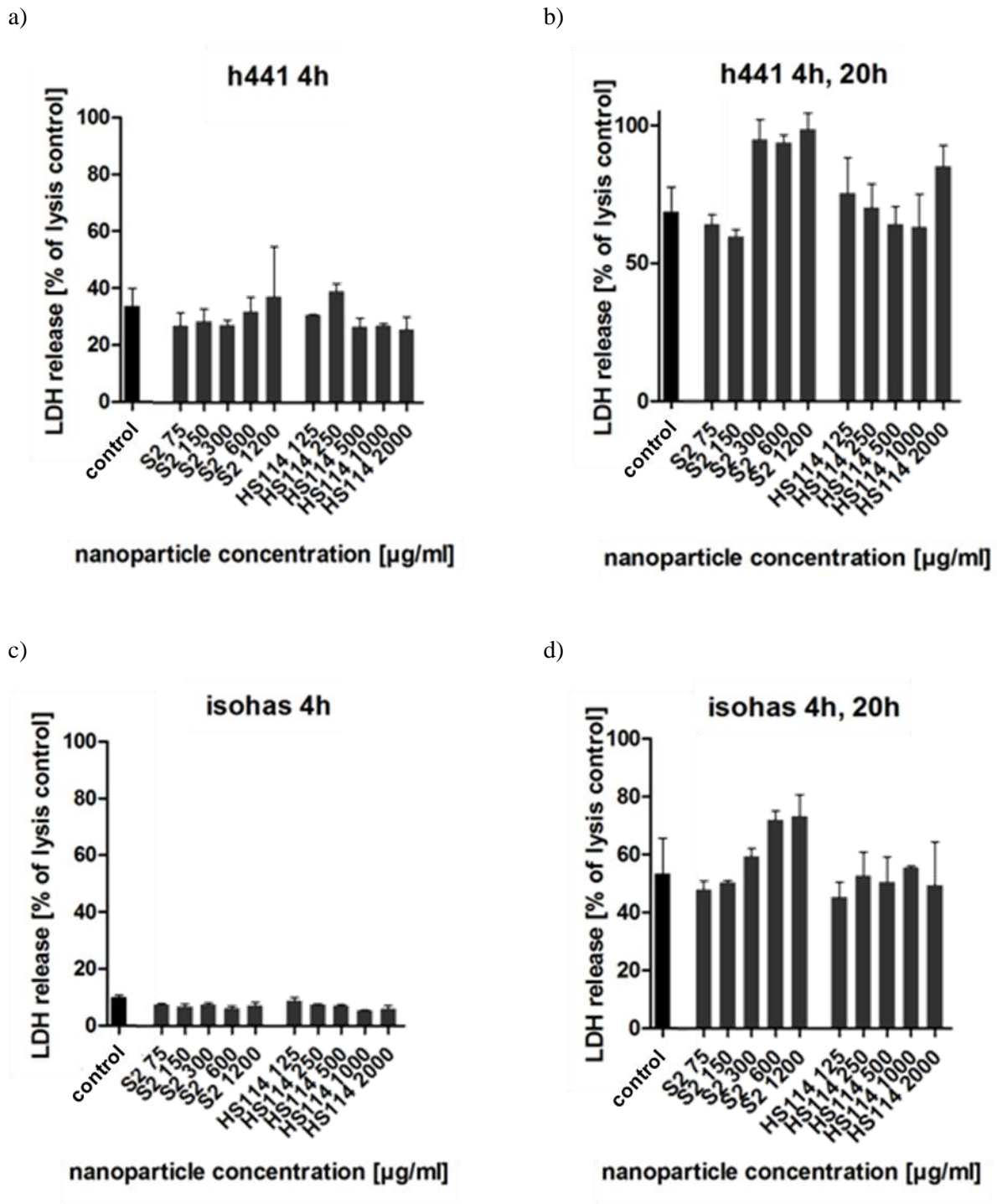
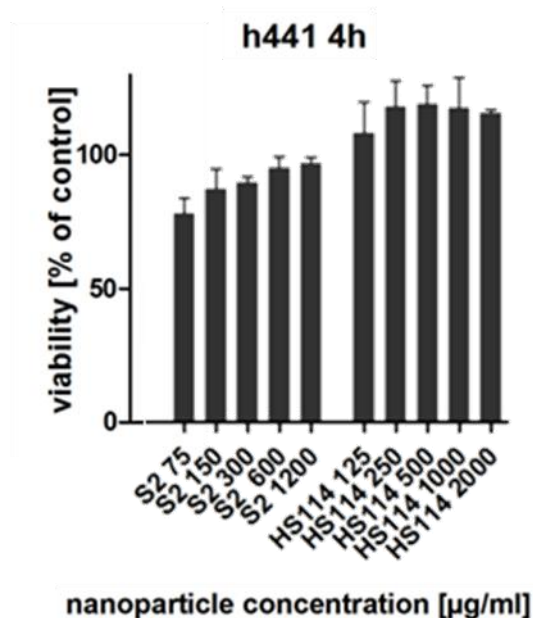


Figure 4.56 LDH release tests of a) h441 cells and b) iso-HAS cells after incubation with magnetically (S2) and non-magnetically (HS114) functionalized polyorganosiloxane nanoparticles measured after 4 hours (a)+c) and 20 hours (b)+d)) of incubation

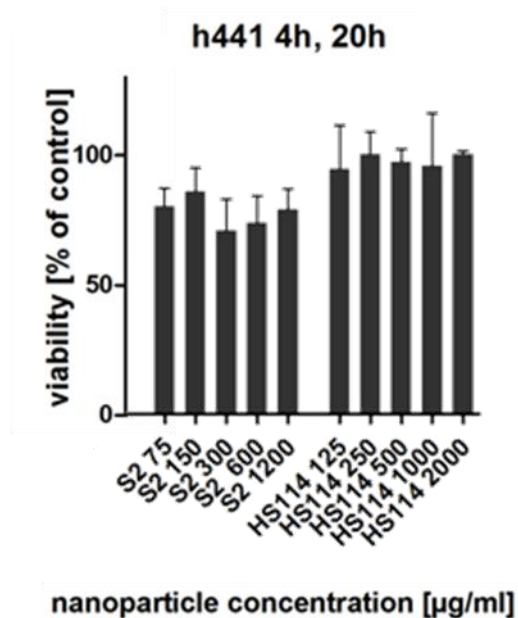
The results of the MTS viability tests are illustrated in Figure 4.57. For all investigated systems, the

viabilities of the magnetically loaded particles are slightly lower than the values determined for the non-magnetically loaded particles. However, the measured viabilities are still in a moderate range. Even if high sample concentrations (1200 $\mu\text{g/mL}$) are applied, cell viabilities above 75 % are obtained.

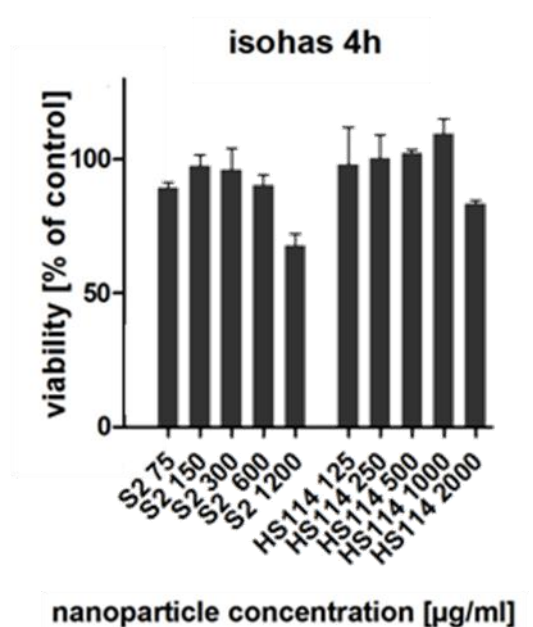
a)



b)



c)



d)

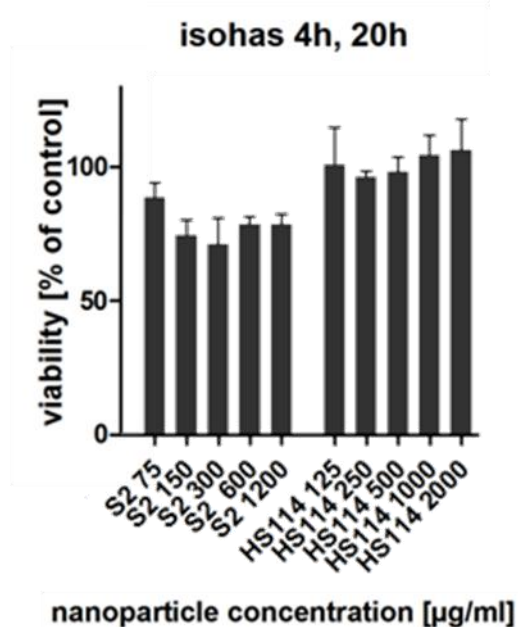


Figure 4.57 MTS viability testings using a)+b) H441 and c)+d) ISO-HAS cells after incubation with magnetically (S2) and non-magnetically (HS114) loaded nanoparticles monitored after 4 hours (a)+c) and 20 hours (b)+d)) of incubation

The LDH release tests revealed no significant difference between the membrane destruction induced

by the two investigated particle species in case of concentrations below 300 $\mu\text{g/mL}$. Nevertheless, the magnetically loaded particles show an increased effect on the cell viability compared to non-magnetically functionalized particles. Hence, even though the particles show a comparable influence on the membrane integrity, the magnetically functionalized particles cause a decrease in the cell viability compared to non-magnetically loaded particles. Besides the magnetic functionalization, the investigated particles differ in average particle size and density. These properties could influence the cellular uptake and toxicity of the particles. Nevertheless, further investigations on the particle uptake mechanism and distribution within the cells are necessary to evaluate the influences of the different parameters on the toxicity of the investigated systems.

In summary, the obtained results indicate a cellular uptake of magnetically loaded polyorganosiloxane nanoparticles into H441 and ISO-HAS cells. The fluorescence labeling via rhodamine-modified monomers was found to be efficient for an easy detection of the particles via fluorescence microscopy. The particles could easily be monitored due to the incorporated rhodamine molecules. LDH release and viability tests revealed slightly higher cytotoxicities compared to non-magnetically loaded particles. Nevertheless, cell viabilities above 75 % were found for both investigated cell types after incubation for 4 h. The magnetically loaded particles showed no effects on the membrane integrity in concentrations below 150 $\mu\text{g/mL}$ (H441) and 300 $\mu\text{g/mL}$ (ISO-HAS), respectively.

4.2.3.5 Biofunctionalization

4.2.3.5.1 Introduction

The biofunctionalization of nanomaterials is sufficient to increase the biocompatibility and allows for specific interactions with target molecules as well as a controlled cellular uptake as described in Chapter 2.2.5.3. The biofunctionalization of the magnetically loaded particles can be performed via amide formation between amine functionalized biomolecules and the free chain-end of the surface attached PEG molecules. A classic linking reaction is the EDC induced coupling.⁶⁴ The reaction was carried out in buffer solution (MES-buffer, 50 mM, pH = 4-5) at room temperature. The reaction mixture was stirred overnight and dialysed against water to remove residual biomolecules. Two different functionalizations were probed: biotinylation and insulin functionalization of fluorescein-labeled particles carrying a magnetic content of 2.3 wt-% Fe_xO_y -I. Since biotin shows a strong specific binding to streptavidin, biotin-modified nanomaterials are commonly used to study interactions between target molecules like streptavidin labeled cells or oligonucleotides. The surface functionalization with insulin was reported to hinder the cellular uptake of nanoparticles.¹²⁷ This effect could potentially be used in cell sorting or separation methods wherein the irreversible cellular uptake is supposed to complicate the subsequent analysis of the target objects and thus, is undesired. To monitor the success of the coupling reactions ζ -potential measurements were used. The biotinylated

¹²⁷ Gupta, A. K.; Berry, C.; Gupta, M.; Curtis, A. *IEEE T. Nanobiosci.* **2003**, 2, 255

sample was additionally analysed using the HABA/Avidin complex which shows a characteristic UV/VIS absorption in the presence of biotin. A schematic illustration of biofunctionalized magnetofluorescent polyorganosiloxane nanoparticles is illustrated in Figure 4.58.

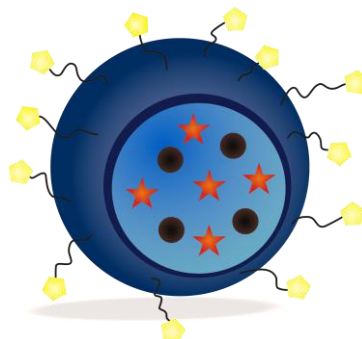


Figure 4.58 Schematic illustration of biomodified, magnetofluorescent polyorganosiloxane nanoparticles

4.2.3.5.2 Biotinylation of Flu-Fe_xO_y-I_{2.3%}@POS-PEG-II

Biotin, also known as vitamin H, is a water-soluble vitamin that plays an important role in human metabolism. As prosthetic group in several carboxylases, it is responsible for carbon dioxide transfer. Biotin shows a basic character due to the presence of the ureido carbonyl group. Although a protonation of the thioether is possible, it is reported in literature that the sulphur atom plays no significant role in the enzymatic carboxylation reaction.¹²⁸ Biotin has a high specific affinity to avidin or streptavidin. The biotin/streptavidin bond is one of the strongest non-covalent bonds found in biological systems. The specific interaction between biotin and streptavidin is a valuable model system for specific binding or targeting experiments.⁶³ Various biotinylation reactants are available. Typically, a spacer is attached to the biotin molecule via an amide formation between the carboxyl group of the biotin and the amine functionalized spacer. By varying the terminal group of the spacer, biotin molecules carrying various functionalities can be synthesized. In this work, an amine functionalized biotinylation reactant (EZ-Link Pentylamine-Biotin: 5-biotinamidopentylamine) was used to synthesize biotinylated polyorganosiloxane nanospheres (Flu-Fe_xO_y-I_{2.3%}@POS-PEG-II-Biotin) via EDC coupling as shown in Figure 4.59. Addition of EDC to the carboxyl group of the surface attached PEG leads to an activation of the acidic group which eases the following coupling reaction. Residual or unbound biotin was removed via dialysis. For comparison, a blank sample was prepared. In this case, the biotinylation reactant was added to the polyorganosiloxane nanoparticles solution without EDC addition (Flu-Fe_xO_y-I_{2.3%}@POS-PEG-II + Biotin). Therefore, no coupling should take place and a complete removal of the biotin molecules via dialysis should be possible.

¹²⁸ a) Caplow, M. *Biochemistry* **1969**, *8*, 2656; b) Bowen, C. E.; Rauscher, E.; Ingraham, L. L. *Arch. Biochem. Biophys.* **1968**, *125*, 865

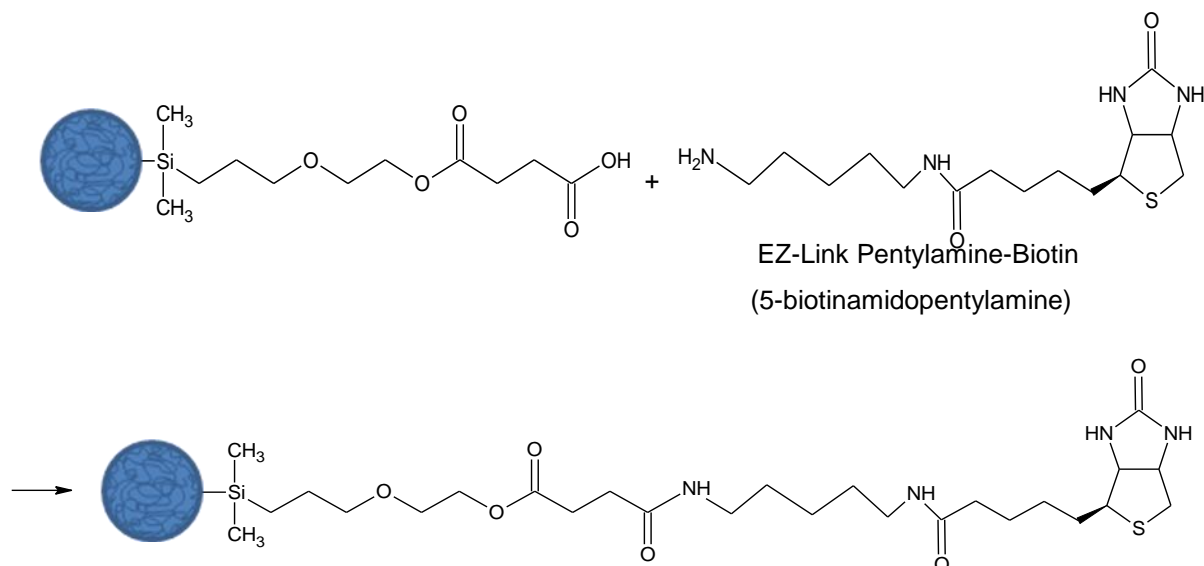


Figure 4.59 Schematic illustration of biotinylation of polyorganosiloxane nanoparticles

Typically, a HABA/Avidin complex is used for the analysis of biotinylated products. The HABA/Avidin complex shows an intensive orange color. In presence of biotin molecules the HABA dye is displaced by biotin due to its high affinity to avidin. A decrease of the absorption peak at 500 nm (A_{500}) results. Figure 4.60 shows the absorption spectra of the HABA/Avidin complex in presence of different samples. As expected, the addition of pure pentylamine biotin, which was used as biotinylation reactant, causes a drastic decrease in A_{500} . In case of a mixture containing Flu- $\text{Fe}_x\text{O}_y\text{-I}_{2.3\%}\text{@POS}$ and the biotinylation reactant pentylamine biotin (Flu- $\text{Fe}_x\text{O}_y\text{-I}_{2.3\%}\text{@POS-PEG-II} + \text{Biotin}$), no change in the absorption was detected. This proves that no adsorption of biotin onto the polyorganosiloxane surface occurs and residual or unbound biotin can completely be removed via dialysis. Addition of the biotinylated sample Flu- $\text{Fe}_x\text{O}_y\text{-I}_{2.3\%}\text{@POS-PEG-II-Biotin}$ leads to a decreased absorption. This result indicates the success of the coupling reaction as biotin groups bind to avidin. It could be shown that unbound biotin can be removed via dialysis meaning that the decrease in the adsorption peak after addition of Flu- $\text{Fe}_x\text{O}_y\text{-I}_{2.3\%}\text{@POS-PEG-II-Biotin}$ results from covalently bound biotin.

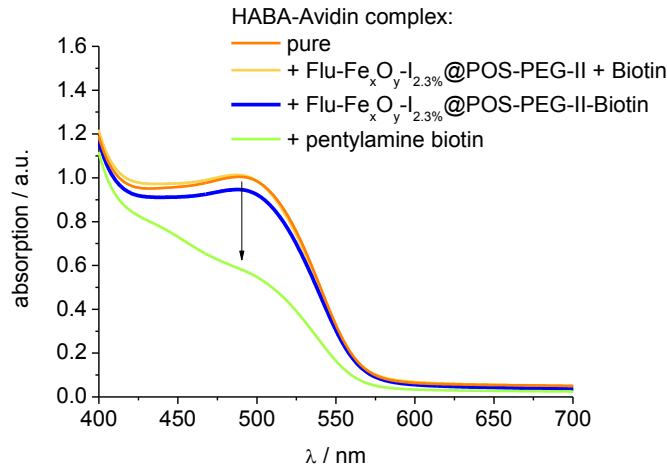


Figure 4.60 Absorption spectra of polyorganosiloxane nanoparticles before ($\text{Flu-Fe}_x\text{O}_y\text{-I}_{2.3\%}\text{@POS-PEG-II}$) and after biotinylation ($\text{Flu-Fe}_x\text{O}_y\text{-I}_{2.3\%}\text{@POS-PEG-II-Biotin}$) as well as $\text{Flu-Fe}_x\text{O}_y\text{-I}_{2.3\%}\text{@POS}$ /pentylamine biotin mixture ($\text{Flu-Fe}_x\text{O}_y\text{-I}_{2.3\%}\text{@POS-PEG-II + Biotin}$)

Characterizations via gel electrophoresis measurements which are commonly used for the analysis of surface modification processes was not possible (Agarose gel, 0.3 %). However, the success of the coupling reaction can also be monitored via ζ -potential measurements. The carboxyl groups of the PEG polymer cause a negative ζ -potential due to the dehydrogenation in neutral and basic media. After attachment of the biotin, a positive ζ -potential is observed which can be attributed to the basic character of biotin. For the reference system ($\text{Flu-Fe}_x\text{O}_y\text{-I}_{2.3\%}\text{@POS-PEG-II + Biotin}$) a negative ζ -potential was determined which proves that no coupling or adsorption takes place in absence of EDC. These results confirm the conclusions of the HABA/Avidin experiments.

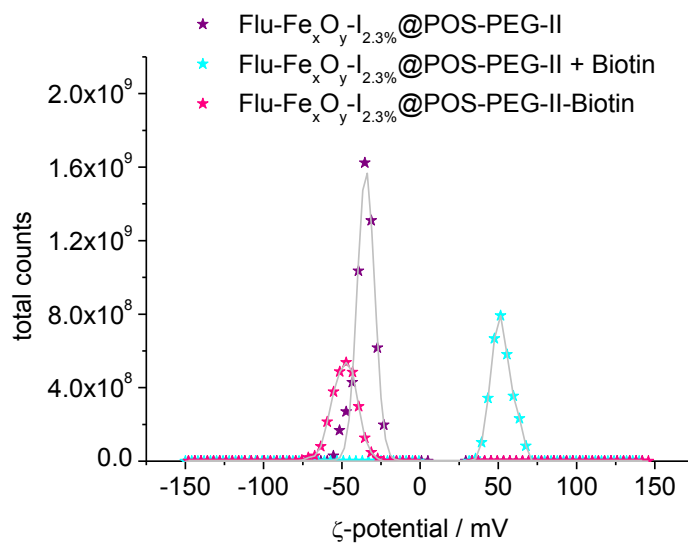


Figure 4.61 ζ -potential measurements of polyorganosiloxane nanoparticles in aqueous dispersion ($c \approx 10$ g/L) before ($\text{Flu-Fe}_x\text{O}_y\text{-I}_{2.3\%}\text{@POS-PEG-II}$) and after biotinylation ($\text{Flu-Fe}_x\text{O}_y\text{-I}_{2.3\%}\text{@POS-PEG-II-Biotin}$) as well as $\text{Flu-Fe}_x\text{O}_y\text{-I}_{2.3\%}\text{@POS-PEG}$ /pentylamine biotin mixture ($\text{Flu-Fe}_x\text{O}_y\text{-I}_{2.3\%}\text{@POS-PEG-II + Biotin}$)

Dynamic light scattering measurements of the sample Flu-Fe_xO_yI_{2.3%}@POS-PEG-II before and after biomodification reveal a slight increase in the hydrodynamic radius after the EDC induced coupling reaction. As explained before, the light scattering measurements of the PEGylated samples seem to be strongly influenced by interparticular interactions between the PEG chains which lead to extraordinary high particle radii (additional filtration shows no effect on the light scattering data). The biotinylated sample shows a comparable average radius which indicates the presence of large aggregates or particle-particle interactions. These aggregates can be separated via further filtration of the sample resulting in an average particle radius of 98 nm for the biotinylated sample. This value is still comparatively high meaning that the presence of smaller aggregates cannot be excluded. Nevertheless, the obtained radii are still in an adequate range regarding potential biomedical *in vivo* and *in vitro* applications.

Table 4.24 Hydrodynamic particle radii of Flu-Fe_xO_y-I_{2.3%}@POS-PEG-II before and after biotin coupling determined via DLS in aqueous dispersion ($c \approx 10$ g/L)

sample	R _h / nm
Flu-Fe _x O _y -I _{2.3%} @POS-PEG-II	144.5
Flu-Fe _x O _y -I _{2.3%} @POS-PEG-II-Biotin	182.0
Flu-Fe _x O _y -I _{2.3%} @POS-PEG-II-Biotin*	98.0

after additional filtration using HV450 nm

Cell testings were performed in analogy to the procedure described above for the PEGylated particles. In case of the biotin labelled particles, no satisfying results were obtained, since the fluorescence of the incorporated fluorescein molecules was too weak for an adequate detection. To obtain useful information, a biotin functionalization of rhodamine-labeled particles has to be performed which is ongoing research at the moment.

Concluding, biomodification of the PEGylated nanoparticles was achieved via EDC coupling with biotin. The success of the coupling reaction was shown using a HABA/Avidin complex and ζ -potential measurements. These results confirm that the carboxyl chain-end of the PEG chains attached to the polyorganosiloxane surface provides the possibility of an additional functionalization. Hence, the aspired high flexibility of the system was achieved, not only regarding fluorescent core and hydrophilic surface modification. An effortless and effective biofunctionalization can be performed. The resulting system offers a multitude of advantageous properties like fluorescent labeling, biocompatibility and specific binding sites. This flexibility towards independent functionalization in combination with the magnetic loading of the polyorganosiloxane nanoparticles makes them encouraging materials for a broad range of biomedical applications including cell sorting and separation, targeted drug delivery and hyperthermia. In order to clarify the multiplicity of the

functionalizability, an alternative biomodification is discussed in the following section.

4.2.3.5.3 Insulin-Functionalization of Flu-Fe_xO_y-I_{2.3%}@POS-PEG-II

Insulin belongs to the class of peptide hormones. It plays an important role in regulation of human carbohydrate and fat metabolism.¹²⁹ It is especially well-known for its blood sugar reducing function. In literature, it is reported that insulin-coated nanoparticles specifically attach to the cell expressed surface receptors of the human fibroblasts which leads to a prevention of endocytosis.¹²⁷ This effect could be useful for cell sorting applications which aim to prevent endocytosis in order to avoid a disturbance of subsequent analysis of the target cells. The EDC induced coupling uses the terminal amino-functionality of the insulin to generate an amide bond between the insulin and the carboxyl-functionalized polyorganosiloxane nanoparticles as discussed before for the biotinylation. For comparison a mixture of insulin and polyorganosiloxane nanoparticles was prepared in absence of the coupling agent EDC. The coupling process was monitored via ζ -potential measurements since gel electrophoresis analysis was not adequate. The ζ -potential measurements of the particles before and after insulin-coupling are illustrated in Figure 4.62.

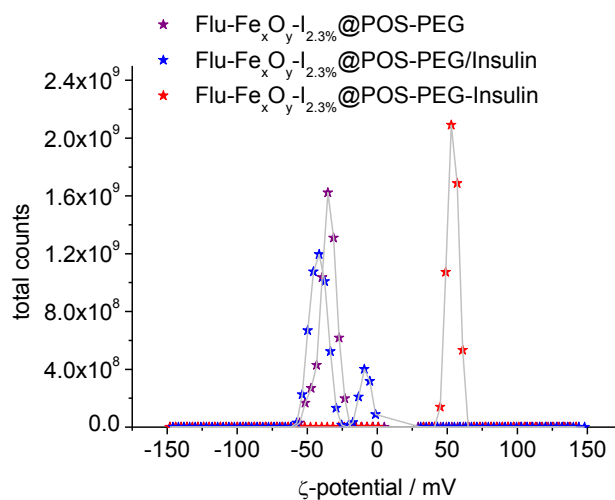


Figure 4.62 ζ -potential measurements of fluorescein-labeled particles in aqueous dispersion ($c \approx 10$ g/L) before (Flu-Fe_xO_y-I_{2.3%}@POS-PEG-II) and after insulin coupling (Flu-Fe_xO_y-I_{2.3%}@POS-PEG-II-Insulin) as well as Flu-Fe_xO_y-I_{2.3%}@POS /Insulin mixture (Flu-Fe_xO_y-I_{2.3%}@POS-PEG-II + Insulin)

The spectra indicate the success of the coupling reaction: The initially negatively charged PEGylated polyorganosiloxane nanoparticles show a positive ζ -potential after the coupling reaction. The mixture of polyorganosiloxane particles and insulin (prepared without EDC addition) shows two peaks. The negative potential of the PEGylated siloxane particles is clearly visible. The additional peak can be attributed to an adsorption of insulin to the particle surface which causes a compensation of the surface charges and induces partial aggregation and sedimentation, respectively. Thus, a ζ -potential of

¹²⁹ Forth, W. *Allgemeine und spezielle Pharmakologie und Toxikologie*, 9ed., Elsevier, 2005

approximately zero is observed. Nevertheless, a successful coupling of insulin to the polyorganosiloxane nanoparticles was achieved in presence of EDC.

As described above, the fluorescence intensity of the fluorescein-labeled particles was too weak to allow for an adequate detection in cell testings. Hence, insulin functionalization of rhodamin-labeled particles becomes mandatory to investigate the cellular uptake and toxicity of the particles

Particle size analysis via dynamic light scattering revealed the presence of large aggregates after the insulin-modification. The hydrodynamic radii were determined to increase from 144.5 nm to approximately 300.0 nm after the EDC-mediated coupling reaction. This result is in good agreement with the ζ -potential measurements which indicate a partial adsorption of insulin to the particle surface which could give rise to potential bridging effects and hence aggregation.

Table 4.25 Hydrodynamic particle radii of Flu-Fe_xO_y-I_{2.3%}@POS-PEG-II before and after insulin coupling determined via DLS in aqueous dispersion ($c \approx 10$ g/L)

sample	R _h / nm
Flu-Fe _x O _y -I _{2.3%} @POS-PEG-II	144.5
Flu-Fe _x O _y -I _{2.3%} @POS-PEG-II-Insulin	300.0

In summary, insulin functionalized magnetofluorescent polyorganosiloxane nanoparticles were synthesized via an EDC assisted coupling reaction. Since an insulin-coating is reported to prevent endocytosis, the synthesized particles are potential candidates for cell sorting applications which aim to avoid a cellular uptake of the magnetic beads used for separation. The results of the last two sections prove that the heterofunctional PEG surface coating in combination with EDC coupling is an effective approach to generate biofunctionalized nanoparticles with a high flexibility regarding the choice of the biological material.

4.2.3.6 Summary

Multifunctional magnetically loaded polyorganosiloxane nanoparticles were synthesized. The core-shell architecture of the polyorganosiloxane system offers the possibility of independent core and surface modification. Fluorescent labeling was achieved by incorporation of dye-labeled monomers into the core of the siloxane system. The labeling was probed using three monomers carrying fluorescein, rhodamine or coumarin functionalities. Highly fluorescent particles were obtained. Fluorescein and rhodamine-labeling did not affect the particle sizes compared to non-fluorescent particles. In case of coumarin-labeling larger particles with a broad size distribution and the tendency to aggregation were formed. The influence on the particle size distribution most probably results from the poor solubility of the coumarin modified monomer in the silane mixture used to generate the

polyorganosiloxane core. DBS, acting as stabilizing agent for the growing polyorganosiloxane network, adsorbs onto the insoluble material. Hence, the DBS available for the stabilization of the polyorganosiloxane nanoparticles is reduced and larger particles result. The dye labeling process slightly decreases the encapsulation efficiency of the iron oxide nanoparticles which can probably be traced back to impurities like 18-crown-6 ether in the dye labeled monomers. Adsorption of the crown ether onto the iron oxide surface could decrease the interaction between the magnetic nanoparticles and the silane monomers and thus, decrease the encapsulation efficiency. The particle surface was further modified via a grafting onto process of heterofunctional poly(ethylene glycol) (allyl-PEG-carboxyl) using a hydrosilation reaction. The PEG molecules are sufficient to provide water-solubility and biocompatibility of the polyorganosiloxane nanoparticles. Via combination of core and surface modification water-soluble magnetofluorescent particles were obtained. However, the grafting process significantly decreased the fluorescent properties of the incorporated dyes. This effect can possibly be attributed to quenching caused by the platinum catalyst used in the hydrosilation reaction. The rhodamine-labeled samples were found to be least susceptible to quenching effects. The use of heterofunctional PEG also allows for a further modification via amide formation between the free carboxyl chain end and amine functionalized biomolecules. Biotin and insulin functionalization of the magnetofluorescent polyorganosiloxane nanoparticles was successfully achieved via EDC coupling. Via biofunctionalization, the compatibility of the particles with biological systems can be increased and specific binding sites are provided. This offers the possibility of specific interactions between the polymeric particles and target systems which is an important requirement for magnetic cell sorting applications. Specific binding can also be combined with drug delivery applications in order to provide controlled distribution and targeting of the nanocontainers. Hence, undesired side effects and distribution can be decreased. Cell testings using endothelial lung cells (ISO-HAS-1) and H441 cells revealed relatively low cytotoxicities and cellular uptake of the PEG coated particles. The fluorescent labeling allows for an easy detection of the particles inside the cells. This proves the applicability of the magnetically loaded polyorganosiloxane nanoparticles in biomedicine.

In summary, a versatile polymeric system was generated. The incorporation of magnetic nanoparticles in combination with independent core and surface modification of the polymeric network system offers an immense field of possible applications. Besides contrast enhancement and imaging approaches, drug delivery and hyperthermia can be envisioned as imaginable applications. The independent core and surface modifications allows for a high flexibility. Hence, the system can effortlessly be adjusted to the desired application. The synthesized nanoparticles provide various qualifications for the use in biomedical applications like low cytotoxicity, the possibility of magnetic manipulation and fluorescent detection as well as specific binding sites via surface attached biomolecules. Hence, magnetically loaded nanoparticles

5 Conclusions and Outlook

5.1 Conclusion

Polyorganosiloxane nanoparticles can be synthesized via polycondensation of silane monomers in aqueous dispersion. The formation of core-shell architectures using functional monomers offers a broad range of modifications including independent core and surface functionalization. Hence, a highly flexible system is obtained which offers many qualifications for a potential use in biomedical applications.

In this work, the synthesis of multifunctional polyorganosiloxane core-shell particles carrying additional magnetic moieties was successfully demonstrated. Magnetic iron oxide nanoparticles were synthesized via a coprecipitation process of iron(II)- and iron(III)-chloride in basic solution. The resulting nanoparticles contained both magnetic iron oxides, magnetite and maghemite, and were stabilized via electrostatic interactions and formed stable aqueous dispersions. The influence of the coprecipitation medium and the ratio between the iron chlorides on size, composition, magnetic and surface properties of the resulting particles was investigated. The application of a Fe(II):Fe(III) ratio of 1:2 as well as the use of ammonium solution as precipitation media resulted in an increased particle size. Hydrodynamic radii were determined to vary between 3.2 nm and 9.1 nm. All particles showed superparamagnetic behaviour with saturation magnetizations between 37.3 emu/g and 50.7 emu/g.

The synthesized particles were successfully incorporated into a polyorganosiloxane core-shell system during the condensation reaction of silane monomers in aqueous dispersion in a quasi-admicellar polymerization. The highly magnetically loaded nanocontainers provided the opportunity of multicompartment functionalizations.

The encapsulation efficiency was found to strongly depend on the size of the iron oxide nanoparticles. The smallest representative of the synthesized iron oxides ($R_h = 3.2$ nm) could be encapsulated in a highly efficient process (encapsulation efficiency: 92 % relative to offered amount of iron oxide). The magnetically loaded nanocontainers showed particle radii below 80 nm dependent on the magnetic iron oxide content (up to 4.6 wt-%). The incorporation of larger iron oxide nanoparticles ($R_h = 5.6$ nm and 9.1 nm) was found to be less efficient. Encapsulation efficiencies below 60 % were revealed.

Highly fluorescent, magnetically loaded polyorganosiloxane nanoparticles were synthesized via incorporation of dye-labeled monomers into the core of the polyorganosiloxane core-shell system. The use of dye-labeled monomers resulted in a decrease of the encapsulation efficiency of the magnetic

material which can be attributed to impurities and poor solubilities of the dye-labeled monomer which hinder the encapsulation process.

Biocompatible, water-soluble magnetically loaded polyorganosiloxane nanoparticles were synthesized via hydrophilic surface modification using heterofunctional poly(ethylene glycol). The PEG chains were covalently bond to the polyorganosiloxane surface via a grafting onto process resulting in hydrodynamic particle radii of approximately 30 nm.

A combination of core and surface functionalization lead to biocompatible, magnetofluorescent particles which showed a high colloidal stability in aqueous media, including buffers and cell media. The fluorescent properties of the samples were found to be distinctively decreased compared to non-PEGylated particles due to degradation of the dyes during the grafting process. Via fluorescence microscopy, the particle behavior in aqueous solution was investigated. This straightforward visualization of the superparamagnetic properties proved a magnetic response in presence of external flow fields (flow rate: 0.83 mm/s) which is specifically important for a potential use in magnetically guided *in vivo* applications. Cellular testings indicated a cellular uptake of the particles into endothelial lung cells and revealed low cytotoxicities.

Additionally, the surface grafted heterofunctional PEG allowed for an additional biomodification via EDC coupling of biotin and insulin. The described biofunctionalization allows for a potential use in targeting applications for example using the specific interactions between biotin and streptavidin/avidin and investigations on a controlled cellular uptake due to the different recognition of surface groups via cell membranes and membrane receptors.

Concluding, a highly flexible system which provides the opportunity of several independent functionalizations was synthesized. The presented polyorganosiloxane nanoparticles provide various qualifications which make them promising candidates for biomedical applications, including

- superparamagnetic properties
- fluorescence-labeling
- colloidal stability in aqueous media
- biocompatibility and low cytotoxicity
- specific binding sites.

A broad range of possible applications covering diagnostic, analytic and therapeutic approaches like contrast enhancement, labeling and imaging, magnetic cell sorting, hyperthermia and drug delivery can be envisioned.

5.2 Outlook

The presented nanoparticles offer excellent properties for a potential use in biomedical applications. The general applicability was already proved via cell testings including cellular uptake and cytotoxicity; however, further investigations on the behavior in biological environment are mandatory. The cellular uptake and cytotoxicity of the particles in dependence on surface functionalization and cell types should be probed. This issue is aim of an ongoing cooperation with Prof. Dr. C. James Kirkpatrick and Prof. Dr. Roland Stauber from the “University Medical Center” of the Johannes Gutenberg-Universität Mainz. *In vivo* analysis via magnet resonance imaging is another interesting topic. Furthermore, *in vitro* applications like magnetic cell sorting or separation methods could be probed. The particles could potentially be used as magnetic beads in lab-on-a-chip or μ -total analysis systems (μ -TAS).

Additionally, an enhancement of the reaction conditions should be topic of future works. Especially, the incorporation of larger iron oxide amounts and further investigations on the encapsulation process are scientifically interesting. For example, the effect of different surfactant concentrations should be tested. Higher surfactant concentrations should be sufficient to hinder the occurring instabilities of the dispersion in presence of higher iron oxide amounts. Nevertheless, an additional effect on the particle size of the resulting polyorganosiloxane nanoparticles has to be taken into account. The dye-labeling was found to be sufficient for the detection of the particles in cell testings; however, due to the occurring quenching effects, the incorporation of quantum dots which are generally less susceptible to environmental influences like quenching should be considered. The hydrosilation reaction which was used for the grafting of poly(ethylene glycol) to the particles surface generally yields low quantities of water-soluble material. Additionally, the requirement of a platinum catalyst involves several disadvantages. Besides the probability of quenching effects, the high cytotoxicity of platinum compounds makes them an unsatisfactory choice. A promising alternative to the hydrosilation reaction is click-chemistry. Using Diethynyltetramethyldisiloxane (M-Ac) instead of Tetramethyldisiloxane (M-H) as end-capping agent would result in an acetylene functionalized surface. Commercially available azide functionalized poly(ethylene glycol) could then be covalently bond to the surface via 1,3-dipolar cycloaddition.

The encapsulation of different magnetic materials like highly magnetic cobalt or nickel particles would also be an interesting continuation of this work.

6 Materials and Methods

6.1 Materials

Water was purified with a milliQ deionizing system (Waters, Germany). All chemicals were used as received: diethoxydimethylsilane (D), trimethoxymethylsilane (T), ethoxytrimethylsilane (M), dodecyl benzenesulfonic acid (DBS) (Wacker Chemie), (p-chloromethylphenyl)trimethoxysilane (ClBz-T) (ABCR, Germany), EZ-Link Pentylamine-Biotin: 5-biotinamidopentylamine (Pierce) all other chemicals were purchased from Sigma-Aldrich. Magnetic separation columns were received from Miltenyi Biotec, magnets were purchased from www.magnet-shop.net.

6.1.1 Synthesis of Magnetic Iron Oxide Nanoparticles

Magnetic iron oxide nanoparticles (Fe_xO_y -I) were synthesized by coprecipitation of Fe(III)- and Fe(II)-salts in NaOH solution as reported elsewhere.¹³⁰ Briefly, an aqueous solution of $\text{FeCl}_3 \cdot 6 \text{H}_2\text{O}$ (0.1 M) and $\text{FeCl}_2 \cdot 4 \text{H}_2\text{O}$ (0.1 M) was added dropwise to 50 mL of alkaline solution (1 M NaOH) under vigorous stirring for 30 min at room temperature. The black precipitate was washed three times with water and collected by centrifugation. After addition of HCl solution (0.1 mL, 37 %) a stable aqueous dispersion was obtained. After drying, 0.7 – 1.7 g of dark brown powder was obtained.

6.1.2 Encapsulation of Magnetic Nanoparticles into Polyorganosiloxane System

The premixed monomers D, T and ClBz-T (Table 6.1) were added dropwise to a solution of 125 g water, the surfactant/catalyst dodecyl benzenesulfonic acid (DBS) (1.53 mmol) and the iron oxide nanoparticles through a syringe pump (15 mL/h) under continuous mechanical stirring at room temperature. The solution was stirred for 1 week before the monomer mixture for the shell was added dropwise (10 mL/h). After additional stirring for three days the dispersion was filtered before the end-capping was performed.

The bare polyorganosiloxane nanospheres were synthesized in an equivalent way and with the same amounts of monomers without addition of the iron oxide nanoparticles to the aqueous dispersion.

¹³⁰ Mikhaylova, M.; Kim, D. K.; Bobrysheva, N.; Osmolowsky, M.; Semenov, V.; Tsakalakos, T.; Muhammed, M. *Langmuir* **2004**, *20*, 2472

Table 6.1 Amount of monomer D, T and ClBz-T used in each step of the synthesis

	D / g	T / g	ClBz-T / g
core	5.0	7.0	3.0
shell	3.0	7.0	-

6.1.2.1 End Capping Process

To prevent particles from aggregation free SiOH groups were end capped by addition of 2.5 g of ethoxytrimethylsilane (M) to 12.5 g of the dispersion and stirred overnight. Afterwards, 1.25 g of M were added and stirring was continued for 5 h. The dispersion was destabilized by precipitation in 150 mL methanol and centrifuged. The precipitate was dissolved in 50 mL of toluene and residual methanol and water were removed by rotary evaporation at 40 °C in vacuum. 0.8 g of M were added to the remaining solution which was precipitated into 400 mL of methanol after stirring over night. The precipitate was collected by centrifugation. This yielded 0.8 – 1.0 g of brown powder.

6.1.2.2 Magnetic Separation

In a typical procedure, 1.0 g of nanospheres was dissolved in toluene and filtered through a commercially available magnetic separation column (Miltenyi Biotec: MACS[®] separation columns) under application of an external magnetic field (arrangement of several neodymium ring magnets (NdFeB) with magnetizations between 100 and 300 mT). Several washing steps were performed to rinse out the non-retained particles.

6.1.3 Magnetofluorescent Polyorganosiloxane Nanoparticles

For the synthesis of fluorescent labeled magnetically loaded polyorganosiloxane nanoparticles, the core monomer ClBz-T was partially substituted by a dye labeled monomer. The dye labeling of the monomers was performed via substitution reaction of the chloro atom of the ClBz-T monomer.

6.1.3.1 Fluorescent labeling of ClBz-T (DyeBz-T)

The dye labeled monomers were synthesized by O. Koshkina as reported in her diploma thesis.⁸⁷ Briefly, 1 equivalent cesium salt of dye, 3 equivalent ClBz-T, CsI and 18-crown-6 ether were dissolved in 140 mL THF (Table). After stirring for two days under argon atmosphere and exclusion of light, the solvent was removed in vacuum. The residue was dissolved in dichloromethane, washed with water and dried using magnesium sulfate. After evaporation of the solvent, purple (Rho-Bz-T: Rhodamine-(p-trimethoxysilyl)-benzylester), respectively orange (Flu-Bz-T: Fluorescein-(p-trimethoxysilyl)-benzylester) oil were obtained.

Dye-Bz-T	reaction batch
Rhodamine-(p-trimethoxysilyl)-benzylester),	4.05 g Cesium salt of Rhodamine B 1.4 mL 18-crown-6 ether 4.87 g ClBz-T 1.79 g CsI
Fluorescein-(p-trimethoxysilyl)-benzylester)	2.21 g Cesium salt of Fluorescein 1.0 mL 18-crown-6 ether 3.63 g ClBz-T 1.30 g CsI

6.1.3.2 Magnetofluorescent Polyorganosiloxane Nanoparticles (Dye-Fe_xO_y-I@POS)

The premixed monomers D, T and DyeBz-T were added dropwise through a syringe pump (15 mL/h) to a solution of 125 g of water, the surfactant/catalyst dodecyl benzenesulfonic acid (DBS) (1.53 mmol) and the iron oxide nanoparticles under continuous mechanical stirring at room temperature. The solution was stirred for 1 week before the monomer mixture for the shell was added dropwise (10 mL/h). Since a subsequent surface modification was desired, the additional monomer T-H was used for the formation of the shell (Table 6.2). After additional stirring for three days the dispersion was filtered before the end-capping was performed.

Table 6.2 Amount of monomer D, T, ClBz-T, Dye-Bz-T and T-H used in each step of the synthesis

sample		D / g	T / g	DyeBz-T / g	DyeBz-T / g	T-H / g
Flu-Fe _x O _y -I _{2.3%} @POS	core	5.0	7.0	2.0	1.0	-
	shell	3.0	6.0	-	-	1.0
Rho-Fe _x O _y -I _{2.3%} @POS	core	5.0	7.0	2.0	1.0	-
	shell	3.0	6.0	-	-	1.0
Coum-Fe _x O _y -I _{2.3%} @POS	core	5.0	7.0	2.0	1.0	-
	shell	3.0	6.0	--	-	1.0

6.1.4 Surface Functionalization of Magnetofluorescent Polyorganosiloxane Nanoparticles

6.1.4.1 Hydrid-functionalized Polyorganosiloxane Nanoparticles

Hydrid-functional groups have to be introduced to the polyorganosiloxane nanoparticles before the PEG can be covalently linked to the surface. To provide a high number of binding sites the hydrid groups were incorporated into the particles shell during the particle synthesis as well as the end-

capping process. Therefore, 1 g of T monomer was replaced by 1 g of triethoxysilane (T-H) monomer during the assembly of the particle shell as reported in Chapter 6.1.2. The end-capping process was altered as described below.

To 18.75 g of the aqueous polyorganosiloxane dispersion 11.25 g of tetramethyldisiloxane (M-H) was added and stirred overnight. Afterwards, the dispersion was destabilized by precipitation in 150 mL of methanol and centrifugated. The precipitate was dissolved in 50 mL toluene and residual methanol and water were removed by rotary evaporation at 40 °C in vacuum. 2.6 g of tetramethyldisiloxane was added and the solution was stirred overnight.

6.1.4.2 Synthesis of Heterofunctional Poly(ethylene glycol) (PEG)

a-allyl-w-carboxy-poly(ethylenen glycol) was synthesized via anionic polymerization following a method first reported from O. Rheingans.⁶¹ The whole process was operated in a water-free atmosphere using a Schlenk line. THF was dried using sec-butyl lithium and for drying of allyl alcohol a molecular filter was used.

First, 640 mg (5 mmol) of naphthaline dissolved in 5 mL THF were dropped to a 5 mL THF solution of 195.5 mg (5 mmol) potassium. A deep green color appeared after a few minutes. After stirring for one hour the initiator (allyl alcohol, 0.85 g, 14.6 mmol) was deprotonated by addition to the freshly prepared naphthaline potassium solution.

761 mg (2.88 mmol) of 18-crown-6 ether were dissolved in 50 mL THF in a 250 mL three-neck-flask and 145 mg (2.5 mmol) of the initiator (allyl alcohol) was added. The freshly prepared naphthaline potassium solution was injected until a persistent green coloration was obtained. Ethylene oxide was condensed into the solution using a gas condenser filled with an acetone-dry-ice mixture. The solution was stirred for two days. For molecular weight control, GPC measurements were performed at different stages of the reaction. Afterwards, the sample was concentrated and precipitated in isopropanol at -18 °C. The resulting solid was separated via filtration and purified by refluxing in benzol after addition of charcoal. After freeze-drying from benzene solution a white powder was obtained.

6.1.4.3 Hydrosilation Reaction

In a typical procedure, 10 equivalent heterofunctional PEG (typically 1.0 mg) was dissolved in 5 mL of toluene in a 100 mL three-neck-flask at 50 °C. Afterwards, the toluene solution of polyorganosiloxane nanoparticles (1 equivalent, typically 5 mL of toluene solution $c = 20$ mg/mL) was added and the setup was rinsed with argon. The catalyst (Karstedt-catalyst dissolved in xylene (2.1-2.4 % platinum), 0.1 mL) was injected through a septum and the solution was stirred for two days at 55 °C.

The toluene was removed by rotary evaporation and the viscous residue was dissolved in 20 mL of deionized water. After ultrasonic treatment the turbid solution was dialyzed to remove free PEG chains. After two weeks, a clear slightly colored solution was obtained.

6.1.5 Biomodification

The coupling of biomolecules to the carboxyl chain-end of the surface attached poly(ethylene glycol) was performed via EDC coupling.

1 mL of fluorescent, magnetically loaded polyorganosiloxane nanoparticles in aqueous solution ($c \approx 10$ g/L) was mixed with 4 mL MES buffer (50 mM, pH = 4-5). The biomolecular compound (50 mg) was dissolved in 5 mL MES buffer and added to the particle solution. Afterwards, 100 mg EDC was added to initiate the coupling reaction. After stirring overnight, the particles were isolated via dialysis against water.

6.2 Methods

6.2.1 Electron Microscopy

6.2.1.1 Transmission Electron Microscopy (TEM)

Transmission electron microscopy (TEM) was performed with a Philips CM-12 microscope at 120 kV. Samples were prepared by air-drying drops of aqueous solutions on carbon films supported by copper grids.

6.2.1.2 Cryogenic Electron Microscopy (cryo-TEM)

The quick-freezing of the cryo-TEM samples was performed using a Vitrobot (FEI) in liquid propan. Plasma cleaning of the grids (Quantifoil “Holey Carbon Films” R2/1) was performed for 30 seconds directly before use.

6.2.2 Asymmetrical flow field-flow fractionation (AF-FFF)

The asymmetrical flow field-flow fractionation (AF-FFF) from Consensus consisted of an AF-FFF channel system 2.0. Poly(ethersulfone) Membranes were utilized as semipermeable walls (MWCO: 4 kDa). As eluent degassed milliQ water with NaCl (5 mmol/L) and TWEEN 20 (100 mg/L) was used. A Waters 486-UV detector operating at 254 nm monitored the eluting particles. Commercially available poly(styrene) nanoparticles were used for calibration.

6.2.3 Light Scattering

Dynamic light scattering (DLS) was performed at 20°C using a multi-angle light scattering setup with an ALV/CGS-8F DLS/SLS 5022F goniometer, an ALV-7004 Correlator, a 35 mW HeNe-Laser ($\lambda_0 = 633$ nm) and an APD avalanche photodiode optic detection system. Measurements were performed between 30° and 150° at 8.5°-intervals. To each sample a 5 mM solution of NaBr was added and was filtered with Millex-LG filters (pore size 0.2 μm , Millipore).

6.2.4 Super Conducting Quantum Interference Device (SQUID)

The superconducting quantum interference device (SQUID) measurements of the dried samples were performed in a gelatine capsule using a Quantum Design Squid-Magnetometer MPMS XL at 5 K and at 300 K with magnetic field strengths between -80 000 and 80 000 Oe.

6.2.5 Mössbauer Spectroscopy

A constant acceleration Mössbauer spectrometer with a ^{57}Co -source in Rh was used for the measurements of the dried samples. The isomeric shift was measured relative to $\alpha\text{-Fe}$ at room temperature and at 80 K. For data analysis the software “Recoil” was used.

6.2.6 MALDI-TOF

The MALDI-TOF measurements were performed using a TofSpec E instrument from Micromass. All samples were measured in the linear mode. HABA and potassium trifluoroacetate were used as matrix and ionization salt.

6.2.7 Size Exclusion Chromatography (SEC)

Size exclusion chromatography was performed in THF solution using MZ-SDplus 5 μm columns which were purchased from MZ-Analysetechnik. For detection, a Waters 2410 RI detector was used. Calibration was performed using polystyrene standards.

6.2.8 Fluorescence Measurements

6.2.8.1 Fluorescence Spectroscopy

For fluorescence spectroscopy a Jasco FP-6500 spectrofluorometer was used. The source was a DC-powered 150 W Xenon lamp which employs a photometric ratio system. All samples were measured applying a scanning rate of 100 nm/min.

6.2.8.2 Fluorescence Microscopy

Fluorescence microscopy was performed using a Zeiss Imager in combination with an Exfo light source, a Princeton Instruments electron multiplying CCD-camera and a 40x objective which was purchased from Zeiss. For fluorescence detection, a filter set from Edmund Optics was used. Flow cell were purchased from VitroCom (ID: 0.1 x 2.0 x 100 mm, wall: 0.1 mm).

6.2.9 ζ -potential

ζ -potentials measurements were performed using a Malvern Zetasizer Nano ZS. For measurements of iron oxide and iron oxide/DBS solutions, undiluted samples were used. PEG containing samples were

diluted with Milli-Q water before measurement (1:10 dilution, initial concentration: $c \approx 10$ g/L).

6.2.10 Cell Testings

For cell testings, the cells were incubated in presence of the magnetic nanoparticles (100 μ L of aqueous solution corresponding to 10 vol-% of nanoparticles in cell culture medium) in serum free medium (RPMI1640). After two hours, FCS (5 μ L) is added and the particles are further incubated for 2 h.

7 Appendix

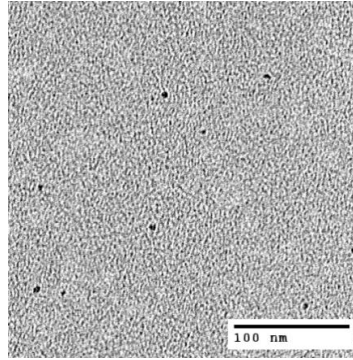


Figure 7.1 TEM image of aqueous $\text{Fe}_x\text{O}_y/\text{DBS}$ mixture prepared by slow addition of DBS (10 mL/h) to an iron oxide dispersion ($c(\text{Fe}_x\text{O}_y) = 0.02 \text{ g/L}$, $S = 0.02$)

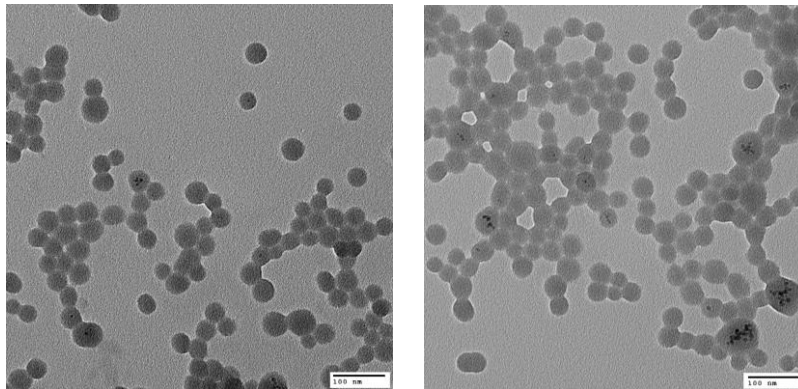


Figure 7.2 TEM images of $\text{Fe}_x\text{O}_y\text{-I}_{2.3\%}\text{POS}$ after deposition from aqueous dispersion

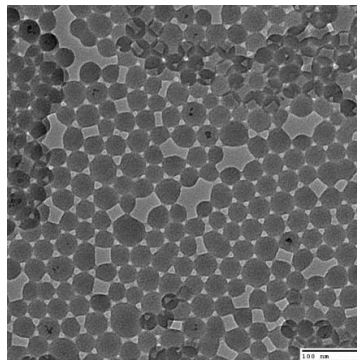


Figure 7.3 TEM of „non-magnetic“ fraction obtained after magnetic separation of $\text{Fe}_x\text{O}_y\text{-I}_{2.3\%}\text{@POS}$ (deposition from toluene solution)

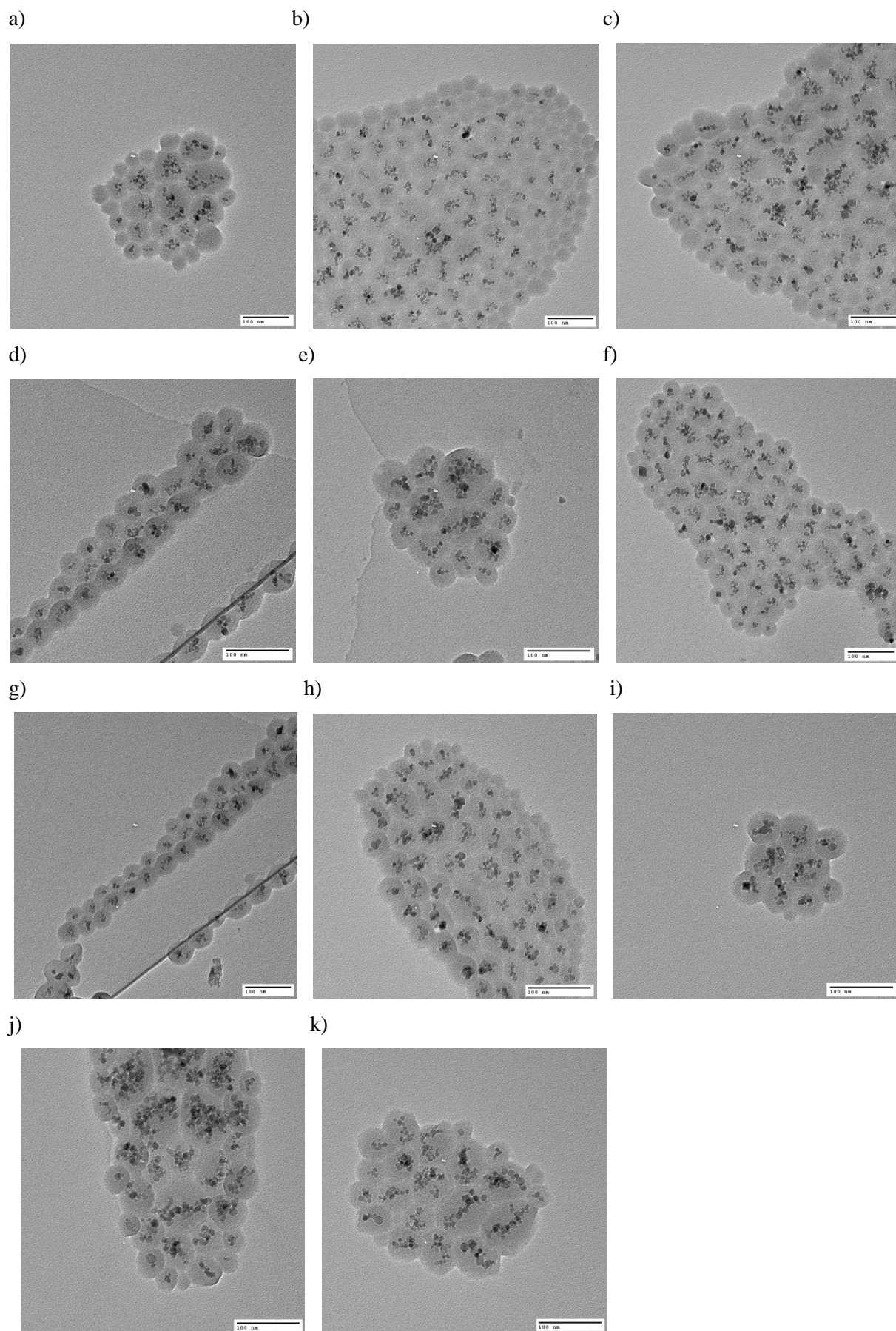


Figure 7.4 TEM images of magnetically loaded polyorganosiloxane nanoparticles after magnetic fractionation used for statistic evaluations of particle size and number of encapsulated particles: a-c) Fe_xO_y-

I_{2.3%}@POS; d)-g) Fe_xO_y-I_{1.5%}@POS; h)-k) Fe_xO_y-I_{1.2%}@POS

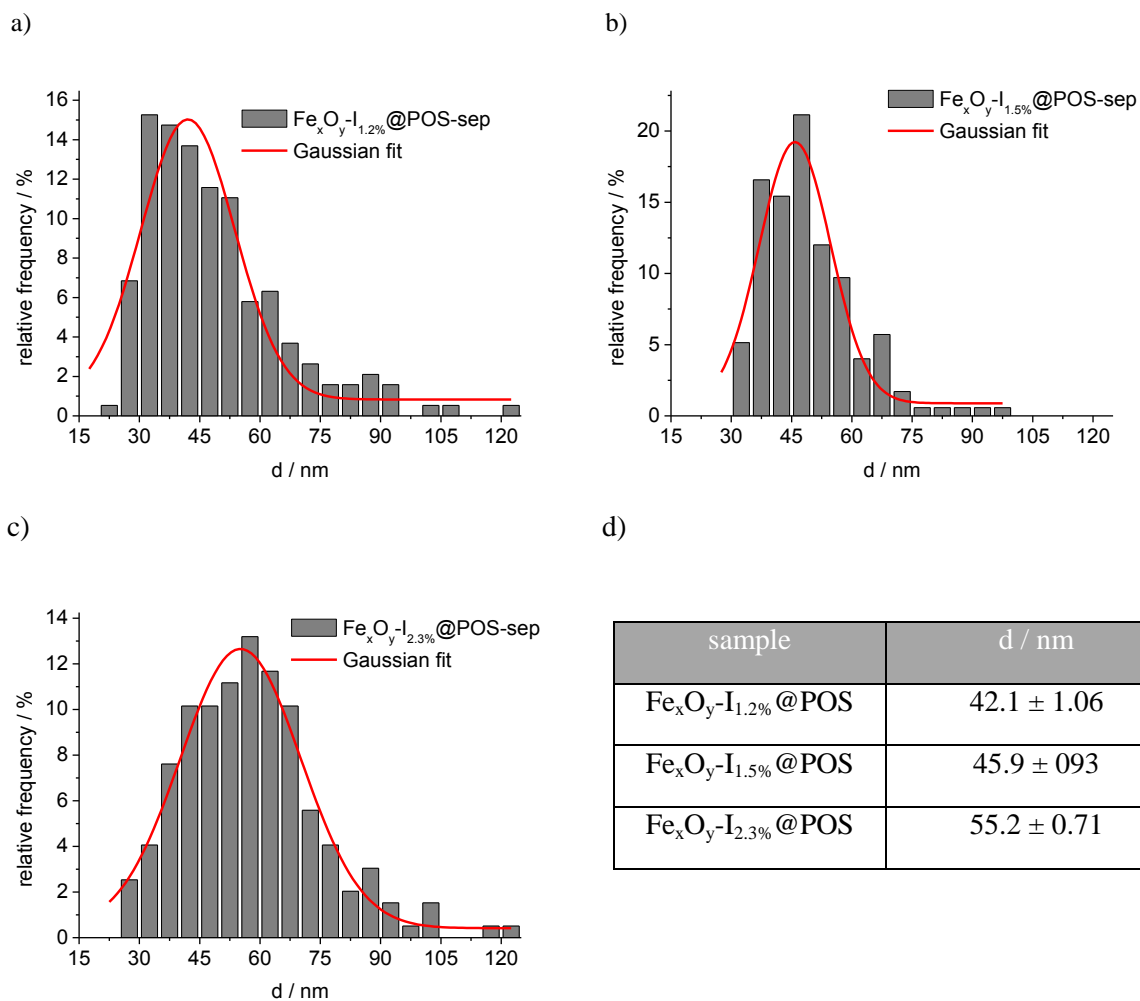


Figure.7.5 a-c) Particle size distribution histogram of magnetically loaded polyorganosiloxane nanoparticles determined from TEM images after deposition from toluene solution and d) results of Gaussian fits

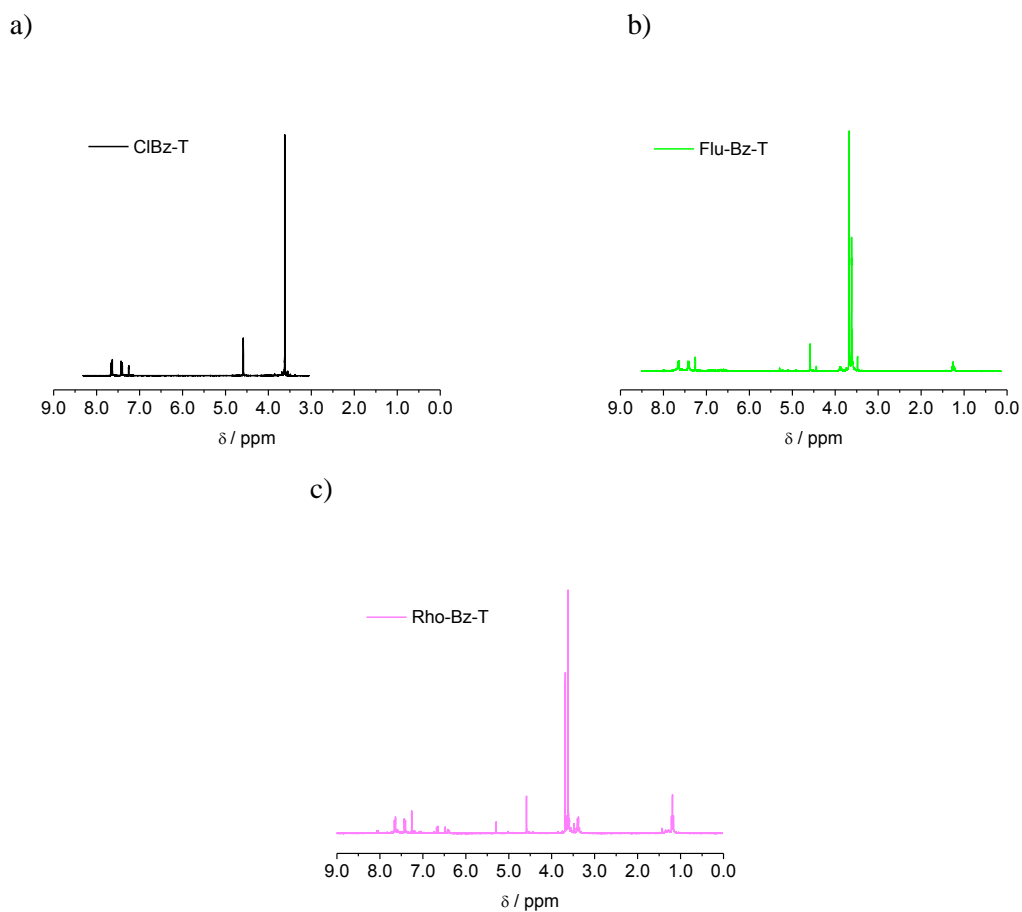


Figure 7.6 $^1\text{H-NMR}$ spectra of a) CIBz-T, b) Flu-Bz-T and c) Rho-Bz-T (with 18-crown-6 ether peak at 3.5 ppm)

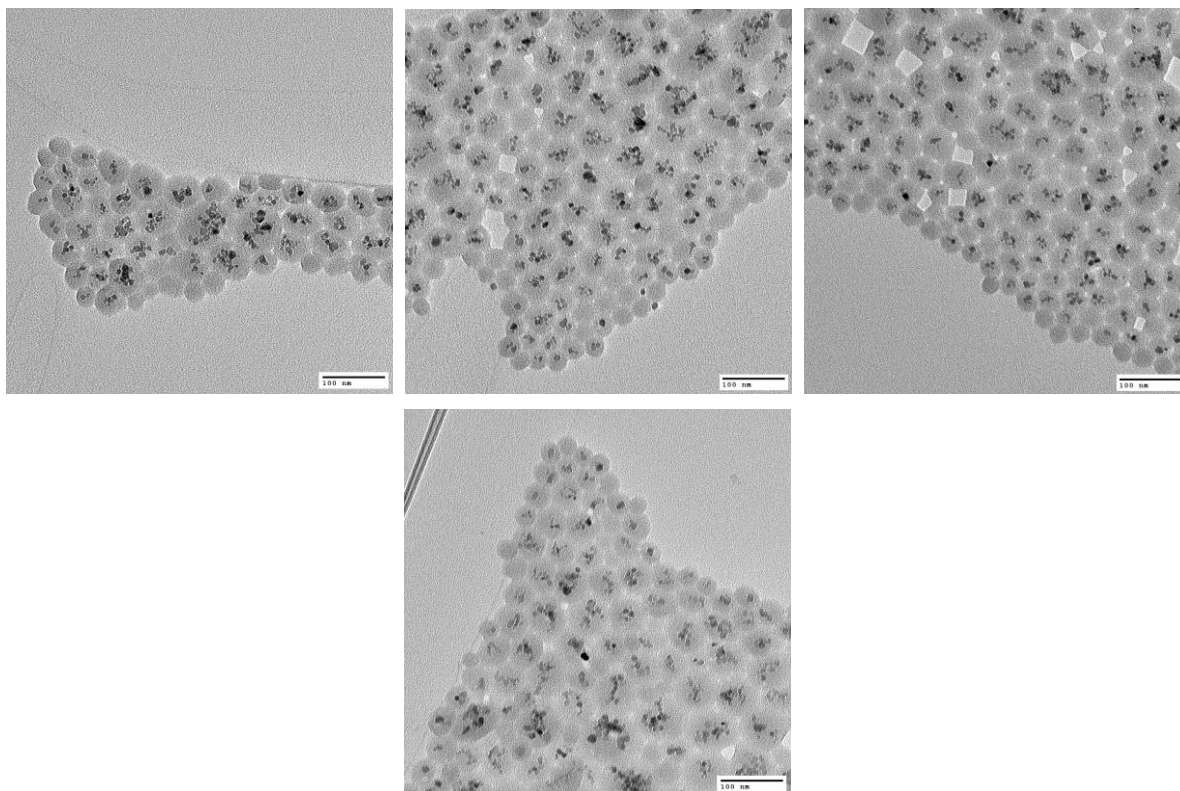


Figure 7.7 TEM images of Flu- $\text{Fe}_x\text{O}_y\text{-I}_{2.3\%}\text{@POS}$ after magnetic separation used for statistic evaluations

on the number of encapsulated particles

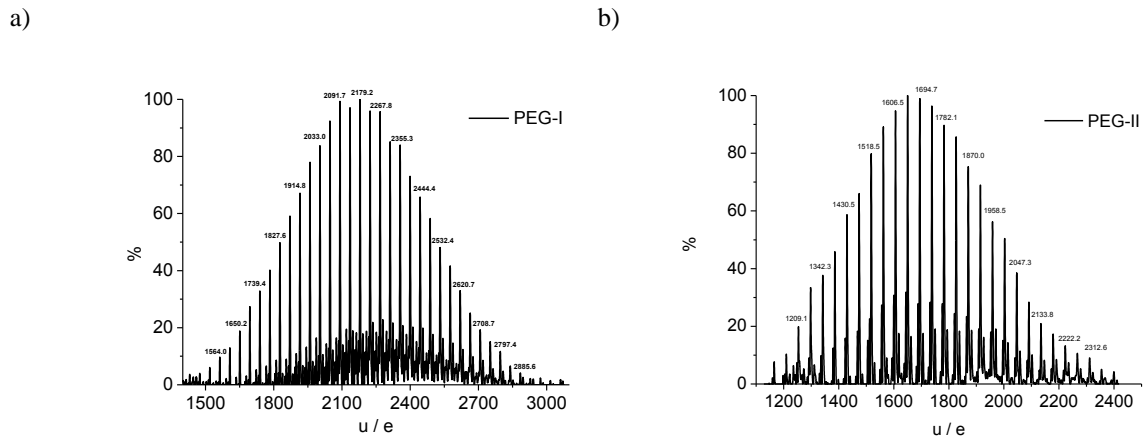


Figure 7.8 MALDI-TOF analysis of poly(ethylene glycol): a) PEG-I; b) PEG-II

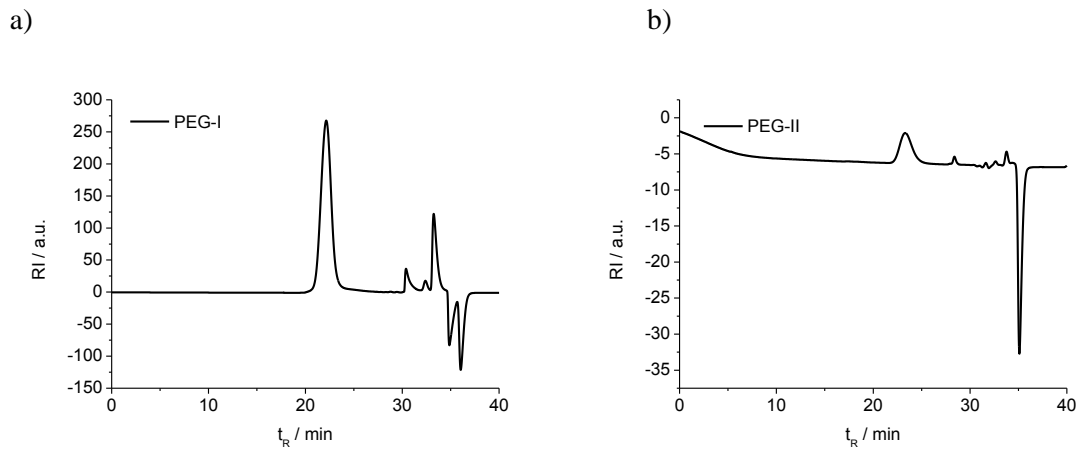


Figure 7.9 GPC measurements of poly(ethylene glycol): a) PEG-I; b) PEG-II

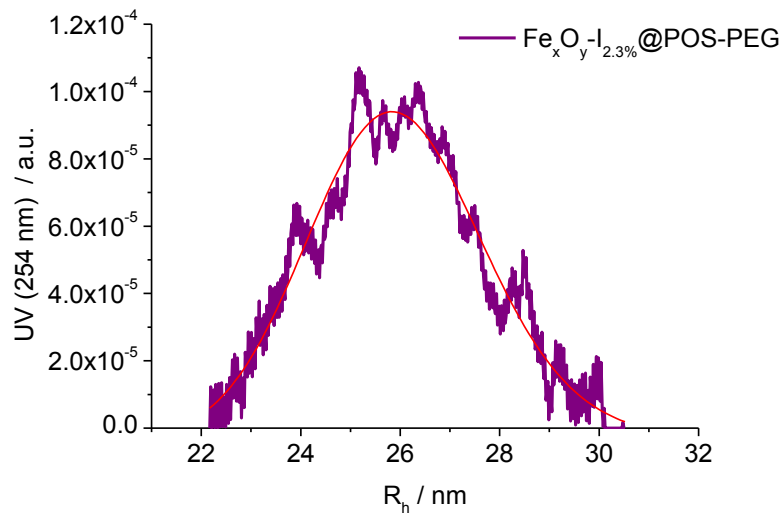


Figure 7.10 Particle size determination via AF-FFF of $\text{Fe}_x\text{O}_y\text{-I}_{2.3\%}\text{@POS-PEG}$

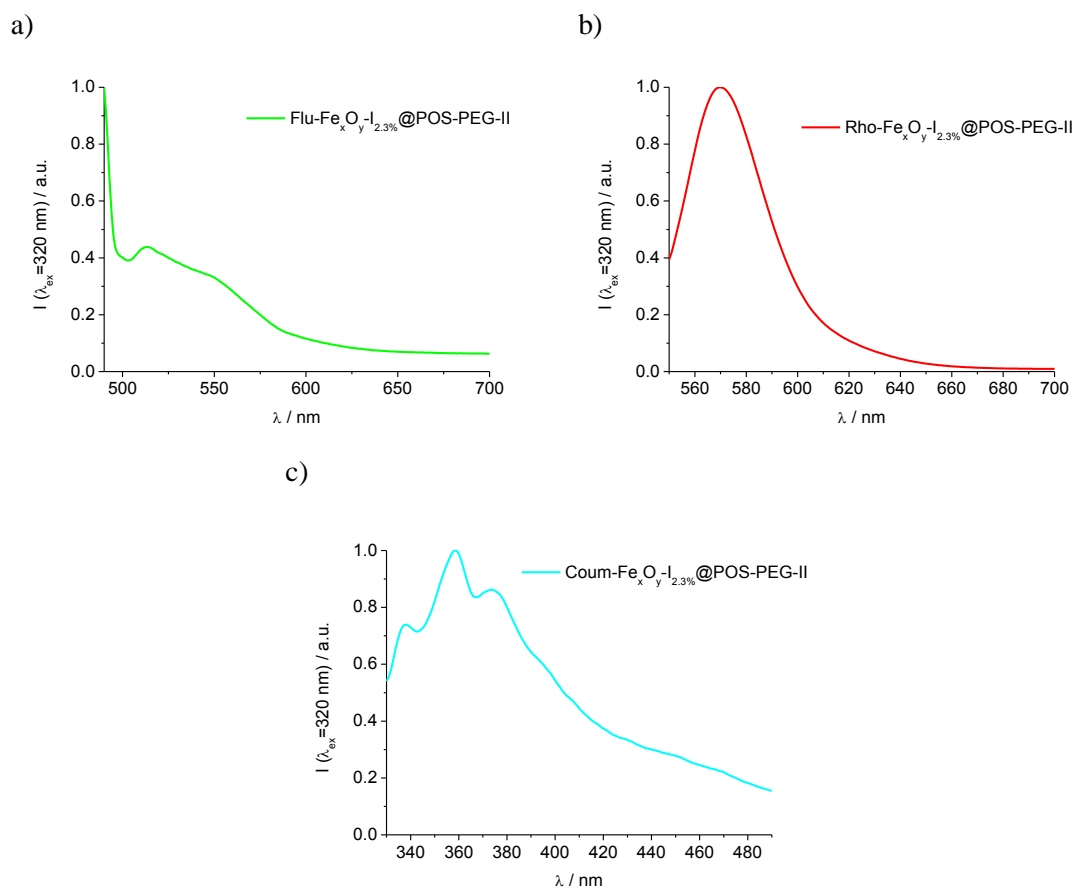


Figure 7.11 Emission spectra of dye labeled, magnetically loaded polyorganosiloxane nanoparticles: a) Flu- $\text{Fe}_x\text{O}_y\text{-I}_{2.3\%}\text{@POS-PEG}$; b) Rho- $\text{Fe}_x\text{O}_y\text{-I}_{2.3\%}\text{@POS-PEG}$; c) Coum- $\text{Fe}_x\text{O}_y\text{-I}_{2.3\%}\text{@POS-PEG}$

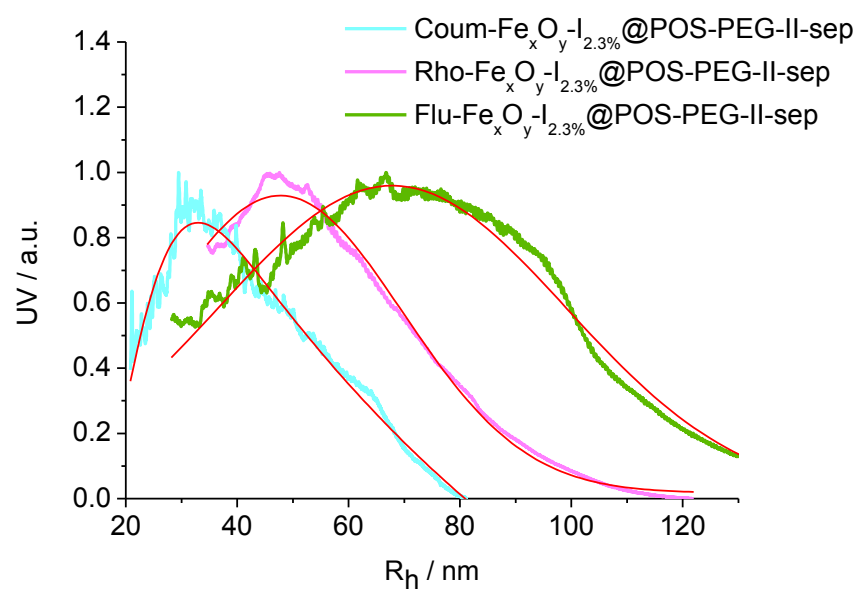


Figure 7.12 AF-FFF measurements of water-soluble magnetofluorescent polyorganosiloxane nanoparticles after magnetic fractionation

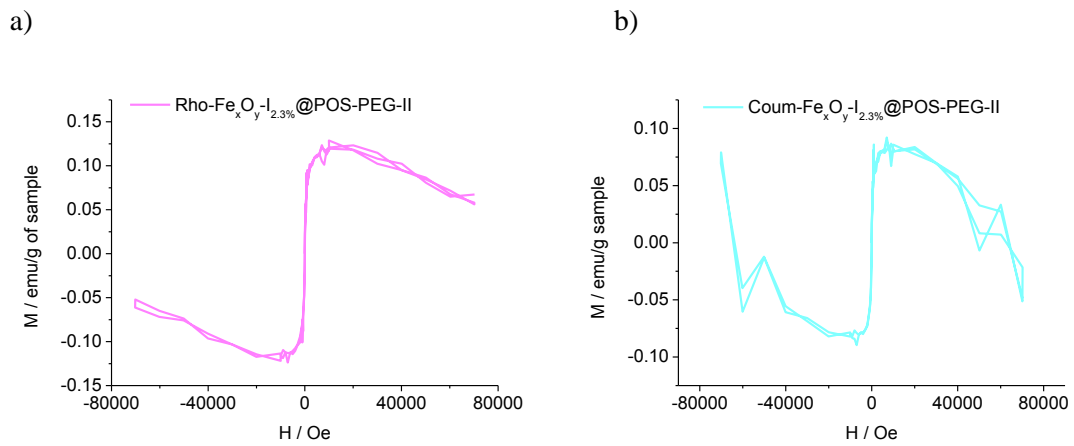


Figure 7.13 Magnetization curves of a) Rho-Fe_xO_y-I_{2.3%}@POS-PEG and b) Coum-Fe_xO_y-I_{2.3%}@POS-PEG

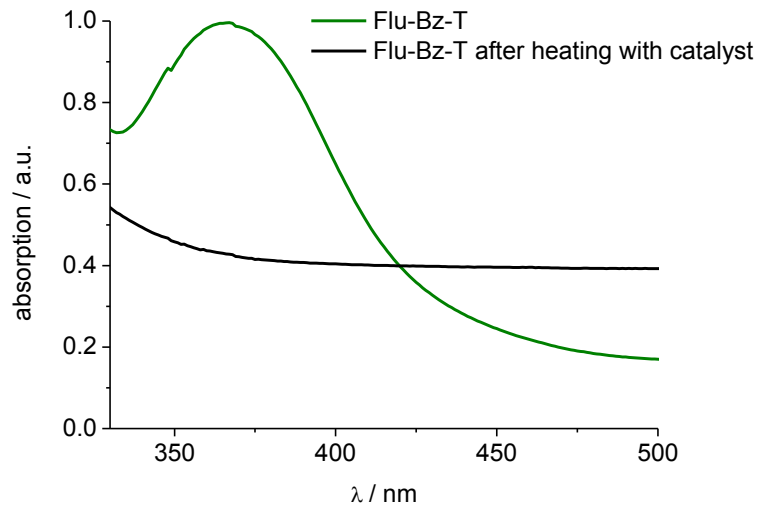


Figure 7.14 UV/VIS spectrum of Flu-Bz-T before and after heating with catalyst (overnight at 55 °C under argon atmosphere)

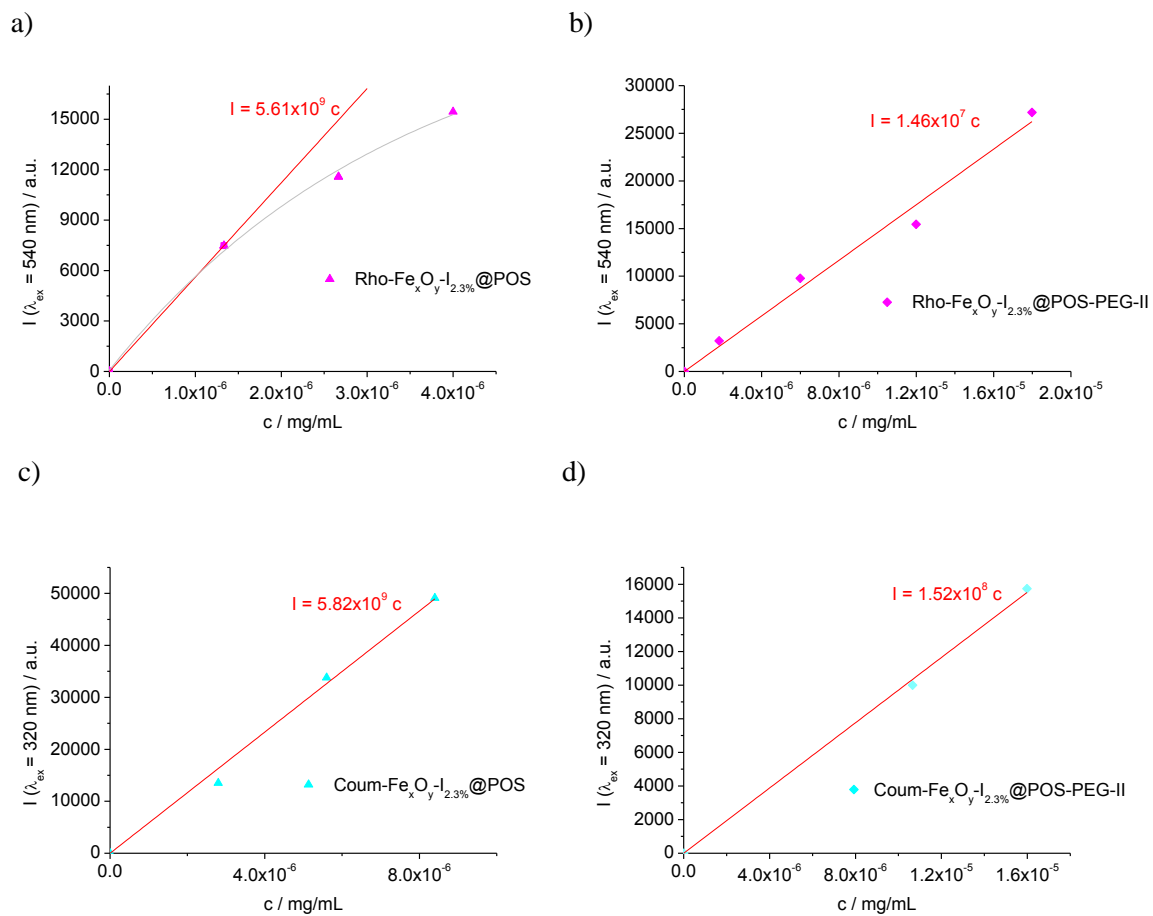
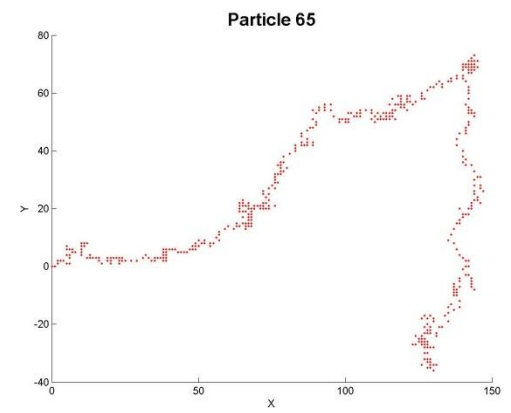
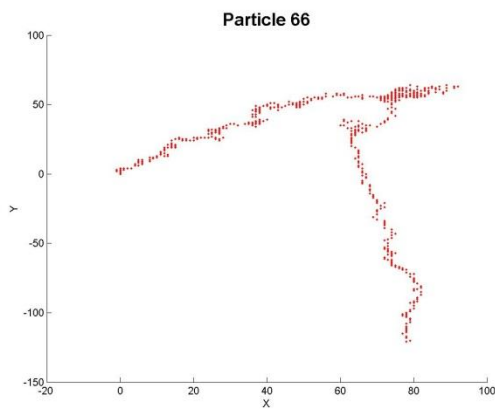
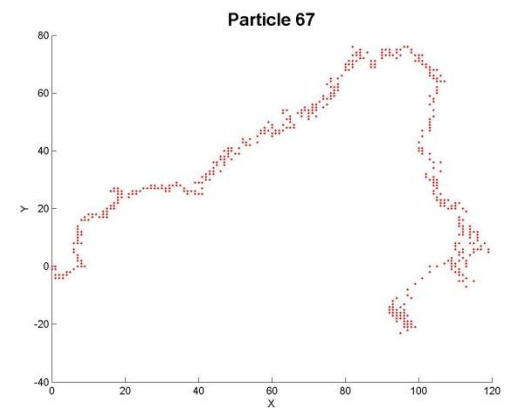
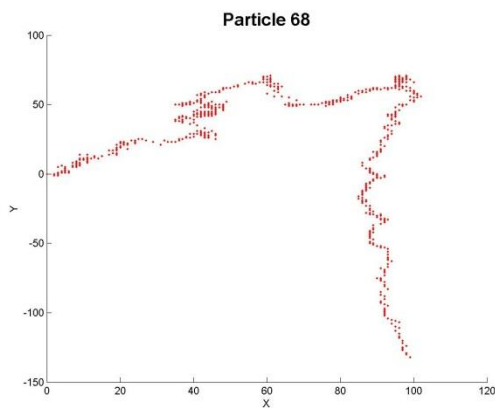
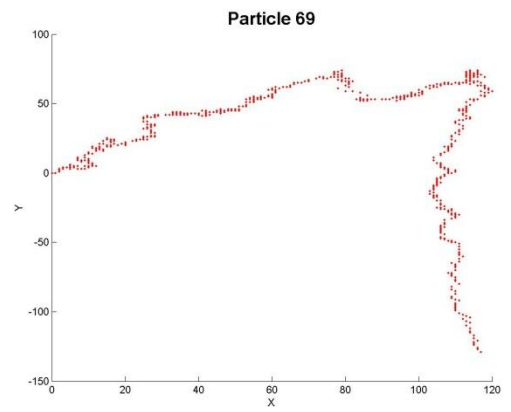
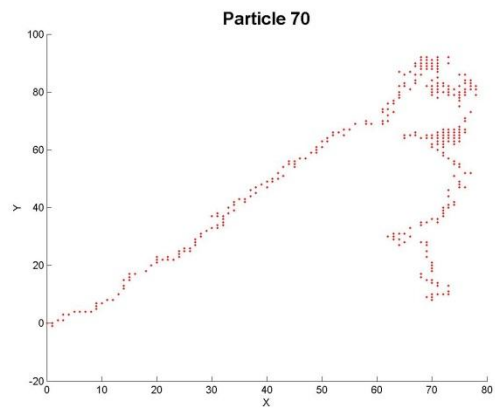
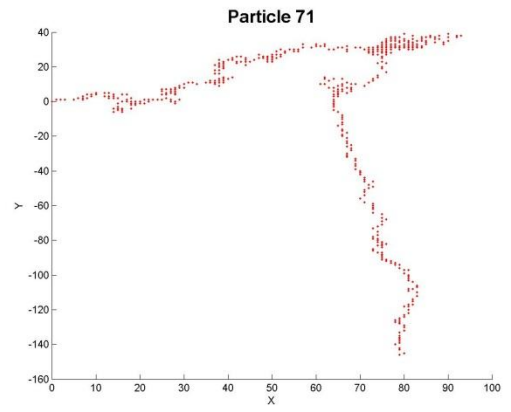
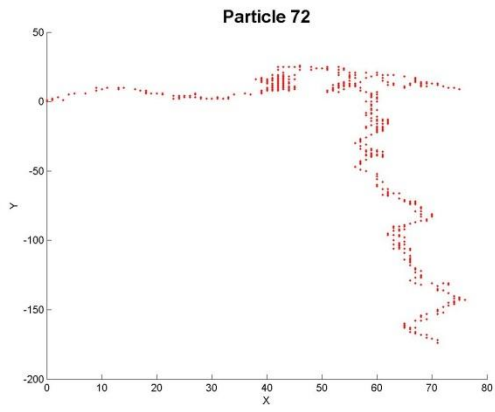
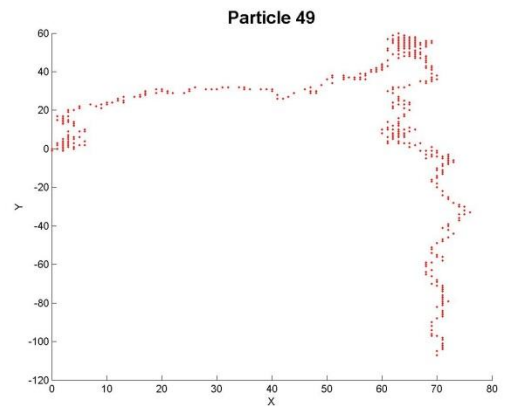
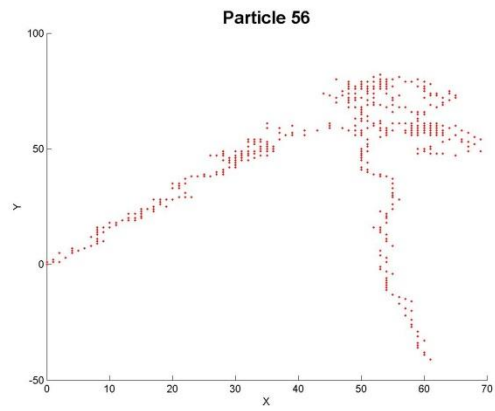
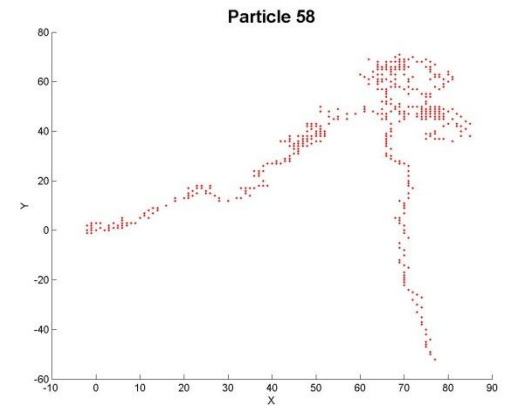
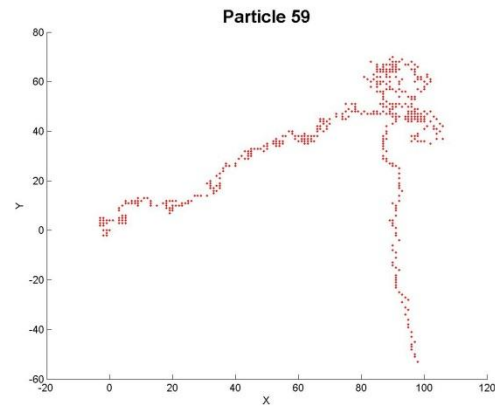
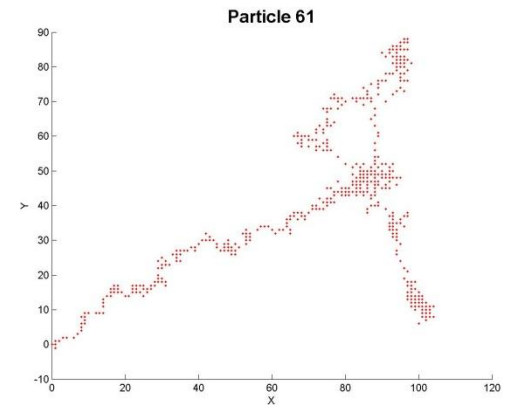
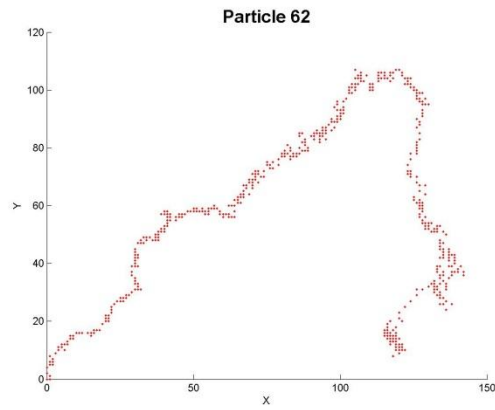
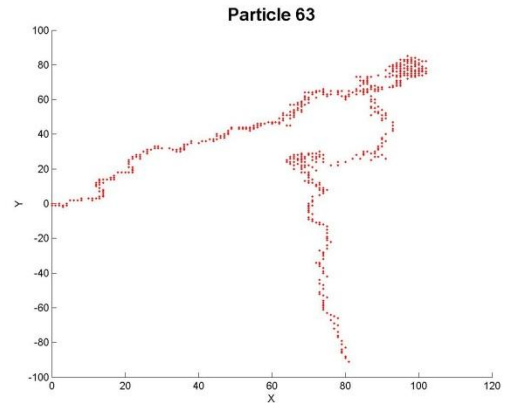
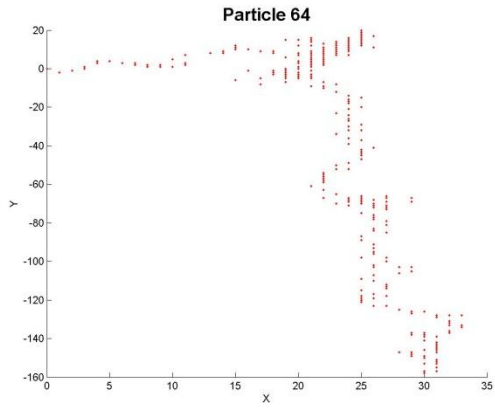
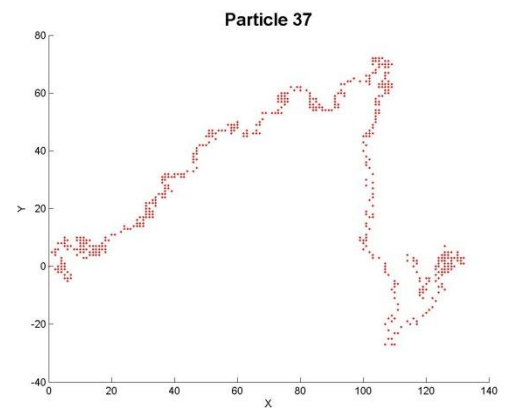
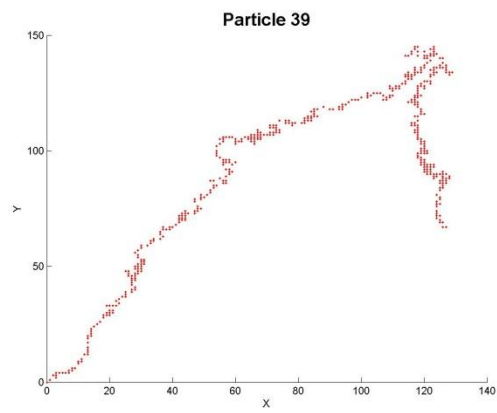
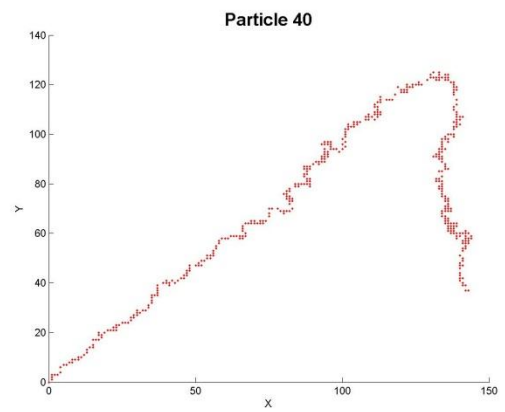
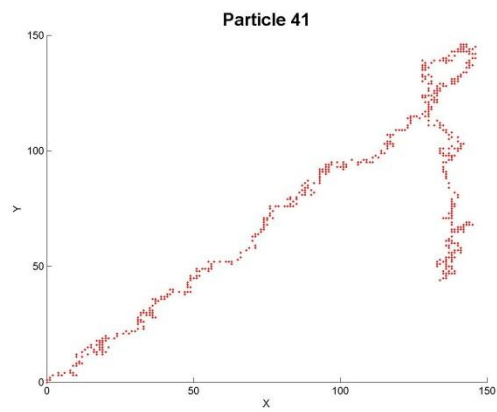
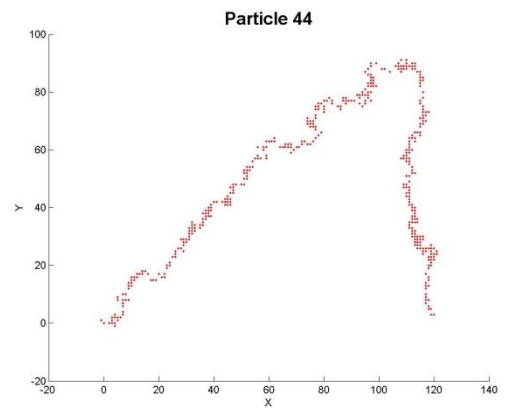
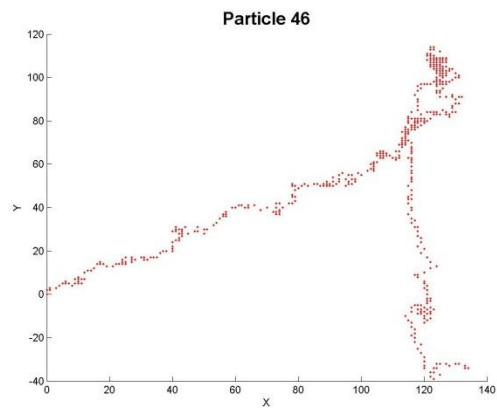
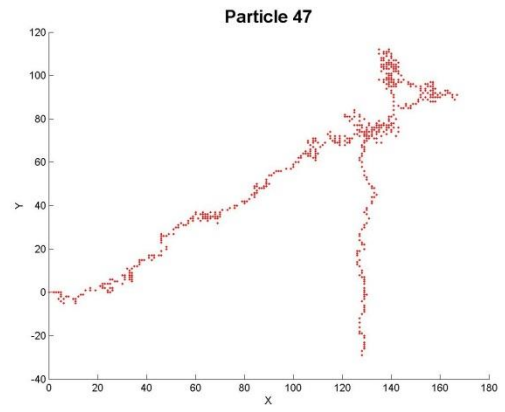
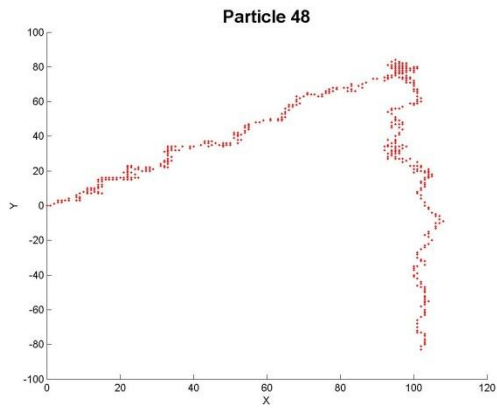
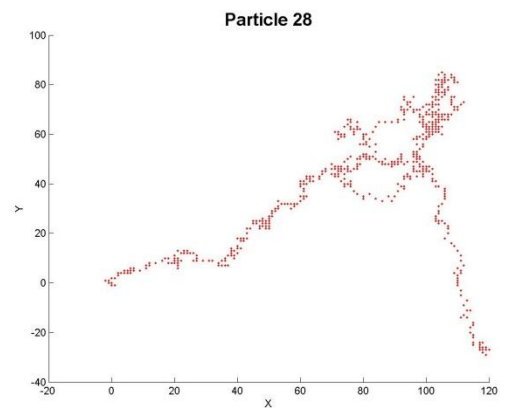
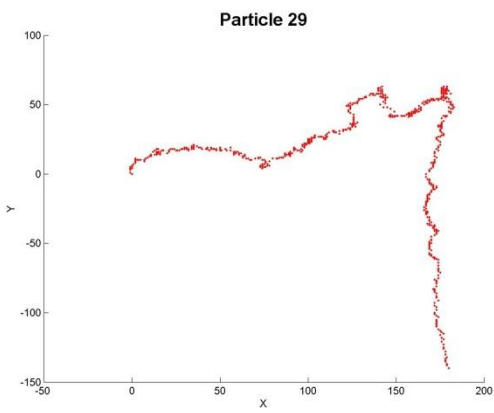
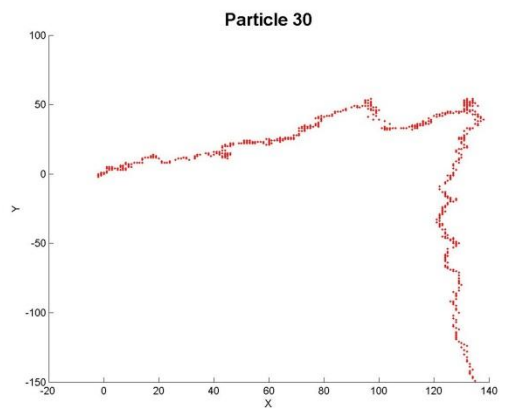
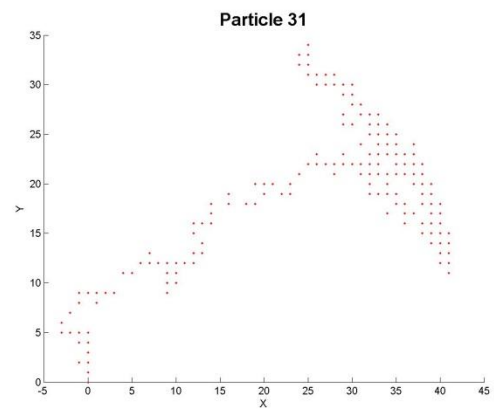
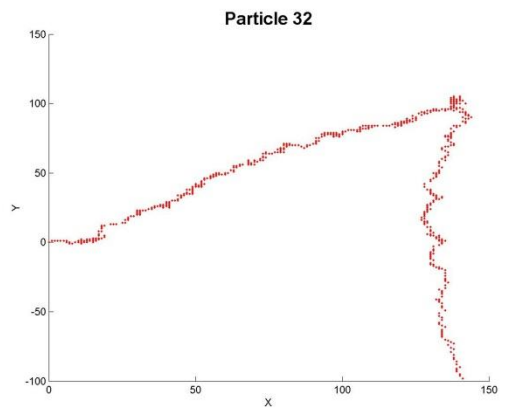
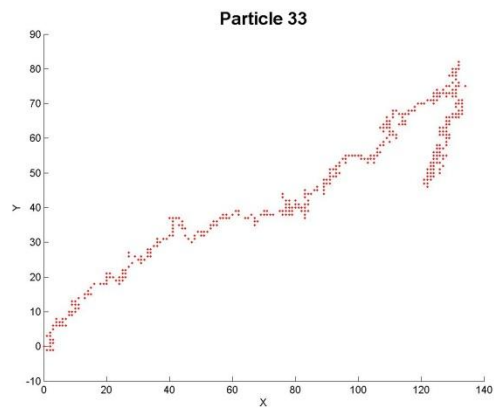
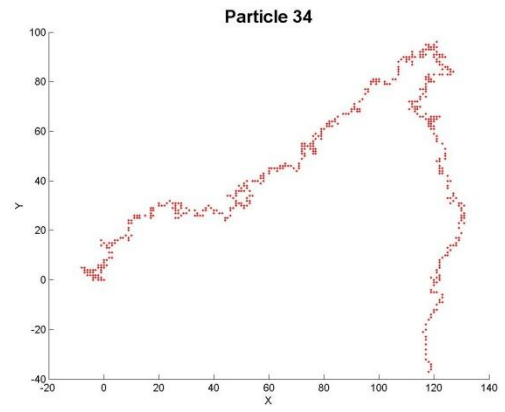
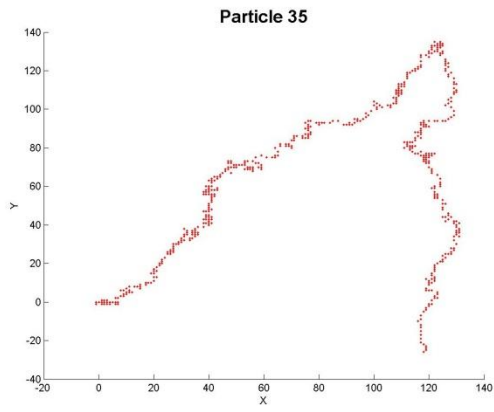


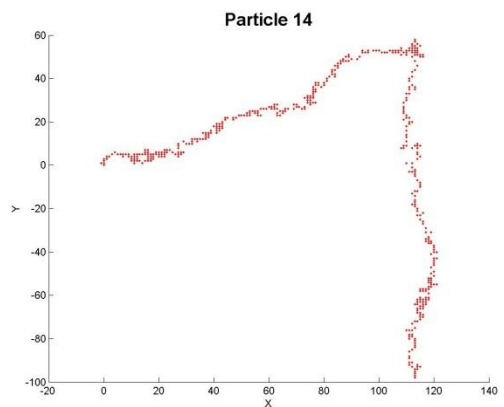
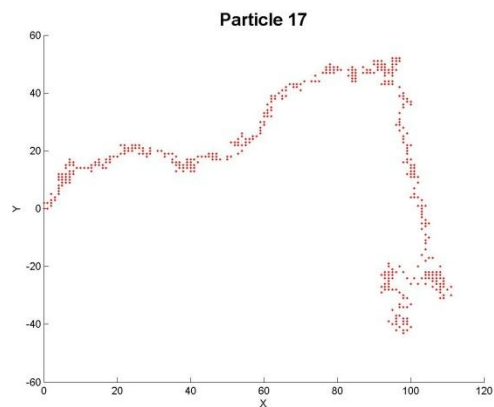
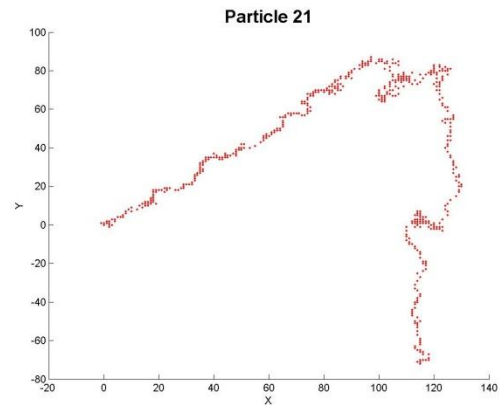
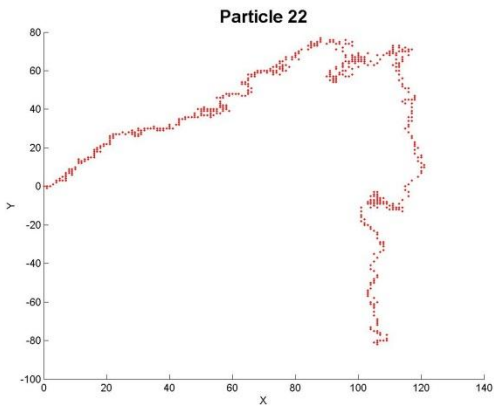
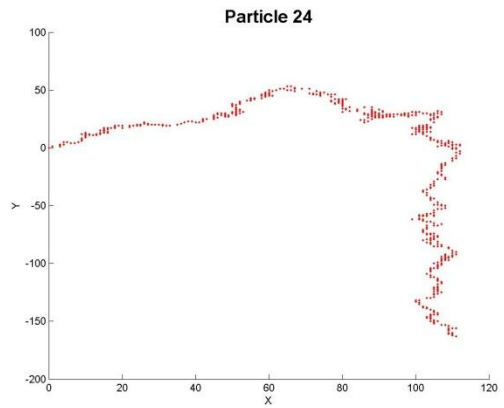
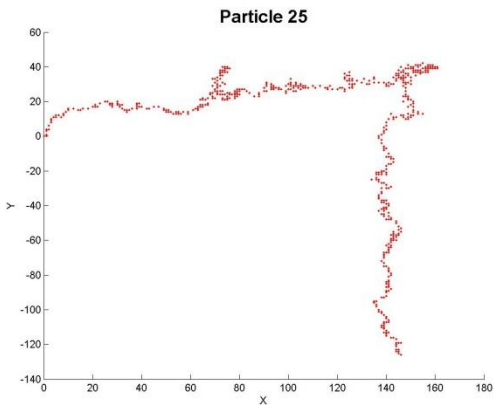
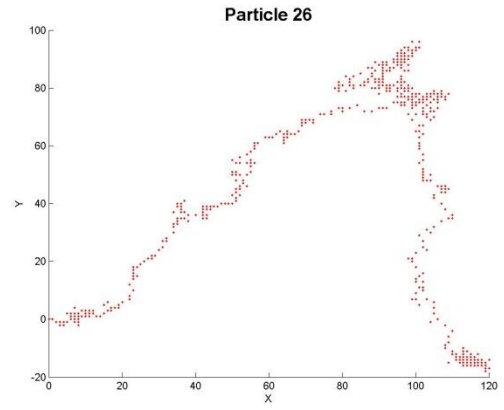
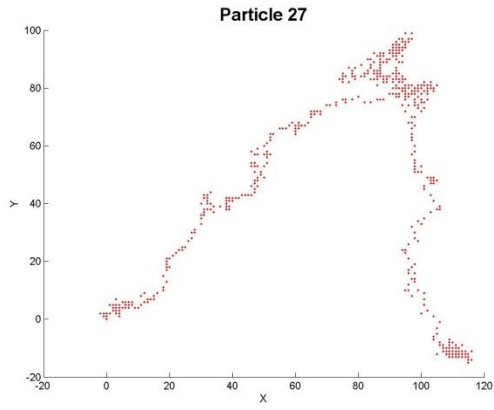
Figure 7.15 Concentration dependent fluorescence intensity of dye labeled polyorganosiloxane nanoparticles: a) rhodamine and c) coumarine labeling before and b) rhodamine and d) coumarine labeling after surface modification











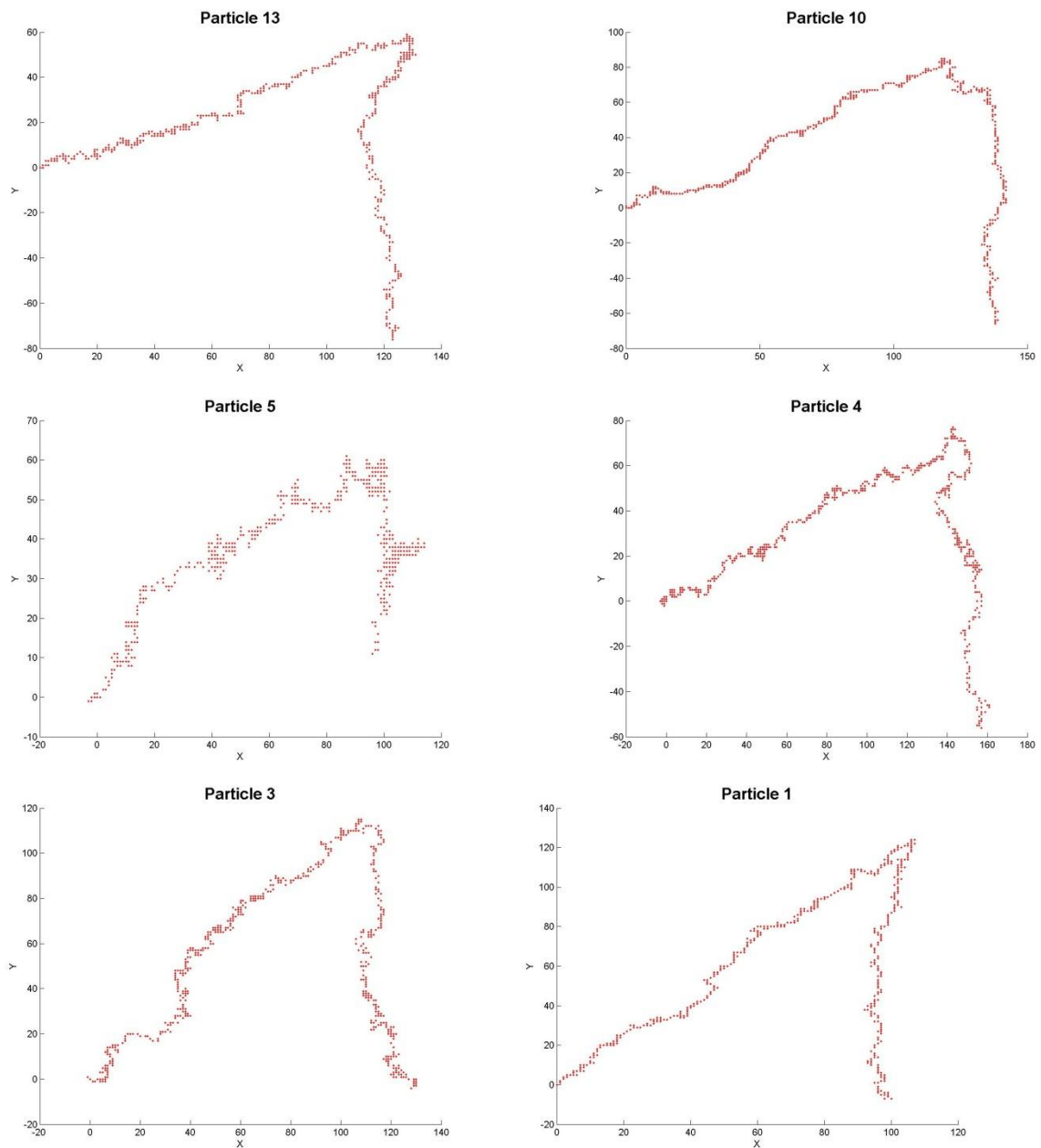


Figure 7.16 Position traces of rhodamine-labeled particles monitored via fluorescence microscopy and data extraction using a MATLAB-based computer program

Magnetic calculations:

$$B(x) = \frac{Br}{\pi} \left[\arctan \frac{AB}{2x\sqrt{4x^2 + A^2 + B^2}} \right] - \left[\arctan \frac{AB}{2(L+x)\sqrt{4(L+x)^2 + A^2 + B^2}} \right]$$

with the material-specific remanent flux density Br and the dimensions of the magnet $AxBxL$

$$\begin{aligned} B(x)B'(x) &= \left(\frac{Br}{\pi} \right)^2 \left(\frac{AB(8x^2 + A^2 + B^2)}{(A^2B^2 + 4x^2(4x^2 + A^2 + B^2))\sqrt{4x^2 + A^2 + B^2}} \right. \\ &\quad \left. - \frac{AB(8(x+L)^2 + A^2 + B^2)}{(A^2B^2 + 4(x+L)^2(4(x+L)^2 + A^2 + B^2))\sqrt{4(x+L)^2 + A^2 + B^2}} \right) \left(\arctan \left(\frac{AB}{2x\sqrt{4x^2 + A^2 + B^2}} \right) \right. \\ &\quad \left. - \arctan \left(\frac{AB}{2(x+L)\sqrt{4(x+L)^2 + A^2 + B^2}} \right) \right) \end{aligned}$$

$$B(x)B'(x) \approx \left(\frac{Br}{\pi} \right)^2 \frac{1}{L}$$

Table 7.1 Components of RPMI1640

COMPONENTS	Molecular Weight	Concentration (mg/L)	Molarity (mM)
Amino Acids			
Glycine	75	10	0.133
L-Arginine	174	200	1.15
L-Asparagine	132	50	0.379
L-Aspartic acid	133	20	0.150
L-Cystine	240	20	0.0833
L-Glutamic Acid	147	20	0.136
L-Glutamine	146	300	2.05
L-Histidine	155	15	0.0968
L-Hydroxyproline	131	20	0.153
L-Isoleucine	131	50	0.382
L-Leucine	131	50	0.382
L-Lysine hydrochloride	183	40	0.219
L-Methionine	149	15	0.101
L-Phenylalanine	165	15	0.0909
L-Proline	115	20	0.174
L-Serine	105	30	0.286
L-Threonine	119	20	0.168
L-Tryptophan	204	5	0.0245
L-Tyrosine	181	20	0.110
L-Valine	117	20	0.171
Vitamins			
Biotin	244	0.2	0.000820
Choline chloride	140	3	0.0214
D-Calcium pantothenate	477	0.25	0.000524
Folic Acid	441	1	0.00227
i-Inositol	180	35	0.194
Niacinamide	122	1	0.00820
Para-Aminobenzoic Acid	137	1	0.00730
Pyridoxine hydrochloride	206	1	0.00485
Riboflavin	376	0.2	0.000532
Thiamine hydrochloride	337	1	0.00297
Vitamin B12	1355	0.005	0.0000037
Inorganic Salts			
Calcium nitrate (Ca(NO ₃) ₂ 4H ₂ O)	236	100	0.424
Magnesium Sulfate (MgSO ₄ ·7H ₂ O)	246	100	0.407
Potassium Chloride (KCl)	75	400	5.33
Sodium Bicarbonate (NaHCO ₃)	84	2000	23.81
Sodium Chloride (NaCl)	58	6000	103.45
Sodium Phosphate dibasic (Na ₂ HPO ₄) anhydrous	142	800	5.63
Other Components			
D-Glucose (Dextrose)	180	2000	11.11
Glutathione (reduced)	307	1	0.00326
Phenol Red	376.4	5	0.0133

8 Abbreviations

$[\eta]$	intrinsic viscosity
μ_{mag}	magnetic moment
μ	permeability
μ_0	permeability in vacuum
μ_2	second cumulant
α	polarizability
χ	magnetic susceptibility
δ	isomeric shift
ΔE_Q	quadrupole splitting
$\varepsilon, \varepsilon_0$	dielectric constant
η	viscosity
κ	Debye-Hückel-parameter
λ	wavelength
μ	electrophoretic mobility
$n\tau$	scattering interval
π	osmotic pressure
θ	scattering angle
σ	<i>surface charge</i>
Ψ	surface potential
ζ	zeta potential
A	acceleration
A	distance between ions and surface
a_η	Kuhn-Mark-Houwink parameter
A	baseline
A_2	second virial coefficient
Abs	absorption
AF-FFF	asymmetrical flow field-flow fractionation
B	constant
B	magnetic induction
B_r	material-specific remanent flux density

C	concentration
CIBz-T	p-chlormethylphenyltrimethoxysilane
Cmc	critical micell concentration
Coum	Coumarin
Coum-T	<i>O</i> -4-methylcoumarinyl- <i>N</i> -[3-(triethoxysilyl)-propyl]-carbamate
cryo-TEM	cryogenic transmission electron microscopy
<i>D</i>	diameter
<i>D</i>	diffusion coefficient
<i>D</i>	diethoxydimethylsilane
DBS	dodecylbenzene sulfonic acid
DLS	dynamic light scattering
DLVO-Theorie	Derjaguin, Landau, Verwey and Overbeek-theory
Dye-Bz-T	dye labeled CIBz-T
Dye-T	dye labeled monomer
<i>E</i>	elemental charge
<i>E</i>	energy
EDX spectroscopy	energy dispersive X-ray spectroscopy
ELS	electrophoretic light scattering
Emu	electromagnetic unit
$f_1(ka)$	Henry function
<i>F</i>	force
F_m	magnetic force
F_s	drag force
FFF	field-flow fractionation
F_{fr}	friction force
Fl	fluorescence
Flu	fluorescein
Flu-Bz-T	p-fluoreceinylmethylphenyltrimethoxysilane
$g_1(t), g_2(t)$	<i>autocorrelation function</i>
GPC	gel permeation chromatography
<i>H</i>	size of diamagnetic shell
<i>H</i>	magnetic field strength
H_{hf}	hyperfine splitting
<i>I</i>	Intensity
<i>I</i>	ionic strength
IC	internal conversion
IX	intersystem crossing

J	magnetic polarization
K	Avogadro constant
k_c	reaction rate of condensation reaction
k_h	reaction rate of hydrolysis reaction
K	Kuhn-Mark-Houwink parameter
M	mass
M	magnetic moment
M	molecular weight
M	ethoxytrimethylsilane
M	magnetization
M-Ac	Diethynyltetramethyldisiloxane
MALDI-TOF mass analysis	matrix assisted laser desorption/ionisation-time of flight mass analysis
M-H	tetramethyldisiloxane
micro-TAS	micro-total analysis system
M_n	number average molecular mass
MRI	magnetic resonance imaging
MRT	magnetic resonance tomography
M_S	saturation magnetization
M_w	weight average molecular mass
M_z	z-average molecular weight
N	stoffmenge
n_D	<i>refractive</i> index
N	particle number
N_A	Avogadro constant
N_L	Loschmidts Zahl
NMR	nuclear magnetic resonance
Oe	Oersted
$P(q)$	form factor
PEG	poly(ethylene glycol)
Ph	phosphorescence
PMMA	poly(methylmethacrylate)
Q	scattering vector
Q	cross section
R	Rayleigh Ratio
R, R'	organic groups
R_g	radius of gyration

R_h	hydrodynamic radius
Rho	rhodamine
Rho-Bz-T	p-rhodaminylmethyl-phenyltrimethoxysilane
RI	refractive index
RT	room temperature
S	fleet ratio
SDS	sodium dodecyl sulfonic acid
SEC	size exclusion chromatography
SLS	static light scattering
SQUID	superconducting quantum interference device
SR	irradiation-free relaxation
T	time
t_r	retention time
t_R	relaxation time
T	Temperature
T	Trimethoxymethylsilane
T	Tesla
T_B	blocking temperature
T_C	Curie temperature
TEM	transmission electron microscopy
T-H	triethoxysilane
THF	tetrahydrofuran
T-vinyl	Trimethoxyvinylsilane
UV	ultraviolet range of spectrum
v	velocity
V	volume
\dot{V}	flow rate
V_e	elution volume
VIS	visible range of light
z	charge number

9 Acknowledgement

10 Curriculum vitae

Stefanie Utech

Dipl.-Chem.

Date of birth February 1th, 1983
Contact E-Mail: utech@uni-mainz.de

Marital status Unmarried
Nationality German

Dissertation

- 12/2007 - dato **Dissertation at the Institute of Physical Chemistry, University of Mainz, Mainz, Germany, in the group of PD Dr. M. Maskos**
Thesis submission: January 2011
Title: *Multifunctional magnetically loaded polyorganosiloxane nanocomposites for biomedical applications*
- 12/2007 – 11/2010 **Scientific co-worker at the “Institut für Mikrotechnik Mainz GmbH (IMM)”, Mainz, Germany**

Education

- 11/2007 **Diploma in chemistry (grade: “sehr gut“)**
- 05/2007 - 11/2007 Diploma thesis at the Institute of Physical Chemistry, University of Mainz, Mainz, Germany, in the group of PD Dr. M.Maskos
Title: *Magnetic polyorganosiloxane nanoparticles*
- 03/2007 **Diploma examination (grade: “sehr gut“)**

- 05/ 2004 **Intermediate diploma in chemistry (grade: “gut“)**
04/2002 - 11/2007 Basic and advanced studies in chemistry at the University of Mainz, Mainz, Germany

School education

- 1993 - 2002 **Käthe-Kollwitz Gymnasium, Neustadt / Weinstraße, Germany**
Abitur (grade: 1.9)
1989 - 1993 Elementary school, Neustadt / Weinstraße, Germany

Awards, scholarships and experiences

- 02/2008 - to date **Member of POLYMAT – Graduate school of excellence, Mainz, Germany**
05/2010 – 06/2010 **Travel scholarship** funded by POLYMAT for a research stay at the Australian Institute for Bioengineering and Nanotechnology (AIBN) of the University of Queensland, Brisbane, Australia, in the research group of Prof. M. Monteiro
Subject: *Synthesis and characterization of microarm and block-co-polymers for nanoparticle stabilization*
06/2009 **Poster award** at the international symposium of “Frontiers in Polymer Science“, Mainz, Germany
Title: *Magnetic polyorganosiloxane nanoparticles*
07/2006 – 09/2006 **Assistant scientist** at the University of Mainz, Mainz, Germany, in the group of Dr. Patrick Théato
Subject: *Novel water-soluble reactive ester polymer architectures*
09/2005 – 03/2006 **DAAD scholarships** for a research stay at the School of Chemical and Biological Engineering of the Seoul National University, Seoul, South Korea, in the research group of Prof. K. Char
Subject: *Influence of magnetic ironoxide nanoparticles on the microphase-separation of PS-block-PI copolymers*
01/2005 – to date **Supervisor of student lab courses and exercises for advanced students** in physical chemistry and macromolecular chemistry at the Institute of Physical Chemistry, University of Mainz, Mainz, Germany

Advanced training and further education

Trainings	Polymer synthesis, Kirchberg, Germany (2008)
	Thermodynamics of polymer containing mixtures, Cadzand-Bad, Netherlands (2008)
	Nanoparticles, Titisee-Neustadt, Germany (2009)
	Physics of biopolymers, Istanbul, Turkey (2009)
Soft skill courses	Scientific writing and poster preparation (2008)
	Oral presentation (2008)
	Introduction to good scientific practice (2009)

Publications

Utech, S.; Bantz, C.; Koshkina, O.; C.; Kasper, J.; Pierrat S.; Kirkpatrick, C. J.; Maskos, M.

Magnetofluorescent polyorganosiloxane nanoparticles carrying biomolecular functionalizations, in preparation

Brunsen, A.; Utech, S.; Maskos, M.; Jonas, U.; Knoll, W.

Magnetic dextran-based hydrogels for biomedical applications

J. Magn. Magn. Mater., submitted

Scherer, C.; Utech, S.; Scholz, S.; Noskov, S.; Kindervater, P.; Graf, R.; Thünemann, A. F.; Maskos, M.

Synthesis, characterization and fine-tuning of bimodal poly(organosiloxane) nanoparticles

Polymer **2010**, *51*, 5439

Utech, S.; Scherer, C.; Krohne, K.; Carrella, L.; Rentschler, E.; Gasi, T.; Ksenofontov, V.; Felser, C.; Maskos, M.

Magnetic polyorganosiloxane core-shell nanoparticles – synthesis, characterization and magnetic fractionation

J. Magn. Magn. Mater **2010**, *322*, 3519

Scherer, C.; Noskov, S.; Utech, S.; Bantz, C.; Müller, W.; Krohne, K.; Maskos, M.

Characterization of polymer nanoparticles by asymmetrical flow field-flow fractionation (AF-FFF)

J. Nanosci. Nanotech. **2010**, *10*, 6834

Utech, S.; Scherer, C.; Maskos, M.

Multifunctional, multicompart ment polyorganosiloxane magnetic nanoparticles for biomedical applications

J. Magn. Magn. Mater. **2009**, *321*, 1386

Conference contributions

Oral presentations

Multifunctional magnetic polyorganosiloxane core-shell nanocomposites for biomedical applications

239th American Chemical Society National Meeting, San Francisco, USA (2010)

Magnetically functionalized polyorganosiloxane core-shell nanospheres for biomedical applications

IMM Young Scientist's Workshop, Mainz (2010)

Multifunctional magnetic core-shell nanocomposites for biomedical applications

First International Conference on Multifunctional, Hybrid and Nanomaterials, Tours, France (2009)

Magnetically loaded polyorganosiloxane nanoparticles for biomedical applications

IMM Young Scientist's Workshop, Mainz (2009)

Magnetic polyorganosiloxane nanoparticles

IMM Young Scientist's Workshop, Mainz (2008)

Poster presentations

Multifunctional magnetically loaded polyorganosiloxane nanocomposites for biomedical applications

Third International NanoBio Conference, Zürich, Schweiz (2010)

Magnetic polyorganosiloxane nanoparticles (awarded poster)

Frontiers in Polymer Science, Mainz (2009)

New magnetic polyorganosiloxane nanoparticles as biologically

functionalized targets for microfluidic applications
Scientific and Clinical Applications on Magnetic Carriers, Vancouver,
Canada (2008)

Additional skills

Languages

German (native language)
English (business fluent)
French (school knowledge)
Spanish (basic knowledge)
Korean (basic knowledge)

Calvin:

“You know what I've noticed, Hobbes? Things don't bother you if you don't think about them. So from now on, I simply won't think about anything I don't like, and I'll be happy all the time!”

Hobbes:

“Don't you think that's a pretty silly and irresponsible way of life?”

Calvin:

“What a pretty afternoon...”

Bill Watterson, Calvin and Hobbes